U.S. DEPARTMENT OF ENERGY

PNNL-22871

Prepared for the U.S. Department of Energy
under Contract DE-AC05-76RL01830

Science-Driven Candidate Search for New Scintillator Materials FY 2013 Annual Report

F Gao
SN Kerisit
YL Xie
D Wu
MP Prange
RM Van Ginhoven
LW Campbell
Z Wang

October 2013

Pacific Northwest NATIONAL LABORATORY

Proudly Operated by Battelle *Since 1965*

PACIFIC NORTHWEST NATIONAL LABORATORY
operated by
BATTELLE
for the
UNITED STATES DEPARTMENT OF ENERGY
under Contract DE-AC05-76RL01830

Printed in the United States of America

Available to DOE and DOE contractors from the
Office of Scientific and Technical Information,
P.O. Box 62, Oak Ridge, TN 37831-0062;
ph: (865) 576-8401
fax: (865) 576-5728
email: reports@adonis.osti.gov

Available to the public from the National Technical Information Service
5301 Shawnee Rd., Alexandria, VA 22312
ph: (800) 553-NTIS (6847)
email: orders@ntis.gov <http://www.ntis.gov/about/form.aspx>
Online ordering: http://www.ntis.gov


This document was printed on recycled paper.
(8/2010)

Science-Driven Candidate Search for New Scintillator Materials FY 2013 Annual Report

F Gao
SN Kerisit
YL Xie
D Wu
MP Prange
RM Van Ginhoven
LW Campbell
Z Wang

October 2013

Prepared for
the U.S. Department of Energy
under Contract DE-AC05-76RL01830

Pacific Northwest National Laboratory
Richland, Washington 99352

Abstract

This annual report presents work carried out during Fiscal Year (FY) 2013 at Pacific Northwest National Laboratory (PNNL) under the project entitled “Science-Driven Candidate Search for New Scintillator Materials” (Project number: PL13-SciDriScintMat-PD05) and led by Dr. Fei Gao.

This project is divided into three tasks, namely (1) *Ab initio* calculations of electronic properties, electronic response functions and secondary particle spectra; (2) Intrinsic response properties, theoretical light yield, and microscopic description of ionization tracks; and (3) Kinetics and efficiency of scintillation: nonlinearity, intrinsic energy resolution, and pulse shape discrimination. Detailed information on the findings and insights obtained in each of these three tasks are provided in this report. Additionally, papers published this fiscal year or currently in review are included in Appendix together with presentations given this fiscal year.

This work was supported by the National Nuclear Security Administration, Office of Nuclear Nonproliferation Research and Development (NA-22), of the U.S. Department of Energy (DOE).

Acronyms and Abbreviations

ABINIT	Electronic structure computer package
DOE	Department of Energy
ERSP	Electronic ReSPonse
FY	Fiscal Year
KMC	Kinetic Monte Carlo
LLNL	Lawrence Livermore National Laboratory
NA-22	Office of Nuclear Nonproliferation Research and Development
NWEGRIM	NorthWest Electron and Gamma-Ray Interaction with Matter
PNNL	Pacific Northwest National Laboratory
STE	Self-Trapped Exciton
STH	Self-Trapped Hole
WFU	Wake Forest University
YAG	Yttrium Aluminum Garnet ($Y_3Al_5O_{12}$)
YAP	Yttrium Aluminum Perovskite ($YAlO_3$)

Contents

Figures

Tables

1.0 Objective and Summary

The main objective of this PNNL project is to further develop, apply, and validate a suite of computational modeling tools to explore the relationship between material properties and scintillator performance by determining the key elementary processes that give rise to a material's light yield, decay times, nonproportionality, energy resolution, and potential particle discrimination capability.

For the purposes of our work, the scintillation process, which is the chain of processes that begins with the interaction of an incident γ-quantum with a scintillator material and terminates with the emission of low-energy photons, is divided into three stages: (1) the energy cascade or electron-hole pair production stage; (2) the thermalization stage where hot electrons and holes thermalize to the edges of the band gap; and (3) the transport, recombination, and luminescence stage. We have made significant progress in developing and applying a suite of simulation tools for modeling all three stages. Under Task 1, we worked to develop theoretical and modeling capabilities based on *ab initio* calculations to provide first-principles based input to our simulations of the three stages of scintillation. Under Task 2, we determined the intrinsic response properties of a range of scintillators materials, finishing our work on halides and extending our research to oxides. Under Task 3, we modeled the nonlinear quenching processes that take place in the third stage and lead to the nonproportional behavior of all scintillators at low incident energies.

Our modeling results agree with a wide range of experimental measurements and other theoretical studies, including z-scan experiments to correlate quenching mechanisms, scintillator light yields, track radii near the track end, and thermalization distances. Additionally, we continue to collaborate with NA-22-funded researchers at LLNL, who are generating first-principles inputs for our kinetic model of scintillation, and at WFU, who are conducting experiments to validate our model predictions. Through the continuing development of a firm theoretical understanding of scintillator physics, work under this project will provide a pathway to optimize current scintillators and lead to the science-driven candidate search for new scintillator materials.

A task-by-task description of this fiscal year's progress follows. All publications and invited presentations are attached in Appendix A in order of presentation.

2.0 Task 1: Ab initio calculations of electronic properties, electronic response functions and secondary particle spectra

2.1 Summary of progress

A quantum theory of electron thermalization was developed and electron-longitudinal optical phonon scattering rates were calculated for CsI. Excited-state electronic properties of halide scintillators were calculated using a parallelized version of our electronic response code.

2.2 Publications/Presentations

L.W. Campbell and F. Gao *Journal of Luminescence* 137 (2013) 121

M. P. Prange, R.M. Van Ginhoven, N. Govind, and F. Gao *Physical Review B* 87 (2013) 115101

R.M. Van Ginhoven and P.A. Schultz *Journal of Physics: Condensed Matter* submitted.

2.3 Progress during FY13

A significant amount of work was done in the previous funding cycle to apply phenomenological models of electron-phonon scattering for predicting the time and spatial scales for electron thermalization in inorganic scintillators. These simulations showed that hot electrons generated during the electron cascade following γ-ray excitation thermalized on the time scale of picoseconds and over distances ranging from 10's to 100's of nanometers. These fairly long predicted thermalization distances indicated that the thermalization stage plays a significant role in determining the proportion of separated electron-hole pairs and thus will have a direct impact on the scintillation yield. The newly recognized importance of the thermalization stage prompted us to begin the development of a next-generation model of electron thermalization rooted more deeply in quantum mechanics. In contrast to the phenomenological models it replaces, our quantum mechanical treatment of electron-phonon interactions requires only the structure of the material as input and accounts for phonons throughout the Brillouin zone. Additionally, anisotropic effects on phonon scattering are fully included from the beginning.

The calculations for this model proceed in three stages: (1) density functional perturbation theory calculation of the phonons using ABINIT; (2) calculation of the scattering potentials; and (3) evaluation of the scattering rates for specific carrier trajectories. Stages (2) and (3) are performed using an in-house code developed this fiscal year. We have developed our model in a way that allows the efficient use of highly parallel computing resources for each of these three stages. In our model, the carriers are represented as classical particles traveling with a specified velocity. In order to sum the effects of carrier interactions with the very numerous phonon modes, our code initially relied on the tetrahedron method to compute integrals over the Brillouin zone of the crystal; but this approach suffered large errors for low-energy electrons due to the combination of singular behavior of the integrand and the complicated shape of the surface of kinematically allowed scatterings in momentum space. In response to these difficulties, we have developed an adaptive integration technique that provides an integration grid guaranteed to represent the surface of kinematically-allowed scattering faithfully. We have completed simulations of low-energy excited electrons interacting with longitudinal optical modes (Fröhlich scattering) using this

adaptive integration technique. The resulting scattering rates as a function of the excited electron's kinetic energy are shown in Figure 1 and compared to two other models. We find that our model predicts slightly weaker scattering than the phenomenological model used to date. Current work focuses on scattering from non-polar phonons that is the dominant energy loss process for hot electrons or those propagating through non-polar materials.

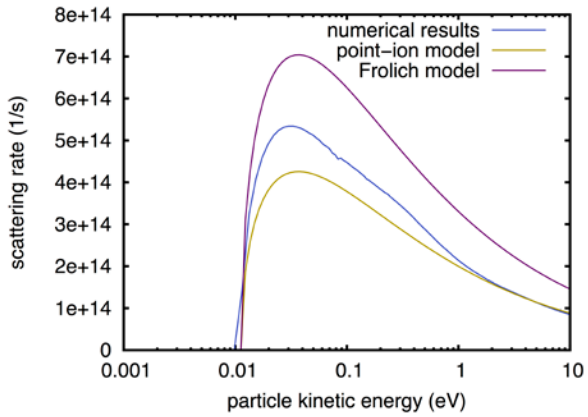

Figure 1. Phonon scattering rates in CsI derived from our newly developed first-principles method**.**

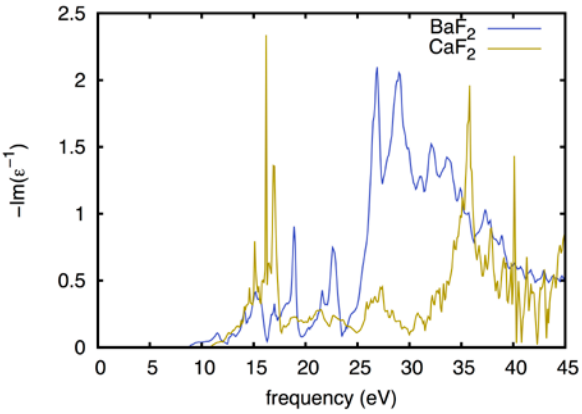

Figure 2. Computed loss function for two alkaline-earth halide scintillators.

Work under this task also included the continuing development and application of the in-house electron structure code ERSP to provide first-principles based input to our Monte Carlo model of the energy cascade. Previous work focused on computing, using ERSP, the dielectric function, loss function, lifetime and scattering rate of quasi-particles due to electronic losses, and secondary particle spectrum due to plasmon decay in two alkali halide scintillators, namely, NaI and CsI, and a manuscript summarizing this work was submitted to and recently published in the *Journal of Luminescence*. This fiscal year, ERSP was transformed from a single-processor code to a parallel multi-processor code. This change allowed for calculating the inverse dielectric function, the self-energy, and distribution of secondary particles resulting from selected excitations in CaF_2 and BaF_2 using high-performance computing resources. For our work, the self-energy is the most relevant quantity since its imaginary part is directly related to the cross section for an excited electron to create a secondary excitation. A key feature of ERSP over other electronic structure packages, which rely on a plasmon-pole model for the inverse dielectric function, is that the full dielectric matrix is used to construct the screened Coulomb interaction W that plays a central role in the GW approximation used to obtain the self-energy.

In Figure 2, we compare the calculated loss function (negative imaginary part of the long-wavelength inverse dielectric function) and cross section for exciting electron-hole pairs in the two materials. These materials have served as test cases, allowing us to vet recent code developments as we prepare to treat more complicated materials such as SrI_2.

Finally, work has been completed this fiscal year on the electronic and structural properties of Tl and Na dopant centers in alkali halides as well as on the formation, mobility, and stability of self-trapped excitons and self-trapped holes in pure and Tl-doped alkali halides using density functional theory calculations. This work has led to two manuscripts: one published in *Physical Review B* and a second manuscript submitted to *Journal of Physics: Condensed Matter*.

3.0 Task 2: Intrinsic response properties, theoretical light yield, and microscopic description of ionization tracks

3.1 Summary of progress

Cross sections were derived and NWEGRIM simulations were performed to calculate the intrinsic response properties of halide and oxide scintillators (SrI_2, YAP, and YAG). Links between the electron-hole pair production channels, ionization track structure and observed nonproportional response were explored. In addition, we have been working to transform NWEGRIM from an in-house research code to a shared code that can be used by other researchers in the community. The code is also being transformed to a FORTRAN 90 platform for easy maintenance and to facilitate future development.

3.2 Publications/Presentations

J. Bang, Z. Wang, F. Gao, S. Meng and S. Zhang *Physical Review B* 87 (2013) 205206

R.T. Williams, J.Q. Grim, Q. Li, K.B. Ucer, G.A. Bizarri, S. Kerisit, F. Gao, P. Bhattacharya, E. Tupitsyn, E. Rowe, V.M. Buliga and A. Burger *Proceedings of SPIE* in review

(Invited) F. Gao 2013 SPIE Meeting, August 26-29 2013, San Diego, CA

(Invited) F. Gao International Conference on Advanced Scintillation Materials 2013, September 23-27, Kharkov, Ukraine

3.3 Progress during FY13

Work in the previous funding cycle focused on calculating the intrinsic response properties of a series of halide scintillators, namely NaI, CsI, BaF_2, CaF_2, and $LaBr_3$, using NWEGRIM. This fiscal year, work under this task initially focused on modeling the intrinsic response properties of SrI_2. Although originally patented by Hofstadter and co-workers in the 1960s, SrI_2 had not received any attention for scintillation applications until it was recently re-considered by researchers at LLNL, who showed it to have a very high scintillation light yield. Various cross sections for electrons (interband transition, plasmon excitation, and core-shell ionization) for SrI_2 were developed to simulate electron-hole pair production for incident photon energies varying from 50 eV to 1 MeV. From these simulations, the mean energy required to create an electron-hole pair, *W*, and the Fano factor, *F*, were determined as a function of incident energy, as shown in Figure 3. As seen for other scintillator materials, *W* fluctuates at low energies but reaches a constant value of 8.1 eV at high incident energies. *F* shows a similar behavior and converges to a value of 0.3.

By combining the results obtained previously for other halide scintillators with those from the SrI_2 simulations, we can begin to extract trends amongst this family of scintillators as well as identify the intrinsic material properties that give rise to observed response properties. Table 1 summarizes some important properties of the halide scintillators simulated to date. We found that the most proportional materials, namely $LaBr_3$ and SrI_2, are those that exhibit linear ionization tracks in our simulations as this track structure minimizes the extent of nonlinear quenching at low incident energies. Our simulations also

show that this phenomenon is related to the fact that these materials show a greater proportion of electron-hole pairs generated via interband transition. Therefore, we expect bright and proportional scintillators to have: (1) a low value of W; (2) a small number of energy loss channels (ideally, only interband transition); and (3) a linear ionization track structure.

Table 1. Intrinsic properties, track structures and energy loss channels of electrons in halide scintillators.

Material	**CaF_2**	**BaF_2**	**CsI**	**NaI**	**$LaBr_3$**	**SrI_2**
Max. theoretical LY (ph/MeV)	50,505	52,356	82,333	91,743	105,263	123,457
W (eV)	21.4	19.1	12.0	10.9	9.5	8.1
F	0.23	0.19	0.30	0.28	0.21	0.23
e-h pair channels (%)						
Interband	63.1	63.7	65.2	60.2	72.1	72.2
Plasmon	31.6	29.3	18.2	29.1	21.9	19.2
Core-shell ionization	4.4	4.4	11.1	6.4	3.2	4.3
Track structure	clustered	clustered	slightly clustered	slightly clustered	linear	linear
Min. E of constant LY (keV)	0.8	0.9	10.0	2.0	2.0	0.2

Further work under this task focused on modeling a second family of scintillators, oxides. Therefore, electron cross sections were developed for $Y_3Al_5O_{12}$ (YAG) and $YAlO_3$ (YAP). As for other scintillators, simulations were carried out for incident photon energies varying from 50 eV to 1 MeV. These simulations predicted values of *W* that converged at high incident energies to 14.3 eV and 10.5 eV for YAP and YAG, respectively, and *F* values that converged to 0.18 and 0.27 for YAP and YAG, respectively. Both materials show a large discontinuity at 2.1 keV, which corresponds to the photoelectric absorption of the L_3 shell of Y. Most of the electron-hole pairs are generated by interband transition in both YAP and YAG, similar to SrI_2 and $LaBr_3$ but unlike CaF_2, BaF_2, CsI, and NaI, for which a greater proportion of plasmon excitation and core-shell ionization was predicted. The calculated spatial distributions of electron-hole pairs in YAP and YAG show that all electron-hole pairs are distributed along the tracks of fast electrons in both materials. YAP exhibits a linear track structure, whereas electron-hole pairs are slightly clustered along the track in YAG, which gives rise to a greater proportion of regions of high excitation densities in YAG compared to YAP. This finding is consistent with the experimental observation that YAG shows a less proportional response than YAP. Although our simulations show that most of the electron-hole pairs are produced by interband transition in both YAP and YAG, some electrons with low energies interact with phonons in YAG, thus decreasing their kinetic energies and bringing them below the minimum energy required to create a new electron-hole pair.

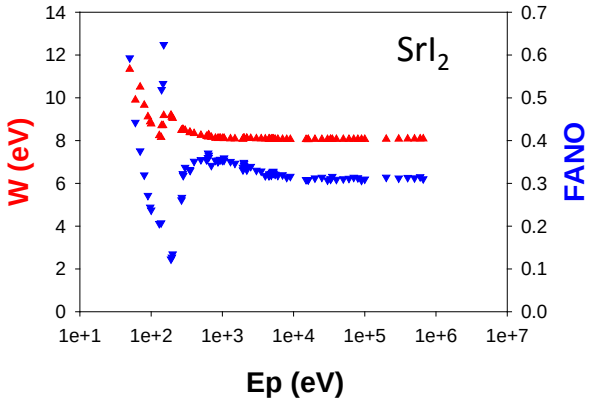

Figure 3. Mean energy per electron-hole pair, *W*, and Fano factor, *F*, as a function of incident photon energy, E_p, for SrI_2.

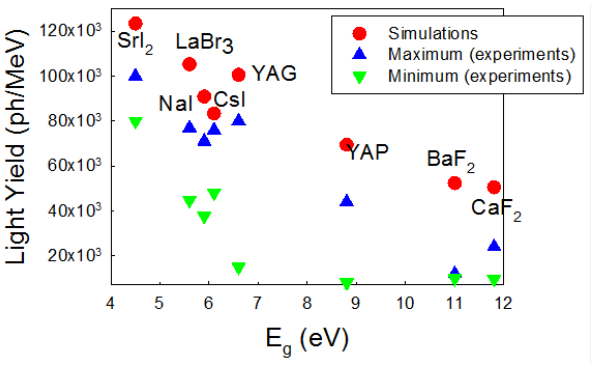

Figure 4. Maximum theoretical light yield as a function of band gap energy of all scintillators modeled to date.

The maximum theoretical light yields predicted by NWEGRIM for all the scintillators simulated to date are shown in Figure 4 and compared to experimental measurements. As expected, the calculated light yields are greater than the experimental measurements as they do not include non-radiative decay of thermalized electron-hole pairs. Nonetheless, they provide useful upper limits on the light yield of a given scintillator and can provide a basis for developing general rules for discovering new scintillator materials. In addition, absolute light yields are notoriously very difficult to determine and measure experimentally; therefore, the calculated maximum light yields can provide upper bounds for experimental determination of absolute light yields.

4.0 Task 3: Kinetics and efficiency of scintillation: nonlinearity, intrinsic energy resolution, and pulse shape discrimination

4.1 Summary of progress

Kinetic Monte Carlo simulations of the photon density response of Tl-doped CsI and NaI were carried out to model the nonlinear quenching processes responsible for the nonproportional response of scintillators at low incident energies. The development of a kinetic Monte Carlo model of scintillation in Eu-doped SrI_2 was also initiated.

4.2 Publications/Presentations

Z. Wang, R.T. Williams, J.Q. Grim, F. Gao and S. Kerisit *Physica Status Solidi B* 250 (2013) 1532

S. Kerisit, Z. Wang, R.T. Williams, J.Q. Grim and F. Gao *IEEE Transactions on Nuclear Science* in review

(Invited) S. Kerisit International Conference on Advanced Scintillation Materials 2013, September 23-27, Kharkov, Ukraine

4.3 Progress during FY13

This fiscal year, work under this task focused mostly on simulated the processes of nonlinear quenching of thermalized electron-hole pairs. Nonlinear quenching processes are believed to give rise to the nonproportional behavior exhibited by all inorganic scintillators at low incident γ-ray energies due to the increase in stopping power and the resulting increase in electron-hole pair density with decreasing incident energy. Therefore, it is critical to incorporate an accurate description of nonlinear quenching processes in our KMC code of scintillation. Photon density response (or z-scan) experiments carried out at WFU by Prof. Richard T. Williams and co-workers provide a perfect opportunity to derive model parameters for nonlinear processes. Therefore, we have carried out KMC simulations of the z-scan experiments in collaboration with Prof. Williams, who provided us with data from their measurements and also helped us with the interpretation of their experimental results. We initially considered thallium-doped CsI and NaI and this work has led to one publication in *Physica Status Solidi B* and a second manuscript currently in review with *IEEE Transactions on Nuclear Science*.

In this work, the simulation parameters were determined from a wide range of experimental and quantum mechanical studies on pure and Tl-doped NaI and CsI. Notably, the energy barriers calculated in this project by Prange et al. (*Phys. Rev. B* 87 (2013) 115101) were used directly in the KMC model to describe STE and STH diffusion and yielded good agreement with the experimental rising times. The results of the KMC simulations were thoroughly compared with experimental data on the kinetics and efficiency of scintillation of these materials as a function of temperature and Tl concentration and good agreement was observed. The models thus derived were then used in KMC calculations aimed at simulating the conditions in the z-scan experiments. For Tl-doped NaI excited with 5.9 eV photons, good agreement with experiment was obtained when describing STE-STE interactions via dipole-dipole Förster

transfer and a value of the dipole-dipole transfer radius (R_{dd}) of 2.9 nm, as shown in Figure 5. This indicates that nonlinear quenching is predominantly second order in NaI in these conditions. For CsI at the same excitation energy, the experiments show some contribution from a third-order quenching mechanism. When separating the second and third order components, the KMC simulations yielded good agreement with the second-order component for a value of R_{dd} of 3.7 nm.

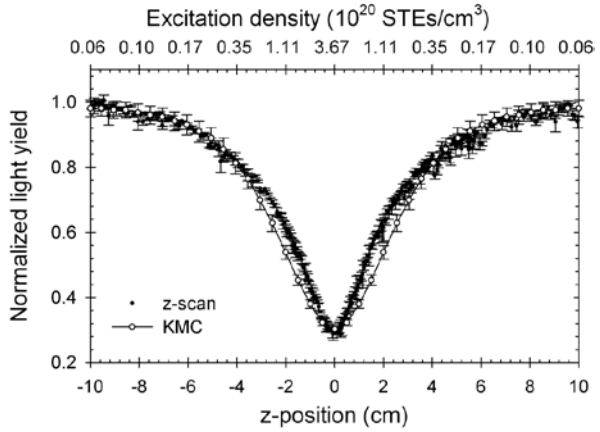

Figure 5. Calculated (open circles) and experimental (solid circles) normalized light yield for NaI(0.1%Tl) as a function of excitation density (5.9-eV excitation).

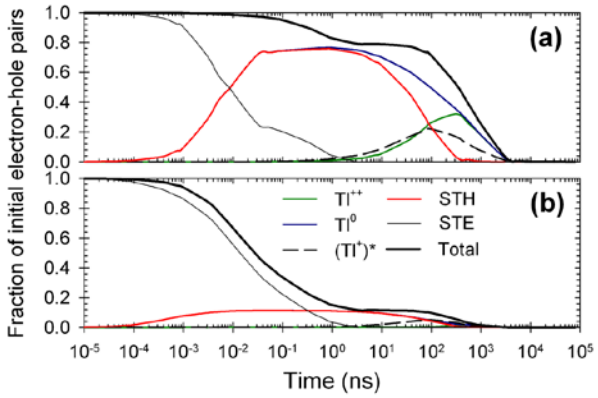

Figure 6. Time evolution of the species considered in the KMC model at (a) 7.60×10^{18} STEs/cm^3 and (b) 3.67×10^{18} STEs/cm^3.

The KMC model allows for elucidating the elementary processes that give rise to the observed scintillation behavior in CsI and NaI. For example, Figure 6 shows the time evolution of the species populations for NaI(Tl) at two excitation densities. This figure shows that the early stages of the scintillation process (<100 ps), where exciton dissociation and nonlinear quenching occur at the same time, are critical to explaining the observed density-dependent scintillation behavior. When combined with the ionization tracks generated with NWEGRIM, this new model with accurate representation of second order nonlinear quenching interactions will enable realistic simulations of the nonproportional γ-ray and electron response of inorganic scintillators.

Finally, work is also underway to develop a KMC model of scintillation in Eu-doped SrI_2 following the same approach as used for CsI and NaI. Importantly, SrI_2 showed a pure third-order quenching behavior in the conditions of the photon density response experiments carried out at WFU. Therefore, this task will allow us to derive model parameters for simulating third-order quenching processes.

Appendix A

Publications and Invited Presentations

Journal of Luminescence 137 (2013) 121–131

Contents lists available at SciVerse ScienceDirect

Journal of Luminescence

journal homepage: www.elsevier.com/locate/jlumin

Excited state electronic properties of sodium iodide and cesium iodide

L.W. Campbell *, F. Gao

Pacific Northwest National Laboratory, 3335 Q Avenue Mail Stop J4-80, Richland, WA 99354, United States

ARTICLE INFO

Article history:
Received 11 September 2012
Received in revised form
22 December 2012
Accepted 28 December 2012
Available online 4 January 2013

Keywords:
Electronic screening
Electronic lifetime
Electron cascade
Plasmon decay
Sodium iodide
Cesium iodide

ABSTRACT

We compute from first principles the dielectric function, loss function, lifetime and scattering rate of quasiparticles due to electronic losses, and secondary particle spectrum due to plasmon decay in two scintillating alkali halides, sodium iodide and cesium iodide. Particular emphasis is placed on quasiparticles within several multiples of the bandgap from the band edges. A theory for the decay spectra of plasmons and other electronic excitations in crystals is presented. Applications to Monte Carlo radiation transport codes are discussed.

1. Introduction

Predicting the response of a material to the passage of charged particle radiation is a challenging computational problem, particularly at low energies where the electronic structure cannot be treated as an electron gas. At a basic level, the physics is well known. We start with a high energy electron present in the material; perhaps one liberated from a core or valence state by an x-ray or gamma photon through photoelectric absorption or Compton scattering, perhaps created by radioactive decay or gamma ray induced pair production, or perhaps introduced by a beam or external high energy physics event. As the electron traverses the material, the Coulomb field of the charged projectile excites further electronic excitations. This will result in a partial transfer of the primary electron's energy and momentum to the excitation, resulting in the excitation of a core or valence electron to a conduction band. The resulting conduction electron may also be highly energetic, capable of creating additional electronic excitations. The hole may be produced in a highly excited state, whose atomic relaxation creates further electron–hole pairs through the Auger process. For electrons in the lower conduction band and valence holes, energy losses to phonons compete with electronic processes and become dominant close to the threshold for electronic excitation. The electronic cascade stops when no individual electron or hole has enough energy to excite a valence electron across the bandgap, thus preventing further electronic processes in the cascade. The end result is that the original energy of the initial charged particle has become distributed among a number of hot conduction electrons and valence holes. In semiconductor detectors, these charge carriers are the measured signal, creating a current pulse which is picked up with attached electronic instrumentation. In scintillator materials, the process leading to the signal continues—charge carriers will continue to lose energy to phonons until they become thermalized, and then either recombine to produce optical photons that are picked up with photodetectors, or are trapped or recombine non-radiatively and do not contribute to the measured signal. An accurate understanding of the electronic cascade process will be useful for the design of radiation detectors, the search for new detector materials, and the interpretation of the signals of such detectors.

Available codes dealing with this subject typically look at tracks rather than microscopic response [1,2]. While high energy knock-off electrons are tracked, those secondary particles whose energy is below a cutoff threshold are not explicitly followed and their effects accounted for in an average way. In this approximation, the low energy excitations simply provide a "stopping power" or continuous energy loss per unit distance by which the primary electron travels. This involves knowing the parameters that give rise to the stopping power in each material, and does not allow computational studies of such issues as the average signal or its variance from first principles. While a number of attempts have been made to extend the scope of the simulation to consider each electronic excitation, such simulations to date rely on electron-gas like approximations [3–5] or free atom approximations [6,7] that lead to questionable values when the electron energy falls low enough for band structure

* Corresponding author.
E-mail address: luke.campbell@pnnl.gov (L.W. Campbell).

0022-2313/$ - see front matter © 2013 Published by Elsevier B.V.
http://dx.doi.org/10.1016/j.jlumin.2012.12.058

effects to significantly affect its dispersion. Since it is just this low energy response that determines when the electron cascade will end, it is important to include a more realistic model of the low energy electronic behavior.

The response to a charged particle is ultimately a problem involving the basic methods of predicting electronic excited states and response functions, where the particle of radiation is treated as a quasiparticle excitation in the medium. Calculations of the electronic response have long been used to predict such quantities as the dielectric function, optical absorption spectrum, and electron energy loss spectrum (EELS) [8–12]. The rate of excitations produced by a perturbing field (such as the Coulomb field of the radiation particle) is found using the imaginary part of the dielectric screening of the material. Summing up all such excitations that are allowed by relevant conservation laws gives the total rate at which the perturbation produces excitations, corresponding to the rate at which the radiation particle scatters out of its current state to a state of lower energy. Experimentally measured optical absorption or electron energy loss spectra, with assumed free-electron energy dispersion relations and plane wave electrons propagating in the solid, have been used to calculate inelastic mean free paths and stopping powers of electrons in alkali halides using summations of this type [13]. When the dielectric function is calculated in the random phase approximation (RPA) and corrected by the distribution of the electron wave function in the material, these summations are equivalent to finding the imaginary part of the self-energy in Hedin's *GW* approximation [14] (not an acronym, the *G* stands for Green's function operator, and *W* is the screened Coulomb interaction operator). This *GW* approximation is widely used to reproduce excited state quasiparticle properties, and has been employed to calculate the electronic lifetime of hot electrons in the metals Cu and Al [15], the imaginary self-energy [16] and electronic response including electronic lifetime [17] of hot electrons and holes in the semiconductor silicon, and the inelastic mean free path and stopping power of electrons up to 10 MeV in Au, Ag, and Cu [18]. Carrying out electron lifetime calculations in the *GW* approximation with a full RPA dielectric function allows to avoid extrapolating the zero wave vector loss function, and thus avoid simplistic approximations of the loss function dispersion. In this way, realistic behavior for the prominent plasmon-like excitations can be included while simultaneously allowing for correct limiting behavior at high and low wave vectors.

In order to understand the scintillation process from first principles, we chose to start with two common scintillating radiation detector materials, sodium iodide and cesium iodide, and investigate the screening, average lifetime of excited electron states, and the spectrum of secondary particles produced by plasmon excitations within the RPA and *GW* approximations. The lifetime is closely related to such quantities of interest as the mean free path, stopping power, and valence excitation cross sections. These quantities, and the secondary particle spectra of plasmon decay, served as input into the Monte Carlo code NorthWest Electron and Gamma Ray Interaction in Matter (NWEGRIM) in order to predict the signals from beta and gamma radiation and associated track nanostructure [4,5]. Because core-level excitations and atomic relaxation depend almost entirely on the element of the atom involved in the excitation [19], and because the core level excitations and decay modes are well tabulated [20], these processes can already be handled accurately by standard Monte Carlo radiation transport techniques. We thus concentrate on excitations of the valence electrons, which are difficult to handle in a simple fashion since they are strongly affected by the electronic structure of the material under consideration. While the NWEGRIM results on NaI and CsI have previously been reported [21,22], this is the first description of the *ab initio* electronic structure calculations used in those studies. NWEGRIM outputs a spatial distribution of conduction electrons and holes whose energies have fallen below the threshold for exciting further valence to conduction band transitions. This distribution is passed as input to further simulations that investigate the diffusion of the hot charge carriers until thermalization and trapping [22], which in turn is input into a kinetic Monte Carlo simulation for the diffusion and ultimate recombination of the charge carriers to produce the final signal in the form of light [23,24].

2. Theory

In this section, and elsewhere in this paper, we work exclusively in atomic units ($e=\hbar=m_e=1$) unless otherwise noted. We will cover the basic theory of electronic screening, the rate at which electrons suffer losses while traversing the material, and the spectrum of secondary particles produced during these losses.

2.1. Screening

In semiconductors and insulators the longitudinal dielectric function in the limit of the Random Phase Approximation (RPA) takes the form [25,26]

$$\begin{aligned}&\text{z.epsi;}_{\mathbf{K},\mathbf{K}'}(\mathbf{q},\omega)\\&=\delta_{\mathbf{K},\mathbf{K}'}-\frac{4\pi}{|\mathbf{q}+\mathbf{K}||\mathbf{q}+\mathbf{K}'|}\sum_{c}^{\text{unocc}}\sum_{v}^{\text{occ}}\int_{\text{B.Z.}}\frac{d^3k}{(2\pi)^3}\\&\quad\times\left[\frac{\rho_{cv}(\mathbf{k},\mathbf{q}+\mathbf{K})\rho^*_{cv}(\mathbf{k},\mathbf{q}+\mathbf{K}')}{\omega-\text{z.epsiv;}_c(\mathbf{k})+\text{z.epsiv;}_v(\mathbf{k}-\mathbf{q})+i\eta}-\frac{\rho_{vc}(\mathbf{k},\mathbf{q}+\mathbf{K})\rho^*_{vc}(\mathbf{k},\mathbf{q}+\mathbf{K}')}{\omega+\text{z.epsiv;}_c(\mathbf{k})-\text{z.epsiv;}_v(\mathbf{k}-\mathbf{q})+i\eta}\right],\end{aligned}\tag{1}$$

where the notation unocc restricts the sum to unoccupied bands and occ to occupied bands, B.Z. indicates the integral is to be taken over the first Brillouin zone, the wave vector $\mathbf{q}$ is restricted to the first Brillouin zone, $\mathbf{K}$ and $\mathbf{K}'$ are reciprocal lattice vectors, and the notation for the density matrix elements reflects the fact that a density operator of wave vector $\mathbf{q}$ can only connect Bloch waves $\psi_{n,\mathbf{k}}(\mathbf{r})$ with wave vectors differing by $\mathbf{q}$

$$\rho_{nn'}(\mathbf{k},\mathbf{q}+\mathbf{K})=\int d^3r\,\psi_{n,\mathbf{k}}(\mathbf{r})\psi^*_{n',\mathbf{k}-\mathbf{q}}(\mathbf{r})e^{-i(\mathbf{q}+\mathbf{K})\cdot\mathbf{r}}.\tag{2}$$

This is a form which can be conveniently calculated using modern electronic structure codes. Once sufficient matrix elements in the reciprocal lattice vector space have been found to adequately express the response, the inverse longitudinal dielectric function $\text{z.epsi;}^{-1}_{\mathbf{K},\mathbf{K}'}(\mathbf{q},\omega)$ is found as a matrix inverse.

The RPA does not include interactions between the conduction electrons and holes, and thus cannot reproduce excitons. Excitons are fundamental to the process of scintillation, they are vital to the process of transport of the thermalized charge carriers in a scintillator, and the decay of excitons can produce scintillation light (although in NaI and CsI, most of the light yield comes from thallium activator dopants). However, experimentally the oscillator strength of excitons is small, so that although they produce well-defined peaks they are expected to be a relatively minor perturbation to the overall process of the creation of charge carriers in the crystal and the decay of multi-eV collective excitations. The fine structure from effects beyond the RPA is likely to be washed out during the integration process leading to the total quasiparticle lifetime and thus effects on the lifetime are likely to be small. Conduction electron–hole interactions are known to shift the location of plasmon resonances by a couple of eV in semiconductors [27], although their effect in alkali halide collective excitations is unknown. This could potentially change the plasmon decay spectrum by creating the bulk of the

excitations at a different energy than what is calculated. This effect is a subject for future research.

2.2. Rate of loss

We take the initial state of our system $|\Psi_I\rangle$ as the ground state $|\Psi_0\rangle$ of an N electron system except for a single additional electron in a conduction band n with wave vector $\mathbf{k}$ that represents the radiation particle traversing the crystal,

$$|\Psi_I\rangle = a^\dagger_{n,\mathbf{k}}|\Psi_0\rangle \tag{3}$$

and the final state $|\Psi_\alpha\rangle$ as a series of particle–hole excitations of the N particle system $|\Psi_{ph}\rangle$ of total energy ω_{ph} with an additional electron in conduction band n' and wave vector $\mathbf{k}'$ representing the scattered radiation particle,

$$|\Psi_\alpha\rangle = a^\dagger_{n',\mathbf{k}'}|\Psi_{ph}\rangle. \tag{4}$$

The rate at which the radiation particle transfers energy to electronic excitations of the initial state I of the material is given by Fermi's golden rule [28]

$$\Gamma_I = 2\pi\sum_\alpha |\langle\Psi_\alpha|H_{\text{int}}|\Psi_I\rangle|^2\delta(\omega_{\alpha I}), \tag{5}$$

where $\omega_{\alpha I}$ is the energy difference between the state α and state I. The interaction Hamiltonian can be taken as the Coulomb interaction between the charge density of the radiation electron and the material

$$H_{\text{int}} = \sum_{\mathbf{K}}\int_{\text{B.Z.}}\frac{d^3q}{(2\pi)^3}\frac{4\pi}{q^2}\rho_r(-\mathbf{q}-\mathbf{K})\rho(\mathbf{q}+\mathbf{K}), \tag{6}$$

where $\rho(\mathbf{q})$ is the charge density operator for the electrons of the material and $\rho_r(\mathbf{q})$ is the charge density operator for the radiation electron

$$\rho_r(\mathbf{q}) = \sum_{n,n'}\int_{\text{B.Z.}}\frac{d^3k}{(2\pi)^3}a^\dagger_{n',\mathbf{k}-\mathbf{q}}a_{n,\mathbf{k}}\rho_{nn'}(\mathbf{k},\mathbf{q}). \tag{7}$$

Neglecting exchange terms between these two density operators and generalizing to also allow the case where the radiation particle is a hole, we obtain

$$\begin{aligned}\Gamma_n(\mathbf{k}) = 2\pi\sum_{n'}\sum_{\mathbf{K}\mathbf{K}'}\int_{\text{B.Z.}}\frac{d^3q}{(2\pi)^3}&\frac{4\pi}{|\mathbf{q}+\mathbf{K}|^2}\frac{4\pi}{|\mathbf{q}+\mathbf{K}'|^2}\\ &\times\rho_{nn'}(\mathbf{k},\mathbf{q}+\mathbf{K})\rho^*_{nn'}(\mathbf{k},\mathbf{q}+\mathbf{K}')\\ &\times\sum_{ph}\langle\Psi_{ph}|\rho(\mathbf{q}+\mathbf{K})|\Psi_0\rangle\langle\Psi_0|\rho^\dagger(\mathbf{q}+\mathbf{K}')|\Psi_{ph}\rangle\\ &\times\delta(\omega(1-2f_{n'})-\text{z.epsiv;}_n(\mathbf{k})+\text{z.epsiv;}_{n'}(\mathbf{k}-\mathbf{q})),\end{aligned} \tag{8}$$

where f_n is the occupation function for band n (for metals, or finite temperatures, we would need to consider occupation as a function of wave number as well. In the case of materials with a bandgap, where the bandgap energy is much larger than the temperature, this functional dependence on $\mathbf{k}$ can be suppressed).

The inverse dielectric function can be expressed in terms of density matrix elements of the exact many particle states [29,30]

$$\begin{aligned}\text{z.epsi;}^{-1}_{\mathbf{K},\mathbf{K}'}(\mathbf{q},\omega)-\delta_{\mathbf{K},\mathbf{K}'} = &\frac{4\pi}{|\mathbf{q}+\mathbf{K}||\mathbf{q}+\mathbf{K}'|}\\ \times\sum_n\Bigg[&\frac{\langle\Psi_0|\rho(\mathbf{q}+\mathbf{K})|\Psi_n\rangle\langle\Psi_n|\rho^\dagger(\mathbf{q}+\mathbf{K}')|\Psi_0\rangle}{\omega-(E_n-E_0)+i\eta}\\ -&\frac{\langle\Psi_0|\rho^\dagger(\mathbf{q}+\mathbf{K}')|\Psi_n\rangle\langle\Psi_n|\rho(\mathbf{q}+\mathbf{K})|\Psi_0\rangle}{\omega+(E_n-E_0)+i\eta}\Bigg].\end{aligned} \tag{9}$$

If we define W as the screened Coulomb interaction

$$W_{\mathbf{K},\mathbf{K}'}(\mathbf{q},\omega) = \frac{4\pi}{|\mathbf{q}+\mathbf{K}||\mathbf{q}+\mathbf{K}'|}\text{z.epsi;}^{-1}_{\mathbf{K},\mathbf{K}'}(\mathbf{q},\omega), \tag{10}$$

then using Eq. (9) the rate of loss for an electron in a crystal becomes

$$\begin{aligned}\Gamma_n(\mathbf{k}) = 2i\sum_{n'}\int_0^\infty d\omega\int_{\text{B.Z.}}\frac{d^3q}{(2\pi)^3}&\sum_{\mathbf{K},\mathbf{K}'}\\ &\times\rho_{nn'}(\mathbf{k},\mathbf{q}+\mathbf{K})\rho^*_{nn'}(\mathbf{k},\mathbf{q}+\mathbf{K}')W^{(A)}_{\mathbf{K},\mathbf{K}'}(\mathbf{q},\omega)\\ &\times\delta(\omega(1-2f_{n'})-\text{z.epsiv;}_n(\mathbf{k})+\text{z.epsiv;}_{n'}(\mathbf{k}-\mathbf{q})),\end{aligned} \tag{11}$$

where $W^{(A)}_{\mathbf{K},\mathbf{K}'} = (W_{\mathbf{K},\mathbf{K}'}-W^\dagger_{\mathbf{K},\mathbf{K}'})/2$ is the anti-Hermitian part of W.

With a few simple transformations, this result can be related to other well known quantities. The one electron Green's function in energy space can be written as [30]

$$G(\mathbf{r},\mathbf{r}',E) = \sum_n\int_{\text{B.Z.}}\frac{d^3k}{(2\pi)^3}\frac{\psi_{n,\mathbf{k}}(\mathbf{r})\psi^*_{n,\mathbf{k}}(\mathbf{r}')}{E-\text{z.epsiv;}_n(\mathbf{k})+i\eta(1-2f_n)}. \tag{12}$$

With this expression, the popular *GW* expression for the self-energy [14]

$$\Sigma(\mathbf{r},\mathbf{r}',E) = i\int\frac{d\omega}{2\pi}G(\mathbf{r},\mathbf{r}',E-\omega)W(\mathbf{r},\mathbf{r}',\omega) \tag{13}$$

has diagonal orbital matrix elements given by

$$\begin{aligned}\langle n,\mathbf{k}|\Sigma(E)|n,\mathbf{k}\rangle = i\int\frac{d\omega}{2\pi}\sum_{n'}\int_{\text{B.Z.}}\frac{d^3q}{(2\pi)^3}&\sum_{\mathbf{K},\mathbf{K}'}W_{\mathbf{K},\mathbf{K}'}(\mathbf{q},\omega)\\ &\times\frac{\rho_{nn'}(\mathbf{k},\mathbf{q}+\mathbf{K})\rho^*_{nn'}(\mathbf{k},\mathbf{q}+\mathbf{K}')}{E-\omega-\text{z.epsiv;}_{n'}(\mathbf{k}-\mathbf{q})+i\eta(1-2f_{n'})}.\end{aligned} \tag{14}$$

The screened interaction can be expressed in spectral form

$$\begin{aligned}W_{\mathbf{K},\mathbf{K}'}(\mathbf{q},\omega) = &\frac{4\pi}{|\mathbf{q}+\mathbf{K}|^2}\delta_{\mathbf{K},\mathbf{K}'}\\ &+\frac{i}{\pi}\int_0^\infty d\omega'\left[\frac{1}{\omega-(\omega'-i\eta)}-\frac{1}{\omega+(\omega'-i\eta)}\right]W^{(A)}_{\mathbf{K},\mathbf{K}'}(\mathbf{q},\omega').\end{aligned} \tag{15}$$

Inserting this spectral representation in Eq. (14), we see that

$$\Gamma_n(\mathbf{k}) = 2|\text{Im}\langle n,\mathbf{k}|\Sigma(\text{z.epsiv;}_n(\mathbf{k}))|n,\mathbf{k}\rangle|. \tag{16}$$

A significant body of work exists on calculating the self-energy in the *GW* approximation [31]. Reducing our expression to this method thus allows us to take advantage of this published experience in this study.

2.3. Secondary particle spectra

Eq. (11) shows that the energy loss of charged particles is due to a suitably weighted sum over electronic excitations of all energy transfers ω and momentum transfers $\mathbf{q}$ from the particle to the medium. The function inside the integrand is thus the (unnormalized) excitation spectrum. The inverse dielectric function is seen to have a central importance in determining the weights of the excitations, and Eq. (1) shows how this function is composed of individual particle–hole excitations from valence bands v and wave vectors $\mathbf{k}-\mathbf{q}$ to conduction bands c and wave vectors $\mathbf{k}$. Thus, we can similarly expect to decompose any electronic excitation into a spectrum of secondary conduction electrons and holes that result from the decay of the excitation with the specified energy and momentum transfer.

A primary motivation for this decomposition comes from collective resonances where the dielectric screening nearly vanishes, thus amplifying the perturbing field over large distances and providing a strong channel for losses. These resonances, called plasmons, are common in condensed media and are a major player in electronic losses. The mechanisms described in the previous subsections are well known and describe the influence of the plasmons (among other excitations) on losses, but the subsequent decay of the plasmon excitations has not been well studied. Chung and Everhart [32] have

previously developed a theory for plasmon decay in nearly free electron metals. Here, we extend the theory to crystalline semiconductors and insulators and apply it not just to plasmons but to any electronic excitation.

A rigorous derivation of the form of the secondary particle spectra is provided in Appendix A. We find that the unnormalized spectrum for the promotion of a valence electron from band v and wave vector $\mathbf{k}-\mathbf{q}$ to a conduction band c with wave vector $\mathbf{k}$ by an excitation with energy transfer ω and momentum transfer $\mathbf{q}$ for reciprocal lattice vector contributions $\mathbf{K},\mathbf{K}'$ is given by the partial loss function $L_{cv;\mathbf{K}\mathbf{K}'}(\mathbf{k};\mathbf{q},\omega)$, as defined in Eq. (A.12). Secondary particle spectra are taken by forming suitable sums and integrals over $L_{cv,\mathbf{K}\mathbf{K}'}(\mathbf{k};\mathbf{q},\omega)$. The unnormalized energy spectrum of the secondary conduction electrons, for example, is given by

$$L_{\mathbf{K}\mathbf{K}'}(E;\mathbf{q},\omega)=\sum_{c}^{\text{unocc}}\sum_{v}^{\text{occ.}}\int_{\text{B.Z.}}\frac{d^3k}{(2\pi)^3}\delta(E-\text{z.epsiv;}_c(\mathbf{k}))L_{cv;\mathbf{K}\mathbf{K}'}(\mathbf{k};\mathbf{q},\omega). \tag{17}$$

If local fields are neglected, the inverse dielectric functions become diagonal and, up to a normalization constant,

$$L_{cv}(\mathbf{k};\mathbf{q},\omega)\propto\left|\rho_{cv}(\mathbf{k},\mathbf{q})\right|^2\delta(\omega-\text{z.epsiv;}_c(\mathbf{k})+\text{z.epsiv;}_v(\mathbf{k}-\mathbf{q})), \tag{18}$$

where $\mathbf{q}$ is now allowed to extend beyond the first Brillouin zone. This approximation has the advantage that the inverse dielectric function does not need to be pre-computed prior to evaluation of the normalized secondary particle spectrum.

3. Methods

To obtain the initial orbitals for our calculation, we used the ABINIT electronic structure code [33–35]. ABINIT uses a plane wave basis set to perform density functional theory (DFT) [36] computations on periodic crystals. A lattice parameter of 4.57 Å was chosen for CsI [37–39] and 6.46 Å for NaI [37]. The wave function was found in the local density approximation (LDA) on two separate primary and secondary $\mathbf{k}$-point grids, each a $10\times10\times10$ grid in the first Brillouin zone. The primary $\mathbf{k}$-point grid is a Γ point centered grid, while the secondary grid is shifted by $0.001\,\mathbf{b_1}+0.0005\,\mathbf{b_2}$ from the primary grid where $\mathbf{b_1}$, $\mathbf{b_2}$, and $\mathbf{b_3}$ are the primitive reciprocal lattice vectors of the crystal. This shift was chosen so that the offset between grids gives a wave vector $\mathbf{q}$ adequate to reproduce the limit $\mathbf{q}\to0$ for which later calculations of the electronic response are sufficiently converged while still large enough to avoid numerical errors due to finding a small difference in close quantities. A converged electronic structure was obtained with a plane wave cutoff energy of 20 hartree. Troullier Martins pseudopotentials [40] were used. Cs was represented by the 6*s* valence and 5*p* semi-core electrons, Na by the 3*s* valence electron, and I by the 5*s* and 5*p* valence electrons. All more tightly bound electrons were considered non-interacting core electrons and handled through their effects on the pseudopotentials.

No electronic excitations are possible for quasiparticles with energies less than the bandgap from the band edge—the quasiparticle must give up at least one bandgap's worth of energy to promote a valence electron to the conduction band, and it must itself have an unoccupied orbital of the required energy into which it can decay. DFT methods are notorious for underestimating the bandgap. Using the Kohn–Sham energy eigenvalues [36] directly in Eq. (1) would have led to quasiparticles exciting losses at energies lower than what is physically possible. Our LDA ground state electronic structure results give bandgaps which are too small by a factor of around two, as indicated in Table 1. To correct for this, we adjust the band energies with a *GW* calculation, using the native ABINIT capabilities. A plasmon pole screening matrix found with 30 bands, a wave function cutoff of 4 hartree, and a dielectric matrix cutoff of 3.6 hartree, plus a self-energy calculation with 50 bands, a cutoff energy of 10 hartree, and an exchange cutoff energy of 6 hartree was sufficient to converge the calculation to within 0.004 eV. For the purpose of simulating ionization losses of radiation particles, an accurate estimate of the bandgap is crucial since the amount of ionization per incident energy is strongly bandgap dependent. Because of a significant discrepancy remaining between the *GW*-calculated bandgap and the range of experimental bandgaps, we further increased the bandgap using a scissors operator [41,42] to bring our estimates of ionization more closely in line with what would be expected of the actual material. Conduction band energies of CsI were increased uniformly by 1.5 eV, those of NaI by 0.75 eV. This enforces an optical bandgap of 6.28 eV for CsI and 5.89 eV for NaI.

Table 1
Energies of selected transitions between the highest valence band and lowest conduction band. Column *GW*(1) lists ABINIT calculated *GW* bandgaps which were used for orbital energies in our calculations, *GW*(2) lists self-energies calculated using methods described in this work. Experimental values for NaI taken from [47–49]; values for CsI from [47,48,50,51].

Material	Transition	Bandgap (eV)			
		LDA	*GW* (1)	*GW* (2)	Experiment
NaI	$\Gamma\to\Gamma$	3.41	5.14	6.07	5.9, 5.8, 5.75
CsI	$\Gamma\to\Gamma$	3.15	4.78	5.49	6.1, 6.3, 6.37, 6.0
CsI	$M\to\Gamma$	3.08	4.74	5.44	

The density matrix elements $\rho_{nn'}(\mathbf{k},\mathbf{q}+\mathbf{K})$ are evaluated using the Kohn–Sham orbitals. The self-energy operator has been shown to be very nearly diagonal in this basis set [43], implying that the orbitals with many body effects included are very similar to those found in DFT calculations.

The anti-Hermitian part of the dielectric matrix of Eq. (1) is given in Eq. (A.10). This is evaluated on the primary $\mathbf{k}$ point grid for finite $\mathbf{q}$ via the tetrahedron method [44], which finds the contribution from the constant energy surfaces of the delta function over the entire integration volume. The Hermitian components can then be obtained through

$$\text{z.epsi;}^{(H)}_{\mathbf{K},\mathbf{K}'}(\mathbf{q},\omega)=\delta_{\mathbf{K},\mathbf{K}'}+\frac{2}{\pi}\mathcal{P}\int_0^\infty d\omega'\,\text{z.epsi;}^{(A)}_{\mathbf{K},\mathbf{K}'}(\mathbf{q},\omega')\frac{\omega'}{\omega'^2-\omega^2},$$

where $\mathcal{P}$ indicates the principal part of the integral. This method has the attractive feature that electronic losses become strictly zero for energy transfers ω below the lowest possible transition energy, preventing the bleed-over into the bandgap which occur when using broadened sums over the calculated k-points. However, it should be remembered that our calculations were carried out at the RPA level of theory, and thus will miss the excitonic losses that occur at less than the bandgap energy.

At $\mathbf{q}=0$ the Coulomb potential has a singularity when one or both of the reciprocal lattice vectors $\mathbf{K}$, $\mathbf{K}'$ equal to zero. However, in the limit $\mathbf{q}\to0$ the quantity

$$\frac{4\pi}{|\mathbf{q}+\mathbf{K}||\mathbf{q}+\mathbf{K}'|^2}\rho_{nn'}(\mathbf{k},\mathbf{q}+\mathbf{K})\rho^*_{nn'}(\mathbf{k},\mathbf{q}+\mathbf{K}') \tag{19}$$

is well defined in cubic materials for non-degenerate (and non-equal) bands n and n' for all $\mathbf{K}$, $\mathbf{K}'$ because of the orthogonality of the bands. As such, the actual function integrated in the dielectric function expression is well behaved. We determine $\text{z.epsi;}^{(A)}_{\mathbf{K},\mathbf{K}'}(\mathbf{q}\to0,\omega)$ by calculating the low wave vector density matrix elements for the small but finite $\mathbf{q}$ between the primary and secondary $\mathbf{k}$ point grids.

The loss is found using Eq. (16), and the imaginary part of the self-energy is evaluated using Eq. (A.5). In this case, the density matrix elements will occur between the same bands, so the singularity at $\mathbf{q}=0$ must be dealt with. This singularity is integrable. For tetrahedral integration cells containing the singular point, the loss is split into singular and non-singular parts

$$\mathrm{Im}\langle n,\mathbf{k}|\Sigma(E)|n,\mathbf{k}\rangle = \langle n,\mathbf{k}|\Sigma_{\mathrm{ns}}(E)|n,\mathbf{k}\rangle + \langle n,\mathbf{k}|\Sigma_{\mathrm{s}}(E)|n,\mathbf{k}\rangle, \tag{20}$$

$$\begin{aligned}\mathrm{Im}\langle n,\mathbf{k}|\Sigma_{\mathrm{ns}}(E)|n,\mathbf{k}\rangle = \frac{1}{\pi}\sum_{\mathbf{K},\mathbf{K}'}\sum_{n'}\int_0^\infty d\omega\int_{\mathrm{B.Z.}}\frac{d^3q}{(2\pi)^3}[W^{(A)}_{\mathbf{K},\mathbf{K}'}(\mathbf{q},\omega)\\ \times\rho_{nn'}(\mathbf{k},\mathbf{q}+\mathbf{K})\rho^*_{nn'}(\mathbf{k},\mathbf{q}+\mathbf{K}')-A_{nn'}(\omega)/q^2]\\ \times\delta(E-\mathrm{z.epsiv;}_{n'}(\mathbf{k}-\mathbf{q})+\omega(2f_{n'}-1)),\end{aligned} \tag{21}$$

$$\begin{aligned}\mathrm{Im}\langle n,\mathbf{k}|\Sigma_{\mathrm{s}}(E)|n,\mathbf{k}\rangle = \frac{1}{\pi}\sum_{n'}\int_0^\infty d\omega\int_{\mathrm{B.Z.}}\frac{d^3q}{(2\pi)^3}A_{nn'}(\omega)/q^2\\ \times\delta(E-\mathrm{z.epsiv;}_{n'}(\mathbf{k}-\mathbf{q})+\omega(2f_{n'}-1)),\end{aligned} \tag{22}$$

where

$$A_{nn'}(\omega) = 4\pi[\mathrm{z.epsi;}^{-1}_{0,0}(\mathbf{q}\to 0,\omega)]^{(A)}\left|\rho_{nn'}(\mathbf{k},\mathbf{q}\to 0)\right|^2.$$

The non-singular term $\mathrm{Im}\langle n,\mathbf{k}|\Sigma_{\mathrm{ns}}(E)|n,\mathbf{k}\rangle$ is integrated normally. The singular $\mathrm{Im}\langle n,\mathbf{k}|\Sigma_{\mathrm{s}}(E)|n,\mathbf{k}\rangle$ is integrated numerically over the constant-energy plane of the tetrahedron. While the singular evaluation is more time intensive, it is only needed for a small number of integration cells and is thus feasible.

The real part of the correlation self-energy can be found by determining $\mathrm{Im}\langle n,\mathbf{k}|\Sigma(E)|n,\mathbf{k}\rangle$ over the full range of E where losses exist, and taking a Hilbert transform. The total self-energy is then found by adding the exchange self-energy. The quasiparticle energies can be recovered by adding the self-energy to the DFT Kohn–Sham eigenvalues and subtracting off the DFT exchange–correlation energy. While quasiparticle energies are not the primary focus of this work, we did take the opportunity to use the machinery developed here to calculate the bandgap of the materials under study since it essentially came at no additional cost and could be used to help validate our calculations.

We follow the usual practice of using the Kohn–Sham eigenvalues for the band energies when evaluating $\Sigma(E)$. If we denote the Kohn–Sham eigenvalues as $\mathrm{z.epsiv;}^{\mathrm{KS}}_n(\mathbf{k})$, then

$$\mathrm{z.epsiv;}_n(\mathbf{k}) = \mathrm{z.epsiv;}^{\mathrm{KS}}_n(\mathbf{k}) + \langle n,\mathbf{k}|\Sigma(\mathrm{z.epsiv;}_n(\mathbf{k}))|n,\mathbf{k}\rangle.$$

This leads to $\langle n,\mathbf{k}|\Sigma(\mathrm{z.epsiv;}^{\mathrm{KS}}_n(\mathbf{k}))|n,\mathbf{k}\rangle$ being evaluated away from the true quasiparticle energy. This is handled in the typical fashion by computing the renormalization constant [31]

$$Z_n(\mathbf{k}) = \left[1-\left.\frac{\partial\langle n,\mathbf{k}|\Sigma(E)|n,\mathbf{k}\rangle}{\partial E}\right|_{E=\mathrm{z.epsiv;}^{\mathrm{KS}}_n(\mathbf{k})}\right]^{-1} \tag{23}$$

such that

$$\langle n,\mathbf{k}|\Sigma(\mathrm{z.epsiv;}_n(\mathbf{k}))|n,\mathbf{k}\rangle = Z_n(\mathbf{k})\langle n,\mathbf{k}|\Sigma(\mathrm{z.epsiv;}^{\mathrm{KS}}_n(\mathbf{k}))|n,\mathbf{k}\rangle.$$

The rate of interaction of quasiparticles are thus given by

$$\Gamma_n(\mathbf{k}) = 2\left|\mathrm{Im}[Z_n(\mathbf{k})\langle n,\mathbf{k}|\Sigma(\mathrm{z.epsiv;}^{\mathrm{KS}}_n(\mathbf{k}))|n,\mathbf{k}\rangle]\right|,$$

which we approximate as

$$\Gamma_n(\mathbf{k}) = 2\left|[\mathrm{Re}\,Z_n(\mathbf{k})][\mathrm{Im}\langle n,\mathbf{k}|\Sigma(\mathrm{z.epsiv;}^{\mathrm{KS}}_n(\mathbf{k}))|n,\mathbf{k}\rangle]\right|. \tag{24}$$

The lifetime of a quasiparticle is

$$\tau_n(\mathbf{k}) = \frac{1}{\Gamma_n(\mathbf{k})}.$$

The evaluation of the decay spectra was carried out in the limit of neglecting local fields, using Eq. (18). The decay particles are resolved by an energy ΔE, so that the quantity generated is the energy integral of Eq. (17) between $E-\Delta E/2$ and $E+\Delta E/2$. Integrals of this form are discussed in Lehmann and Taut [44].

3.1. Application to Monte Carlo radiation transport simulations

In Monte Carlo radiation transport codes, electrons are propagated as free classical particles that can interact with materials through various physical processes, such as exciting bremsstrahlung radiation or ionizing core or valence electrons. Below a set energy cutoff, the particle track will be short compared to the macroscopic sizes of objects typically under consideration. No discrete excitations of lesser energy are allowed. Instead, the electron energy loss due to multiple low energy electronic excitations is handled in an average fashion. As the electron traverses matter, energy is continuously deposited at a rate that depends both on the material properties and the electron energy.

To extend this classical approach to lower energies and include all energy losses as discrete events, the chance of interaction of the electron must be known for every type of excitation, including the continuum of transitions involving valence to conduction band excitations. Typically, the chance of excitation is handled through the cross sections $\sigma_i(\mathrm{z.epsiv;})$ or inverse mean free paths $\lambda_i^{-1}(\mathrm{z.epsiv;})$ for each type of event i, which are related through the density of atoms N/V

$$\lambda_i^{-1}(\mathrm{z.epsiv;}) = \sigma_i(\mathrm{z.epsiv;})N/V. \tag{25}$$

The rate at which a particle of velocity $\mathbf{v}$ creates excitations of type i is related to $\lambda_i^{-1}(\mathrm{z.epsiv;})$ by

$$\Gamma_i(\mathrm{z.epsiv;}) = \lambda_i^{-1}(\mathrm{z.epsiv;})|\mathbf{v}|. \tag{26}$$

In this work, we have calculated the total rate at which the electron produces transitions from valence to conduction bands. This can be directly compared to the rate of other energy loss and scattering processes to directly include excitations from the valence band (core electron excitations, with their discrete energy levels and less complicated excitation probabilities, are already considered in these transport codes). Since the quantities worked within the codes are $\sigma_i(\mathrm{z.epsiv;})$ or $\lambda_i^{-1}(\mathrm{z.epsiv;})$, the valence excitation rate will be converted to an effective cross section per atom or mean free path. This allows the relative probabilities of creating a valence excitation to other kinds of excitations to be correctly determined. However, care must be taken not to confuse this with actual spatial path lengths, since comparisons are done for free classical particles with energy dispersion $\mathrm{z.epsiv;}(\mathbf{v}) = \mathbf{v}\times\mathbf{v}/(2m_e)$ rather than the band dependent energy dispersion of actual electrons in matter. True mean free paths for particles in a band can be extracted from the lifetimes through the relation [37] $\mathbf{v}_n(\mathbf{k}) = \nabla_{\mathbf{k}}\mathrm{z.epsiv;}_n(\mathbf{k})$ if spatial information on the track microstructure or nanostructure is needed.

A classical description of track producing particles can still be a useful approximation [4,5] when dealing with individual valence excitations. In this case, the quantities found in this work can be used to parametrize the curves for interband transitions and plasmon losses, which approximate the full set of valence to conduction transitions. With a proper parametrization, such simulations can reproduce detector response to ionizing radiation, including a full accounting of each charge carrier produced.

4. Results

The calculated LDA and the initial ABINIT *GW* band structure predicts that CsI has an indirect bandgap, with the minimum energy valence to conduction transition from the M point in the valence band to the Γ point in the conduction band. This predicted indirect gap is very close to the minimum optical gap

(at the Γ point). Reported measurements of the CsI bandgap are from ultraviolet absorption experiments, and consequently we only have the optical bandgap to compare. Our calculations of NaI lack this complication, with a minimum bandgap for the Γ to Γ point transition.

The experimentally accessible dielectric constant can be shown to be z.epsi; $= 1/$z.epsi;$^{-1}_{0,0}(\mathbf{q}\to 0,\omega\to 0)$ [26]. However, our calculations are carried out on a static lattice. In a real ionic solid, the application of a macroscopic longitudinal electric field at accessible frequencies would cause the ions to move in response, thus screening the field to a greater extent than is found from the electronic response alone. Fortunately, we can still make meaningful comparisons to measured values. At $\mathbf{q}\to 0$ and at frequencies far below the energy of the lowest transition, the perturbing field is essentially static as far as the electrons are concerned. In this limit, it makes no difference if the perturbing field is longitudinal or transverse—the electrons of the material are just reacting to a constant field within its volume. If we choose frequencies well below the lowest electronic transition we can use optical measurements to determine the electronic response. If this frequency also happens to be well above that of the highest phonon mode in the material, the lattice will be unable to keep up with the rapidly changing field. Under the approximation that the magnetic susceptibility of the medium is very close to the vacuum susceptibility, the index of refraction of the medium is given by [45] $n(\omega)=\sqrt{\text{z.epsi;}(\mathbf{q}\to 0,\omega)}$. We therefore can compute the index of refraction in the low frequency limit and compare it to measured values in the wide gap between the highest phonon mode and lowest electronic transition (a value referred to as n_∞, to distinguish it from the static value n_0). This is shown in Table 2.

Fig. 1 shows the dielectric function $1/$z.epsi;$^{-1}_{0,0}(\mathbf{q}\to 0,\omega)$, while Fig. 2 shows the diagonal loss function z.epsi;$^{-1}_{\mathbf{KK}}(\mathbf{q},\omega)$ for several momentum transfers. Several interesting features are evident in these plots. Plasmons result from anomalous dispersion causing the real part of the dielectric function to dip below zero within the region of transitions and then rise again past the localized region of high imaginary part resulting from the transitions. When the real part is near zero in this crossing and there are only weak transitions to populate the imaginary part, the dielectric function is much less than one indicating that the internal field is increased compared to the applied external field. This amplification of the internal field is a collective resonance of the material and corresponds to the plasmon. At plasmon resonances, the inverse dielectric function exhibits prominent peaks indicating regions of strong losses.

In CsI, an incipient plasmon in the 12–13 eV region resulting from the valence to conduction transitions is seen to be preempted by the rise of Cs 5*p* to conduction transitions in the 15–20 eV region of the spectrum, resulting in only a weak plasmon-like peak in the loss spectrum with a maximum at 12.7 eV (peak A in Fig. 3). A second broad plasmon is evident in the 18–29 eV region, due to the combined effect of the valence and semi-core electrons. This second plasmon has prominent peaks at 20.1 and 22.9 eV (peaks B and C, respectively, in Fig. 3). Plasmons in the free electron gas are well understood due to their analytical solution, and exist only at low momentum transfers. We see a similar behavior here, with the plasmon resonances dying away at higher $\mathbf{q}$ values. The structure between 13 and 21 eV that gives the double plasmon structure is found to be mostly due to transitions from orbitals with Cs 5*p* character. There is a small contribution from valence to conduction transitions, but contributions from orbitals with I 5*s* character, while not strictly zero, are found to be negligible with contributions of less than 1 part in 100 compared to valence and Cs 5*p* orbitals in this energy region. The binding energy of the Cs 5*s* shell is 22.7 eV [52]. If these orbitals were included in the calculations we would expect to see contributions in the screening functions between about 23 and 31 eV, which could have an effect on the second double plasmon peak. However, comparison with the I 5*s* orbitals suggests that the effect of this shell is negligible. Investigating the magnitude of this effect will be the subject of future work. It is encouraging, however, that the loss function at low momentum transfer is similar to that observed by Creuzberg [46], with a prominent peak at 10.3 eV (peak A′ in Fig. 3) and pair of higher amplitude peaks at 17.9 and 21.3 eV, as shown in Fig. 3 (peaks B′ and C′, respectively, in Fig. 3). In fact, our calculations reproduce many of the minor peaks seen in this reference as well, at a consistent 2–3 eV greater energy than observed in the experiment. The overestimation of the energies of the plasmon peaks is similar to what is observed in silicon. When the bandgap is corrected with *GW* calculations but the response function is computed with RPA, the Si plasmon peak is overestimated by approximately 2–3 eV [27]. Bethe–Salpeter corrections in Si, which introduce the conduction electron–hole interactions, correct this overestimation. In our calculations, the scissors operator introduces a uniform blue-shift of 1.5 eV while the complete set of bandgap corrections (including the scissors operator) from the DFT eigenvalues would be expected to result in a blue-shift on the order of 3 eV because a major effect of the *GW* correction is an overall energy increase of the conduction levels [42]. This indicates that, as was the case with silicon, the plasmon peaks are well reproduced in the RPA when using the bare DFT eigenvalues as the particle energies. We thus suspect that, as with silicon, Bethe–Salpeter calculations of the screening will allow a good representation of the plasmon structure while preserving the correct bandgap.

In NaI, the screening lacks strong core to conduction transitions and is thus simpler. A region of strong transitions emerges in the imaginary part of the dielectric function between 6 and 10 eV, and the recovery of the real part from below zero gives rise to a collective plasmon-like structure at around 18 eV. The presence of continued valence to conduction transitions in the 10–18 eV region delays the onset of the plasmon from its free-electron value of 9.05 eV. Again, the plasmon energy is overestimated compared to measured electron energy loss spectra [46], this time by about 5 eV. Much as with CsI, the plasmon is seen to be a phenomenon which occurs at low momentum transfer. At higher momentum transfers, the peak decreases in amplitude. In addition, it can be seen that, unlike CsI, the plasmon increases in energy with increasing momentum transfer before broadening sufficiently that it is no longer recognizable as a well defined excitation.

The electronic scattering rate of conduction electrons in NaI is shown in Fig. 4, and the same quantity for conduction electrons and Cs 5*p* character holes in CsI is shown in Fig. 5. The valence bands are shallow enough that their holes cannot excite any further electronic losses. The NaI bands with I 5*s* character show little dispersion, with energies ranging from 9.35 to 9.65 eV below the valence band maximum and a narrow range of loss rates between 1.85×10^{14} Hz and 2.0×10^{14} Hz. The six bands in CsI with strong Cs 5*p* character are nearly non-dispersive, with

Table 2
Indices of refraction from calculation and experiment [47]. For comparison, the value obtained from the full RPA screening calculations we performed are given and the value corresponding to that calculated by the ABINIT code for the screening matrix used in the initial *GW* calculations.

Material	Calculation ($\omega\to 0$)		Experiment (n_∞)
	This work	ABINIT	
NaI	1.69	1.81	1.73
CsI	1.64	1.84	1.743

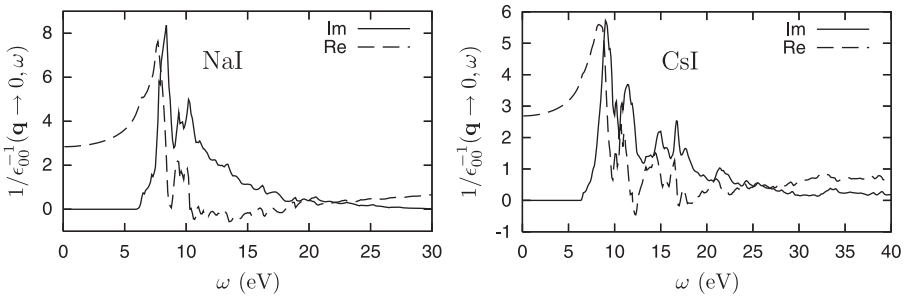

Fig. 1. The zero wave vector dielectric function of NaI (left) and CsI (right).

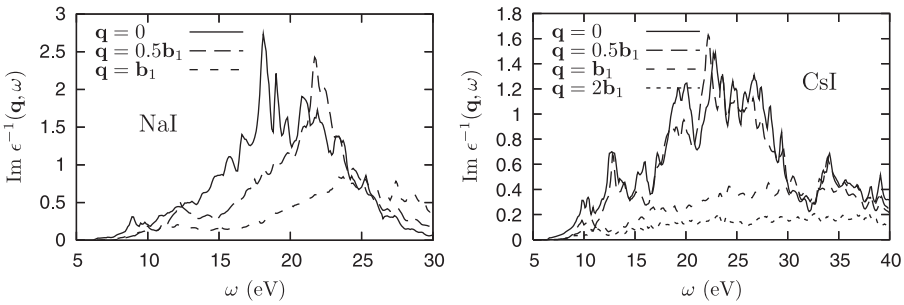

Fig. 2. The diagonal part of the loss function of NaI (left) and CsI (right) at various wave vectors in the direction of a primitive reciprocal lattice vector. Here, we use the convention that $\text{z.epsi}^{-1}(\mathbf{q},\omega)=\text{z.epsi}^{-1}_{\mathbf{K},\mathbf{K}}(\mathbf{q}',\omega)$ for $\mathbf{q}=\mathbf{q}'+\mathbf{K}$ with $\mathbf{q}'$ confined to the first Brillouin zone. The reciprocal lattice vectors have magnitude $|\mathbf{b}|=1.50$ Å^{-1} for NaI and $|\mathbf{b}|=1.37$ Å^{-1} in CsI.

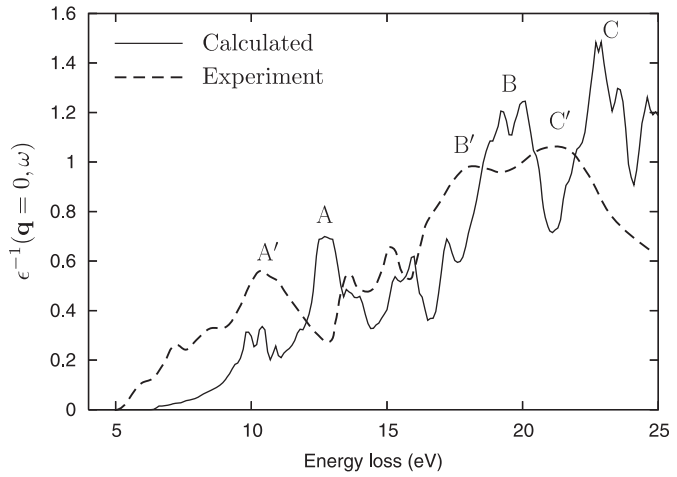

Fig. 3. The zero wave vector loss function of CsI (Solid) compared to the experimental electron energy loss spectrum of Creuzberg [46] (dashed). All major peaks are reproduced, but the calculated results are blue shifted by approximately 2–3 eV compared to the experiment. Major peaks are labeled, with corresponding calculated and measured peaks denoted by the same letter, but with a prime given to the label of the measured peaks.

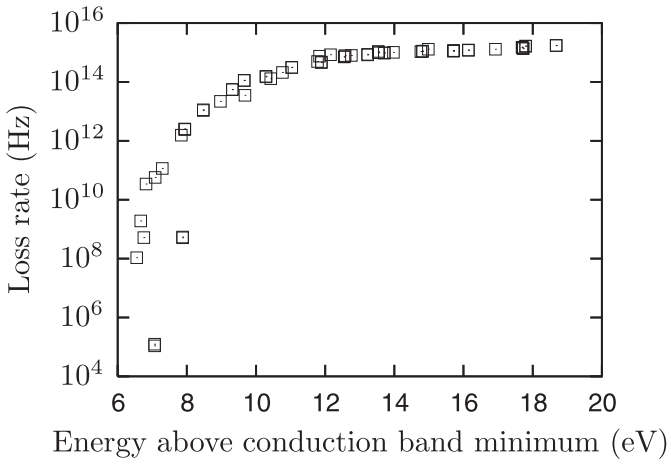

Fig. 4. Scattering rate of NaI conduction electron quasiparticles plotted against their energy.

energies close to 6.2 eV below the valence band maximum. Because these semi-core states are so close to one bandgap energy from the band edge, their lifetimes are strongly influenced by minor shifts in their energies. This sensitivity to the bandgap, neglect of excitons which allow excitation channels below the bandgap and self-trapping behavior which can lower the hole energy, suggests that the lifetimes of the shallowest Cs 5*p* states in the real material may vary by several orders of magnitude from our calculations. Because the calculated loss rate saturates at around 10^7 Hz for the deepest Cs 5*p* holes, we expect that states in the actual material with energies below the valence band maximum by a value significantly greater than one bandgap will tend to have loss rates in this range. The two CsI bands with I 5*s* character are also nearly non-dispersive, with energies ranging from 8.98 to 9.08 eV below the valence band maximum. The losses from these iodine 5*s* bands are much less affected by minor shifts in band structure, with loss rates near 1.3×10^{15} Hz. The I 5*s* holes in CsI are not plotted due to the narrow range of their properties and relatively flat dependence of loss on energy.

These figures illustrate how as quasiparticle energies decrease toward the excitation threshold, the rate of excitation drops dramatically and vanishes at the threshold. This is due to an increasingly restricted phase space available to the scattered and excited particles in the excitation rate and loss function integrals, to the point that at the threshold there is no available energy-allowed momentum states to scatter into. Similar behavior has long been known for the Fermi liquid, where quasiparticles at the fermi surface are lossless and the rate of loss increases with increasing energy for the same reason we see here [30]. However, in real materials quasiparticles at the threshold for electronic

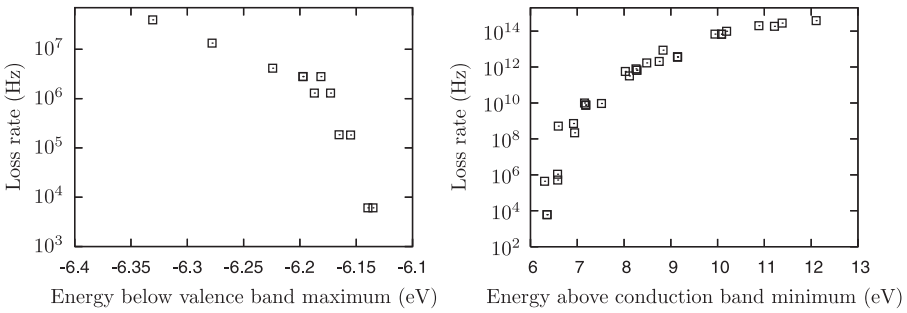

Fig. 5. Scattering rate of hole quasiparticles in the Cs 5*p* bands (left) of CsI and CsI conduction electron quasiarticles (right) plotted against their energy.

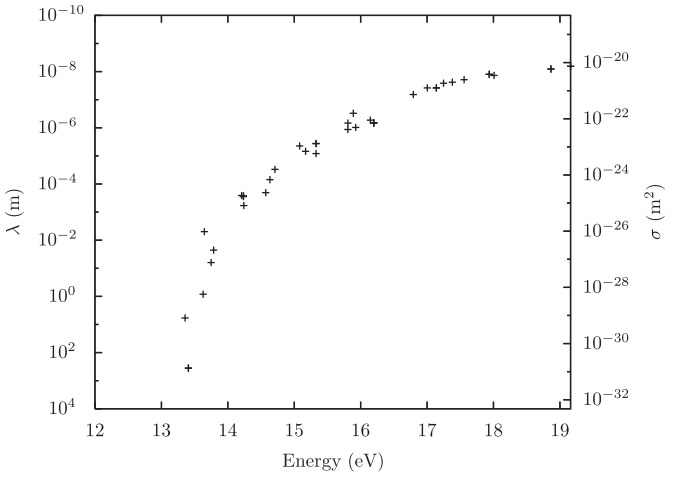

Fig. 6. Effective mean free path λ(z.epsiv;) and effective cross section σ(z.epsiv;) of CsI valence quasiparticles plotted against their energy as measured from the valence band maximum, the zero of energy used in the NWEGRIM Monte Carlo radiation transport code. In this figure, the magnitude of the classical particle velocity is determined by $|\mathbf{v}| = \sqrt{2\text{z.epsiv;}/m_e}$. The very long mean free paths near the excitation threshold are the result of considering electronic excitations alone—in a real material the mean free path would be significantly reduced for lower energy quasiparticles due to phonon excitations.

excitations do experience losses by scattering off the lattice to produce photons, an effect not considered in this work.

We note that the electronic losses follow a well defined curve as a function of quasiparticle energy. This feature is necessary to allow the classical Monte Carlo radiation transport to work at all. If quantum effects were to spread the loss rates for similar energies but different wave vectors out over many orders of magnitude, methods treating the radiation particles as ballistic objects would fail at low energies. Instead, while there is some variance in the loss rates, we see that the particles can be reasonably well approximated as having a rate of scattering that largely depends on energy with some added fluctuation. The relative fluctuations become largest near the threshold for electronic excitations. In practice, this is not expected to be a problem because near the threshold vibrational losses dominate. The effective mean free paths of conduction electrons in CsI are shown in Fig. 6.

The spectrum of energies of secondary electrons and holes at zero momentum transfer for selected energy transfers corresponding to plasmon-like excitations are shown in Fig. 7 for NaI and Fig. 8 for CsI. The single plasmon peak of NaI is seen to be composed of a majority of valence to conduction transitions, but excitations from the I 5*s* band to conduction bands have a noticeable minority contribution. The lower energy peak at 12.4 eV in CsI is seen to be made up of entirely valence to conduction transitions, which should be expected based on energy conservation alone. The pair of peaks at 21.1 and 21.9 eV in CsI are almost entirely the result of transitions from Cs 5*p*-like orbitals to conduction states, with a small contribution from valence to conduction transitions and an almost negligible contribution from I 5*s* orbitals to conduction orbitals. These peaks could nearly be considered as typical core-level excitations superimposed on valence to conduction interband transitions, except that the collective screening brings these transitions into resonance and enhances the rate of these transitions.

5. Discussion

We have developed a technique for computing the electronic losses of quasiparticles in semiconductors and insulators. This procedure will give quasiparticle lifetimes and rates of scattering as well as the spectra of secondary particles produced by the scattering. We envision this information as aiding efforts to use low energy radiation transport Monte Carlo codes to simulate the measured signal of novel radiation detector materials. This method has been applied to sodium iodide and cesium iodide, materials commonly used in radiation scintillation detectors. Several aspects of the calculated electronic structure are in reasonably good agreement with experimentally measured values, such as the bandgap, index of refraction, and electron energy loss functions, although our novel predictions such as rate of loss or secondary spectra do not yet have experimental support.

The simulation of secondary particle spectra is still fairly primitive. These early results are calculated neglecting local fields and have been found only at selected energy and momentum transfers corresponding to peaks in the energy loss spectrum, where they can be interpreted as the decay of plasmons. We envision calculation of these spectra and associated cross sections for a grid of energy and momentum transfers that allow replacement of the parametrized free electron gas like models currently used in the Monte Carlo radiation transport simulations with the *ab initio* quantities at low energy and momentum transfers where band structure is expected to have a significant effect on the electronic scattering process.

There are several areas where additional progress would be useful in simulating electronic stopping of charged particles. The inclusion of Bethe–Salpeter effects in the screening will allow the consideration of exciton states, will improve the low energy structure of the dielectric function, and will refine the location of the plasmon resonance. An extension of the method to cover non-cubic materials, whose dielectric response as $\mathbf{q}\rightarrow 0$ is a tensor rather than a scalar, would be useful. In addition, we have only considered electronic losses of the charge carriers. For an accurate end-of-track simulation, the phonon losses will also be needed.

With vacuum levels close to the conduction band minimum, CsI in particular [53] is attractive as a photocathode and offers the

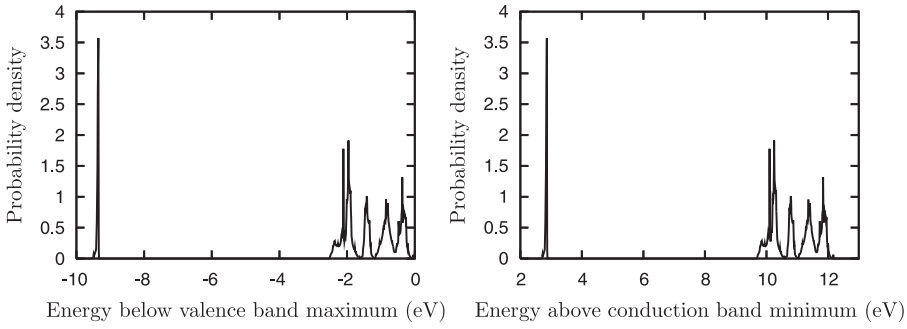

Fig. 7. Secondary spectrum of holes (left) and conduction electrons (right) in NaI for the peak of the 18.1 eV plasmon-like excitation at zero momentum transfer. Note that since the energy of the excitation is fixed, both hole and conduction electron spectra have the same shape and differ only by an overall shift of their energy.

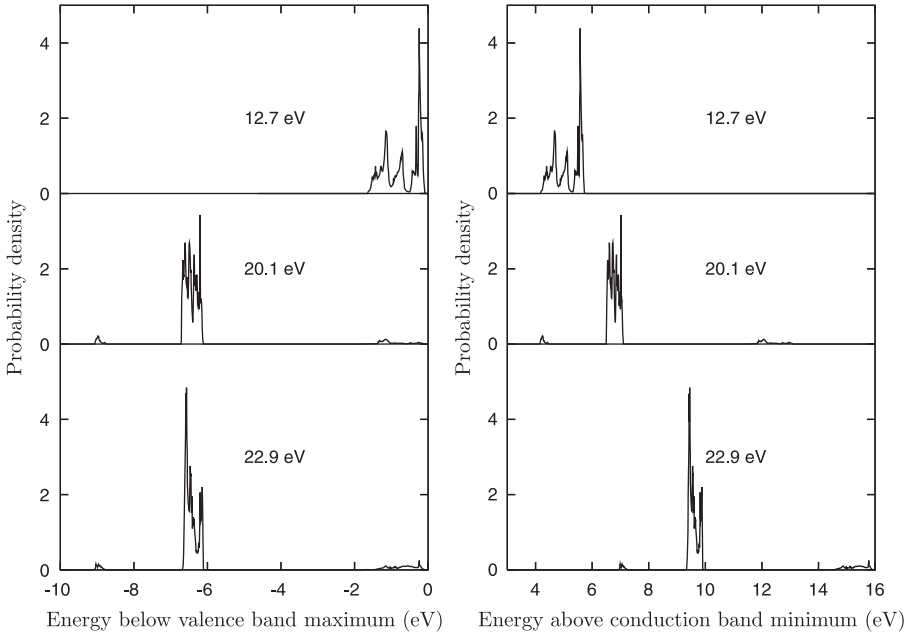

Fig. 8. Secondary spectrum of holes (left) and conduction electrons (right) in CsI for peaks of plasmon-like excitations at zero momentum transfer.

possibility of combining electron energy loss with energy measurements of the emitted secondary electrons to directly resolve the secondary particle spectra for various energy and momentum transfers. Further refinement of coupling between these *ab initio* calculations and Monte Carlo radiation transport codes could lead to comparisons of calculated values of electron escape depth and quantum efficiency of alkali halide photocathodes with measured values.

Acknowledgments

This research was supported by the National Nuclear Security Administration, Office of Nuclear Nonproliferation Research and Engineering (NA-22), of the US Department of Energy (DOE) at the Pacific Northwest National Laboratory, a multiprogram national laboratory operated by Battelle for the U.S. Department of Energy under Contract DE-AC05-76RL01830.

Appendix A. Derivation of the secondary particle spectrum

In this appendix we will put the assumption that the electronic excitations can be decomposed into individual particle–hole like excitations on firmer theoretical footing.

The spectral representation of W from Eq. (15) allows us to separate the self-energy into an exchange part Σ_x and correlation part Σ_c

$$\langle n,\mathbf{k}|\Sigma_x(E)|n,\mathbf{k}\rangle = 4\pi\sum_{n'}^{\mathrm{occ}}\int_{\mathrm{B.Z.}}\frac{d^3q}{(2\pi)^3}\sum_{\mathbf{K}}\frac{|\rho_{nn'}(\mathbf{k},\mathbf{q}+\mathbf{K})|^2}{|\mathbf{q}+\mathbf{K}|^2}, \tag{A.1}$$

$$\langle n,\mathbf{k}|\Sigma_c(E)|n,\mathbf{k}\rangle = \frac{i}{\pi}\int_0^\infty d\omega\sum_{n'}\int_{\mathrm{B.Z.}}\frac{d^3q}{(2\pi)^3}\sum_{\mathbf{K},\mathbf{K}'}W^{(A)}_{\mathbf{K},\mathbf{K}'}(\mathbf{q},\omega)\frac{\rho_{nn'}(\mathbf{k},\mathbf{q}+\mathbf{K})\rho^*_{nn'}(\mathbf{k},\mathbf{q}+\mathbf{K}')}{E-\mathrm{z.epsiv};_{n'}(\mathbf{k}-\mathbf{q})-(\omega-i\eta)(1-2f_{n'})}, \tag{A.2}$$

where occ means that the sum is taken only over occupied bands. The exchange self-energy is purely real, only the correlation contribution leads to losses. Define a matrix in the space of reciprocal lattice vectors

$$M_{\mathbf{K}',\mathbf{K}}(\mathbf{k},\mathbf{q},E,\omega) = i\frac{\rho_{nn'}(\mathbf{k},\mathbf{q}+\mathbf{K})\rho^*_{nn'}(\mathbf{k},\mathbf{q}+\mathbf{K}')}{E-\mathrm{z.epsiv};_{n'}(\mathbf{k}-\mathbf{q})-(\omega-i\eta)(1-2f_{n'})}. \tag{A.3}$$

Split this matrix into a Hermitian and an anti-Hermitian part, $M^{(H)}_{\mathbf{K}',\mathbf{K}}(\mathbf{k},\mathbf{q},E,\omega)$ and $M^{(A)}_{\mathbf{K}',\mathbf{K}}(\mathbf{k},\mathbf{q},E,\omega)$, respectively. We now have

$$\langle n,\mathbf{k}|\Sigma_c(E)|n,\mathbf{k}\rangle = \frac{1}{\pi}\int_0^\infty d\omega\sum_{n'}\int_{\mathrm{B.Z.}}\frac{d^3q}{(2\pi)^3}\times\mathrm{Tr}[M(\mathbf{k},\mathbf{q},E,\omega)W^{(A)}(\mathbf{q},\omega)]. \tag{A.4}$$

$\mathrm{Tr}[M^{(H)}(\mathbf{k},\mathbf{q},E,\omega)W^{(A)}(\mathbf{q},\omega)]$ is pure imaginary while $\mathrm{Tr}[M^{(A)}(\mathbf{k},\mathbf{q},E,\omega)W^{(A)}(\mathbf{q},\omega)]$ is entirely real. Therefore,

$$\mathrm{Im}\langle n,\mathbf{k}|\Sigma(E)|n,\mathbf{k}\rangle = \frac{1}{\pi}\int_0^\infty d\omega \sum_{n'}\int_{\mathrm{B.Z.}}\frac{d^3q}{(2\pi)^3} \times \mathrm{Tr}[M^{(H)}(\mathbf{k},\mathbf{q},E,\omega)W^{(A)}(\mathbf{q},\omega)]$$

and

$$\Gamma_n(\mathbf{k}) = \frac{2}{\pi}\left|\int_0^\infty d\omega\sum_{n'}\int_{\mathrm{B.Z.}}\frac{d^3q}{(2\pi)^3}\sum_{\mathbf{K},\mathbf{K}'} i\rho_{nn'}(\mathbf{k},\mathbf{q}+\mathbf{K})\rho^*_{nn'}(\mathbf{k},\mathbf{q}+\mathbf{K}') \times W^{(A)}_{\mathbf{K},\mathbf{K}'}(\mathbf{q},\omega)\delta(\mathrm{z.epsiv};_n(\mathbf{k})-\mathrm{z.epsiv};_{n'}(\mathbf{k}-\mathbf{q})-\omega(1-2f_{n'}))\right|. \tag{A.5}$$

The rate of creation of excitations with energy ω, wave vector $\mathbf{q}$, and reciprocal lattice vectors $\mathbf{K}$ and $\mathbf{K}'$ thus becomes

$$\gamma_{n;\mathbf{K},\mathbf{K}'}(\mathbf{k};\mathbf{q},\omega) = \frac{2}{\pi}\sum_{n'} iW^{(A)}_{\mathbf{K},\mathbf{K}'}(\mathbf{q},\omega)\rho_{nn'}(\mathbf{k},\mathbf{q}+\mathbf{K})\rho^*_{nn'}(\mathbf{k},\mathbf{q}+\mathbf{K}') \times\delta(\mathrm{z.epsiv};_n(\mathbf{k})-\mathrm{z.epsiv};_{n'}(\mathbf{k}-\mathbf{q})-\omega(1-2f_{n'})) \tag{A.6}$$

such that

$$\Gamma_n(\mathbf{k}) = \left|\int d\omega\int_{\mathrm{B.Z.}}\frac{d^3q}{(2\pi)^3}\sum_{\mathbf{K},\mathbf{K}'}\gamma_{n;\mathbf{K},\mathbf{K}'}(\mathbf{k};\mathbf{q},\omega)\right|. \tag{A.7}$$

This rate $\gamma_{n;\mathbf{K},\mathbf{K}'}(\mathbf{k};\mathbf{q},\omega)$ can then be considered an un-normalized spectrum of electronic excitations produced by an electron in band n with momentum $\mathbf{k}$.

We consider these electronic excitations to act as intermediate particles, and find the decay spectra of the excitations themselves. We can determine the secondary particles produced by a given conduction electron via a two-step process—first, find the electronic excitation quasiparticles; and second, resolve the decay of these quasiparticles.

We note that

$$W_{\mathbf{K},\mathbf{K}'}(\mathbf{q},\omega) = \frac{4\pi}{|\mathbf{q}+\mathbf{K}||\mathbf{q}+\mathbf{K}'|} \times\sum_{\mathbf{K}_1,\mathbf{K}_2}[\mathrm{z.epsi};_{\mathbf{K},\mathbf{K}_1}(\mathbf{q},\omega)]^{-1}\mathrm{z.epsi};^{\dagger}_{\mathbf{K}_1,\mathbf{K}_2}(\mathbf{q},\omega)[\mathrm{z.epsi};^{\dagger}_{\mathbf{K}_2,\mathbf{K}'}(\mathbf{q},\omega)]^{-1} \tag{A.8}$$

from which it is easy to show that

$$W^{(A)}_{\mathbf{K},\mathbf{K}'}(\mathbf{q},\omega) = \frac{-4\pi}{|\mathbf{q}+\mathbf{K}||\mathbf{q}+\mathbf{K}'|} \times\sum_{\mathbf{K}_1,\mathbf{K}_2}[\mathrm{z.epsi};_{\mathbf{K},\mathbf{K}_1}(\mathbf{q},\omega)]^{-1}\mathrm{z.epsi};^{(A)}_{\mathbf{K}_1,\mathbf{K}_2}(\mathbf{q},\omega)[\mathrm{z.epsi};^{\dagger}_{\mathbf{K}_2,\mathbf{K}'}(\mathbf{q},\omega)]^{-1}. \tag{A.9}$$

From Eq. (1) we have for positive frequencies

$$\mathrm{z.epsi};^{(A)}_{\mathbf{K},\mathbf{K}'}(\mathbf{q},\omega>0) = i\pi\frac{4\pi}{|\mathbf{q}+\mathbf{K}||\mathbf{q}+\mathbf{K}'|}\sum_c^{\mathrm{unocc}}\sum_v^{\mathrm{occ.}}\int_{\mathrm{B.Z.}}\frac{d^3k}{(2\pi)^3} \times\rho_{cv}(\mathbf{k},\mathbf{q}+\mathbf{K})\rho^*_{cv}(\mathbf{k},\mathbf{q}+\mathbf{K}')\delta(\omega-\mathrm{z.epsiv};_c(\mathbf{k})+\mathrm{z.epsiv};_v(\mathbf{k}-\mathbf{q})) \tag{A.10}$$

This has the interpretation of the applied field causing transitions of electrons from occupied valence orbitals v with momentum $\mathbf{k}-\mathbf{q}$ and energy $\mathrm{z.epsiv};_v(\mathbf{k}-\mathbf{q})$ to unoccupied conduction orbitals c with momentum $\mathbf{k}$ and energy $\mathrm{z.epsiv};_c(\mathbf{k})$. These are the decay particles we are interested in. We then arrive at

$$W^{(A)}_{\mathbf{K},\mathbf{K}'}(\mathbf{q},\omega) = \frac{-16\pi^3 i}{|\mathbf{q}+\mathbf{K}||\mathbf{q}+\mathbf{K}'|}\sum_c^{\mathrm{unocc}}\sum_v^{\mathrm{occ.}}\int_{\mathrm{B.Z.}}\frac{d^3k}{(2\pi)^3} \times\sum_{\mathbf{K}_1,\mathbf{K}_2}\frac{[\mathrm{z.epsi};_{\mathbf{K},\mathbf{K}_1}(\mathbf{q},\omega)]^{-1}[\mathrm{z.epsi};^{\dagger}_{\mathbf{K}_2,\mathbf{K}'}(\mathbf{q},\omega)]^{-1}}{|\mathbf{q}+\mathbf{K}_1||\mathbf{q}+\mathbf{K}_2|} \times\rho_{cv}(\mathbf{k},\mathbf{q}+\mathbf{K}_1)\rho^*_{cv}(\mathbf{k},\mathbf{q}+\mathbf{K}_2)\delta(\omega-\mathrm{z.epsiv};_c(\mathbf{k})+\mathrm{z.epsiv};_v(\mathbf{k}-\mathbf{q})). \tag{A.11}$$

We can immediately see that, up to a normalization factor, the loss function is composed of excitations from c to v and a final momentum of $\mathbf{k}$ with an un-normalized joint distribution function of

$$L_{cv;\mathbf{K}\mathbf{K}'}(\mathbf{k};\mathbf{q},\omega) = -4\pi^2 i\sum_{\mathbf{K}_1,\mathbf{K}_2}\frac{[\mathrm{z.epsi};_{\mathbf{K},\mathbf{K}_1}(\mathbf{q},\omega)]^{-1}[\mathrm{z.epsi};^{\dagger}_{\mathbf{K}_2,\mathbf{K}'}(\mathbf{q},\omega)]^{-1}}{|\mathbf{q}+\mathbf{K}_1||\mathbf{q}+\mathbf{K}_2|} \times\rho_{cv}(\mathbf{k},\mathbf{q}+\mathbf{K}_1)\rho^*_{cv}(\mathbf{k},\mathbf{q}+\mathbf{K}_2)\delta(\omega-\mathrm{z.epsiv};_c(\mathbf{k})+\mathrm{z.epsiv};_v(\mathbf{k}-\mathbf{q})) \tag{A.12}$$

such that

$$W^{(A)}_{\mathbf{K},\mathbf{K}'}(\mathbf{q},\omega) = \frac{4\pi}{|\mathbf{q}+\mathbf{K}||\mathbf{q}+\mathbf{K}'|}\sum_c^{\mathrm{unocc}}\sum_v^{\mathrm{occ.}}\int_{\mathrm{B.Z.}}\frac{d^3k}{(2\pi)^3}L_{cv;\mathbf{K}\mathbf{K}'}(\mathbf{k};\mathbf{q},\omega). \tag{A.13}$$

We may identify the function L as the partial contribution to the loss function due to the given excitation.

References

[1] MCNP5 User's Manual, LANL Reports LA-UR-03-1987. Available from: ⟨http://mcnp-green.lanl.gov/pdf/MCNP5_Manual_Volume_I_LA-UR-03-1987.pdf⟩.
[2] S. Agostinelli, et al., Nucl. Instrum. Methods A 506 (2003) 250; J. Allison, et al., IEEE Trans. Nucl. Sci. 53 (2006) 270; GEANT4 Physics Reference Manual. Available from: ⟨http://geant4.web.cern.ch/geant4/UserDocumentation/UsersGuides/PhysicsReferenceManual/html/PhysicsReferenceManual.html⟩.
[3] J.D. Martínez, R. Mayol, F. Salvat, J. Appl. Phys. 67 (1988) 2955.
[4] F. Gao, L.W. Campbell, R. Devanathan, Y. Xie, L. Corrales, A.J. Peurrung, W.J. Weber, Nucl. Instrum. Methods A 579 (2007) 292.
[5] F. Gao, L.W. Campbell, R. Devanathan, Y. Xie, Y. Zhang, A.J. Peurrung, W.J. Weber, Nucl. Instrum. Methods B 255 (2007) 286.
[6] F.P. Santos, T.H.V.T. Dias, P.J.B.M. Rachinhas, C.A.N. Conde, J. Appl. Phys. 89 (2001) 8202.
[7] G.W. Fraser, A.F. Abbey, A. Holland, K. McCarthy, A. Owens, A. Wells, Nucl. Instrum. Methods A 350 (1994) 368.
[8] M. Palummo, O. Pulci, A. Marini, L. Reining, R. Del Sole, Phys. Rev. B 74 (2006) 235431.
[9] J.P. Walter, M.L. Cohen, Phys. Rev. B 5 (1972) 3101.
[10] M.S. Hybertsen, S.G. Louie, Phys. Rev. B 35 (1987) 5585.
[11] S. Baroni, R. Resta, Phys. Rev. B 33 (1986) 7017.
[12] J.L.P. Hughes, J.E. Sipe, Phys. Rev. B 53 (1996) 10751.
[13] T. Boutboul, A. Akkerman, A. Breskin, R. Chechik, J. Appl. Phys. 79 (1996) 6714.
[14] L. Hedin, Phys. Rev. 139A (1965) 796.
[15] I. Campillo, J.M. Pitarke, A. Rubio, E. Zarate, P.M. Echenique, Phys. Rev. Lett. 83 (1999) 2230.
[16] J.A. Soininen, J.J. Rehr, E.L. Shirley, J. Phys.: Condens. Matter 15 (2003) 2573.
[17] B. Arnaud, S. Lebègue, M. Alouani, Phys. Rev. B 71 (2005) 035308.
[18] A.P. Sorini, J.J. Kas, J.J. Rehr, M.P. Prange, Z.H. Levine, Phys. Rev. B 74 (2006) 165111.
[19] R. Mayol, F. Salvat, J. Phys. B: At. Mol. Opt. Phys. 23 (1990) 2117.
[20] D.E. Cullen, J.H. Hubbell, L. Kissel, EDPL97: The Evaluated Data Library, '97 Version, Report UCRL-50400, vol. 6, rev. 5, 1997.
[21] F. Gao, Y. Xie, S. Kerisit, L.W. Campbell, W.J. Weber, Nucl. Instrum. Methods Phys. Res. A 652 (2011) 564.
[22] Z. Wang, Y.-L. Xie, B.D. Cannon, L.W. Campbell, F. Gao, S. Kerisit, J. Appl. Phys. 110 (2011) 064903.
[23] S. Kerisit, K.M. Rosso, B.D. Cannon, IEEE Trans. Nucl. Sci. 55 (2008) 1251.
[24] S. Kerisit, K.M. Rosso, B.D. Cannon, F. Gao, Y. Xie, J. Appl. Phys. 105 (2009) 114915.
[25] S.L. Adler, Phys. Rev. 126 (1962) 413.
[26] N. Wiser, Phys. Rev. 129 (1963) 62.
[27] V. Olevano, L. Reining, Phys. Rev. Lett. 86 (2001) 5962.
[28] J.J. Sakurai, Modern Quantum Mechanics, Addison Wesley, Reading, 1994.
[29] D. Pines, Elementary Excitations in Solids, Perseus, Reading, 1999.
[30] J.W. Negele, H. Orland, Quantum Many-Particle Systems, Addison Wesley, Reading, 1988.
[31] W.G. Aulbur, L. Jönsson, J.W. Wilkins, Solid State Phys. 54 (2000) 1.
[32] M.S. Chung, T.E. Everhart, Phys. Rev. B 15 (1977) 4699.
[33] abinit.org and ABINIT code. Available from: ⟨http://www.abinit.org⟩.
[34] X. Gonze, J.-M. Beuken, R. Caracas, F. Detraux, M. Fuchs, G.-M. Rignanese, L. Sindic, M. Verstraete, G. Zerah, F. Jollet, M. Torrent, A. Roy, M. Mikami, Ph. Ghosez, J.-Y. Raty, D.C. Allan, Comput. Mater. Sci. 25 (2002) 478.

[35] X. Gonze, G.-M. Rignanese, M. Verstraete, J.-M. Beuken, Y. Pouillon, R. Caracas, F. Jollet, M. Torrent, G. Zerah, M. Mikami, Ph. Ghosez, M. Veithen, J.-Y. Raty, V. Olevano, F. Bruneval, L. Reining, R. Godby, G. Onida, D.R. Hamann, D.C. Allan, Z. Kristallogr. 220 (2005) 558.
[36] W. Kohn, L.J. Sham, Phys. Rev. 140 (1965) A1133.
[37] N.W. Ashcroft, N.D. Mermin, Solid State Physics, Saunders College, Fort Worth, 1976.
[38] K. Asaumi, Phys. Rev. B 29 (1984) 1118.
[39] T.B. Rymer, P.G. Hambling, Acta Cryst. 4 (1951) 565.
[40] N. Troullier, J.L. Martins, Phys. Rev. B 43 (1991) 1993.
[41] G.A. Baraff, M. Schlüter, Phys. Rev. B 30 (1984) 3460.
[42] F. Gygi, A. Baldereschi, Phys. Rev. Lett. 62 (1989) 2160.
[43] M.S. Hybertsen, S.G. Louie, Phys. Rev. B 34 (1986) 5390.
[44] G. Lehmann, M. Taut, Phys. Status Solidi B 54 (1972) 469.
[45] J.D. Jackson, Classical Electrodynamics, Wiley, New York, 1975.
[46] M. Creuzberg, Z. Phys. 196 (1966) 433.
[47] W.J. Tropf, T.J. Harris, M.E. Thomas, in: R.W. Waynant, M.N. Ediger (Eds.), Electro-Optics Handbook, McGraw-Hill, New York, 2004.
[48] J.E. Eby, K.J. Teegarden, D.B. Dutton, Phys. Rev. 116 (1959) 1099.
[49] J.C. Phillips, Phys. Rev. 136 (1964) A1705. Note that when compared to Fig. 11, Table VII appears to have a misprint for the NaI $\Gamma_{15}^{-3/2} \rightarrow \Gamma_1$ transition.
[50] K. Teegarden, G. Baldini, Phys. Rev. 155 (1967) 896.
[51] J.J. Hopfield, J.M. Worlock, Phys. Rev. 137 (1965) A1455.
[52] J.A. Bearden, A.F. Burr, Rev. Mod. Phys. 39 (1967) 125.
[53] T.H. DiStefano, W.E. Spicer, Phys. Rev. B 7 (1973) 1554.

Formation, stability, and mobility of self-trapped excitations in NaI and $NaI_{1-x}Tl_x$ from first principles

M. P. Prange,[1] R. M. Van Ginhoven,[2] N. Govind,[3] and F. Gao[1]

[1]*Fundamental and Computational Sciences Directorate, Pacific Northwest National Laboratory, Richland, Washington 99352, USA*

[2]*Energy and Environment Directorate, Pacific Northwest National Laboratory, Richland, Washington 99352, USA*

[3]*William R. Wiley Environmental Molecular Sciences Laboratory, Pacific Northwest National Laboratory, Richland, Washington 99352, USA*

(Received 9 August 2012; revised manuscript received 4 February 2013; published 4 March 2013)

We study the formation, mobility, and stability of self-trapped excitons (STE) and self-trapped holes and electrons in NaI and NaI(Tl) using embedded cluster hybrid density functional theory calculations. This method employs an array of classical charges to provide an environment simulating the interior of an ionic solid in which the electronic structure of a modestly sized quantum-mechanical cluster is computed including nonlocal exchange effects which are necessary to describe localized excitations in NaI. In contrast with previous models, we find that both carriers in pure NaI have similar mobilities, with an activation energy of $\sim$0.2 eV. We propose an alternate interpretation including a new migration mechanism for the STE. In Tl-doped material excitons preferentially trap at dopants, inducing off-center distortions that have a structure unlike an STE and provide a mechanism for light emission at multiple wavelengths.

DOI: 10.1103/PhysRevB.87.115101 PACS number(s): 71.35.Cc, 71.35.Aa, 72.20.Ee, 72.20.Jv

I. INTRODUCTION

Recent progress in multiscale modeling of scintillating radiation detectors shows great promise.[1] Such efforts, however, require a *quantitative* understanding of all relevant microscopic processes which can then be correctly parametrized in meso- or macroscale models. While some quantities are accessible by measurement, the picture is often incomplete and sometimes qualitatively incorrect. This paper presents results using first-principles calculations that capture important details of the microscopic physics of NaI that are crucial to understanding and modeling of detector performance.

Thallium-doped NaI is of particular interest because it is widely used and the standard material against which new scintillators are compared.[2] In scintillation radiation detection, highly energetic radiation causes a cascade of secondary excitations in the crystal. Some of these excitations ultimately relax by the emission of visible light which is measured as a proxy for the energy of the incident radiation. The energy resolution of scintillators is limited by the nonproportionality of light yield to incident energy.[3]

Despite decades of experimental[4–8] and theoretical[5,9–12] study, microscopic understanding of the competing modes of energy transport and conversion in alkali halides is incomplete, and the interaction of energy carriers with dopants is only partially understood. Experimental and theoretical studies show that the luminescence efficiency depends on the spatial distribution of the secondary excitations, with higher densities of excitations producing fewer luminescence photons per unit deposited energy for low excitation energies.[3,13–15] This falloff of luminescence efficiency at low energies and high excitation densities is common in scintillators but especially pronounced in NaI(Tl). It is attributed to quenching of the secondary excitations by nonradiative processes that leave the energy carried by a pair (or more, for higher order processes) of secondary excitations in the vibrational modes of the scintillator and hence unavailable for luminescence.

We address the formation and diffusion of holes and excitons in pure and Tl-doped NaI, which are the important secondary excitations for luminescence. Self-trapped holes (STHs) (V_k centers) consist of a missing electron in a valence band and an accompanying strong lattice distortion, and a self-trapped exciton (STE) can be thought of as an STH surrounded by a bound electron. In both cases the lattice relaxation in the pure material resembles the formation of an I_2^- ion within the bulk crystal[16] with two I atoms moving markedly together. Such self-trapped excitations were qualitatively explained theoretically by the 1970s,[17,18] but improvement of theoretical understanding is ongoing, and a fully detailed description has not yet been achieved.[19,20]

During a scintillation event in NaI or NaI(Tl), these self-trapped excitations are initially created in a track, the structure of which depends on the particular exciting radiation. After creation, the self-trapped excitations execute diffusive motion until their decay. In the Tl-doped material, the dominant mechanism for light emission is STE capture by a Tl dopant (activator) followed by photon emission by the Tl. In the absence of such activator sites, the dominant process for light emission is direct radiative decay of STEs. The dominant quenching mechanism is STE-STE annihilation, in which two excitons collide and are destroyed. In both cases, light emission involves a single STE and hence depends linearly on the STE density while the quenching mechanism, which requires (at least) a binary collision, depends on higher powers of the excitation density leading to decreased luminescence efficiency at high excitation densities. Meanwhile, STHs and free carriers are also produced in the track. They can combine to form excitons (including STEs) or luminescence photons. Thus, a detailed understanding of scintillator performance in these systems requires understanding of the motion of STEs, free electrons, and STHs in order to predict the time evolution of the populations of each type of excitation and their ultimate fates. Various attempts have been made to describe scintillation efficiency by modeling the time and spatial dependence of secondary excitations using Monte-Carlo approaches, models based on rate equations, or ones based on diffusion equations. These are reviewed in Ref. 13. All these approaches are

limited by the paucity of knowledge regarding the microscopic dynamics of low-energy excitations.

Previously proposed models,[15,21] based on optical experiments,[22,23] assumed a highly mobile STE and a slower STH, while we find that in pure NaI both carriers have similar mobilities, with an activation energy of ∼0.2 eV. We propose an alternate interpretation, in which an electron hops from an STE to an STH at a different site, effectively exchanging the STE and STH. Our calculations suggest this migration mechanism should have a much lower barrier, consistent with measurements. Excitons migrating via this mechanism are likely to exhibit dynamics with different dependencies on temperature and local excitation density than excitons migrating by the conventional hopping mechanism. Importantly for theories of scintillation efficiency, STEs hopping by this mechanism can-not participate directly in STE-STE annihilation, since the destination site for this mechanism must contain an STH. Hence the existence of two different hopping barriers has implications for detector nonproportionality.

As is well known, accurate calculations of localized states in alkali halides are challenging because density functional theory (DFT) using semilocal exchange-correlation potentials often provides a qualitatively incorrect picture [e.g., neither STEs nor STHs are stable compared to undistorted structures in NaI (Ref. 24)]. To circumvent this problem we employ hybrid DFT with nonlocal exchange.

Most previously reported calculations on alkali halide systems (e.g., Refs. 25, 10, and 11) have been performed using some form of pure Hartree Fock (HF) theory. Notable exceptions are Derenzo and Weber[26] and Rivas-Silva *et al.*[27] who used MP2 and QCISD levels of theory, respectively, to calculate emission energies. These previous works relied on small or symmetry constrained models to improve calculation tractability or to explore a specific proposed geometry. Since confinement effects limit the deformations available, small clusters discourage localized states which involve such distortion or lattice polarization. On the other hand, the use of pure HF, which completely neglects the correlation energy, favors localized states. Hence there is the possibility that these two errors partially cancel leading to qualitatively correct results. This work (with as many as 136 *ab initio* atoms and no constraints on the symmetry of the deformation) is a substantial improvement over previous efforts in this area.[10,11,25–27]

II. COMPUTATIONAL METHODS

As in past work,[11,17,18,28,29] we use an embedded cluster method to facilitate tractable calculations. Our calculations include a large (∼10 000) array of fixed point charges, located at lattice positions of the undistorted crystal. This array provides an electrostatic potential which closely reproduces the classical Ewald potential of the perfect crystal throughout a central region in the interior of the array. The atoms on surface of the cluster are fixed throughout the calculation, and the interior atoms are allowed to relax. A schematic diagram of a cluster model is shown in Fig. 1.

Within the quantum-mechanical region, the electronic structure was computed by means of hybrid DFT using CRENBL ECP (Ref. 31) basis sets for Na and I and Stuttgart RLC basis sets[32] for Tl. Unless otherwise stated,

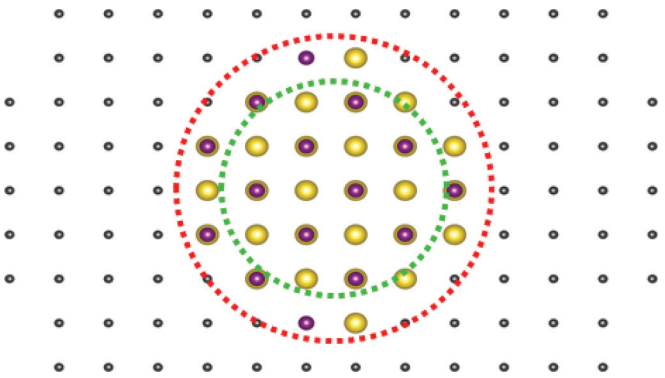

FIG. 1. (Color online) Cutaway view of embedded cluster model of NaI. Classical charges are shown in gray, Na atoms in gold, and I atoms in purple. In this model there are 16 248 charges and 136 atoms. Atoms within the inner circle are allowed to relax during geometry optimization, while those atoms between the circles are held fixed. This image and all images in this paper depicting structures were created using VESTA (Ref. 30).

the cluster models contained 136 quantum-mechanical atoms. The positions of 51 of these were varied in the optimizations. For each Na atom in the cluster two electrons were treated by means of an effective core potential. For each I, 46 electrons were so treated. The calculations presented here are scalar ones that do not include the spin-orbit interaction. The Becke half-and-half[33] (BHH) exchange-correlation potential was used. Unless otherwise stated, calculations were carried out using the NWCHEM code.[34]

III. RESULTS

A. Pure NaI

To characterize localized excitations we constrained the number of spin-up and spin-down electrons and searched for the nuclear coordinates that minimized the total energy of the cluster model subject to these constraints. The results of such a procedure are the geometry and energy of the lowest energy state of each type: a doublet of charge +1 in the case of the STH and a neutral triplet in the STE case. We find that on-center self-trapped holes and excitons are stable in NaI compared to delocalized states, but electrons do not self-trap in pure NaI clusters in our calculations even for pure HF which is known to favor self-trapped states.[20]

In our models, the two I atoms participating in the STE are separated by 3.36 Å, close to the measured (3.23 Å)[35] and theoretical (3.31 Å) isolated I_2^- bond length and far from the I-I separation in the undistorted NaI crystal (4.58 Å). Our isolated I_2^- bond length is in good agreement with other calculations,[36] and the actual STE I-I separation is also in agreement with other theoretical results.[37] The energy of the STE is calculated to be 5.68 eV above the (singlet) ground state of the undistorted crystal and 0.7 eV below the lowest energy triplet state of the undistorted crystal. The measured excitation energy is 5.61 eV.[38] In addition, we calculated an emission energy of 4.27 eV for the STE, in good agreement with the experimentally measured value of 4.207 eV.[39] We also find an on-center STH which resembles the STE (3.38 Å I-I separation) with the electron removed.

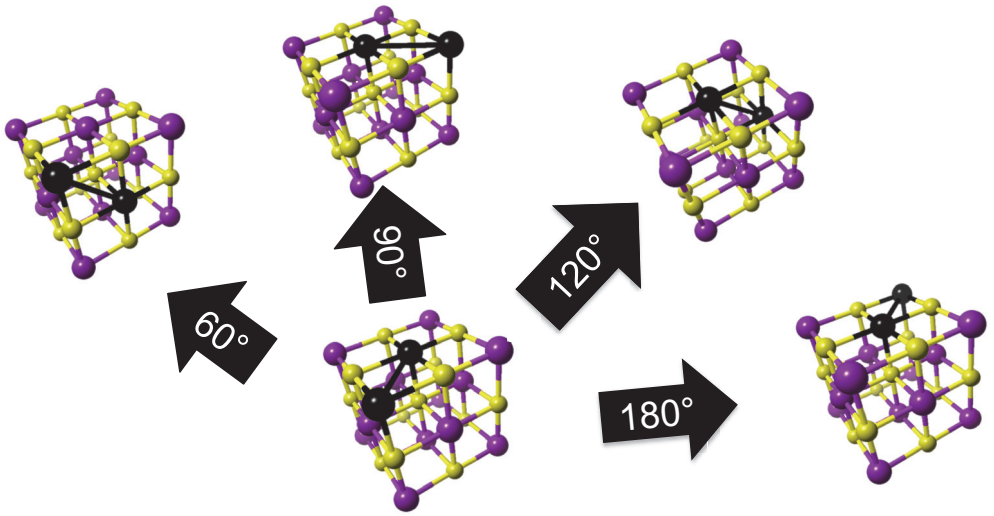

FIG. 2. (Color online) The four near-neighbor hops available to the STE or STH in NaI.

Our calculations estimate the energy of this STH to be 0.50 eV lower than a delocalized hole in the undistorted crystal.

Assuming the conventional picture in which self-trapped excitations migrate via the transfer of lattice distortion and spin density between adjacent lattice sites, we calculated the energy barrier for hopping of the STE and STH in NaI for each of the four possible hop angles between iodine neighbor pairs in the rocksalt structure which are depicted in Fig. 2.

For each hop and type of self-trapped excitation, cluster models were relaxed with the excitation positioned at either end of the jump. The transition state was estimated by relaxing the interior atoms of the cluster except the two I atoms directly participating in the self-trapped excitation (the active halogens) from a starting geometry calculated as the average of the geometries before and after the jump. We have reported this energy difference as the migration barrier in Table I. For all STH jumps, the hole orbital at the transition state is shared among the three halogens involved in the jump. Most of the orbital resides on the central I that participates in the STH before and after the jump, with smaller but significant contributions from the other two iodines involved. Previous work in other alkali halide systems has found similar transition states.[40] Shluger and co-workers[40] postulated the existence of a "one-center" self-trapped hole state near the transition state for the 60° STH jump. They found this state to be unstable; we find the same conclusion for our system in the present work. The energy difference between a one-center trapped hole and the STH provides an upper bound for the transition barrier and provides an explanation for the nearly identical barriers since any of the hops could be accomplished by first transitioning to the one-center state which appears to be adiabatically connected to all the STH states in which the single center participates.

TABLE I. Calculated migration barriers for STH and STE in pure NaI.

Hop angle (deg)	STH barrier (eV)	STE barrier (eV)
60	0.225	0.199
90	0.285	0.267
120	0.241	0.274
180	0.223	0.258

We show the spin density for the relaxed STH and for the transition state of the 120° hop in Fig. 3. In our simulations, the behavior of the hole in the STE hops is very similar to that of the hole in the corresponding STH hops. The STE electron becomes delocalized in the transition state for all hop angles in our clusters.

Popp and Murray[8] estimated a barrier of 0.18 eV for the 60° STH jump, in reasonable agreement with our value of 0.225 eV. On the other hand, experimental estimates of the STE hopping barrier are much lower. For example, Nagata and co-workers[22,23] reported 0.07 eV for Tl-doped NaI. The magnitude of this barrier is directly related to the thermally activated mobility of the STE, and our results suggest that the conventional picture of the low-energy kinetics of STEs should be reexamined. In particular, we expect, based on our calculations, the STE and STH to have nearly identical mobilities. The lower barrier ascribed to the STE can be attributed to the migration of electrons hopping from an STE to a nearby STH. Since the geometries of the STH and STE are similar, we expect the barrier for such a hop to be low. In fact the energy gained by relaxing the neutral triplet state starting in the STH geometry (so that the final configuration is an STE) is 0.02 eV. The hopping barrier can be expected to be of the same order of magnitude.

B. Tl impurities

NaI is commonly doped with Tl, which substitutes for Na at a lattice site to create a light-emitting center. The transfer of energy from diffusing self-trapped excitations to these luminescence centers, while believed to play a significant role in scintillator performance, is not well understood. To investigate this process, we simulated Tl impurities in our models. The lowest energy singlet state for our clusters involves only modest displacements around the Tl to accommodate the larger size of the dopant compared to the Na atom it replaces.

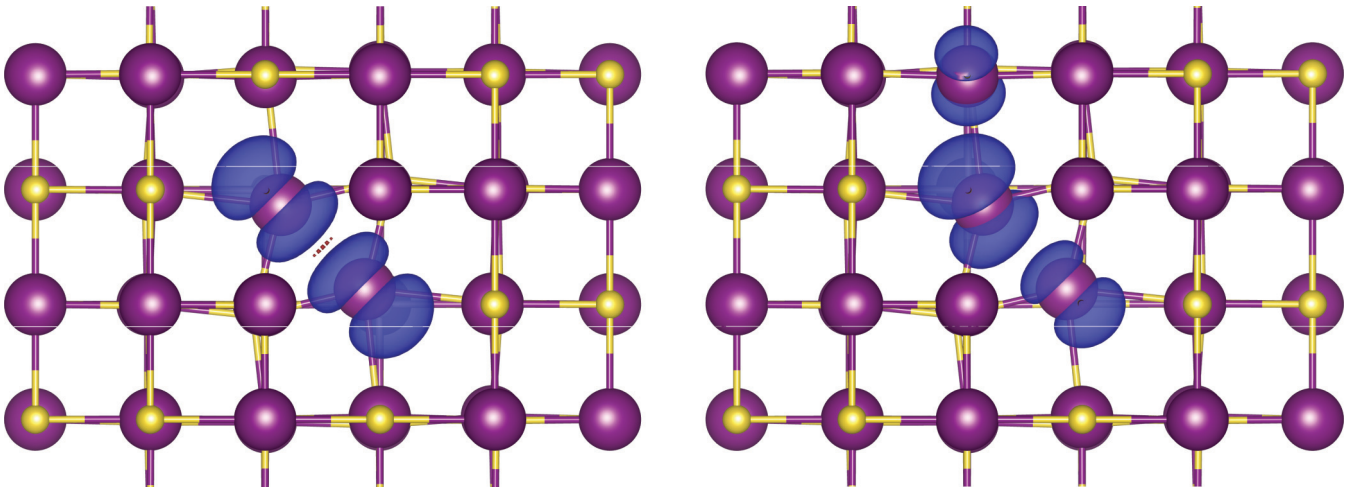

FIG. 3. (Color online) Spin density isosurfaces drawn at 0.001 electrons/bohr^3 around an STH (left panel) and the transition state for a 120° STH jump (right panel).

By optimizing the geometry from various starting points and spin populations, we find a rich collection of stable trapped excitations from this state including two distinct neutral triplet excitons as well as a single trapped hole and a trapped electron.

The two nearly degenerate (the energy of the edge configuration is higher by 0.04 eV in our model) triplet excitations are depicted in Fig. 4. We note that, unlike the bulk self-trapped excitations, the Tl-trapped excitons are stable in LDA and

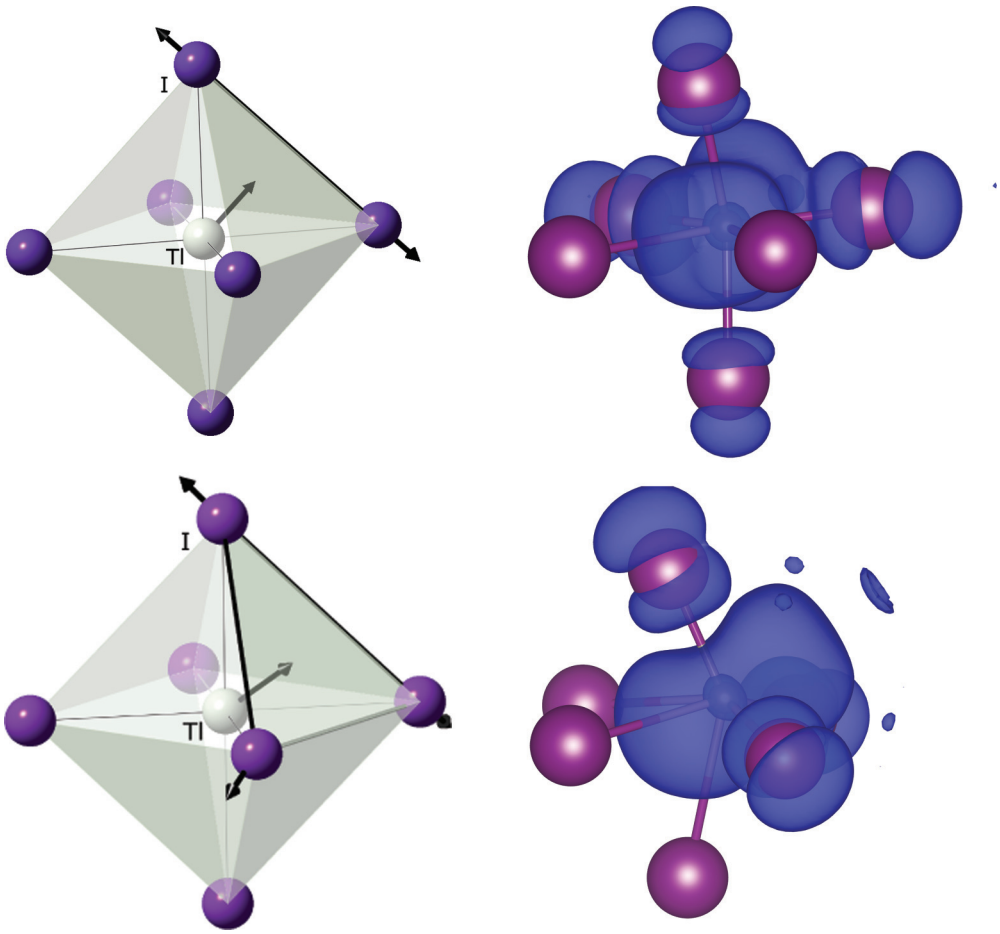

FIG. 4. (Color online) The left column shows schematic diagrams of the displacements relative to a perfect NaI crystal lattice of a Tl impurity participating in two different exciton states. The right column shows the optimized coordinates of the coordinating octahedron that holds the Tl impurity along with a spin density isosurface drawn at 0.001 electrons/bohr^3.

PBE theories, although PBE reverses the relative energies of the two excitons. In bulk NaI, each Na cation is octahedrally coordinated by I anions. The Tl in the singlet ground state sits similarly in the center of a nearly regular octahedron with I at each vertex. The relaxations accompanying the trapping of the triplet states involve the movement of the Tl towards either an edge or face of the octahedron which expands to accommodate the Tl. In both cases the spin density associated with the triplet exciton is localized on the Tl and the accommodating I atoms (cf. Fig. 4). The orbitals involved in the excitons have *s* character around the Tl and *p* character around the I atoms. Calculations of the barrier between the two Tl-trapped excitons were done using cluster models. Additionally, we used the nudged elastic band method as implemented in the SEQQUEST code[41,42] to estimate the barrier. Both LDA[43] and PBE[44] functionals were used. These calculations all indicate that the barrier is very low and that the Tl can rattle around nearly freely in the octahedron formed by the nearest iodines.

We found these Tl-trapped triplet states to be stable compared to a (bulk) STE near a singlet Tl by $\sim$0.25 eV and hence expect diffusing STEs to be trapped when they encounter Tl impurities. Even though the excited states are essentially degenerate, the excitation depicted in Fig. 4(a) has a luminescence energy of 3.46 eV, while the excitation depicted in (b) has a luminescence energy of 2.85 eV due to the slope of the ground-state potential energy surface between the excited state geometries. These calculated transition energies compare well with low-temperature experiments on NaI(Tl)[39] finding bands centered at at 3.76 and 2.95 eV. In other doped alkali halide systems these A_T and A_X emissions have similar structure.[45,46]

The off-site displacement of the Tl center is due to broken symmetry on the excited state potential energy surface induced by the presence of an electron with *p* orbital character. We expect the same type of distortion to occur for the triplet exciton, the trapped electron (Tl^0), and the singlet excited state (Tl*).

We propose that the localized triplet states depicted in Fig. 4 play a role in the transfer of energy from free, diffusing STEs to fixed luminescence centers by capturing the spin density associated with the STE and thereby destroying the STE. The distortion around the Tl, which cannot migrate, replaces the STE. We have succeeded in relaxing a lattice STE in a layer adjacent to a Tl impurity's surrounding octahedron, hence we estimate the radius for capture of a diffusing STE by a Tl impurity to be of the order of the lattice constant.

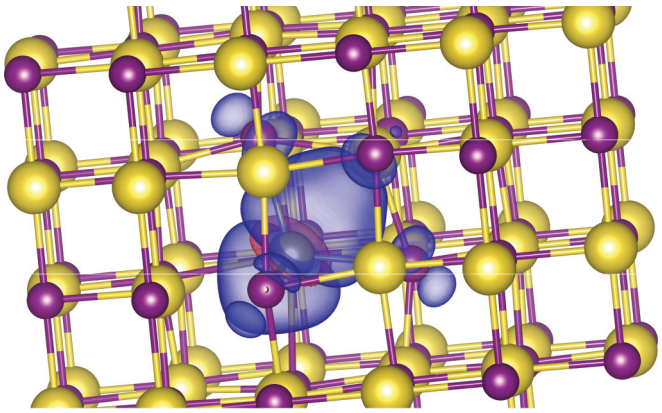

FIG. 5. (Color online) Spin density isosurface drawn at 0.0005 electrons/bohr^3 in a 136-atom cluster containing a Tl^0.

TABLE II. Bond lengths and relaxation energies (energy difference between positively charged clusters in undistorted and fully relaxed geometries) for the STH in pure NaI for several cluster models of different sizes. BHH xc was used for these calculations, so the first line of this table and Table IV are identical. The bond lengths are in Å and the energies in eV.

Cluster size	Bond length	Relaxation energy
48	3.383	0.50
80	3.371	0.69
136	3.357	0.72

Finally, we have found a shallow but stable minimum in which an electron is localized on a Tl impurity (i.e., a Tl^0). The relaxation around this state resembles the exciton in which the octahedron edge lengthens to accommodate the displacement of the Tl (the top row of Fig. 4). This Tl^0 state is only 0.1 eV lower in energy than a delocalized electron in the relaxed singlet (Tl^+) geometry. The spin density of the Tl^0 state is depicted in Fig. 5.

IV. DISCUSSION

To explore the dependence of the physics of self-trapped excitations on cluster size and exchange-correlation treatment, we varied each approximation in baseline calculations of the STH. Table II shows the bond length of the I_2^- in the STH and the relaxation energy (energy gained by allowing the I_2^- to form in a positively charged cluster) for three cluster sizes. In Table III we show various energy differences in neutral cluster models of the same size as those used in Table II. We list the energy difference between the lowest unoccupied orbital (LUMO) and the highest occupied orbital (HOMO) of the singlet configuration at the relaxed singlet (i.e., bulklike ground state) geometry. We also list the excitation energy which is computed as the difference between the total energy of the relaxed triplet (i.e., STE) geometry and the total energy of the relaxed singlet (ground state). Finally we list luminescence energies which were calculated as the difference between the triplet and singlet potential energy surfaces at the relaxed triplet (STE) geometry. From these convergence studies, we estimate the errors due to finite cluster size in energies are $\sim$0.1 eV and in bond lengths are $\sim$0.05 Å.

TABLE III. Calculated energy differences (in eV) for neutral cluster models of different sizes. We show singlet HOMO-LUMO gaps and excitation and luminescence energies for the STE.

Cluster size	HOMO-LUMO	Excitation	Luminescence
48	7.39	5.74	4.49
80	7.23	5.57	4.17
136	7.16	5.68	4.27
Experiment		5.61 (Ref. 38)	4.207 (Ref. 39)

TABLE IV. Bond length, 60° migration barriers, and relaxation energies (energy difference between positively charged clusters in undistorted and fully relaxed geometries) for the STH in pure NaI for several xc functionals which are described further in the text. All calculations in this table used identical 48-atom models. The bond lengths are in Å and the energies in eV.

Functional	60° barrier	Bond length	Relaxation energy
BHH	0.225	3.383	0.50
HF	0.193	3.370	1.55
B3LYP	0.150	3.383	−0.04
Becke 0.325 and 0.625	0.140	3.423	0.18

In Table IV we present the 60° migration barrier, bond length, and relaxation energy for the STH computed with several exchange-correlation (xc) functionals but otherwise identical cluster models. In addition to BHH (Ref. 33) (used for all other results in this paper), results obtained using B3LYP,[47] HF, and a modified BHH in which the fraction of of HF exchange is reduced from 1/2 to 0.325 are tabulated. The bond length is rather insensitive to xc treatment, but, surprisingly, the migration barrier is smaller in the HF theory than in the BHH one. The relaxation energy, however, is monotonic in the fraction of HF exchange included in the otherwise semilocal functional. In fact, the STH, while locally stable, is higher in energy than the undistorted structure in the B3LYP theory. Based on these calculations it is our opinion that in the case of ionic solids such as the alkali halides, the uncertainty in the calculated energies due to the exchange-correlation treatment is larger than that due to finite cluster size effects.

V. CONCLUSION

We have studied trapped excitations in NaI with *ab initio* hybrid DFT using large systems. We find an on-center STE and STH in the pure material and excitons trapped on Tl impurities in NaI(Tl). Our calculations are in very good agreement with available experimental data and largely consistent with the conventional picture of scintillation in NaI except for the STE hopping mobility, for which we find a much higher barrier (close to that for the STH) in our calculations. We suggest further work to validate the barriers and energy levels published here as well as a theoretical description of other microscopic properties outside the scope of this paper, such as STE-STE annihilation, and STE radiative and nonradiative decay lifetimes. It is also our hope that models of scintillation efficiency, parametrized with *ab initio* results such as the ones presented here and including both STE migration mechanisms be constructed and tested.

ACKNOWLEDGMENTS

This research was supported by the National Nuclear Security Administration, Office of Nuclear Nonproliferation Research and Engineering (NA-22), of the U.S. Department of Energy (DOE). A portion of this research was performed using EMSL, a national scientific user facility sponsored by the Department of Energy's Office of Biological and Environmental Research and located at Pacific Northwest National Laboratory. Additionally, a portion of the research was performed using PNNL Institutional Computing at Pacific Northwest National Laboratory.

[1] Z. Wang, Y. Xie, B. D. Cannon, L. W. Campbell, F. Gao, and S. Kerisit, J. Appl. Phys. **110**, 064903 (2011).
[2] G. F. Knoll, *Radiation Detection and Measurement*, 3rd ed. (Wiley, New York, 2000).
[3] R. Devanathan, L. R. Corrales, F. Gao, and W. Weber, Nucl. Instrum. Methods Phys. Res. A **565**, 637 (2006).
[4] J. C. Phillips, Phys. Rev. **136**, A1705 (1964).
[5] R. T. Williams, K. S. Song, W. L. Faust, and C. H. Leung, Phys. Rev. B **33**, 7232 (1986).
[6] K. Teegarden and G. Baldini, Phys. Rev. **155**, 896 (1967).
[7] J. E. Eby, K. J. Teegarden, and D. B. Dutton, Phys. Rev. **116**, 1099 (1959).
[8] R. Popp and R. Murray, J. Phys. Chem. Solids **33**, 601 (1972).
[9] C. H. Leung and K. S. Song, J. Phys. C **12**, 3921 (1979).
[10] A. L. Shluger, N. Itoh, V. E. Puchin, and E. N. Heifets, Phys. Rev. B **44**, 1499 (1991).
[11] V. E. Puchin, A. L. Shluger, K. Tanimura, and N. Itoh, Phys. Rev. B **47**, 6226 (1993).
[12] C.-R. Fu, L.-F. Chen, and K. S. Song, J. Phys.: Condens. Matter **11**, 5517 (1999).
[13] W. Moses, G. Bizarri, R. T. Williams, S. Payne, A. Vasil'ev, J. Singh, Q. Li, J. Grim, and W. Choong, IEEE Trans. Nucl. Sci. **59**, 2038 (2012).
[14] R. B. Murray and A. Meyer, Phys. Rev. **122**, 815 (1961).
[15] S. Payne, N. Cherepy, G. Hull, J. Valentine, W. Moses, and W.-S. Choong, IEEE Trans. Nucl. Sci. **56**, 2506 (2009).
[16] R. T. Williams and K. S. Song, J. Phys. Chem. Solids **51**, 679 (1990).
[17] A. M. Stoneham, J. Phys. C **7**, 2476 (1974).
[18] K. S. Song, A. M. Stoneham, and A. H. Harker, J. Phys. C **8**, 1125 (1975).
[19] N. Itoh and A. M. Stoneham, *Materials Modification by Electronic Excitation* (Cambridge University Press, Cambridge, UK, 2001).
[20] A. M. Stoneham, Modell. Simul. Mater. Sci. Eng. **17**, 084009 (2009).
[21] S. Kerisit, K. M. Rosso, B. D. Cannon, F. Gao, and Y. Xie, J. Appl. Phys. **105**, 114915 (2009).
[22] S. Nagata, K. Fujiwara, and H. Nishimura, J. Lumin. **47**, 147 (1990).
[23] H. Nishimura and S. Nagata, J. Lumin. **40-41**, 429 (1988).
[24] J. L. Gavartin, P. V. Sushko, and A. L. Shluger, Phys. Rev. B **67**, 035108 (2003).
[25] R. C. Baetzold and K. S. Song, J. Phys.: Condens. Matter **3**, 2499 (1991).
[26] S. E. Derenzo and M. J. Weber, Nucl. Instrum. Methods Phys. Res. A **422**, 111 (1999).
[27] J. F. Rivas-Silva, L. Rodríguez-Merino, M. Berrondo, and A. Flores-Riveros, Int. J. Quantum Chem. **77**, 785 (2000).
[28] P. V. Sushko, A. L. Shluger, and C. A. Catlow, Surf. Sci. **450**, 153 (2000).
[29] N. Govind, P. Sushko, W. Hess, M. Valiev, and K. Kowalski, Chem. Phys. Lett. **470**, 353 (2009).

[30]K. Momma and F. Izumi, J. Appl. Crystallogr. **44**, 1272 (2011).
[31]L. F. Pacios and P. A. Christiansen, J. Chem. Phys. **82**, 2664 (1985).
[32]F. Weigend and R. Ahlrichs, Phys. Chem. Chem. Phys. **7**, 3297 (2005).
[33]A. D. Becke, J. Chem. Phys. **98**, 1372 (1993).
[34]M. Valiev, E. Bylaska, N. Govind, K. Kowalski, T. Straatsma, H. V. Dam, D. Wang, J. Nieplocha, E. Apra, T. Windus *et al.*, Comput. Phys. Commun. **181**, 1477 (2010).
[35]E. C. M. Chen and W. E. Wentworth, J. Phys. Chem. **89**, 4099 (1985).
[36]A. Md Asaduzzaman and G. Schreckenbach, Theor. Chem. Acc. **122**, 119 (2009).
[37]P. E. Cade, A. M. Stoneham, and P. W. Tasker, Phys. Rev. B **30**, 4621 (1984).
[38]A. Song and R. T. Williams, *Self-Trapped Excitons*, Springer Series in Solid-State Sciences (Springer, New York, 1996).
[39]P. A. Rodnyi, *Physical Processes in Scintillators*, 1st ed. (CRC Press, Boca Raton, 1997).
[40]A. L. Shluger, L. N. Kantorovich, E. N. Heifets, E. K. Shidlovskaya, and R. W. Grimes, J. Phys.: Condens. Matter **4**, 7417 (1992).
[41]A. E. Mattsson, P. A. Schultz, M. P. Desjarlais, T. R. Mattsson, and K. Leung, Modell. Simul. Mater. Sci. Eng. **13**, R1 (2005).
[42]P. A. Schultz, SEQQUEST code, http:/dft.sandia.gov/Quest.
[43]J. P. Perdew and A. Zunger, Phys. Rev. B **23**, 5048 (1981).
[44]D. R. Hamann, Phys. Rev. B **40**, 2980 (1989).
[45]A. Fukuda, Phys. Rev. B **1**, 4161 (1970).
[46]L. S. Dang, Y. M. d'Aubigné, R. Romestain, and A. Fukuda, Solid State Commun. **26**, 413 (1978).
[47]A. D. Becke, J. Chem. Phys. **98**, 5648 (1993).

Off-center Tl and Na dopant centers in CsI

R M Van Ginhoven[1] and P A Schultz[2]

[1] Pacific Northwest National Laboratory, Richland, WA 99352

[2] Sandia National Laboratory, Albuquerque, NM

E-mail: Renee.VanGinhoven@pnnl.gov,paschul@sandia.gov

Abstract. We use density functional theory calculations to characterize the electronic and structural properties of the Tl and Na dopant centers in CsI. We find that the Tl and Na centers can accept one or two electrons and couple to long-range relaxations in the surrounding crystal lattice to distort strongly off-center to multiple distinct minima, even without a triplet excitation. The long-range distortions are a mechanism to couple to phonon modes in the crystal, and are expected to play an important role in the phonon-assisted transport of polarons in activated CsI and subsequent light emission in this scintillator.

PACS numbers: 71.20.Ps,78.55.Fv,71.55.Ht

Submitted to: *J. Phys.: Condens. Matter*

1. Introduction

There has been considerable interest in recent years in the development of new materials and optimization of current materials for use as scintillating radiation detectors. Signal production in scintillating detectors involves conversion of cascade energy into optical emission. This is a relatively slow process involving transport of carriers to luminescent centers, in competition with other processes that dissipate a portion of the initial energy. Prediction of the performance of new or improved materials requires an understanding of these transport processes. Cesium Iodide doped with Thallium or Sodium (CsI:Tl, CsI:Na), is widely used as an effective scintillating material. Despite many careful studies over several decades [1], the mechanisms for energy transport and light emission, and the role of the dopant atoms in this material are not well understood. Previous cluster-based *ab initio* calculations of Tl in CsI and NaI clusters have demonstrated the need for relatively large systems to adequately describe the surrounding lattice response, but only examined symmetric lattice distortions [2].

We use density functional theory (DFT) to investigate the electronic and structural properties of Na and Tl dopants in CsI, along with related intrinsic defects, to elucidate the behavior of these dopants. It is well established that standard DFT using semilocal exchange-correlation potentials does not correctly describe the expected energy carriers in the pure alkali halides, either self-trapped holes, also known as V_k centers, or self-trapped excitons (STE) [3, 4]. However, we are not attempting to model the STE or V_k center. For defects with well-localized electronic states, such as the vacancy and dopant impurity point defects we investigate here, we expect a semilocal description to provide a fully adequate and decisive description of the defect structure and behavior.

In addition to having a stable neutral state and a localized triplet excitation, a defect-trapped exciton (DTE), we find that each dopant center can accept one or two electrons. All of the charge states of substitutional Tl and Na distort off-center, and couple to surprisingly long-range distortions in the surrounding crystal lattice. Three symmetry-distinct distortions are found, into the 001-face, into the 110-edge, and along the 111-bond directions, and are stable even without having trapped a local triplet excitation (exciton). These distortions involve long-range lattice deformations that would naturally couple to phonon modes, and include local structural deformations that would facilitate capture and transport of excitons. This provides a novel mechanism to explain the emission behavior activated by the dopants.

2. Computational Methods

The density functional supercell calculations for CsI:Tl were performed with the periodic pseudopotential SeqQuest code[5]. The spin-polarized local-density approximation (LDA) calculations used the form parameterized by Perdew and Zunger[6] and the generalized gradient functional used was formulated by Perdew, Burke and Ernzerhof[7]. Carefully optimized[8] norm-conserving pseudopotentials[9] (PP) were used for all

atoms: the cesium PP included its semicore $5p^6$ electrons among the valence electrons along with a non-linear core correction[10] (R_{nlc}=2.5 Bohr), and the [core]$5p^6 6s^{0.1}$ atom used a hardened d-potential (R_l=1.4) for its local potential; an otherwise standard s^2p^5 iodine PP used a hardened l=3 (R_l=1.2) potential for the local potential as the optimal l=2 potential (R_l=1.57) proved too soft for good transferability; and the $5d^{10}$ shell of thallium was placed in the valence and used as the local potential, while its p-potential was tuned (R_l=1.57) for better transferability. The double-zeta plus polarization basis sets were constructed of contracted Gaussian functions.

We used the local moment countercharge method to solve the Poisson Equation for charged supercells[11] and extrapolated to bulk asymptotic limits using the finite defect supercell model.[12] Bulk screening energy outside the supercell[12] was evaluated using the experimental static dielectric constant,[13] 5.65, and an internal screening depth of 1.8 Bohr (∼0.9 Å). The numerical results are not highly sensitive to these values, and the convergence of results extrapolated from different sized supercells confirms the accuracy of this approach.

The defect calculations were performed with the supercell fixed at the theoretical equilibrium lattice parameter: 4.417 Å for LDA and 4.680 Å for PBE, The experimental lattice constant is 4.567 Å.[13]. The measured bulk modulus for B2 structure CsI is 12.6 GPa[14]. Our computed LDA bulk modulus is 16.6 GPa, slightly stiffer than experiment, and the PBE value is 9.7 GPa, slightly softer than experiment, like for the lattice constant, bracketing the experimental value as LDA and PBE usually do. Supercells ranged from 3x3x3 (54-site) to 6x6x6 (432-site) scaled versions of the primitive 2-atom cell of the CsI B2 structure, and used 3^3 grids for sampling the Brillioun Zone in the 54-site cell and 2^3 k-grids for the larger cells. The atomic configurations were energy-relaxed to within 1 meV of a local minimum, with forces on atoms less than 0.01 eV/Å. Supercell size tests (with LDA) indicated that 54-site and 128-site failed to adequately contain the extensive strain fields around the defects, while 250-site results were well-converged compared to 432-site results. Results reported in this paper are extrapolated from 250-site supercell calculations. Formation energies are quoted in the Cs-rich limit, i.e., the bulk bcc Cs and CsI define the atomic reference chemical potentials. In this context, the computed formation energy of the neutral Cs vacancy is 3.74(4.22) eV and of the I vacancy, 0.50(0.54) eV using PBE(LDA). The heat of formation of B2 structure CsI, from bulk bcc Cs and the I_2 molecule elemental references are computed to be 3.71 eV in LDA and 3.42 eV in PBE. These heats of formation, using the conventions outlined by Zhang and Northrup[15] to compute defect formation energies, can be used to convert the defect formation energies from one limit (Cs-rich) to another (I-rich).

3. Results

Calculations were performed for a purposefully selected set of defects, two intrinsic defects, the Cs vacancy V_{Cs} and the I vacancy V_I, and then for the dopant atoms Tl and Na, both known to substitute on the Cs site: Tl_{Cs} and Na_{Cs}. In Tl-doped CsI, the

Tl-dimer substitutional, $(Tl_2)_{Cs}$, is a common defect, and was also included in this series of calculations. Furthermore, this dimer proves especially important to set a useful limit on the position of the valence band edge. An extensive search was undertaken to find all the stable charge states and determine their optimum structure. The resulting defect level diagram, summarizing the positions of the ground state charge transitions within the CsI band gap, is presented in Figure 1.

The doubly ionized Tl dimer center state is only barely in the band gap in the DFT calculations, both LDA and PBE, and, in the absence of a more definitive marker to locate the band edge on this diagram, its (+/++) transition is adopted as the valence band edge (VBE). The VBE cannot be directly computed in the same total energy calculations used to obtain the defect level energies, but we can use this defect, cleanly identified as a local defect state, and therefore in the band gap, as the upper bound of the position of the VBE. As we shall see later, this choice is likely overly conservative.

The V_{Cs} has charge transitions only slightly above the $(Tl_2)_{Cs}$ (+/++) transition, near the VBE, and the V_I has levels high in the gap. The near-perfect agreement between the levels extrapolated from the 250-sites cells and from the 432-site cells, depicted in Figure 1 for the vacancies, confirms the convergence of these defect level calculations to the infinitely dilute bulk limit. The LDA and PBE calculations agree closely with each other, finding the same charge states and similar ground state structures for all the defects. The computed levels for all defects are, reassuringly, not sensitive to the choice of density functional, lending greater confidence to the analysis of the results[8].

The measured band gap is reported to be 6.1 to 6.4 eV [16, 17, 18]. Our computed defect levels span a range of almost 5 eV, exceeding the Kohn-Sham (eigenvalue) gap for CsI for LDA and PBE in these calculations, which is 3.80 and 3.58 eV, respectively.

The calculation of localized defect levels can be used to identify possible dopants, and defects that may compete with desired emitters for hole or electron trapping. For example, from Figure 1 we can deduce that the iodine vacancy or the negatively charged $(Tl_2)_{Cs}$ may compete with the luminescent Tl or Na dopants, while the cesium vacancy certainly will not.

3.1. Intrinsic defects

The V_I is a commonly occurring defect that plays an important role in energy losses [19], and interferes with light output. We find that this defect can trap either a hole or an electron, with 0, 1, or 2 electrons in the vacancy for the $V_I(+)$, $V_I(0)$, and $V_I(-)$ charge states of the defect (see Figure 1). The neutral V_I, commonly known as the F-center, takes a symmetric O_h structure in spin-polarized calculations, as do both the ionized $V_I(+)$ and the $V_I(-)$, the latter commonly known as the F'-center. Our calculations predict the ionization level for the F-center, the (0/+) transition in Figure 1, to be 3.5 eV above the Tl dimer (+/++) transition, our assumed VBE. The ionization level of the F'-center, the (-/0) transition, is predicted to be 0.8 eV above the F-center

ionization, in excellent agreement with the experimental separation of 0.8 eV [20]. This close agreement lends confidence to the calculations, but should be considered in light of large quoted uncertainties in the experimental analysis of ∼0.5 eV.

Locating the experimental levels relative to a band edge is less definitive, as this defect level position in the gap is not measured directly. The position of the F-center level is deduced through a combination of different experimental analysis, that starts with the photoexcitation of the F-center electron into vacuum, then derives the distance of the conduction band edge (CBE) from the vacuum via measurements of the electron affinity of bulk CsI, and then also includes the size of the band gap. The F-center electron and F'-center electron have vacuum ionization energies quoted at 2.2 and 1.4 eV, respectively, with large uncertainty in the latter[20]. The vacuum to CBE distance is quoted to be 0.3 eV [20, 18] to as large as 0.7 eV [21]. The band gap also adds about 0.2 eV uncertainty. The experimental analyses suggest an ionization level for the F-center of roughly or a little less than 4 eV above the VBE [21, 20, 22]. Our calculation predicts this level is 3.5 eV, or greater, above the VBE, in rather good agreement with this experimental analysis, considering the uncertainties in the experimental analysis. Given that the band gap is explicitly contained within the experimental assessment of this level, this implies that the effective band gap seen by the semi local DFT calculations is within ∼0.5 eV of experiment.

The low defect formation energy of the V_I is consistent with the easy formation of F-centers[19, 23]. The formation energy of of $V_I(+)$ is reduced linearly with the distance of the Fermi level below the F-center transition, where the $V_I(+)$ formation energy exactly matches the formation energy of $V_I(0)$. Taken together, the splitting of the V_I donor states, the implicit agreement with experimental band gap, and the correct physical description of the formation of iodine vacancies, these results indicate that the semilocal LDA and PBE functionals are performing accurately for the ground state defects in CsI.

The V_{Cs} may also trap either a hole or an electron. In LDA, the defect remains in a symmetric structure for each charge level. The relatively high formation energy, near 4 eV, is consistent with this not being a common defect in CsI. However, the V_{Cs} exhibits another interesting feature in the calculations. Using spin-polarized PBE we found a second minima for the neutral doublet state in which a pair of iodine atoms adjacent to the vacancy dimerize, resembling a V_k center geometry [3]. This minima is a shallow metastable state 0.18 eV eV higher than the symmetric configuration. That a V_k-like center is found at all without the use of hybrid functionals implies that this defect is a significant trap with the ability to strongly localize holes at sites in the iodine sub-lattice adjacent to the vacancy. This V_k+V_{Cs} configuration is shown in Figure 2.

3.2. Dopants

Both the Tl and Na dopant centers, in addition to having a stable neutral state, can trap one or two electrons. In addition to these ground state structures, both the LDA and

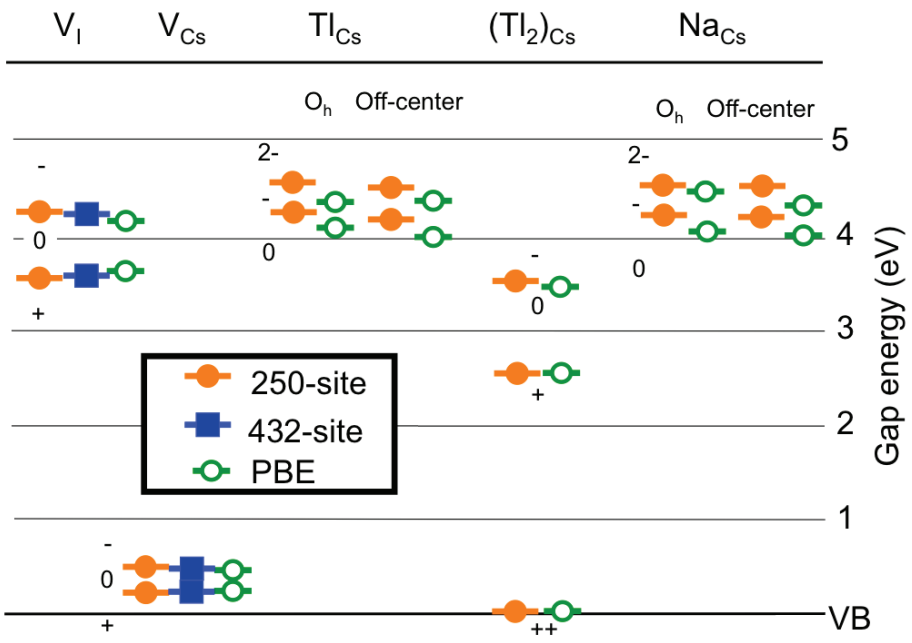

Figure 1. Defect levels in CsI (color online). LDA and GGA (PBE) are both shown, results are the same within error of the techniques. Results are converged at 250 atoms.

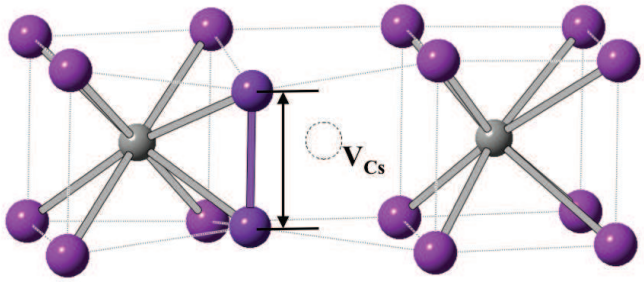

Figure 2. Local minimum with a V_k-like distortion adjacent to a Cs vacancy (V_{Cs}). Iodine is shown in violet violet, Cs is silver. The iodine-iodine distance indicated by the arrow is decreased from the bulk crystal distance of 4.68 Å to 3.45 Å.

the PBE find a neutral triplet DTE to be stable for the Tl and Na dopants. These trap levels are high in the gap, roughly at or above the V_I defect levels. While each charge state has a metastable symmetric on-site configuration, they all have lower-energy off-site distortions, with minima in three distinct directions: toward the 001-face, toward the 110-edge, and a shallower minimum directly toward the nearest-neighbor iodine in the 111-direction. These distortions had been predicted for Tl-trapped excited states in CsCl:Tl, CsBr:Tl, and CsI:Tl[24, 25, 26]. Our calculations confirm the presence of these distortions in the triplet DTE, but we find that these distortions already exist in the ground state, including for the neutral defect.

The magnitudes of these displacements are summarized in Table 1. The distortion is small in the neutral defect (e.g. the Tl^+), reminiscent of a soft-mode ferroelectric

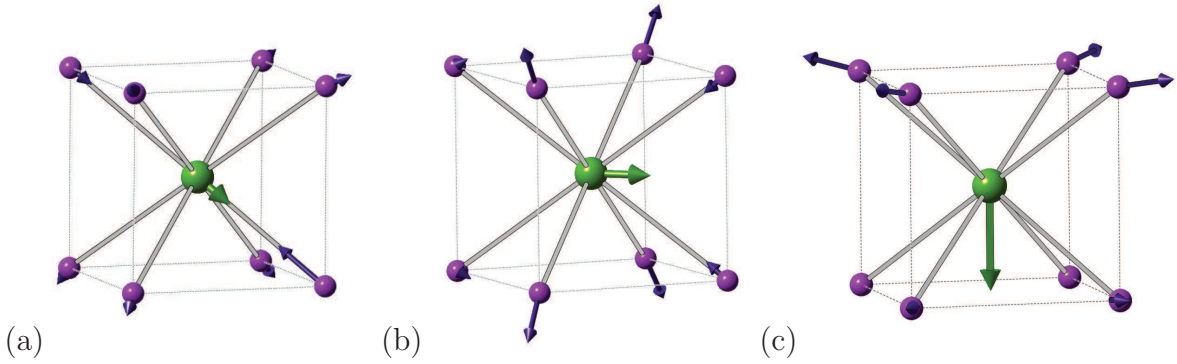

Figure 3. The three off-center structures for the Tl^0 center and nearest neighbor shell of iodine (color online). Tl is shown as light gray (green), I is dark gray (violet). For visual clarity, the arrows are exaggerated by a factor of 2 for the Tl displacement, and by a factor of 10 for the I displacement. The Tl^0 is displaced along the(a) $< 100 >$, (b)$< 110 >$, or $< 111 >$ directions. The displacements are with respect to the symmetric Tl^0 structure.

phase transition seen in dilated TlI crystals [27]. This state has no localized electrons in the gap, yet already exhibits a distinct distortion. The distortion is larger in PBE, perhaps because of the larger lattice constant and softer bulk modulus in PBE, relative to the LDA, are more accommodating to an off-site distortion. The distortion becomes larger in magnitude as localized electrons are trapped at the center. The displacement for the Tl^0 (single trapped electron) center is significant, about 1 Å, about halfway to the face of the cube formed by the nearest-neighbor iodine ions. The localization exhibited here demonstrates that the semilocal functionals, unlike for the STE and V_k center, are not afflicted with a localization problem for these ground state defects.

The structures of the off-center dopants are only found if the surrounding lattice is allowed to relax; distorting the dopant off-site from a symmetric structure causes the dopant to return to the central site. The displacement is accompanied by significant long range distortions in the lattice, involving the coordinated movement of over 100 atoms. The nature of the distortions for the dopant and nearby atoms is depicted in Figure 3. The displacement field around the distorted dopant has pairing distortion reminiscent of incipient V_k centers. This dimerizing distortion is strongest and most apparent in the neighbors of the 110-distorted dopant center shown in Figure 3(b), but this tendency extends deep into the surrounding lattice.

In the neutral singlet ground state, the distorted configurations have energies within 0.02 eV of each other. For dopants with trapped electrons or in the triplet state results for LDA show that the off-center minima are 0.02 to 0.06 eV lower than central position, all within 0.04 eV, in the order $111 > 110 > 100$ (100 is lowest-energy position). For PBE, these energy differences are slightly enhanced. Despite requiring the concerted motion of over 100 atoms, barriers between these states are also low, $\sim$0.01 eV, close to the resolution of the current methods, for hops directly between off-center positions. The low barriers between the local minima are consistent with previous predictions from both

Table 1. Displacement parameters in lattice units for Tl in CsI(Tl) for LDA and PBE in the neutral (Tl^+) state, with 1 (Tl^0), and 2 (Tl^-) trapped electrons, and in the neutral triplet state.

Direction		Tl^+	Tl^0	Tl^-	Triplet
100	LDA	0.01	0.19	0.21	0.31
	PBE	0.11	0.23	0.23	0.36
110	LDA	0.01	0.11	0.13	0.10
	PBE	0.10	0.15	0.14	0.16
111	LDA	0.01	0.03	0.07	0.02
	PBE	0.09	0.08	0.07	0.08

Table 2. Calculated and measured triplet luminescence energy(E_{lum}) for the Tl center in CsI, eV (nm).

LDA (this work)		Experiment [30]	
Geometry	E_{lum}	Peak Assignment	E_{lum}
100	2.90 (427)	$A_X^{'}$	2.25 (560)
110	3.38 (367)	$A_T^{'}$	2.55 (490)
111	3.49 (355)	A_T	3.09 (400)
O_h	3.55 (349)	A_X	3.31 (370)

theory end experimental work [24, 28] for energy transfer between the different excited state emissions assigned directly to the Tl. This result means that dopant atoms may vibrate nearly freely about the cage, except at very low temperatures, as was found for Tl in NaI:Tl[29]. It also implies that the position of the dopant is very strongly affected by local phonon modes or any local distortions.

3.2.1. Off-center Tl and calculated emission energies The current results yield 4 possible Tl-related emission energies, based on the 4 possible positions of the Tl center in the triplet state. These energies, which we calculated as the difference between the triplet and singlet potential energy surfaces at the relaxed triplet (DTE) geometry, are listed in Table 2, along with measured emission energies and suggested assignment based on polarization data[30]. The current results suggest emission from an interconnected potential energy surface of the several configurations of the Tl center. The calculated energies correspond roughly to the observed peaks, but this picture is not complete.

Interpretation of experimental measurements has led to the assignment of the UV peaks to relaxed excited states of the Tl center, and the visible emission peaks to tunneling recombination between the Tl atom and a nearby V_k center[31, 32]. The two visible peaks, ($A_X^{'}$ and $A_T^{'}$) are also postulated to be due to the interaction of a Tl and a perturbed STE either adjacent to the Tl, or offset by one unit cell[33].

Through examination of the distortions in the iodine sublattice in our results, we are

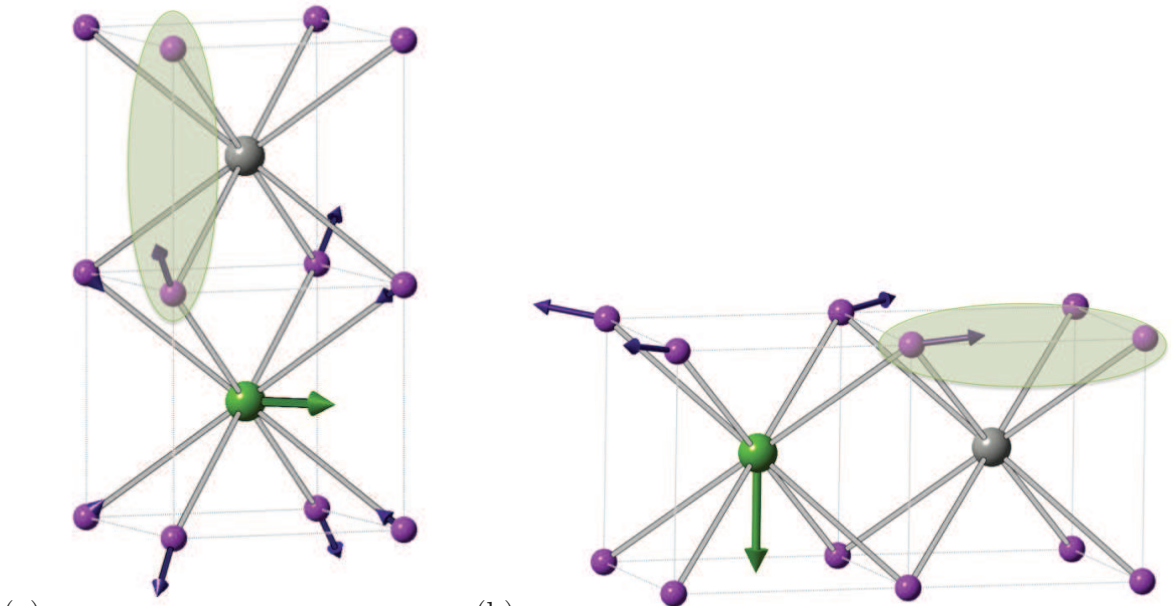

Figure 4. Possible V_k center placements adjacent to 110 (a) and 100 (b) off-center Tl centers. Tl is shown as light gray (green), I is dark gray (violet), Cs is silver.

able to identify several likely locations for a perturbed V_k center. We note that especially for the 110 distorted Tl, we see nearby distortions of the I lattice that resemble incipient V_k centers even in the ground state. Proposed adjacent perturbed V_k centers for the 110 and 100 Tl displacements are shown in Figure 4. There was no obvious candidate for the 111 distortion. Localization of an STE or V_k on one of these iodine pairs should lower the energy of the 100 and 110 states, resulting in lower calculated emission energy, more in line with the experimental values. Quantitative investigation of the localized V_k center and STE, beyond the scope of this work, will require simulation methods with more explicit treatment of exchange, such as hybrid functionals [29, 3].

Finally, we note that the distortion field of the iodine sublattice resembles an array of incipient V_k centers, and therefore may be expected to interact with the transport of energy carriers near Tl or Na dopants. This indicates that transport and emission characteristics related to the off-center distortion of the dopant center will be strongly tied to phonon modes of the crystal.

Acknowledgments

This project is supported by Office of Nuclear Nonproliferation Research and Engineering (NA22), the U.S. Department of Energy. The research was performed in part using EMSL, a national scientific user facility sponsored by the Department of Energy's Office of Biological and Environmental Research and located at Pacific Northwest National Laboratory. Sandia National Laboratories is a multi-program laboratory managed and operated by Sandia Corporation, a wholly owned subsidiary of

Lockheed Martin Corporation, for the U.S. Department of Energy's National Nuclear Security Administration under Contract DE-AC04-94AL85000.

References

[1] M. Nikl. Wide band gap scintillation materials: Progress in the technology and material understanding. *Phys. Stat. Sol.*, 178:595, 2000.

[2] A. Aguado, A. Ayuela, J. M. Lopez, and J. A. Alonso. Lattice distortions around a Tl^+ impurity in NaI:Tl^+ and CsI:Tl^+scintillators: an ab initio study involving large clusters. *Phys. Rev. B*, 58:11964, 1998.

[3] R. M. Van Ginhoven, J. E. Jaffe, S. Kerisit, and K. M. Rosso. Trapping of polarons and excitons in scintillators: CsI, $LaCl_3$, and $LaBr_3$. *IEEE Trans. Nucl. Sci.*, 57:2303–2308, 2010.

[4] S. E. Derenzo and M. J. Weber. Ab initio cluster calculations of hole transport and activator excitation in CsI:Tl and CsI:Na. *IEEE CNF, Nuclear Science Symposium*, 1:164, 1997.

[5] P. A. Schultz. SeqQuest *code (unpublished). See http:/dft.sandia.gov/Quest.*, 1982.

[6] J. P. Perdew and A. Zunger. Self-interaction correction for density-functional approximations for many-electron systems. *Phys. Rev. B*, 23:5048, 1981.

[7] J. P. Perdew, K. Burke, and M. Ernzerhof. Generalized gradient approximation made simple. *Phys. Rev. Lett.*, 77:3865, 1996.

[8] A. E. Mattsson, P. A. Schultz, T. R. Mattsson, K. Leung, and M. P. Desjarlais. Designing meaningful density functional theory calculations in material science—a primer. *Modelling Simul. Mater. Sci. Eng.*, 13:R1, 2005.

[9] D. R. Hamann. Generalized norm-conserving pseudopotentials. *Phys. Rev. B*, 40:2980, 1989.

[10] S. G. Louie, S. Froyen, and M. L. Cohen. Nonlinear ionic pseudo potentials in spin-density-functional calculations. *Phys. Rev. B*, 26:1738, 1982.

[11] P. A. Schultz. Charged local defects in extended systems. *Phys. Rev. Lett.*, 84:1942, 2000.

[12] P. A. Schultz. Theory of defect levels and the "band gap problem" in silicon. *Phys. Rev. Lett.*, 96:246401, 2006.

[13] W. Bührer and W. Hälg. Crystal dynamics of cesium iodide. *Phys. Stat. Sol. (b)*, 46:679, 1971.

[14] Z. P. Chang and G. R. Barsch. Nonlinear pressure dependence of elastic constants and fourth-order elastic constants of cesium halides. *Phys. Rev. Lett.*, 19:1381, 1967.

[15] S. B. Zhang and J. E. Northrup. Cemical potential dependence of defect formation energies in GaAs: Application to Ga self-diffusion. *Phys. Rev. Lett.*, 67:2339, 1991.

[16] J. E. Eby, K. J. Teegarden, and D. B. Dutton. Ultraviolet absorption of alkali halides. *Phys. Rev.*, 116:1099–1105, 1959.

[17] K. Teegarden and G. Baldini. Optical absorption spectra of the alkali halides at 10K. *Phys. Rev.*, 155:896–907, 1967.

[18] T. H. Distephano and W. E. Spicer. Photoemission from CsI: Experiment. *Phys. Rev. B*, 7:1554, 1973.

[19] A. I. Popov and E. Balanzat. F centre production in CsI and CsI-Tl crystals under Kr ion irradiation at 15 k. *Nucl. Instrum. Meth. B*, 166-167:545–549, 2000.

[20] H. W. Sarkas, L. H. Kidder, and K. H Bowen. Photoelectron spectroscopy of color centers in negatively charged cesium iodide nanocrystals. *J. Chem. Phys.*, 102:57–66, 1995.

[21] M. A. H. Chowdhury, S. J. Watts, D. C. Imrie, A. K. McKemey, and A. G. Holmes-Siedle. Studies of radiation tolerance and optical absorption bands of CsI(Tl) crystals. *Nucl. Instrum. Meth. A*, 432:147–156, 1999.

[22] P. V. Galiy, O. Ya Mel'nyk, and O. V. Tsvetkova. Excitonic ionizations of the electron centres in caesium iodide crystal and exoemission of electrons. *J. Lumin.*, 112:105–108, 2005.

[23] K. S. Song and R. T. Williams. *Self-Trapped Excitons*, volume 105 of *Springer Series in Solid-State Sciences*. Springer, New York, 1996.

[24] G. P. Pazzi, M. Nikl, M. Bacci, E. Mihokova, J. Hlinka, P. Fabeni, and L. Salvini. Influence

of Ti^+ concentration on emission and decay kinetics of CsI:Ti^+ single crystals. *J. Lumin.*, 60-61:527–530, 1994.

[25] S. G. Zazubovich. Jahn-Teller effect and partially covalent bond as causes of low symmetry of Ga^+, In^+, and Tl^+ centers in CsCl-type alkali halides. *Phys. Stat. Sol.*, 38:119, 1970.

[26] M. Bacci, E. Mihokova, and K. Polak. Coexistence of Jahn-Teller distortions in an O_h symmetry: A general view including the spin-orbit interaction. *Phys. Rev. B*, 55:14257, 1997.

[27] Mao-Hua Du and David J. Singh. Enhanced born charge and proximity to ferroelectricity in thallium halides. *Phys. Rev. B*, 81:144114, 2010.

[28] M. Nikl, J. Hlinka, E. Mihokova, K. Polak, P. Fabeni, and G. P. Pazzi. Decay kinetics of CsI:Tl luminescence excited in the a absorption band. *Phil. Mag. B*, 67:627–649, 1993.

[29] M. P. Prange, R. M. Van Ginhoven, N. Govind, and F. Gao. Formation, stability and mobility of self-trapped excitations in NaI and NaI(Tl). *Phys. Rev. B*, 87:115101, 2013.

[30] V. Nagirnyi, S. Stolovich, S. Zazubovich, V. Zepelin, E. Mihokova, M. Nikl, G. P. Pazzi, and L. Salvini. Peculiarities of the triplet relaxed excited-state structure and luminescence of a CsI:Tl crystal. *J. Phys. Condens. Matter*, 7:3637–3653, 1995.

[31] Chun-Rong Fu, Ling-Fu Chen, and K S Song. Self-trapped excitons in pure and Na- and Tl-doped caesium halides and the recombination luminescence. *J. Phys. Condens. Matter*, 11:55175532, 1999.

[32] E. Mihokova, V. Nagirnyi, M. Nikl, S. Stolovich, G.P . Pazzi, S. Zazubovich, and V. Zepelin. Relaxed excited state structure and luminescence of thallium-doped caesium chloride and bromide. *J. Phys. Condens. Matter*, 8:4301–4314, 1996.

[33] V. Nagirnyi, S. Zazubovich, V. Zepelin, M. Nikl, and G. P. Pazzi. A new model for the visible emission of the CsI:Tl crystal. *Chem. Phys. Lett.*, 227:533–538, 1994.

Suppression of nonradiative recombination in ionic insulators by defects: Role of fast electron trapping in Tl-doped CsI

Junhyeok Bang,[1] Z. Wang,[2] F. Gao,[2] S. Meng,[3] and S. B. Zhang[1]

[1]*Department of Physics, Applied Physics, and Astronomy, Rensselaer Polytechnic Institute, Troy, New York 12180, USA*

[2]*Pacific Northwest National Laboratory, MS K8-93, P.O. Box 999, Richland, Washington 99352, USA*

[3]*Beijing National Laboratory for Condensed-Matter Physics and Institute of Physics, Chinese Academy of Sciences, Beijing 100190, China*

(Received 4 September 2012; revised manuscript received 9 April 2013; published 23 May 2013)

In semiconductors, defects often assist nonradiative relaxation. However, Tl doping can significantly suppress the nonradiative relaxation in alkali halides to increase scintillation efficiency. Without the Tl, it is known that the creation of Frenkel pairs at self-trapped excitons, assisted by excited electron and hole relaxations, is the reason for the nonradiative relaxation. Here we show by first-principles calculation that Tl doping introduces Tl p states inside the band gap to trap the excited electrons. The trapping is highly effective to within several picoseconds, as revealed by time-dependent density functional theory calculations. It alters the nonradiative relaxation process to result in a noticeable increase in the relaxation barrier from 0.3 to 0.63 eV, which reduces the nonradiative relaxation by roughly a factor of 10^5 at room temperature.

DOI: 10.1103/PhysRevB.87.205206 PACS number(s): 71.55.−i, 71.38.Ht, 72.20.Jv, 78.55.Fv

I. INTRODUCTION

Nonradiative recombination (NRR) of excited carriers is one of the most fundamental phenomena in semiconductors and insulators. NRR can quench luminescence and limit photovoltaic device efficiency. Therefore, understanding NRR also has practical importance.[1–3] However, NRR is often complex involving excited carriers. This leads to difficulties in theoretical analysis and identification of its microscopic origin. As such, key knowledge on NRR is often lacking.

In semiconductors, defects are viewed as the cause for NRR.[4,5] However, in alkali halides counterexamples exist. For example, in scintillation material CsI, which is widely used as a high-energy particle detector,[6,7] a minute amount of Tl doping can significantly suppress NRR and increase light emission efficiency.[8,9] This hints that certain types of defects may improve the efficiency of an optoelectric device. Although there have been considerable efforts to understand the role of Tl,[10–16] the underlying mechanism for the NRR suppression is still unclear. Physical processes in which a dopant reduces rather than increases the NRR is critically important to material research, as it offers clues not only for improved scintillation but also for better LED, laser, photovoltaic, and spintronic devices.

In this work, we present a state-of-the-art treatment of the problem, which includes both hybrid functional calculations for the self-trapped hole (STH) and the self-trapped exciton (STE) and, separately, time-dependent density functional theory (TDDFT) calculations for explicit electron relaxation dynamics. Our study reveals two effects of the Tl: First, there exists a large binding between substitutional Tl and STE of 0.88 eV, therefore an STE is bound to Tl until it undergoes a radiative relaxation or NRR. Second, Tl increases the NRR barrier of the trapped STE significantly to prevent the NRR from happening. It is believed that NRR is caused by the creation and migration of Frenkel pairs. Without the Tl, excited electrons at the conduction band minimum (CBM) and holes at the valence band maximum (VBM) assist the creation of the Frenkel pairs through a strong electron-phonon coupling. With the Tl, however, the excited electron is transferred to the Tl p states within several picoseconds. As a result, the carrier-assisted Frenkel-pair formation paths are blocked, leading to significantly enhanced scintillation efficiency.

II. METHODS

Our structural optimization is based on the spin-polarized density functional theory (DFT) with the hybrid PBE0 functional,[17] as implemented in the VASP code.[18] Projected augmented wave potentials[19] are used for ionic pseudopotentials. Wave functions are expended in a plane-wave basis with an energy cutoff of 290 eV. We use a $5 \times 3 \times 3$ supercell that contains 90 atoms with the [100] direction as the long axis to facilitate the study of interstitial diffusion. Γ point is used for the Brillouin zone integration. Tests with different cell size and k-point sampling suggest that the total energy is converged to within 0.01 eV. The ionic coordinates are fully relaxed until the residual forces are <0.03 eV/Å. To mimic electronic excitation, for pure CsI, we perform constrained DFT calculations in which we remove one electron from the VBM and place it at the CBM. For Tl-doped CsI, we place the excited electron at the Tl level. This is a valid approach because our calculation shows that the electron at the CBM instantaneously transfers to the Tl level. To calculate the energy barrier with nudged elastic band along with hybrid functional is currently difficult. Instead, we generated nine atomic configurations between the initial and final states and then relaxed all the atoms in each configuration except for the two diffusing iodine atoms.

A key to the determination of enhanced scintillation is the time required for electron trapping. The recent development of *ab initio* molecular dynamics (MD) coupled with TDDFT[20] makes this possible. Here, we use the TDDFT formalism implemented in the SIESTA code,[21,22] with norm-conserving Troullier-Martins pseudopotentials,[23] the Perdew-Burke-Ernzerhof (PBE) exchange-correlation functional,[24] and a double-ζ polarized local basis set. The real-space grid is equivalent to a plane-wave cutoff energy of 200 Ry. The time step is 24 attoseconds. We use the Ehrenfest approximation

for ion motion. The supercell for defect contains 54 atoms. To prepare for TDDFT input, we perform electron-ground-state MD simulation at room temperature (RT = 300 K) and then constrained DFT with one electron in the CBM.

III. RESULTS: NONRADIATIVE RECOMBINATION PATHS IN UNDOPED CsI

Scintillation is a fundamental physical phenomenon for energetic particle interaction with solids. When a high-energy particle enters a scintillator material, the energy of the particle is transferred to the surroundings by generating electron and hole pairs. In most alkali halide scintillators, the hole can be localized by lattice distortion, leading to the formation of STH. In CsI, the distortion is the bonding between two adjacent iodine atoms [see Fig. 1(a)], to lower the system energy by 0.31 eV relative to undistorted CsI with delocalized hole. The charge contour plot in Fig. 1(a) reveals that the STH state inside the band gap [see Fig. 2(a)] is an antibonding state. An excited electron in the conduction band can bind to the STH to form an STE. The trapped electron is, on the other hand, delocalized over the supercell. Accordingly, the energy lowering of 0.32 eV due to the STE formation is only 0.01 eV larger than that of the STH [see Table I and Fig. 3(a)]. Not only does the STE itself emit light by radiative recombination, but the diffusion of the STH and STE can also lead to the transfer of their energy to other luminescence centers.[25–29]

The STE can also undergo NRR through Frenkel-pair defect formation and diffusion.[30–32] Figures 1(b)–1(d) show the evolution of the atomic structure during the NRR. First, two adjacent I atoms move along the [100] direction in such a way that the two share one anion lattice site, forming a dumbbell (DB) structure (I_i^{DB}). This leaves behind an I vacancy (V_I). We denote this vacancy-interstitial pair as $(V_I\text{-}I_i^{DB})^{first}$. As the I_i diffuses further away along the [100] direction, it can form additional metastable Frenkel pairs such as the one in Fig. 1(c): $(V_I\text{-}I_i^{TR})^{first}$ with one triple-I-atom chain (TR), as well as the one in Fig. 1(d): $(V_I\text{-}I_i^{DB})^{second}$ with an I DB structure. As the process goes on, the I_i eventually encounters a V_I and recombines, leaving their energy to the lattice as heat.

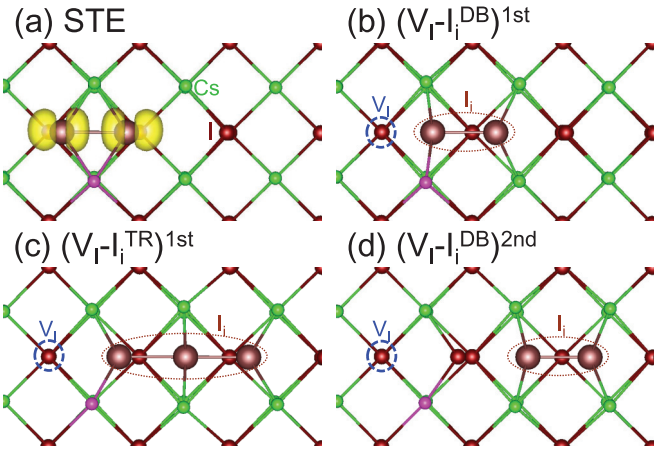

FIG. 1. (Color online) Atomic structures during the I_i diffusion: (a) STE, (b) $(V_I\text{-}I_i^{DB})^{first}$, (c) $(V_I\text{-}I_i^{TR})^{first}$, and (d) $(V_I\text{-}I_i^{DB})^{second}$, where first and second denote the I_i position relative to the V_I. Blue dashed circles denote the V_I's; brown dotted ellipses denote the I_i's. For Tl-doped CsI, the Tl atom replaces the pink Cs atom. In (a), the real-space charge of the STH state [see Fig. 2(a)] is shown by the yellow contours. DB and TR are defined in the text.

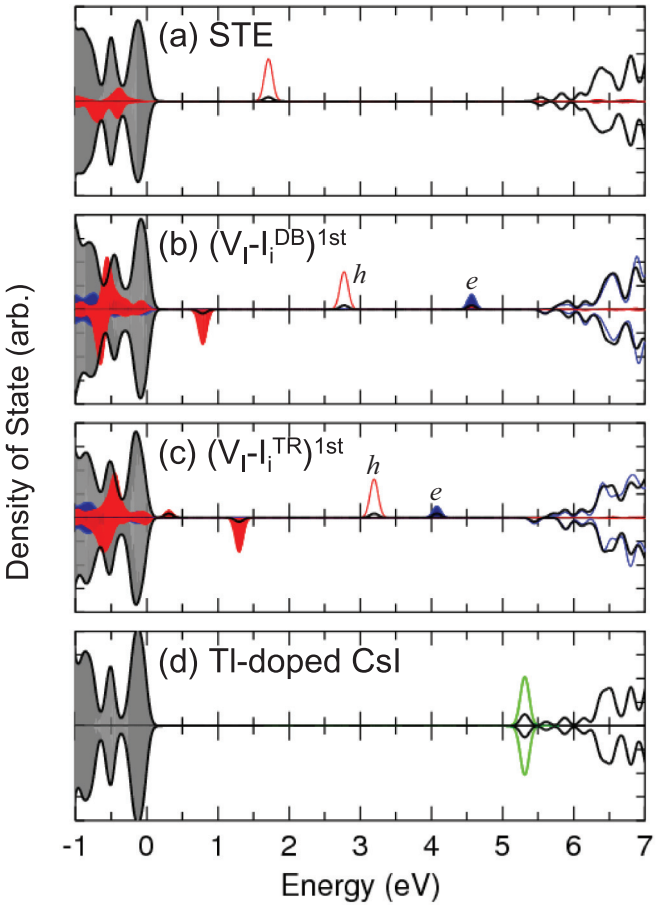

FIG. 2. (Color online) Density of states (DOS) of (a) STE, (b) $(V_I\text{-}I_i^{DB})^{first}$, (c) $(V_I\text{-}I_i^{TR})^{first}$, and (d) Tl-doped CsI. The occupied states are shaded. Red, blue, and green lines denote the projected DOS onto the p states of the I interstitial, the s states of the Cs nearest neighbors to V_I, and the p states of the Tl. All the projected DOS are scaled by a factor of 20 with respect to the total DOS.

Figure 3(a) shows the energy landscape along the NRR path in Fig. 1: From STE to $(V_I\text{-}I_i^{DB})^{first}$, the energy is increased to 0.19 eV; from $(V_I\text{-}I_i^{DB})^{first}$ to $(V_I\text{-}I_i^{TR})^{first}$, the energy is further increased to 0.29 eV. After that, the total energy is nearly flat. The total diffusion barrier for this NRR path [from 1(a) to 1(d) in Fig. 3(a)] is $E_b = 0.30$ eV. The fact that E_b is slightly smaller than the delocalization barrier, 0.37 eV, of the STE [from 1(a) to No STE in Fig. 3(a)] suggests that it prefers NRR over delocalization. By using the rate equation $r = f\ \exp(-E_b/kT)$ and the optical vibration frequency $f = 2 \times 10^{12}\ s^{-1}$ for CsI,[33] we estimate the NRR relaxation time at RT to be 50 ns. This value is on the same order of magnitude with the radiation decay time in CsI.[8,34]

IV. RESULTS: THE EFFECTS OF Tl DOPING

Because of the large binding of 0.88 eV between Tl and STE, Tl doping can significantly affect the formation of STE. A previous study[26] suggested that STE is mobile at RT with a

TABLE I. Energy change at different atomic configurations along the NRR path. Results for CsI with one hole are calculated at the same atomic structures of CsI with one e–h pair to show the effects of the excited electron. The energy is given in unit of eV.

	No self-trapping	Self-trapping	$(V_I\text{-}I_i^{DB})^{first}$	$(V_I\text{-}I_i^{TR})^{first}$	$(V_I\text{-}I_i^{DB})^{second}$
One e–h pair	0.32	STE: 0.0	0.19	0.29	0.29
One hole	0.31	STH: 0.0	0.68	1.15	1.27

barrier as little as 0.15 eV. Thus, STE can be easily trapped at Tl sites, in agreement with experiment.[13,16] Figure 3(b) further shows that Tl doping reduces the STE formation barrier [from No STE to 1(a) in Fig. 3(b)] to <0.01 eV. Hence, most STE exist as Tl-STE pairs.

Tl doping slows down the NRR by increasing the formation energy of Frenkel pairs. We can understand this by examining the evolution of the density of states in Fig. 2 in accordance with that of atomic structures in Fig. 1. Here, we focus on the hole (h) and electron (e) levels marked in Fig. 2, which belong to I_i and V_I, respectively. Going from Fig. 2(a) to Fig. 2(c), the hole level increases; the electron level decreases to enter the band gap. The reason for the change can be attributed to wave-function overlap between e and h, giving rise to level repulsion. As the I_i diffuses away from the V_I, however, the repulsion vanishes. Note that the higher the hole level, the more stable the hole. Thus, throughout the diffusion process in Fig. 1 both the excited electron and hole lower their energies, driving the diffusion forward.

If we remove the excited electron from the system, however, the energy of the Frenkel pairs increases significantly (see Table I). This is precisely what Tl does to slow down and deter NRR. Figure 2(d) shows that the unoccupied p levels of the Tl are below CBM, so the electron in the CBM can be transferred to Tl. Whether such a process is important or not, however, depends on the time required for the transfer. If the time is longer than 50 ns, which is the NRR relaxation time in CsI, then excited carriers will decay nonradiatively. To estimate the electron transfer rate, we performed TDDFT calculations within the PBE functional. Strictly speaking, one may not use PBE here because semilocal functional may not describe charge transfer correctly. Currently, it is still not possible to carry out TDDFT-MD beyond the PBE, such as using a nonlocal hybrid functional. This issue should be considered in future studies.

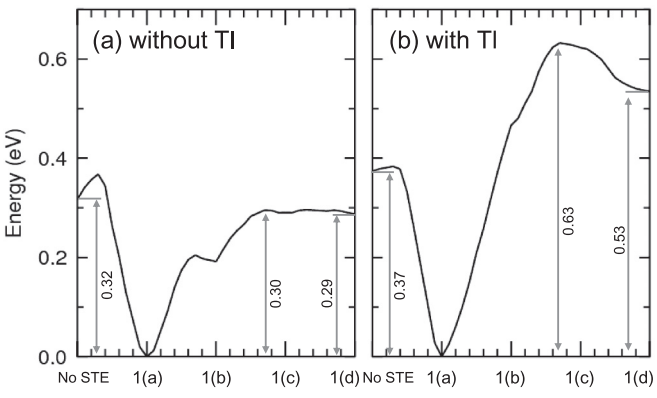

FIG. 3. Total energy landscape along the NRR path for (a) undoped CsI and (b) Tl-doped CsI. The labels in the horizontal axes indicate atomic structures for STE diffusion given in Fig. 1.

Figure 4(a) shows the time evolution of the energy levels for the excited electron in the CBM and the three empty Tl p states.[35] The electron level decreases rapidly towards the Tl p levels, which indicates that electron transfer from the CBM to the Tl p levels has taken place. Accompanied with this electron transfer, ion kinetic energy increases [see Fig. 4(b)]. This is a strong indication that the transfer is mediated by electron-phonon coupling. As a measure of the transfer, Fig. 4(c) shows the change of the amount of electrons in the Tl p levels, defined as $\Delta\rho_{Tl}(t) = \sum_{i=1}^{3}[\rho_{Tl,i}^{(e)}(t) - \rho_{Tl,i}^{(g)}]$ where $\rho_{Tl,i}^{(e)}$ and $\rho_{Tl,i}^{(g)}$ are the amount of electrons in the Tl p_i states, $|Tl, p_i\rangle$, for the excited and ground states, respectively. $\Delta\rho_{Tl}(t=0)$ should be zero if the supercell size is sufficiently large; due to the relatively small cell size and the fact that $|CBM\rangle$ and $|Tl, p_i\rangle$ are coupled states, however, $\Delta\rho_{Tl}(t=0) = 0.3$ electrons in our simulation. Despite this, the qualitative result, e.g., $\Delta\rho_{Tl}(t)$ increases with time, is not affected. In only 150 fs, $\Delta\rho_{Tl}$ is increased to 0.43 electrons.

Upon excitation, the excited electron stays in the CBM for ~20 fs before significant transfer is noticed in Fig 4(c). This initial waiting is also observed in other materials such as TiO_2.[36] Beyond the initial waiting time t_i, the time evolution of the electron transfer can be modeled by[36] $\Delta\rho_{Tl}(t) = A(1 - \exp[-(t/\tau)])$, where τ is the decay time. As mentioned earlier,

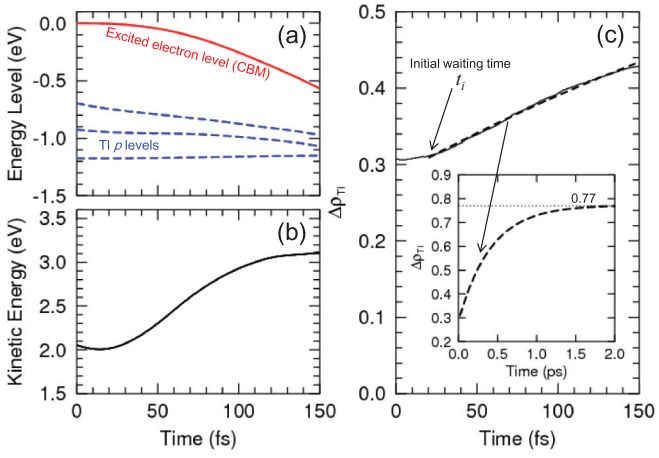

FIG. 4. (Color online) Time evolutions of (a) energy levels, (b) ion kinetic energy, and (c) electron transfer to Tl p levels, $\Delta\rho_{Tl}$. In (a), red and blue lines are the excited electron level and the empty Tl p levels, respectively. In (c), the solid line is the TDDFT result, whereas the dashed line is a fitted result using Eq. (1). t_i is the initial waiting time. The dashed line in the inset in (b) is the same fitting but plotted at a longer time scale. It converges to 0.77 electrons within 2 ps.

$\Delta\rho_{\mathrm{Tl}}(t=0)$ is not zero due to finite cell size; here we modify the above equation to

$$\Delta\rho_{\mathrm{Tl}}(t) = A\left(1-\exp\left[-\frac{t}{\tau}\right]\right)+0.3. \quad (1)$$

Figure 4(c) shows that Eq. (1) with $A=0.47$, $t_i=20$ fs, and $\tau=413$ fs fits the TDDFT results reasonably well. The inset in Fig. 4(c) shows that within 2 ps, about 0.77 electrons are transferred to Tl. We can qualitatively understand the amount of electron transfer as follows: In the Ehrenfest dynamics, the excited electron state evolves into a superposed state between $|\mathrm{CBM}\rangle$ and $|\mathrm{Tl},p_i\rangle$,

$$|\varphi\rangle = a|\mathrm{CBM}\rangle + b_1|\mathrm{Tl},p_1\rangle + b_2|\mathrm{Tl},p_2\rangle + b_3|\mathrm{Tl},p_3\rangle \quad (2)$$

with approximately the same energy. If we assume $|a|^2 = |b_1|^2 = |b_2|^2 = |b_3|^2 = 1/4$, we get $\Delta\rho_{\mathrm{Tl}} = 3/4 = 0.75$ electrons. Note that this discussion considers only a single Tl. If we take into account the coupling of the delocalized $|\mathrm{CB}\rangle$ with multiple (n) Tl atoms nearby, the amount of the electron transfer in the first 2 ps will increase to $\Delta\rho_{\mathrm{Tl}} = 1-1/(3n+1)$, which approaches 1 in the limit $n\to\infty$. This suggests that the excited electron transfer from CBM to Tl is considerably faster than the NRR in CsI by at least several orders of magnitude.

To calculate the NRR barrier for Tl-doped CsI, we use PBE0 but with an excited electron in the Tl p state as shown in Fig. 3(b). The energy difference between STE and $(V_{\mathrm{I}}\text{-}\mathrm{I}_i^{\mathrm{DB}})^{\mathrm{second}}$ increases to ~0.54 eV, which is 0.25 eV higher than that for undoped CsI. One can estimate the reduction in the NRR rate by $R=\exp(\Delta E_b/kT)$. Using $\Delta E_b = 0.63-0.30 = 0.33$ eV and $kT=0.026$ eV, we obtain $R=3\times10^5$ at RT. The corresponding NRR time is roughly 1 ms, which is enough to significantly increase light output.

V. IMPLICATION TO SEMICONDUCTORS

Note that the mechanism to deter NRR (discussed above) is not limited to only alkali halides or to ionic insulators. For example, carrier trapping by BO_2 complexes in Si has been proposed as the main reason for NRR in B-doped Czochralski Si (Cz-Si) solar cell materials.[37] What is intriguing for this system is the lack of deep levels similar to CsI; electrons and holes that are temporarily trapped at near band-edge BO_2 states assist the NRR.[38] It is thus conceivable that one may reduce carrier trapping in Cz-Si by introducing impurities that are capable of taking the carriers away from BO_2.

VI. SUMMARY

Hybrid functional study, coupled with TDDFT, reveals the effect of impurity doping on excited carrier relaxation in ionic insulators. Application to Tl-doped CsI explains the experimentally observed significant increase of scintillation efficiency. The role of the impurity in suppressing NRR is unveiled in terms of the efficient transfer of excited electrons to impurity gap states. Our results suggest that defects/impurities not only can accelerate NRR as often observed,[4,5,38] but can also be used to suppress certain NRRs, provided that the NRR does not involve deep levels as in the Shockley-Read-Hall regime.[4,5] In other words, our understanding of the physics to deter NRR goes beyond just the improvement of current scintillator technology, but for educated defect engineering to suppress NRR in other optoelectronic materials.

ACKNOWLEDGMENTS

This work was supported by the National Nuclear Security Administration, Office of Nuclear Nonproliferation Research and Engineering (NA-22), of the US Department of Energy and by the Computational Center for Nanotechnology Innovations at RPI. F.G. and Z.G.W. acknowledge the use of the supercomputers in the Environmental Molecular Sciences Laboratory, a national scientific user facility sponsored by the US Department of Energy's Office of Biological and Environmental Research. S.M. is grateful for support from NSFC (Grants No. 11074287 and No. 11222431) and MOST (2012CB921403).

[1] A. M. Stoneham, Rep. Prog. Phys. **44**, 1251 (1981).
[2] C. Deibel, T. Strobel, and V. Dyakonov, Adv. Mater. **22**, 4097 (2010).
[3] D. Hertel, S. Setayesh, H.-G. Nothofer, U. Scherf, K. Müllen, and H. Bässler, Adv. Mater. **13**, 65 (2001).
[4] W. Shockley and W. T. Read, Phys. Rev. **87**, 835 (1952).
[5] R. N. Hall, Phys. Rev. **87**, 387 (1952).
[6] M. Nikl, Phys. Status Solidi A **178**, 595 (2000).
[7] N. Yasui, Y. Ohashi, T. Kobayashi, and T. Den, Adv. Mater. **24**, 5464 (2012).
[8] P. Schotanus, R. Kamermans, and P. Dorenbos, IEEE Trans. Nucl. Sci. **37**, 177 (1990).
[9] M. M. Hamada, F. E. Costa, M. C. C. Pereira, and S. Kubota, IEEE Trans. Nucl. Sci. **48**, 1148 (2001).
[10] Z. Wang, Y. Xie, B. D. Cannon, L. W. Campbell, F. Gao, and S. Kerisit, J. Appl. Phys. **110**, 064903 (2011).
[11] S. Kerisit, K. M. Rosso, and B. D. Cannon, IEEE Trans. Nucl. Sci. **55**, 1251 (2008).
[12] S. Kerisit, K. M. Rosso, B. D. Cannon, F. Gao, and Y. Xie, J. Appl. Phys. **105**, 114915 (2009).
[13] S. Zazubovich, Radiat. Meas. **33**, 699 (2001).
[14] J. M. Spaeth, W. Meise, and K. S. Song, J. Phys.: Condens. Matter **6**, 3999 (1994).
[15] V. Nagirnyi, A. Stolovich, S. Zazubovich, V. Zepelin, E. Mihokova, M. Nikl, G. P. Pazzi, and L. Salvini, J. Phys.: Condens. Matter **7**, 3637 (1995).
[16] V. Babin, P. Fabeni, K. Kalder, M. Nikl, G. P. Pazzi, and S. Zazubovich, Radiat. Meas. **29**, 333 (1998).
[17] J. P. Perdew, M. Emzerhof, and K. Burke, J. Chem. Phys. **105**, 9982 (1996).
[18] G. Kresse and J. Furthmuller, Comput. Mater. Sci. **6**, 15 (1996).
[19] P. E. Blochl, Phys. Rev. B **50**, 17953 (1994).

[20]E. Runge and E. K. U. Gross, Phys. Rev. Lett. **52**, 997 (1984).
[21]J. M. Soler, E. Artacho, J. D. Gale, A. García, J. Junquera, P. Ordejón, and D. Sánchez-Portal, J. Phys.: Condens. Matter **14**, 2745 (2002).
[22]S. Meng and E. Kaxiras, J. Chem. Phys. **129**, 054110 (2008).
[23]N. Troullier and J. L. Martins, Phys. Rev. B **43**, 1993 (1991).
[24]J. P. Perdew, K. Burke, and M. Ernzerhof, Phys. Rev. Lett. **77**, 3865 (1996).
[25]R. M. V. Ginhoven, J. E. Jaffe, S. Kerisit, and K. M. Rosso, IEEE Trans. Nucl. Sci. **57**, 2303 (2010).
[26]S. E. Derenzo and M. J. Weber, Nucl. Instrum. Methods Phys. Res., Sect. A **422**, 111 (1999).
[27]G. Blasse, Chem. Mater. **6**, 1465 (1994).
[28]M. Nikl, Meas. Sci. Technol. **17**, R37 (2006).
[29]G. Bizarri, J. Cryst. Growth **312**, 1213 (2010).
[30]A. I. Popov, E. A. Kotomin, and J. Maier, Nucl. Instrum. Methods Phys. Res., Sect. B **268**, 3084 (2010).
[31]N. Itoh, Adv. Phys. **31**, 491 (1982).
[32]N. Itoh, A. M. Stoneham, and A. H. Harker, J. Phys. C **10**, 4197 (1977).
[33]J. F. Vetelino, K. V. Namjoshi, and S. S. Mitra, Phys. Rev. B **7**, 4001 (1973).
[34]C. Amsler, D. Grögler, W. Joffrain, D. Lindelöf, M. Marchesotti, P. Niederberger, H. Pruys, C. Regenfus, P. Riedler, and A. Rotondi, Nucl. Instrum. Methods Phys. Res., Sect. A **480**, 494 (2002).
[35]TDDFT results in Fig. 4(a) reflect the splitting and lowering of the Tl p states due to symmetry breaking by the MD.
[36]W. R. Duncan and O. V. Prezhdo, Annu. Rev. Phys. Chem. **58**, 143 (2007).
[37]J. Schmidt and K. Bothe, Phys. Rev. B **69**, 024107 (2004).
[38]M.-H. Du, H. M. Branz, R. S. Crandall, and S. B. Zhang, Phys. Rev. Lett. **97**, 256602 (2006).

Experimental and computational results on exciton/free-carrier ratio, hot/thermalized carrier diffusion, and linear/nonlinear rate constants affecting scintillator proportionality

R. T. Williams*[a], Joel Q. Grim[a], Qi Li[a], K. B. Ucer[a], G. A. Bizarri[b], S. Kerisit[c], Fei Gao[c], P. Bhattacharya[d], E. Tupitsyn[d], E. Rowe[d], V. M. Buliga[d], and A. Burger[d]

[a]Department of Physics, Wake Forest University, Winston-Salem, NC 27109
[b]Lawrence Berkeley National Laboratory, Berkeley, CA 94720
[c]Pacific Northwest National Laboratory, Richland WA 99352
[d]Department of Physics, Fisk University, Nashville, TN 37208

ABSTRACT

Models of nonproportional response in scintillators have highlighted the importance of parameters such as branching ratios, carrier thermalization times, diffusion, kinetic order of quenching, associated rate constants, and radius of the electron track. For example, the fraction η_{eh} of excitations that are free carriers versus excitons was shown by Payne and coworkers to have strong correlation with the shape of electron energy response curves from Compton-coincidence studies. Rate constants for nonlinear quenching are implicit in almost all models of nonproportionality, and some assumption about track radius must invariably be made if one is to relate linear energy deposition dE/dx to volume-based excitation density n (eh/cm^3) in terms of which the rates are defined. Diffusion, affecting time-dependent track radius and thus density of excitations, has been implicated as an important factor in nonlinear light yield. Several groups have recently highlighted diffusion of hot electrons in addition to thermalized carriers and excitons in scintillators. However, experimental determination of many of these parameters in the insulating crystals used as scintillators has seemed difficult. Subpicosecond laser techniques including interband z scan light yield, fluence-dependent decay time, and transient optical absorption are now yielding experimental values for some of the missing rates and ratios needed for modeling scintillator response. First principles calculations and Monte Carlo simulations can fill in additional parameters still unavailable from experiment. As a result, quantitative modeling of scintillator electron energy response from independently determined material parameters is becoming possible on an increasingly firmer data base. This paper describes recent laser experiments, calculations, and numerical modeling of scintillator response.

Keywords scintillator, nonproportionality, light yield, nonlinear quenching, diffusion, hot electron

1. INTRODUCTION

The paired alternatives for the scintillator material characteristics listed in the title of this paper anticipate the Conclusion, in which predictive trends in scintillator nonproportionality and light yield follow a succession of branch points according to values of a few material parameters. Payne et al [1,2] concluded from empirically modeled electron energy response data from Compton-coincidence light yield that the free-carrier fraction denoted η_{eh} is an important parameter affecting proportionality. One could alternatively talk in terms of the exciton fraction (1 - η_{eh}). We shall see that η_{eh} is a function of time and electron temperature, but a single-valued η_{eh} parameter can be associated with the average value of the evolving $\eta_{eh}(T_e,t)$ during nonlinear quenching. Hence, the first of the branch points according to exciton/free-carrier ratio can be tested for its correlation with scintillator proportionality if we have some way of measuring η_{eh} independent of fitting a proportionality curve. We will describe such an experiment on laser interband Photon Density Response (PDR) in this paper, alongside results from the literature on the more traditional Electron Energy Response (EER) data.

PDR is a measurement of light yield versus absorbed photon density, where each ultraviolet photon produces one interband excitation. Thus PDR is a measure of light yield (or conversely, nonlinear

quenching) as a function of excitation density. EER, on the other hand, is a measurement of light yield versus initial electron energy of a Compton electron [1,2] or K-shell photoelectron [3]. In EER, lower initial electron energy implies higher average excitation density, and one sometimes interprets the EER curves as qualitatively indicating how light yield changes with changing excitation density. But of course the correspondence is complicated due to the fluctuating distribution of excitations created by slowing of the high energy electron, the fact that scintillation light yield is integrated over the entire trajectory of a slowing primary electron and its secondaries, and the strong radial concentration gradient of excitations (mainly charge carriers) produced in the track. Extracting parameter values such as free-carrier fraction, the nonlinear rate constants, and diffusion coefficients (cool and hot) from the complex track structures contributing to EER data is thus very model dependent. In contrast, the horizontal axis in PDR plots is simply excitation density occurring on-axis just inside the sample surface. Furthermore, the energy imparted to each electron-hole pair by absorption of an ultraviolet interband photon is the same and can be tuned. Finally, the gradients of excitation density produced by interband laser absorption are at least an order of magnitude smaller than the gradient of excitation density around an electron track. When carrier mobilities are low or modest, as in most scintillators, we can neglect diffusion effects in the laser PDR geometry in order to deduce dependence of light yield directly on excitation density. From this dependence, one can extract nonlinear quenching rate constants as well as free-carrier fraction η_{eh} by fitting a rate equation to the PDR curve. With measured values of the free-carrier fraction and/or exciton fraction as well as the nonlinear quenching rate constants in hand from PDR experiments, one can then include carrier and/or exciton diffusion in the full rate equation needed to describe the electron track environment and predict electron energy response for comparison to EER measurements. Because nonlinear quenching goes on during the time of hot carrier thermalization in some scintillators, it has been found [4–8] that one needs to account for diffusion coefficients that are functions of electron temperature and therefore indirectly functions of time. This requires calculations and modeling to take into account.

2. EXPERIMENT

The experiment for measuring photon density response is represented schematically in Fig. 1. The experiment and analysis has been described in detail in Ref. [9], where it was called "interband z scan" because of similarity of the experimental setup to the well-known z-scan method of measuring optical nonlinearities of a sample through effects on the transmitted beam as a function of focus.[10] In the interband z scan experiment, the laser beam is totally absorbed within ~ 100 nm of the sample face and luminescence is detected as indicated in Fig. 1. Having acknowledged the setup similarity to conventional z scan measurements, we will henceforth refer to the experiment as photon density response (PDR) since this places it more accurately with respect to other well-known scintillator measurements including electron energy response,[1,2] photon energy response,[11] and gamma energy response.[12][9] In PDR, light yield is measured as a function of excitation *density* under condition of constant excitation *number*. If there is no nonlinearity of light yield, the PDR curve should be flat.

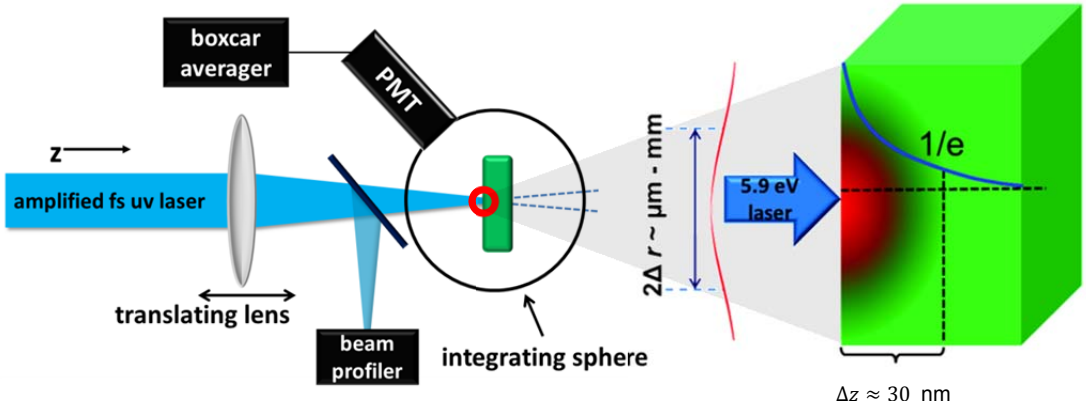

Figure 1. Experimental schematic for interband laser z scan or PDR experiment is shown in the left half. The right half is an enlargement of the sample showing the exponential attenuation profile in the longitudinal direction and the Gaussian beam profile in the transverse plane of the sample surface.

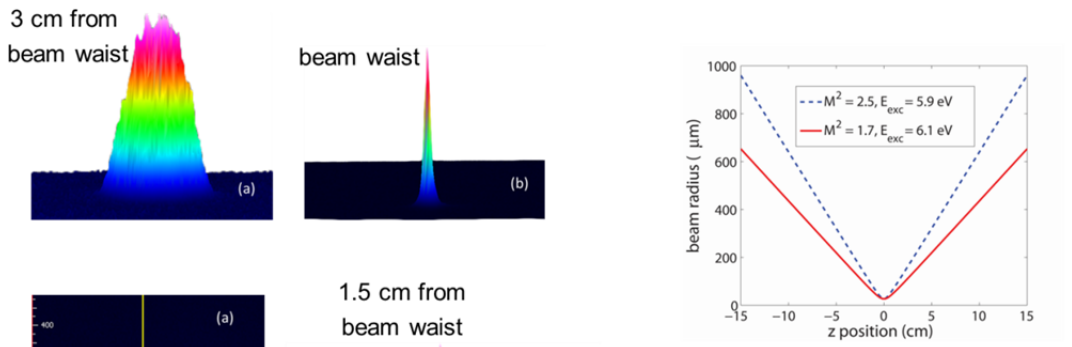

	5.9 eV light	6.1 eV light
Gaussian w_0 (μm)	10.1	19.7
Actual w_0 (μm)	26	30

Figure 2. Measurements of the 4th harmonic ultraviolet pulse transverse profiles are shown for several distances, z, between the beam waist and the entrance face of the sample. The data versus z are fit to the M^2 profile of a non-ideal Gaussian, which changes with alignment of system components for different wavelengths of the 4th harmonic pulse.

3. RESULTS AND DISCUSSION

3.1 BGO and SrI_2; η_{eh}

The raw data of the PDR experiment are shown in the left panel of Fig. 3 for two materials, bismuth germanate ($Bi_4Ge_3O_{12}$, BGO) and strontium iodide (SrI_2). The characteristic dip at the beam waist position (highest fluence versus lens position) suggests why we have called this method "interband z scan."[9] The middle panel shows that by taking into account the beam profile, sample reflectivity, and laser pulse energy, the fluence on the central axis just inside the sample surface can be associated with each z position. The fluence scale is placed across the top of the middle panel in Fig. 3. With further knowledge of the interband absorption coefficient α (cm^{-1}), we can convert fluence to excitation density n_0 *(eh/cm³)* on the central axis, just inside the sample surface. The conversion formula is shown in Fig. 3, where F_0 is the laser fluence (eV/cm^2) and hv is the laser photon energy (eV). In the right panel, the light yield is plotted versus a logarithmic scale of excitation density n_0. The left and right sides ($z < 0$ and $z > 0$) of the z scan plot (middle panel) are averaged when replotting in the standard PDR format (right panel).

Inspection of the right-hand panel in Fig. 3 comparing PDR of BGO and SrI_2 reveals that the roll-off versus excitation density appears quite different in the two materials. In SrI_2, the light yield stays flat for a much longer expanse of excitation density n_0 before plummeting at the end when n_0 is very high. The plummet occurs at excitation densities above 10^{20} eh/cm^3, which is typically found only at the ends of electron tracks. Thus in SrI_2, the experimental light yield is almost flat and at its maximum value for all but track-end values of excitation density. Most of the energy of high energy gamma rays is deposited at lower n_0 than 10^{20} eh/cm^3. Therefore, by direct comparison in Fig. 3, SrI_2 should have better proportionality and higher light yield than BGO, reasoning simply from the characteristic shapes of the photon density response (PDR) curves. This is indeed confirmed by their performance as scintillators. We shall see below that the shape of the SrI_2 PDR fits 3rd order quenching but not 2nd, and the shape of the BGO PDR fits 2nd order quenching but not 3rd. So a prediction of relative proportionality and light yield can already be made just on the basis of whether the nonlinear quenching kinetics is 2nd or 3rd order.

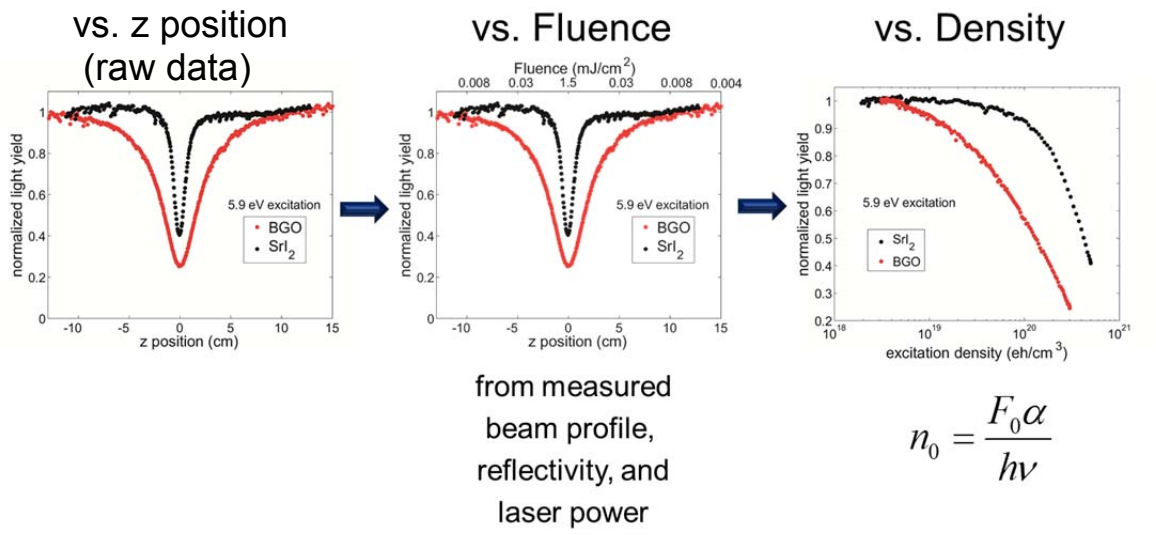

Figure 3. Normalized light yield for BGO (red points, lower curve) and SrI_2 (black points, upper curve) is plotted against three related variables: lens position z (left panel), laser pulse fluence F (middle), and (log) excitation density n_0 (right).

Figure 4 displays the PDR data for BGO and SrI_2 separately, with two different attempts at fitting to rate equation models of PDR also shown. The solid line in each panel is the best fit or attempted fit with a model of 2nd order (dipole-dipole) quenching, and the dashed line is the best fit or attempted fit to a model of 3rd order (free-carrier Auger) quenching. The conclusion is unambiguous in each case, and is summarized in terms of experimentally determined free carrier fraction η_{eh} in the box below each plot. The excitations during nonlinear quenching in BGO are apparently electron-hole pairs (excitons) interacting as dipole radiators and receivers in the near field, whereas in SrI_2 during nonlinear quenching the dominant population is free carriers ($\eta_{eh} = 1$) based on the finding of 3rd order quenching in the PDR data.

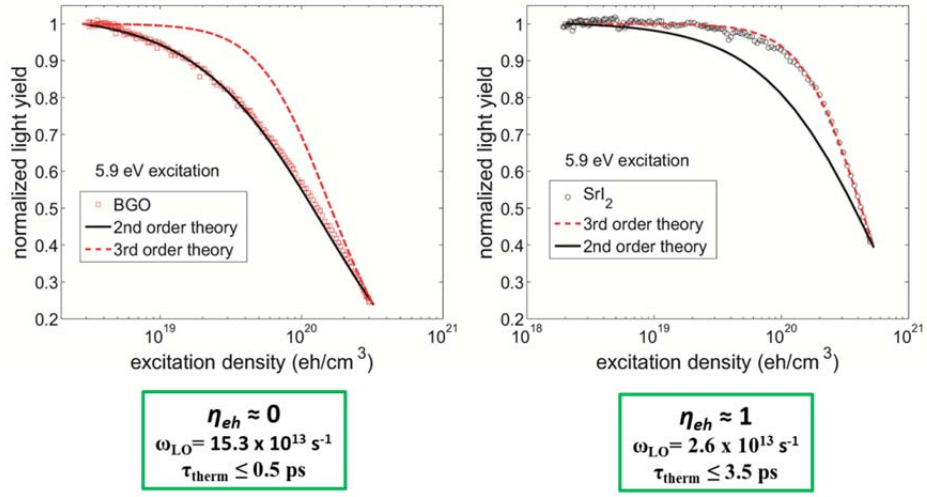

Figure 4. PDR data (open circles) for BGO on the left and SrI_2 on the right. The solid line in each panel is the best fit or attempted fit with a model of 2nd order (dipole-dipole) quenching, and the dashed line is the best fit or attempted fit to a model of 3rd order (free-carrier Auger) quenching. The fits are unambiguous and from this, the values of η_{eh} in each case have been deduced.

3.2 Rate equations and light yield models for PDR

The 2nd order model can be stated quite simply. It is based on the rate equation for exciton population, N (excitons/cm^3), decaying by 1st order radiative decay (rate constant R_1), linear quenching (rate constant K_1), and 2nd order dipole-dipole quenching (rate constant K_2):

$$\frac{dN}{dt} = -(R_1 + K_1)N - K_2(t)N^2 \quad (1)$$

The solved population N(t) is substituted into the light yield equation:

$$LY = \frac{\int_0^\infty R_1 N(t) dt d^3 r}{\int_0^\infty [(R_1 + K_1)N(t) + K_2(t)N^2(t)] dt d^3 r} \quad (2)$$

The result is the solid line fitted or attempted in Fig. 4.

The 3rd order model takes some additional discussion as given below and in Ref. [9]. It is based on the following *approximate* 3rd order rate equation

$$\frac{dn}{dt} = -K_{1e}n - Bn^2 - K_3 n^3 \quad (3)$$

where n is the free carrier density. In a pure material or at local excitation density much higher than that of dopants and defects, bandgap excitation leads to $n_e = n_h = n$. The term $K_{1e}n$ is the trapping rate on deep defects, Bn^2 is the bimolecular pairing rate of electrons and holes to form excitons, and K_3n^3 is the Auger quenching rate. It is more correct to write separate coupled rate equations for electron and hole density and write the 2nd and 3rd order terms proportional to $n_e n_h$ and $(n_e n_h n_e + n_e n_h n_h)$ respectively. The more exact expressions of the bimolecular and Auger rates in coupled rate equations for electrons and holes are in fact used in our data fitting to account for effects of charge separation should it occur, but the form of the simplified Eq. (3) is useful for discussion of concepts in this document.

3.3 $\eta_{eh}(T_e,t)$; born excitons; thermalization and capture of initially hot electrons

We have just seen that η_{eh}, defined as the average or effective value of $\eta_{eh}(T_e,t)$ during nonlinear quenching, can be measured by PDR experiments. The free carrier fraction $\eta_{eh}(T_e,t)$ is an evolving quantity as electrons and holes cool from the nonequilibrium energies of their creation and begin to associate (while also diffusing) as excitons. This raises the question, what was the "born" free carrier fraction $\eta_{eh}\ (t=0)$? For insight, we look at calculations by Vasil'ev on the excitations created by scattering of high energy electrons in BaF_2, including distributions at extremely short time after excitation, down to 0.04 fs.[13]

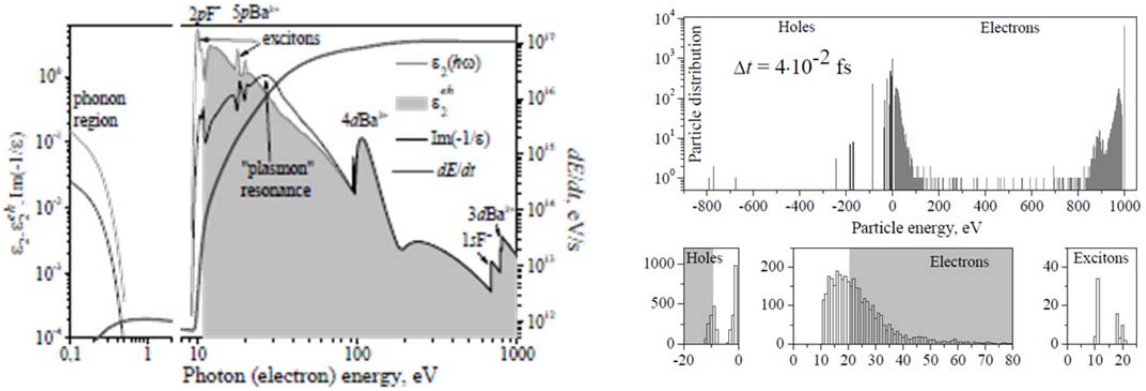

Figure 5. Simulated dielectric function ε_2 in light grey line, partial electron-hole contribution ε_2^{eh} neglecting exciton contribution (grey shading), and energy loss function $Im(-1/\varepsilon)$ in dark line with exciton structure are plotted for BaF_2 in the left panel as functions of photon energy by A. N. Vasil'ev.[13] The right panel shows simulated energy distribution and particle number distribution among electrons, holes, and excitons excited in BaF_2 by a 1 keV electron, evaluated at 0.04 fs after electron passage at the local position. Figures used with permission of A. N. Vasil'ev.[13]

The calculations provide two ways of looking at the exciton fraction at the instant of excitation. In the left panel of Fig. 5, the simulated dielectric function ε_2 in light grey line, partial electron-hole contribution ε_2^{eh} neglecting exciton contributions (grey shading), and energy loss function $Im(-1/\varepsilon)$ in dark line with exciton structure are plotted for BaF_2 as functions of photon energy.[13] The ratio of exciton and free-carrier final

states directly excited by inelastic scattering of the incident electron is given by the partial contributions of these two types of excitations in the energy loss function. Visual separation of those two contributions is best indicated by comparison of ε_2 and ε_2^{eh} as a function of energy. Integration over photon energy spanning the energy deposition of a stopping primary electron suggests that excitons comprise only about 1% of direct excitations by electrons with initial energy greater than 1keV. The fraction should decrease with rising initial electron energy.

In the right panel, simulated energy distribution and particle number distribution among electrons, holes, and excitons excited in BaF_2 by a 1 keV electron, evaluated at 0.04 fs after electron passage at the local position is shown.[13] By integrating the number of valence excitons and the number of electrons or holes in the bar chart representations, we conclude that about 2% of the excitations are bound valence excitons at 0.4 fs after the electron passage at the local position. Core excitons are not counted because they will decay predominantly to energetic electrons and holes, and they do not represent much oscillator strength in any case.

Based on the example of BaF_2, about 2% of excitations by a high energy electron go directly into bound exciton states. The rest are free carriers with some excess kinetic energy to be dissipated before possibly pairing. The electron and hole will tend to move apart according to the initial relative velocities of their wave packets ($\boldsymbol{v}_{ge}$ - $\boldsymbol{v}_{gh}$) based on the local slope of the electron energy bands, while all the time losing energy. As Vasil'ev et al have calculated [7,14], geminate pairs are created if the electron thermalizes within the Onsager radius of the hole it left at creation. Other excitons can continue to form over time, between non-geminate carrier pairs. Exciton formation can be delayed if electron thermalization is slow, as in crystals with low optical phonon frequency. Our hypothesis is that the ratio of exciton fraction and free-carrier fraction during nonlinear quenching depends on the electron thermalization rate, which in turn depends on the optical phonon frequency ω_{LO}.

The relation of electron thermalization time to capture on holes (making excitons) is illustrated in Fig. 6 showing calculations of electron energy relaxation and the fraction of electrons captured on holes as a function of time in CsI and YAP (yttrium aluminum perovskite, $YAlO_3$) by Li et al [15].

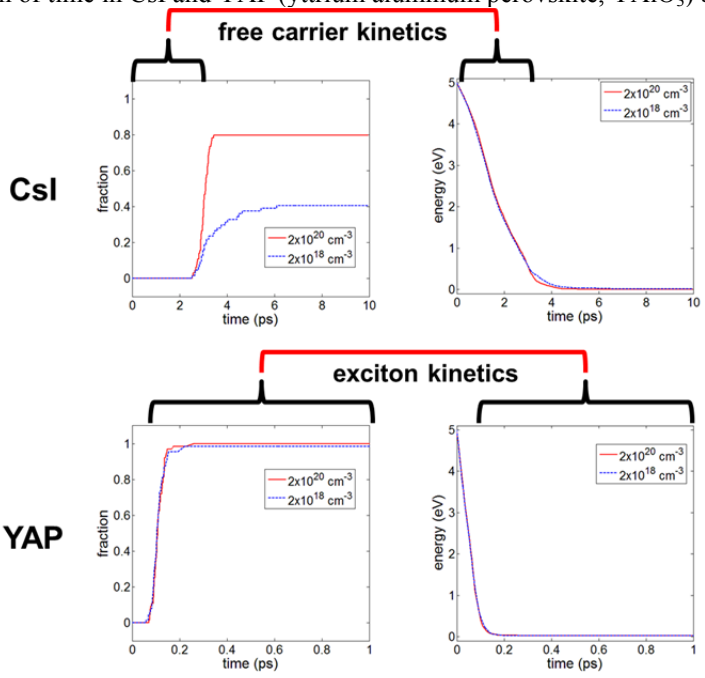

Figure 6. Monte Carlo simulations of the thermalization of hot electrons and capture on holes in CsI and YAP calculated by Li et al.[15] The method is similar to that employed by Wang et al [4,5] and Vasilev et al. [7,14] including calculation of phonon emission rate. The electron is captured when it scatters to a bound state in the electron hole potential that is at least 3 kT below the ionization limit. Results are shown for initial excitation densities of 2 x 10^{20} cm^{-3} (red) and 2 x 10^{18} cm^{-3} (blue).

The calculation method employs Monte Carlo simulation with phonon scattering rates calculated by

methods similar to Wang et al[4,5] and Vasil'ev et al. [7,14] The electron is captured by a hole when it scatters by phonon emission to a bound state in the electron-hole potential that is at least 3 kT below the ionization limit.[15] Notice that the time axes for the YAP and CsI plots are a factor of 10 different. It is seen that electron-hole pairing in CsI is prevented until electron thermalization is nearly complete on a scale of about 3 ps, and then capture proceeds rapidly after that delay. The same happens in the simulations for YAP, except about 30 times faster. Cooling and capture in YAP is substantially subpicosecond, i.e. around 100 fs. In order to match the experimental finding of pure 3rd order quenching in CsI, nonlinear quenching should be mostly complete in 3 ps or less. We have labeled the time intervals in which free-carrier kinetics would apply and in which exciton kinetics would apply, for both materials in Fig. 6.

An experimental observation relevant to this topic comes from picosecond infrared absorption spectroscopy of pure and Tl-doped CsI at room temperature, shown in Fig. 7.[16] The upper and lower panels are for different kinetic energies shared by the electron and hole, $2hv - E_{gap}$ = 0.1 eV and 3.06 eV respectively. The initial spike of absorption nearly coincident with the excitation pulse has a very broad spectrum and may be attributed to free carrier absorption. It can be seen that when the initial excitation is 3.06 eV above the band gap, the free carrier spike is larger relative to the more slowly developing self-trapped exciton absorption. It is relatively smaller for excitation just slightly above the band gap. The rapid drop in free carrier absorption could be due to shallow capture of electrons in high Rydberg states around holes, transferring oscillator strength dominantly to the deep infrared spectrum out of our experimental spectral range, and to self trapping of holes which could transfer hole oscillator strength to the ultraviolet. The re-growth of absorption having a spectrum previously attributed to self-trapped excitons in CsI at room temperature [17] could represent relaxation of self-trapped excitons to their metastable radiative state. The time for that process is seen in Fig. 7 to be about 10 ps, roughly consistent with the calculated electron-hole capture rate for CsI in Fig. 6.

Free-carrier Auger quenching rather than exciton-exciton dipole quenching should apply in the initial time period when the (hot) carriers are free. When the carriers are thermalized and captured on spatially separated traps, their contribution to Auger quenching should effectively terminate. This would be the likely case in CsI:Tl. Holes tend to self-trap right where they are in the host lattice, while electrons should trap mainly on Tl^+, present at 0.1% levels. The main point is that electrons and holes do not generally trap at the same location in scintillators like CsI:Tl, so trapping in a doped crystal can effectively terminate Auger recombination. When the electrons are captured on self-trapped holes to form STE, the dominant quenching term from that sub-population should be 2nd order dipole-dipole, but by then their concentration has been reduced by diffusion and Auger quenching, so they represent only a fraction of the initial electron population. Thus their contribution to quenching can be small compared to the free-carrier contribution in the earlier, denser conditions.

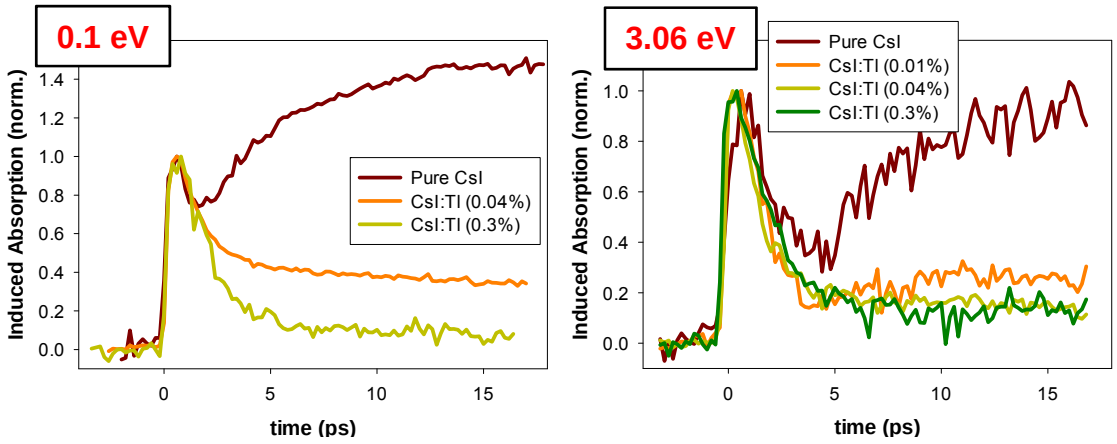

Figure 7. Picosecond infrared absorption spectroscopy of pure and Tl-doped CsI at room temperature. The left and right panels are for different kinetic energies shared by the electron and hole, $2hv - E_{gap}$ = 0.1 eV and 3.06 eV respectively.

3.4 Mixed kinetic order in NaI and Kinetic Monte Carlo simulations of PDR

NaI is the exception that proves the aforementioned rule, in view of its higher ω_{LO} relative to most other iodide scintillators. Whereas nonlinear quenching is pure 3rd order in SrI_2 and CsI, we observe in PDR of NaI that there is a mixture of 2nd order and 3rd order kinetics, depending on how far above the exciton bands the PDR laser excitation is tuned.

The mixed order NaI results in Fig. 8 (left) were excited with 6.1 eV laser photons, which produce hot carriers with up to 0.3 eV excess energy. When the experiments were done with 5.9 eV laser photons only about 0.1 eV above the exciton ionization limit, the PDR can be fit by pure 2nd order quenching, as shown in Fig. 8(right) and Fig. 9. Superimposed in Fig. 9 is the Kinetic Monte Carlo (KMC) simulation of 2nd order quenching[18,19], fitted to the laser PDR data[9]. As mentioned in the Introduction, the PDR experiment is measured without the complex track structure and associated gradients driving diffusion that occur in gamma-ray or electron excited luminescence. This allows KMC fitting of laser PDR to calibrate rate parameters used in the simulation, without having to deal with the track structure complications. This is a valuable tool in conjunction with anticipated KMC fitting of EER data including Compton coincidence (e.g. SLYNCI) and K-dip.

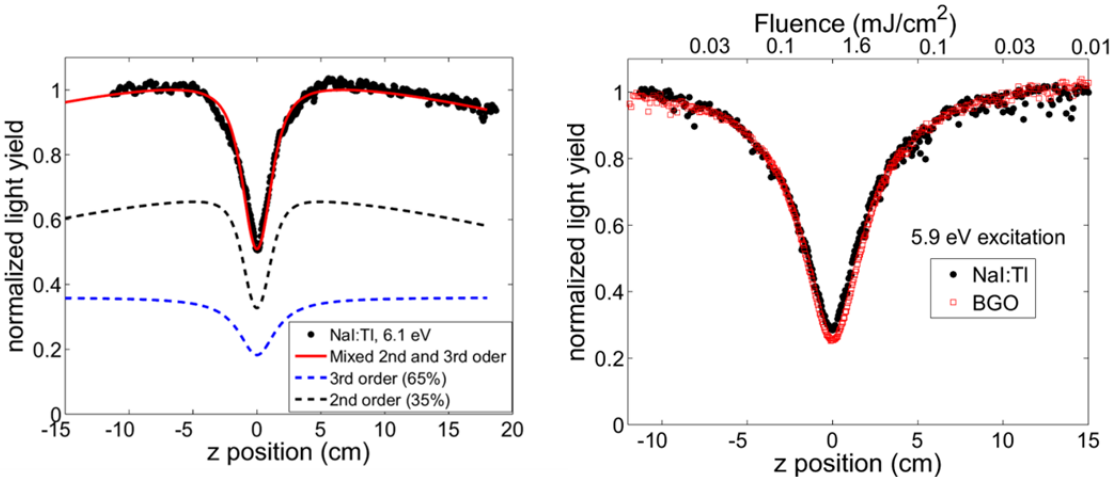

Figure 8 Photon density response of NaI:Tl excited at 6.1 eV and 5.9 eV. For 6.1 eV excitation, the fit corresponds to a mixed population of excited states during nonlinear quenching: 65% free carriers and 35% excitons. For 5.9 eV excitation, the 2nd order model provides a good fit, implying that the excitations are excitons. BGO data with known pure 2nd order kinetics is superimposed for comparison.

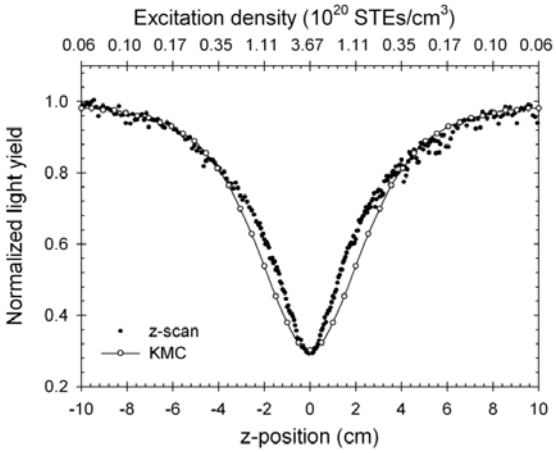

Figure 9. Comparison of the calculated light yield by Kinetic Monte Carlo method (open circles) [18,19] with experimental PDR results (solid circles) [9] for NaI(0.1% Tl) excited by 5.9-eV photons as a function of the position of the beam waist (z-position) and excitation density.

3.5 Hot free-carrier kinetics and associated light yield model

We have been showing 3rd order fits of the PDR data in Figs. 4 and 8 without yet stating exactly what the 3rd order model is. The delay in discussing it is tied up with the phenomenon illustrated in Fig. 6, that slow electron thermalization can introduce a delay in exciton formation. We will build the model for 3rd order quenching in view of finite electron thermalization time in stages, starting from the conventional model that neglects this factor. The basic rate equation that includes 3rd order quenching was given previously as Eq. (3). The conventional assumption is that all of the rate terms compete on the same time scales. We will refer to this as the "conventional Bn^2 model", so named because the 2nd order exciton formation term is responsible ultimately for light emission.

Following an assumption made by Murray and Meyer [20], we consider for the moment that only the free carriers forming excitons (rate Bn^2) will have a chance ultimately to contribute to scintillation light, and so write the following proportionality to the corresponding light yield

$$LY \propto = \frac{\int_0^\infty Bn^2 dt d^3r}{\int_0^\infty (K_{1e}n + Bn^2 + K_3 n^3) dt d^3r} \tag{4}$$

where the rate constants K_{1e}, B, and K_3 were defined in Eq. (3).

Putting aside the 3rd order term for the moment, we note that Murray and Meyer considered only the 1st and 2nd order terms without the indicated time integrals in Eq. (4) and then divided out the common factor of Bn^2, obtaining

$$LY \propto \left(\frac{K_{1e}}{Bn} + 1 \right)^{-1} \tag{5}$$

for the trend of rising light yield with excitation density. They later remarked on the ultimate decreasing light yield expected at very high excitation density, which we include by restoring the Auger term and writing an expression in all 3 orders, similar to Eq. (5). This qualitatively predicts a hump in light yield versus excitation density n:

$$LY \propto \left(\frac{K_{1e}}{Bn} + 1 + \frac{K_3 n}{B} \right)^{-1} \tag{6}$$

It is worth noting that in going from the conventional light yield expression in Eq. (4) to the simplified trend expressed in Eqs. (5) and (6), a step was taken that does not strictly apply to pulsed excitation such as in scintillator operation. Dividing out the Bn^2 rate term can only be done mathematically in a "continuous excitation" experiment where the excited population is continuously resupplied. Then the light yield is proportional simply to the ratio of radiative and total rates of depleting the excited population, as represented in Eqs. (5) and (6). (We also note that J. B. Birks [21] made a similar continuous excitation assumption in deducing the "Birks term" as it has been called by various workers in the scintillator field.) But the real application of scintillators, the measurements of electron energy response, and the photon density response laser experiment all detect the integrated light yield after pulsed excitation. This requires doing the time integrations shown explicitly in Eqs (2) and (4), before forming the ratio. The "continuous excitation model" can be convenient for discussing qualitative trends, but for fitting quantitative data the integrals must be done first and then the ratio formed to predict light yield.

For large carrier density n, where both photon density response and electron energy response experiments generally show a roll-off of light yield due to nonlinear quenching, Eq. (6) predicts an inverse first power dependence ($1/n$) of Light Yield versus n. Figure 10 plots the prediction of Eq. (4) including proper integration, labeled as the "conventional Bn^2 model", in comparison to measured photon density response of SrI_2. The plot of the 2nd order quenching model represented by Eq. (2) is also shown, and neither can fit

the data because they fall off too slowly. In fact, the conventional Bn^2 model falls off even more slowly than the 2nd order exciton model, Eq. (2).

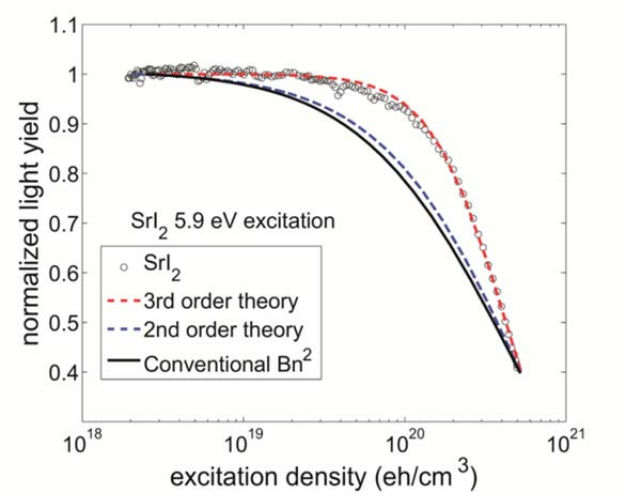

Figure 10. PDR data in SrI_2 (open circles) is shown along with three model attempts to fit the data. The red dashed curve that fits the experimental data uses the 3rd order model to be developed in the next few paragraphs. The blue dashed curve that cannot be made to fit is the 2nd order model described by Eq. (2). The solid curve that also fails to fit the data is the "conventional Bn^2" light yield, Eq. (4), based on the conventional 3rd order rate equation, Eq. (3), in which all terms compete on the same time scale.

The failure of Eq. (4) to fit the roll-off slope in a 3rd order quenching material is one of several experimental results leading us to conclude that the first, second, and third order kinetic terms do not all compete on the same time scale in materials like SrI_2 and the alkali iodides, where hot carriers persist during a significant part of the time for nonlinear quenching. The very fact of finding pure 3rd order quenching in photon density response for SrI_2 and CsI already led us to invoke hot electrons as the physical phenomenon holding off exciton formation and other electron capture channels for a finite time in iodides. The hot electron thermalization time is approximately inversely proportional to optical phonon period [4,5,7,14] and can be as long as 7 ps in CsI.[4,5] There seems almost no other way of explaining the occurrence of pure 3rd order quenching in the iodides having low ω_{LO} while the oxides with high ω_{LO} exhibit pure 2nd order quenching.

The logical extension of this explanation is that not all the rate terms in Eqs. (3) and (4) can be competing in the same time range. Electron capture on traps or dopants (An) or on holes (Bn^2) is strongly suppressed until the electrons have thermalized. This was illustrated by the calculations of electron temperature and of the paired fraction of electrons and holes versus time comparing CsI and YAP in Fig. 12. Therefore, we want to see if the slope of the roll-off of photon density response in SrI_2 and other iodides can be properly fit when we take the thermalization time dependence of each kinetic order into account in the free-carrier rate equation (Eq. 3) and the expression for light yield (Eq. 4). Use of explicitly calculated rate "constants" dependent on time via electron temperature is being pursued in current Monte Carlo simulations of these processes.[15] However, for a simple analysis of the photon density response data that at least takes electron thermalization into account, we have assumed a step-wise time dependence in each kinetic order of the free-carrier rate equation [9] as follows:

$$\frac{dn}{dt} = -An\Theta(t-\tau_{th}) - Bn^2\Theta(t-\tau_{th}) - K_3 n^3\Theta(\tau_{th}-t) \qquad (7)$$

where $\Theta(t-\tau_{th})$ is the Heaviside step function turning on after τ_{th}, and $\Theta(\tau_{th}-t)$ turns off after τ_{th}.

In this way, we assert that the coupling rates into exciton formation (Bn^2) and carrier trapping (An) cannot turn on until it becomes possible to trap electrons on holes or on dopants, i.e. until the electron has thermalized to within the trapping potential depth. (See Fig. 6) Li et al are working to calculate the thermalization time as a function of electron energies excited in the photon density response experiments.[15] However for the time being, we assume that the trapping and bimolecular exciton formation channels turn on after a hot electron thermalization time approximated as 6 ps in iodide crystals.

This estimate of 6 ps is chosen as representative of the 7 ps maximum thermalization time in CsI [4] and the 6 ps capture time of electrons on Tl^+ in CsI:Tl(0.3%) [17]. The free-carrier Auger recombination is similarly modeled as turning off when the carriers thermalize and trap on spatially separated sites (in CsI:Tl and similar activated scintillators, especially halides).

Based on the time-step rate equation in Eq. (7), we can proceed to write the expression for light yield taking hot electron thermalization into account. When integrated over time, the step functions separate the terms acting on different time scales into a product of probabilities of survival as follows:

$$LY = \left(1 - \frac{\int_0^{\tau_{therm}} \int_V K_3 n^3 dt d^3r}{\int_V n(t=0) d^3r}\right) \frac{\int_{\tau_{therm}}^{\infty} \int_V (Bn^2) dt d^3r}{\int_{\tau_{therm}}^{\infty} \int_V (K_1 n + Bn^2) dt d^3r} \left(\frac{\int_{\tau_{therm}}^{\infty} \int_V R_1 N dt d^3r}{\int_{\tau} \int_V (Q_1 N + R_1 N + K_2 N^2) dt d^3r}\right) \quad (8)$$

A crucial feature of Eq. (8) to note is that the 3rd order quenching process is limited to the left-hand bracket governing hot carrier quenching and determining the survival fraction that passes on to the middle bracket of processes such as capture of thermalized carriers on deep traps ($K_1 n$) and on holes (Bn^2). The left-hand bracket as a multiplier imposes approximately a $1/n^3$ slope on the roll-off of light yield at high n, in agreement with the PDR experiments. The time integrals in the middle formally run from τ_{th} out to ∞, but the rates within are all sufficiently fast that the trapping and exciton formation can be virtually complete in tens of picoseconds. The survivors of the middle bracket are excitons, passed on to the right-hand bracket as the exciton density N. The quadratic nature of electron-hole recombination is represented in the exciton formation (middle bracket), but the only radiative rate in the entire multiplied string of brackets is that of generalized (free or trapped) exciton radiative decay $R_1 N$ in the right-hand bracket.

In a more complete treatment to be published [22], it is shown that the free-carrier rate equation Eq. (3) should account separately for the rates of deep trapping $K_1 n$ and shallow trapping $S_1 n$. If the shallow traps thermally release stored charge within the scintillation time window, the $S_1 n$ rate can also contribute to eventual formation of trapped or free excitons and thus becomes another kinetic term in the light yield.

3.6 Auger rate constants

By fitting Eq. (8) to PDR data, we obtain the rate constants K_2 and/or K_3 appropriate to the populations of excitations, as well as η_{eh} specifying the fractional populations. The values of K_3 measured from these PDR (Z scan) experiments in SrI_2, CsI, NaI, and CdTe are compared in the following Table and graph to K_3 measured by other methods in materials that are primarily semiconductors of interest for light-emitting diodes and lasers. The empirical "band-gap rule" of Auger rate constants predicts that K_3 decreases as the

Crystal	K_3 ($cm^6 s^{-1}$) $\times 10^{-29}$	Reference	E_g(eV)	ω_{LO} (s^{-1}) $\times 10^{13}$
InSb	1200	39	0.17	3.7
GaSb	7	39	0.7	4.3
GaAs	0.7	63	1.43	5
CdTe	0.5	Z scan	1.44	3.1
$In_{0.15}Ga_{0.85}N$	0.2	78	2.64	14
$In_{0.09}Ga_{0.91}N$	0.14	78	2.83	14
SrI_2	0.7	Z scan	5.5	2.6
NaI:Tl	3.2	Z scan	5.7	3.47
CsI:Tl	6.6	Z scan	5.8	1.79
CsI	4.5	Z scan	5.8	1.79

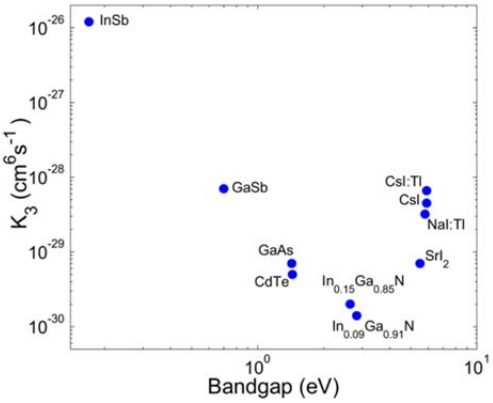

Figure 10. Auger recombination rate constant K_3 ($cm^6 s^{-1}$) is tabulated and plotted versus bandgap for CdTe, SrI_2, NaI, and CsI measured by laser PDR in this work, alongside values from the literature on several semiconductors.

band gap increases. The basic reason for this is that the energy given to the spectator electron or hole by e-h recombination increases with band gap. The corresponding final-state wavevector of the spectator particle increases accordingly, soon exceeding the range of wavevector $\boldsymbol{k}$ in the initial state and thus

progressively closes down the possibility of satisfying ***k*** conservation. Our measured K_3 for CdTe falls in line with the other semiconductors, but K_3 for the iodides with larger band gap lies considerably above the trend extrapolated from the semiconductors.

There are at least two interpretations for the Auger rate constants found in alkali iodides from PDR measurements being higher than predicted by the band-gap rule extrapolated from semiconductors: (1) The hole in alkali halides[23] (and alkaline earth halides [23] including SrI_2 [24] is self-trapped. This localization to one lattice site removes the wave-vector conservation rule that otherwise severely limits possible final states of the Auger transition as band gap increases. If at least one of the interacting carriers is localized (e.g. self-trapped), the initial state already contains a spread of k components, so the Auger rate should not be so restricted. If we feel confident to press details of the data, we can point out that the Auger rate constant of SrI_2 is about 6x smaller than the average of CsI and NaI. Since we have seen that SrI_2 quenches only by Auger recombination, the fact that it has a smaller Auger rate constant than alkali iodides seems to be yet another reason why SrI_2 has better proportionality and light yield. As a possible cause for the difference, one wonders if possibly the hole is not as completely localized in SrI_2 as in the alkali iodides. (2) The electron is hot during the free carrier phase when nonlinear quenching is assumed to occur. The carriers excited by laser in the photon density experiments remain out of equilibrium with the lattice, possessing up to 300 meV excess kinetic energy (up to 2300 K electron temperature) in alkali iodides and up to 1.6 eV in SrI_2 during the Auger recombination observed in the 6.1 eV PDR experiments.[9] It is known that lattice temperature accelerates Auger recombination particularly in wide-gap materials, for the reason discussed just above. At high lattice temperature, phonons can provide the needed momentum in indirect Auger events, as is well known. Similarly, excess electron temperature should also increase the probability of conserving momentum for large energy transfers in Auger recombination. Although moderately hot electrons do not possess mean momenta as large as phonons, neither do hot carriers as sources of momentum imply a 4th participant (phonon) as required in indirect Auger processes. Both reasons support plausibility of the enhanced Auger rates observed in iodide crystals by the PDR experiment.

Yet another alternate interpretation could be that the premise of Eq. (7) and the surrounding discussion is wrong, i.e. that the free-carrier Auger (3rd order) quenching continues well beyond the time limit imposed by carrier cooling and trapping. Then a smaller K_3 rate constant would be deduced from the photon density response. But then we would have to look elsewhere than hot electron thermalization to resolve the observed 3rd order/ 2nd order dichotomy of iodides vs oxides and to account for changing kinetic order upon tuning photon energy about 200 meV above the band gap in iodides. We have not found an alternative explanation for the latter observations.

3.7 Adding electron tracks and predicting electron energy response

We have used laser PDR data measured without the complicating spatial gradients of electron tracks to determine values of η_{eh}, K_2, and K_3. To compare the predictions based on these and other parameters to electron energy response of scintillators, one needs to put the track gradient, diffusion, and excitation density distribution back into the picture. We do this by measuring track radius near the track end and constructing a light yield model that includes carrier diffusion and the linear & nonlinear rate constants to obtain a predicted local light yield as a function of excitation density, $Y_L(n_0)$. Then the distribution of excitation densities from slowing of a high-energy electron of initial energy E_i is calculated, e.g. using Geant4, to yield the distribution of excitation densities, $F_{eh}(n_0,E_i)$. Convolution of these two functions of n_0 yields the electron energy response $Y_e(E_i)$ for comparison to Compton-coincidence and K-dip experiments. [25] The procedures from diffusion, quenching, thermalization, and local light yield up through the final convolution have been developed in Refs. [1,2,4–8,25–29]. A brief overview will be given here, beginning with effects of diffusion and nonlinear quenching in electron tracks.

Refs.[26–28] developed a local light yield model based on the premise that by diluting excitation density and in some cases separating charges in the track core, diffusion of electrons and holes can affect the nonlinear quenching. Refs. [11,26–28] and related works set out to evaluate the dominant trends in light yield resulting from a model corresponding to the rate Eqs. (1) and (2). It was found that the dominant diffusion effects manifest themselves differently in different classes of materials. We will illustrate in turn two competitions in which diffusion can preserve some excitations from the nonlinear quenching that

would otherwise occur. The first competition is simple dilution of carrier pair density by ambipolar diffusion of electrons and holes to diminish the amount of dipole-dipole quenching that would otherwise occur in the dense track core if carriers and excitons were static. The essence of the track-dilution effect of ambipolar diffusion on nonlinear quenching is illustrated for the full exciton rate equation, i.e. Eq. (1) with diffusion included, applied to an assumed cylindrical electron track in Fig. 11. It is simply a competition in whether excitons will more quickly reduce their concentration N by the quenching itself (a loss of the exciton number) or by diffusion to larger radius causing reduction of exciton density and thus of quenching rate, but not necessarily a reduction of exciton number.

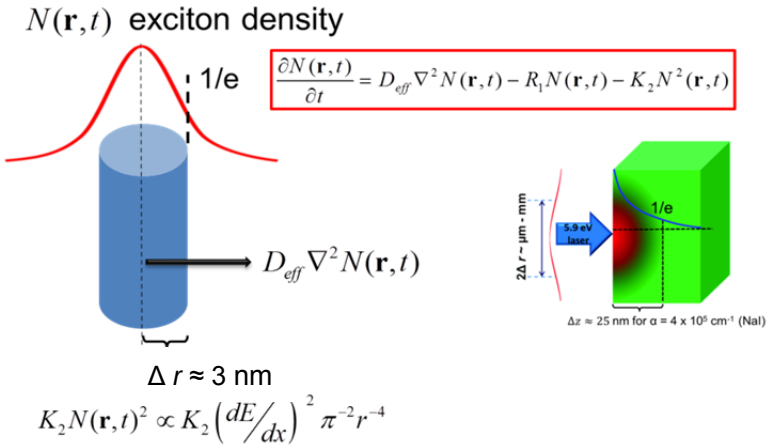

Figure 11. The illustration on the left represents the competition between loss of luminescence due to 2nd order quenching in an electron track, and rescue by diffusion out of the densely populated track core. The illustration on the right compares the weaker gradients in laser interband excitation for PDR.

A physical phenomenon affecting halides more than oxides and semiconductors is spatial charge separation when the electron and hole mobilities are widely unequal. This is especially pronounced when there is self-trapping of holes. The effect is to protect the electron-hole pair from early nonlinear quenching, which requires that electron and hole distributions are spatially overlapped. If, as in alkali halides, the electron mobility is much greater than the hole mobility, the electrons will outrun the holes in the radial concentration gradient of the modeled cylindrical track, trapping separately as independent carriers in preference to pairing as excitons, up to the time of eventual de-trapping and recombination on activators or defects.[26,29] The excitations that are captured as excitons on an activator will emit promptly. In contrast, the excitations that are captured as separated electrons and holes on different activators or defects must recombine more slowly by de-trapping mechanisms. During that process, the fraction of independently trapped carriers (*IF*) will be exposed to deep trapping, particularly by charged defects having a large cross section for independent charge carriers. *IF* in general changes along the track length due to changing electric field effects that accompany the changing excitation density. The trapping hazard is represented by the multiplier of fraction *IF*, called the linear quenched free-carrier fraction k_1.[26,27] The survival fraction is thus $(1-k_1 IF)$. Plotting $(1 - k_1 IF)$ versus on-axis excitation density n_0 for several different hole mobilities μ_h relative to fixed μ_e shows a rising trend versus n_0.

In some ways analogous to the product of "Birks and Onsager" terms in the model described by Payne et al [1,2], the product $(1-QF)(1-k_1 IF)$ approximates the overall probability of an electron-hole pair surviving nonlinear quenching QF in the track core, followed by the probability of being driven to independent status by unequal diffusion and yet surviving deep trapping to recombine radiatively. Figure 12 plots the simulated local light yield in the model of Refs. [26–28] for a series of hole mobilities μ_h while holding μ_e = 8 cm^2/Vs. Without a significant mismatch of μ_e and μ_h, there is no hump. But also without some linear quenching k_1, there is no hump either.

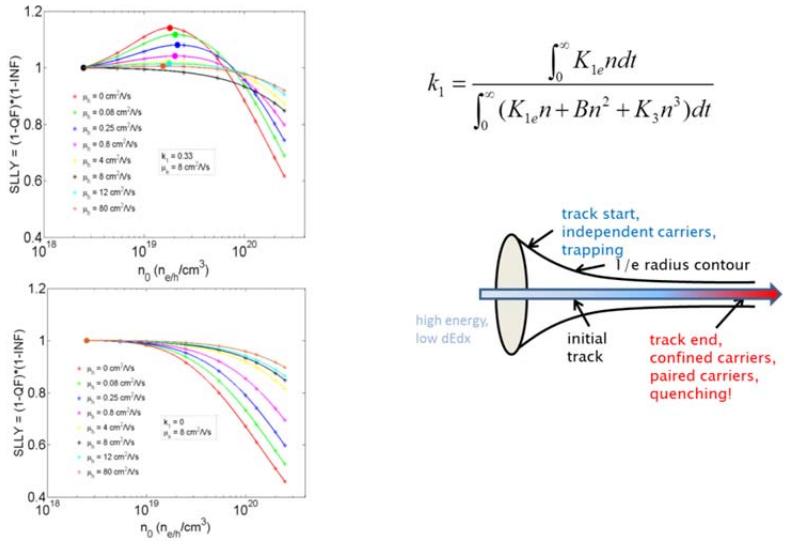

$$k_1 = \frac{\int_0^\infty K_{1e} n dt}{\int_0^\infty (K_{1e} n + Bn^2 + K_3 n^3) dt}$$

Figure 12. Simulated local light yield $Y_L(n_0) = (1\text{-}QF)(1\text{-}k_1IF)$ versus on-axis excitation density n_0 is plotted for different hole mobilities as listed. The electron mobility is fixed at 8 cm^2/Vs. The linear quenched fraction k_1 is 0.33 in the upper frame and 0 in the lower frame.

3.8 Track radius

The track radius determines n_0 corresponding to a given linear energy deposition rate dE/dx and also determines the gradient that promotes radial carrier diffusion. Track radius is thus a crucial parameter of the model, both its initial value at the time of energy deposition, and its evolving value under diffusion of hot and thermalized electrons. For that matter, there is a radius of the hole distribution and a radius of the electron distribution. Depending on whether holes self-trap and how much electrons or holes diffuse, charge separation can build up. This has consequences for both radiative and nonradiative recombination on different time scales. Recent experimental [9] and computational [30] work has deduced probable values for the radius of the nonlinear quenching zone [9] and the radius of the self-trapped hole distribution[30,31] near the track end in NaI and more recently in SrI_2 [32]. The values are all in agreement on approximately 3 nm radius. The data and method for the experimental determination are illustrated in Fig. 13 and have been discussed in more detail in Ref. [9].

The laser fluence in a PDR (z-scan) experiment can be adjusted to produce the same nonlinear quenching at the bottom of the dip as is seen in K-dip spectroscopy at a track-end value of electron energy (e.g. 80 eV) in NaI:Tl. Briefly, K-dip spectroscopy analyzes the light yield attributable to excitation by K-shell photoelectrons of specific energy selected by tuning synchrotron radiation relative to the K edge.[3] It is assumed that the same excitation density n_0 will produce the same amount of nonlinear quenching in each of the two experiments compared in Fig. 13. We equate the peak densities n_0 expressed in Eqs. (9) and (10) and solve for r_{NLQ}, the effective radius in which nonlinear quenching occurs:

$$n_0 = \frac{dE/dx}{\beta E_{gap} \pi \, r_{NLQ}^2} \tag{9}$$

$$n_0 = \frac{F_0 \alpha}{h\nu} \tag{10}$$

$$r_{NLQ}^2 = \frac{h\nu \, dE/dx}{F_0 \alpha \beta E_{gap} \pi} \tag{11}$$

The result in NaI:Tl with $\alpha \approx 4 \times 10^5$ eh/cm^3,[33] $F_0 = 0.4$ mJ/cm^2, $h\nu = 5.9$ eV, dE/dx (at 80 eV) = 64 eV/nm [31], β = 2.5 [34], and $E_{gap} = 5.8$ eV is $r_{NLQ} \approx 3$ nm near the track end. Using the NWEGRIM Monte Carlo code, Gao et al have calculated the radius of the self-trapped hole distribution at track end in NaI to be 2.8 nm[30], as shown in Fig. 14 and discussed briefly below.

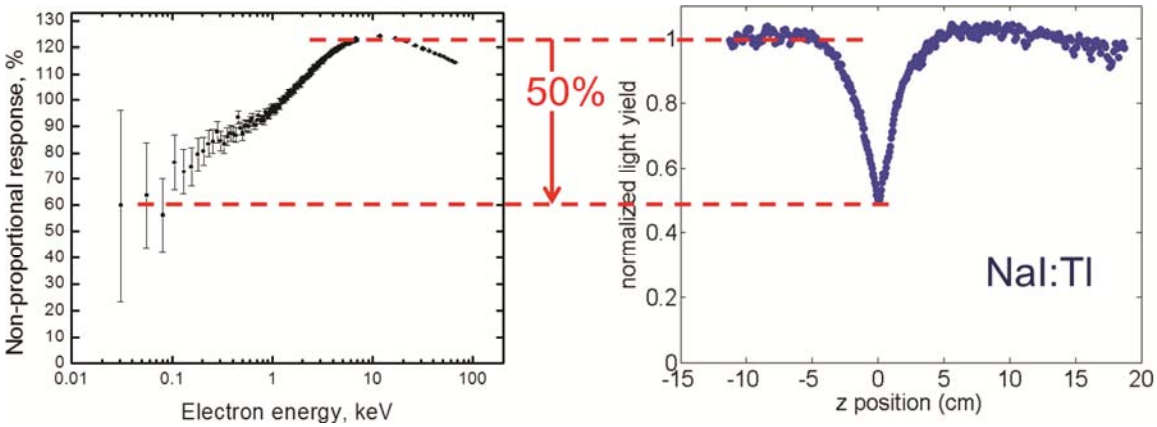

Figure 13. K-dip spectroscopy [3] for NaI:Tl (left) with 50% quenching near the track end. On the right are the z-scan results for NaI:Tl with the uv laser fluence tuned to produce the same level of quenching from Ref. [9].

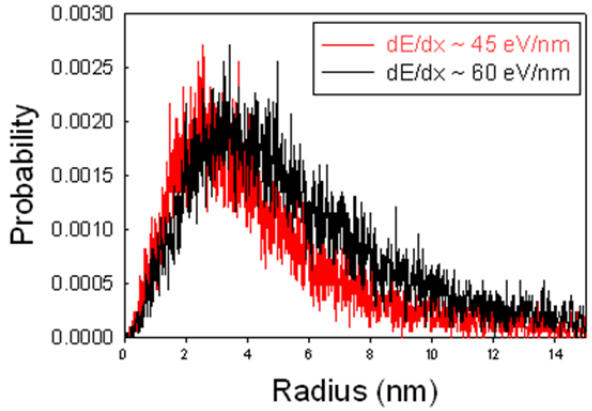

Fig. 14 Calculated probability distribution of electrons at end of the electron cascade (effectively before diffusion and thermalization) near the track end in NaI. This is assumed to approximate the distribution of self-trapped holes.

Although a single value of track radius can be evaluated in the z-scan experiment, its fluctuation cannot be easily determined in experimental measurements, which may be important for the further development of an accurate model of scintillator proportionality. The NorthWest Electron and Gamma Ray Interaction with Matter (NWEGRIM) code,[30] has been developed to simulate the response of scintillator materials, evaluating their intrinsic properties, stopping power, and maximum theoretical light yield. It has been employed to determine the electron distribution in NaI at initial points of creation, i.e. at the end of the electron cascade terminating with the start of phonon cooling at $E_{cbm}+E_{gap}$. This is effectively before diffusion and thermalization. It is likely that the static self-trapped hole distribution in an alkali halide crystal such as NaI is the same as this initial electron distribution radius. As shown in Fig. 14, the peak position of the radial distribution at the track end in NaI is 2.8 nm, and the distribution ranges from 0.1 to 14 nm. This self-trapped hole distribution is in reasonable agreement with that measured by the z-scan experiments in NaI, discussed above. It is also consistent with an earlier estimate by Vasil'ev et al.[31]

3.9 Hot electrons

Carrier pairs are created by slowing of the primary electron, with electron and hole kinetic energies distributed over a wide range. The electrons lose energy very rapidly by secondary e-h production until reaching an energy one bandgap above the conduction band minimum (cbm), and analogously for holes. From there, the cooling is slower by phonon emission (picoseconds or less for LO phonon processes) as equilibrium with the lattice temperature is approached. There are a number of indications that the main part of nonlinear quenching takes only a matter of picoseconds, as does free-carrier diffusion toward an equilibrium distribution [26], so it can be important to consider diffusion and nonlinear quenching while the electrons are still in nonequilibrium energy states.

The extent of electron-hole pair recombination and the distances traveled by hot electrons during thermalization are illustrated in Figure 15 for four halide scintillators, namely, NaI, CsI, CaF_2, and BaF_2. These results have been obtained from a Monte Carlo model of electron thermalization [4,5] that incorporates electron scattering with optical and acoustic phonons and also includes the effects of internal electric fields. The model uses as input the spatial and kinetic energy distributions of electron-hole pairs at the end of the energy cascade, as calculated by NWEGRIM. The kinetic energy distributions of hot electrons at the end of the energy cascade extend up to the band gap energy. Therefore, the majority of the electrons have high kinetic energies relative to the thermal energy. As a result, the distributions of the distances traveled by the electrons that are able to escape the electric field of the STHs and eventually reach thermal energy (referred to as "stopped" electrons) peak between approximately 20 and 60 nm and can extend up to a few hundreds of nanometers (Figure 15 – right). Although the thermalization distances can be large, a significant fraction of the electrons (referred to as "recombined" electrons) are not able to escape the electric field of the STHs and recombine with STHs to form STEs (Figure 15 – left). The increase in stopping power at low incident γ-ray energies generates high electron-hole pair densities, which leads to an increased probability for electron-hole pair recombination. This, in turn, should result in a greater extent of second and/or third-order nonlinear quenching at low incident γ-ray energies. Second order quenching is now treated in the KMC model, with inclusion of third order anticipated at a future time. The MC model predicts that the four materials yield different extents of electron-hole pair recombination due mostly to differences in their electron mean free paths, LO phonon energies, initial densities of electron-hole pairs, and static dielectric constants. In particular, the LO phonon energy is a key factor that affects electron thermalization. Indeed, the higher the LO phonon energy is, the more favored phonon emission is over phonon absorption and the more energy is transferred to the lattice for each phonon emission event. Electron-hole pair recombination occurs in the early stages of the thermalization process and those electrons that recombine with STHs travel distances of at most 10 to 20 nm (Figure 15 – right – inset).

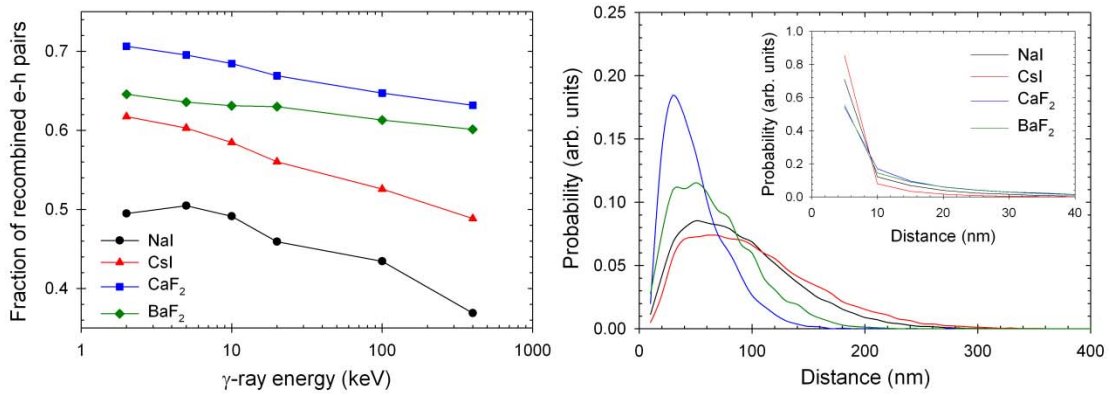

Figure 15. (left) Fraction of recombined electron-hole pairs as a function of incident γ-ray energy for two alkali iodide (NaI and CsI) and two alkaline-earth fluoride (CaF_2 and BaF_2) scintillators. (right) Thermalization distance distributions of the "stopped" electrons for the same four scintillator materials (2-keV incident γ-ray). The inset shows the thermalization distance distributions of the "recombined" electrons from the same simulations.

It appears that the consideration of hot and thermalized diffusion can resolve some subtleties having large consequences for scintillator performance, such as why NaI:Tl and SrI_2:Eu have such different

proportionality and light yield despite having quite similar values of carrier mobility, nonlinear quenching rate constants, and other parameters normally considered to help determine proportionality and light yield. A clue is found from inspecting the conduction band structures through the phonon cooling range in Fig. 16.

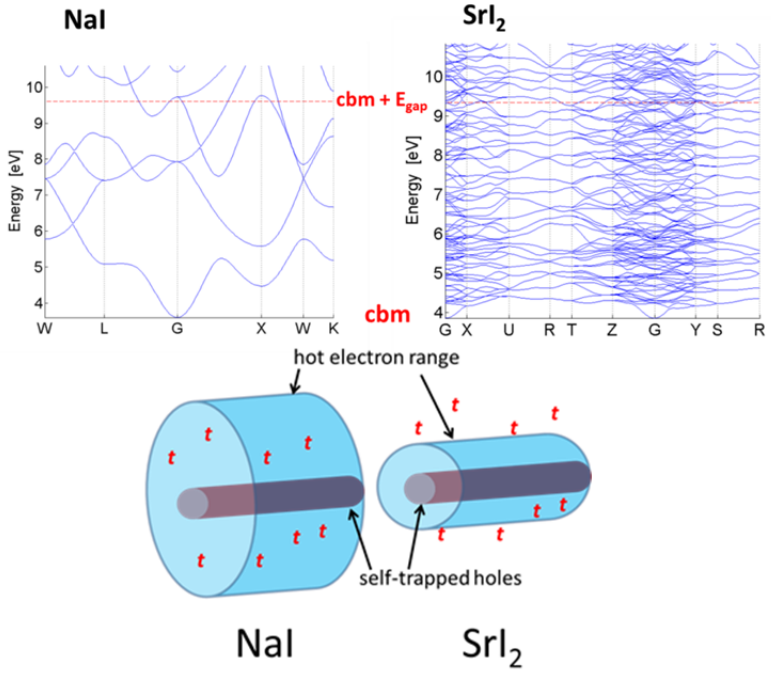

Figure 16. Upper part: Conduction band dispersion curves are compared through the range of phonon-cooling of hot electrons from E_{cbm} up to $E_{cbm} + E_{gap}$ for NaI and SrI_2. Lower part: Hypothesis based on faster diffusion of hot electrons in NaI compared to SrI_2, leaving a track core of self-trapped holes near the center. Recombination by diffusion after thermalization encounters a longer path through the field of deep electrons in NaI.

Just as a visual impression, the conduction bands in NaI are comparatively sparse and not terribly far from free-electron like. In contrast, the conduction bands in SrI_2 are densely packed and generally appear flatter, partly attributable to avoided crossings of some of the densely packed bands. The cause of this visual impression is basically that the hot electron group velocities proportional to slopes of the bands appear lower on average in SrI_2 than in NaI. The difference in packing density of the electronic bands is attributable to the more complex unit cell in SrI_2 (24 atoms) compared to NaI (2 atoms). Calculation of the average group velocities in these two crystals was presented in Ref. [6], and used to form a hypothesis illustrated schematically in the lower part of Fig. 16. If hot electrons diffuse farther radially in NaI than in SrI_2, then the recombination of thermalized and/or shallow-trapped electrons with holes trapped near the track core will have to get through a longer path of quenching (deep-trapping) defects in NaI than in SrI_2. This raises the linear quenched fraction k_1 in NaI relative to SrI_2 (and also relative other halides with complex unit cells – "multivalent halides" in the characterization of Payne et al.[2]). We have already seen in Fig. 12 that increasing k_1 increases the "halide hump" in electron energy response. Proportionality suffers when the hump is large. By definition, k_1 also decreases total light yield.

4. CONCLUSIONS

From the foregoing discussion, it should be possible to look at branch points between basic types of behavior of scintillator materials according to the value (high or low) of a few key parameters. In the following exercise, we will consider four such parameter choices in sequence as a "decision tree" to see if indeed it can predict general characteristics of proportionality and light yield based on a small number of parameters that are measureable apart from the scintillator proportionality measurement itself. If it can be confirmed, it is the beginning of a design rule for scintillator discovery and engineering.

The first parameter to be considered, therefore in some sense the most fundamental, is the (highest) LO phonon frequency. The corresponding branch point is diagrammed in Fig. 17, with experimental plots of PDR illustrating physical consequences of branching to high and low values of ω_{LO}. Low ω_{LO} in the right branch means that the carriers thermalize slowly relative to the time in which the main part of nonlinear quenching occurs. The basis for this conclusion is the experimental observation of *pure* third order quenching kinetics in the PDF data for CsI and SrI_2. Identifying 3rd order quenching with free-carrier Auger recombination, we have concluded that in materials of the right branch, free carriers are too hot during the nonlinear quenching phase to become bound in exciton or trap states. Since the time for electron thermalization by LO phonons in iodide crystals has been calculated [4,5,7,14] to be on the order of a few picoseconds, the above line of reasoning indicates that the main nonlinear quenching is complete within a few picoseconds. This conclusion is consistent with previous time-resolved data directly[25] and indirectly [17] related to nonlinear quenching in CsI. The bottom line for the decision is that free carriers dominate the nonlinear quenching process in the right branch of Fig. 17 corresponding to low ω_{LO}. Most iodides qualify as low ω_{LO}, although we saw in the PDR data of Fig. 8 that the light mass of sodium in NaI puts it in a category of mixed kinetic order, with free carriers and excitons apparently coexisting during nonlinear quenching. Heavy metal bromides and chlorides have not yet been run in the laser PDR experiments because of their larger bandgaps, but we tentatively lump them in the right branch based on ω_{LO} as the class of "heavier halides", especially when the halide is paired with a heavy metal. As a graphic illustration with real data, Fig. 17 includes PDR of SrI_2 as a paradigm of the materials classified in the right branch.

The left branch is for high ω_{LO}, characteristic of oxides and fluorides. High ω_{LO} causes rapid carrier thermalization. The PDR experiments on the oxides (BGO and $CdWO_4$) that have been measured exhibited pure 2nd order quenching, consistent with dipole-dipole annihilation. This indicates that excitons in some electronic state had formed before the main part of nonlinear quenching. BGO is shown as the example of a PDR curve characterizing materials in the left branch. The PDR comparison in the bottom center of Fig. 17, already discussed in Figs. 3 and 4, emphasizes the point that both proportionality and light yield are already affected in an important way by this first material branch point, controlled by the value of ω_{LO}. The winner in both proportionality and light yield at this point is the right branch simply because of the flatter and more advantageous 3rd order PDR curve. Indeed, the known scintillators with combined highest light yield and best proportionality, such as SrI_2:Eu, BaBrI:Eu, and $LaBr_3$:Ce should fall in the right branch, according to ω_{LO} . So do some more modestly-performing scintillators like NaI:Tl, CsI:Tl, but we have not yet considered the second-level branching.

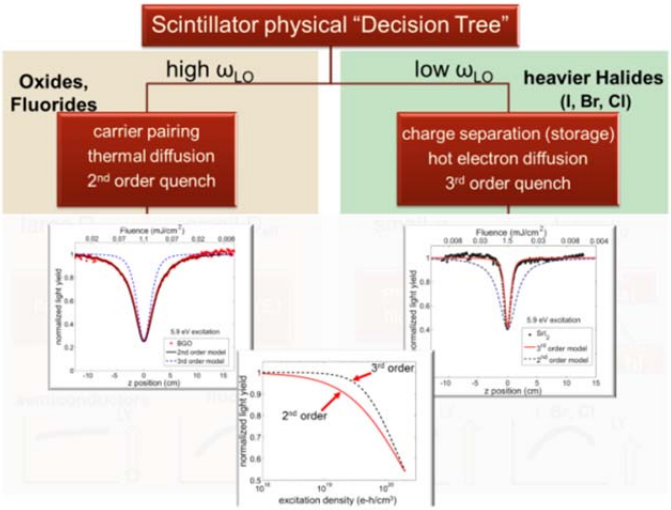

Figure 17. Top level branching between exciton and thermalized ambipolar diffusing pairs on the left and hot free carriers on the right, according to high or low LO phonon frequency.

Materials classified in the left branch have carriers that are thermalized (at least within one LO phonon energy of kT), and possibly paired as some bound state of electron and hole, before the main part of

nonlinear quenching. Then as suggested in the discussion of Fig. 11, it is reasonable to describe effects of diffusion around electron tracks in terms of ambipolar diffusion (coefficient D_{eff}) of thermalized carriers. This becomes the second-level branching parameter on the left side – large or small D_{eff}. Large D_{eff} includes semiconductors used for luminescence (such as ZnSe:Te), and those used for charge collection detectors (high purity Ge, CdTe, CZT) which we include in the present survey by letting energy-dependent charge collection (Q) stand in for energy-dependent light yield (LY). YAP:Ce is also in the branch of large D_{eff} because the near equality of electron and hole effective mass (Setyawan et al mass ratio $m_r = 1.2$ [35]) yields large D_{eff} relative to other oxide crystals.[27] Large D_{eff} allows carriers to escape the nonlinear quenching zone in the track core and thus gives a relatively flat electron energy response curve which is illustrated schematically at the lower left. Because of diffusing to low excitation density, the electron-hole radiative recombination suffers relative to defect trapping and so the light yield (LY) of semiconductor scintillator detectors, and YAP:Ce as well, is modest to low. Charge collection (Q) in semiconductors can be promoted by applied electric field and low defect concentration. Diffusion, albeit in different directions for electrons and holes, is a good thing for charge collection. Characteristic schematic predictions of Q and LY in this class are indicated by the bar chart at lower left.

The second-level right branch toward small D_{eff} applies to most oxides other than YAP:Ce, where higher hole mass begins to weigh on the ambipolar diffusion coefficient. Calculated band effective masses were used indirectly to represent or estimate D_{eff} or its stand-in, m_h/m_e, in Refs. [27] and [35]. Refractive index at the visible scintillation wavelength anticorrelates generally with band gap of the host, which in turn correlates with effective masses at both band edges. This was used in Ref. [11] to organize scintillators by refractive index in a way that amounts approximately to a stand-in for effective mass and therefore for carrier diffusion coefficients. In all three forms of experimental surveys of the nonproportionality (~ roll-off of electron energy response) among oxide scintillators, the trend was confirmed that lower effective diffusion coefficient implies greater nonproportionality, as a broad trend. [11,27,35]

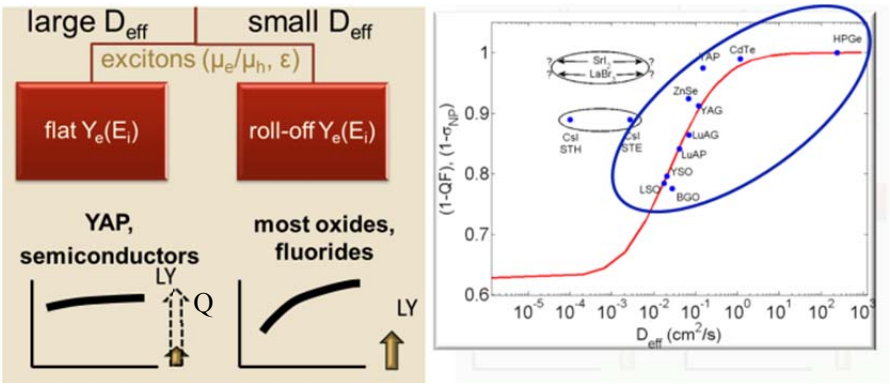

Figure 18. Second level branching of thermalized carrier pairs and excitons according to large or small effective diffusion coefficient D_{eff}, correlating with schemiatic representations of electron energy response curve shape and total light yield (LY, filled arrow) or charge collection (Q, dashed arrow).

The second level branching parameter on the right hand side should, for symmetry, be the diffusion coefficient for hot electrons, "hot D_e." We want to put it quantitatively in those terms in future work, combining quantitative thermalization rate and hot-electron group velocity as a function of energy to calculate hot $D_e(T_e,t)$ over the time and electron temperature interval of nonlinear quenching. For the time being, we have represented the hot electron diffusion coefficient as proportional to the square root of the calculated group velocity over the range of phonon cooling of hot electrons, and simply use hot electron group velocity v_g as the second-level branching parameter on the right side in Fig.19. [6] The operative rule is illustrated by the schematic cylinder tracks depicted in Fig. 16. Most of the halide scintillators that would be on the right side of the top-level branch also have self-trapped holes. Therefore hot electron diffusion implies wide separation of charges and further implies that de-trapping and diffusion over a relatively long time will be involved to recover radiative recombination of the initially separated hot electrons and self-trapped holes. If hot-electron v_g is large, as in NaI and CsI, the electrons returning toward the track core of self-trapped holes for radiative recombination have a long path through a minefield of defect traps (F centers, impurities, extended defects) that can prevent useful scintillation light. We could

expect that the linear quenched fraction k_1 may be substantial in such cases. The consequence for a halide hump in electron energy response and lower light in the simple halides like NaI was discussed in connection with Fig. 16. This is represented by the schematic hump in the generic electron energy response curve depicted at the lower right of Fig. 19. If the value of v_g and hot electron diffusion range is small, as in crystals with complex unit cell like SrI_2 and/or having flat La 4f lower conduction bands like $LaBr_3$, the hot electrons do not go out as far radially and so have a shorter path through the traps toward recombination. The generic predicted response is therefore flatter and higher light yield, both attributable to smaller k_1 due to smaller diffusion path. Notice that materials in this latter classification, including, e.g. SrI_2:Eu, BaBrI:Eu, and $LaBr_3$:Ce, get positive recommendations for good proportionality and light yield at *both* levels of branch points: At the first branching, free carrier dominance in this group leads to pure 3rd order quenching, which has inherently a flatter shape over most of the photon density response. This implies flatter electron energy response and higher light yield. Then at the second-level branch point, small hot-electron diffusion range (small v_g) implies smaller linear quenched fraction k_1 and this means flatter electron energy response and higher light yield yet again. The left second-level branch under the right top-level branch is doubly blessed and comprises a sweet spot in material parameter space for scintillator proportionality and light yield.

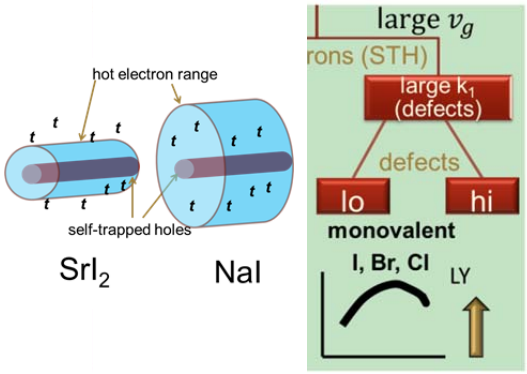

Figure 19. Second level branching on the right side according to hot electron group velocity v_g, standing in for hot electron diffusion coefficient. Existence of self-trapped holes in most halides and concentration of defects also play roles as discussed.

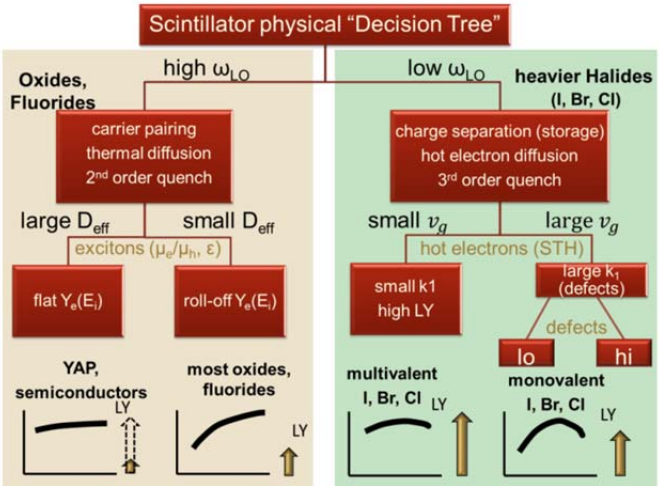

Figure 20. Assembly of all the branching points considered for this decision tree comprising the start of a design rule for proportionality and light yield of inorganic scintillators.

Figure 20 assembles all branches together in one diagram. It was presented previously in Ref. [6], without as much supporting discussion.

Acknowledgment: *Supported by NNSA, Office of Nonproliferation Research and Development (NA-22) contracts DE-NA0001012 and DE-AC02-05CH11231.We thank Steve Payne, Bill Moses, Andrey Vasil'ev and Jai Singh for helpful discussions.*

REFERENCES

[1] S. A. Payne, N. J. Cherepy, G. Hull, J. D. Valentine, W. W. Moses, and W.-S. Choong, "Nonproportionality of Scintillator Detectors: Theory and Experiment," *IEEE Transactions on Nuclear Science* **56**(4), 2506–2512 (2009) [doi:10.1109/TNS.2009.2023657].

[2] S.A. Payne, W.W. Moses, S. Sheets, L. Ahle, N.J. Cherepy, B. Sturm, S. Dazeley, G. Bizarri, Choong Woon-Seng, "Nonproportionality of Scintillator Detectors: Theory and Experiment. II," *Nuclear Science, IEEE Transactions on* **58**(6), 3392–3402 (2011).

[3] I. V Khodyuk, P. A. Rodnyi, and P. Dorenbos, "Nonproportional scintillation response of NaI:Tl to low energy x-ray photons and electrons," *J. Appl. Phys.* **107**(11), 113513, AIP (2010) [doi:10.1063/1.3431009].

[4] Z. Wang, Y. Xie, B. D. Cannon, L. W. Campbell, F. Gao, and S. Kerisit, "Computer simulation of electron thermalization in CsI and CsI(Tl)," *J. Appl. Phys.* **110**(6), 64903, AIP (2011) [doi:10.1063/1.3632969].

[5] Z. Wang, Y. Xie, L. W. Campbell, F. Gao, and S. Kerisit, "Monte Carlo simulations of electron thermalization in alkali iodide and alkaline-earth fluoride scintillators," *Journal of Applied Physics* **112**(1), 014906, American Institute of Physics (2012) [doi:10.1063/1.4736088].

[6] Q. Li, J. Q. Grim, K. B. Ucer, A. Burger, G. A. Bizarri, W. W. Moses, and R. T. Williams, "Host structure dependence of light yield and proportionality in scintillators in terms of hot and thermalized carrier transport," *Phys. Status Solidi RRL* **6**(8), 346–348, WILEY-VCH Verlag (2012) [doi:10.1002/pssr.201206258].

[7] R. Kirkin, V. V Mikhailin, and A. N. Vasil'ev, "Recombination of Correlated Electron-Hole Pairs With Account of Hot Capture With Emission of Optical Phonons," *IEEE Trans. Nucl. Sci.* **59**(5), 2057–2064 (2012) [doi:10.1109/TNS.2012.2194306].

[8] A. Kozorezov, J. K. Wigmore, and A. Owens, "Picosecond dynamics of hot carriers and phonons and scintillator non-proportionality," *J. Appl. Phys.* **112**(5), 53709, AIP (2012) [doi:10.1063/1.4749253].

[9] J. Q. Grim, K. B. Ucer, A. Burger, P. Bhattacharya, E. Tupitsyn, E. Rowe, V. M. Buliga, L. Trefilova, A. Gektin, et al., "Nonlinear quenching of densely excited states in wide-gap solids," *Physical Review B* **87**(12), 125117, American Physical Society (2013) [doi:10.1103/PhysRevB.87.125117].

[10] M. Sheik-Bahae, A. A. Said, T.-H. Wei, D. J. Hagan, and E. W. Van Stryland, "Sensitive measurement of optical nonlinearities using a single beam," *Quantum Electronics, IEEE Journal of* **26**(4), 760–769 (1990) [doi:10.1109/3.53394].

[11] I. V Khodyuk and P. Dorenbos, "Trends and Patterns of Scintillator Nonproportionality," *IEEE Trans. Nucl. Sci.* **59**(6), 3320–3331 (2012) [doi:10.1109/TNS.2012.2221094].

[12] M. Moszynski, "Energy Resolution and Non-proportionality of Scintillation Detectors," *MRS Proceedings* **1038**, 1038–O07–02, Cambridge University Press (2011) [doi:10.1557/PROC-1038-O07-02].

[13] A. Vasil'ev and A. Gektin, "Elementary processes in scintillation and their interconnection in scintillation process," in *Proceedings of the 8th International Conference on Inorganic Scintillators and their Applications (SCINT 2005)*, A. Gektin and B. Grinyov, Eds., pp. 1–6, National Academy of Sciences of Ukraine, Kharkov (2006).

[14] A. Vasil'ev and A. Gektin, "Multiple scale approach to estimation of scintillator characteristics," in *SCINT2013*, Shanghai, China (2013).

[15] Q. Li, J. Q. Grim, N. A. W. Holzwarth, and R. T. Williams, "Hot electron velocity, relaxation time, and range in ultraviolet- and electron-excited scintillators and semiconductors," in *SCINT2013* (2013).

[16] R. T. Williams, K.B. Ucer, J.Q. Grim, A. Burger, A. Gektin, L. Trefilova, "Early Populations and Trapping Rates in Iodide Scintillators Studied by Picosecond Optical Absorption," in *SCINT2013* (2013).

[17] R. T. Williams, K. B. Ucer, J. Q. Grim, K. C. Lipke, L. M. Trefilova, and W. W. Moses, "Picosecond Studies of Transient Absorption Induced by BandGap Excitation of CsI and CsI:Tl at Room Temperature," *IEEE Trans. Nucl. Sci.* **57**(3), 1187–1192 (2010) [doi:10.1109/TNS.2009.2033184].

[18] S. Kerisit, Z. Wang, R. T. Williams, J. Q. Grim, and and F. Gao, “Kinetic Monte Carlo Simulations of Scintillation Processes in NaI(Tl),” *under review, IEEE Trans. Nucl. Sci.* (2013).
[19] Z. Wang, R. T. Williams, J. Q. Grim, F. Gao, and S. Kerisit, “Kinetic Monte Carlo simulations of excitation density dependent scintillation in CsI and CsI(Tl),” *physica status solidi (b)*, n/a–n/a (2013) [doi:10.1002/pssb.201248587].
[20] R. Murray and A. Meyer, “Scintillation Response of Activated Inorganic Crystals to Various Charged Particles,” *Physical Review* **122**(3), 815–826, American Physical Society (1961) [doi:10.1103/PhysRev.122.815].
[21] J. B. Birks, *The Theory and Practice of Scintillation Counting*, p. 662, Pergamon Press (1964).
[22] R. T. Williams, J. Q. Grim, Q. Li, K. B. Ucer, G. A. Bizarri, and A. Burger, “Scintillation Detectors of Radiation: Excitations at High Densities and Strong Gradients,” in *Excitonic and Photonic Processes in Materials*, J. Singh and R. T. Williams, Eds., Springer-Verlag, Heidelberg (2013).
[23] K. S. Song and R. T. Williams, *Self-trapped excitons*, Second, Springer-Verlag, Heidelberg (1996).
[24] A. Aberg, P. Erhart, and B. Sadigh, “First principles study of self-trapped excitons in NaI and SrI2,” *To be published*.
[25] J. Q. Grim, Q. Li, K. B. Ucer, R. T. Williams, G. A. Bizarri, and W. W. Moses, “Electron energy response of NaI:Tl and SrI2:Eu calculated from carrier mobilities and measured first- and third-order quenching,” *Mater. Res. Soc. Communications Research Letters* **2**(04), 139–143 (2012) [doi:10.1557/mrc.2012.27].
[26] R. T. Williams, J. Q. Grim, Q. Li, K. B. Ucer, and W. W. Moses, “Excitation density, diffusion-drift, and proportionality in scintillators,” *physica status solidi (b)* **248**(2), 426–438 (2011) [doi:10.1002/pssb.201000610].
[27] Q. Li, J. Q. Grim, R. T. Williams, G. A. Bizarri, and W. W. Moses, “A transport-based model of material trends in nonproportionality of scintillators,” *J. Appl. Phys.* **109**(17), 123716, AIP (2011) [doi:10.1063/1.3600070].
[28] J. Q. Grim, Q. Li, K. B. Ucer, A. Burger, G. A. Bizarri, W. W. Moses, and R. T. Williams, “The roles of thermalized and hot carrier diffusion in determining light yield and proportionality of scintillators,” *physica status solidi (a)* **209**(12), 2421–2426, WILEY-VCH Verlag (2012) [doi:10.1002/pssa.201200436].
[29] R. T. Williams, Q. Li, J. Q. Grim, and K. B. Ucer, “Dependence of nonproportionality in scintillators on diffusion of excitons and charge carriers,” in *SPIE Optical Engineering + Applications*, L. A. Franks, R. B. James, and A. Burger, Eds., p. 81420Y–81420Y–17, International Society for Optics and Photonics (2011) [doi:10.1117/12.895038].
[30] F. Gao, Y. Xie, S. Kerisit, L. W. Campbell, and W. J. Weber, “Yield, variance and spatial distribution of electron–hole pairs in CsI,” *Nuclear Instruments and Methods in Physics Research Section A: Accelerators, Spectrometers, Detectors and Associated Equipment* **652**(1), 564–567 (2011) [doi:10.1016/j.nima.2010.08.063].
[31] G. A. Bizarri, W. W. Moses, J. Singh, A. N. Vasil’ev, and R. T. Williams, “An analytical model of nonproportional scintillator light yield in terms of recombination rates,” *J. Appl. Phys.* **105**(15), 44507, AIP (2009) [doi:10.1063/1.3081651].
[32] J. Q. Grim, K. B. Ucer, A. Burger, G. A. Bizarri, and R. T. Williams, “SrI2 track radius,” *To be published*.
[33] W. Martienssen, "Uber die excitonenbanden der alkalihalogenidkristalle,” *Journal of Physics and Chemistry of Solids* **2**(4), 257–267 (1957) [doi:10.1016/0022-3697(57)90070-7].
[34] P. Dorenbos, “Fundamental Limitations in the Performance of Ce3+-, Pr3+-, and Eu2+- Activated Scintillators,” *IEEE Trans. Nucl. Sci.* **57**(3), 1162–1167 (2010) [doi:10.1109/TNS.2009.2031140].
[35] W. Setyawan, R.M. Gaume, R. Feigelson, and S. Curtarolo, "The roles of thermalized and hot carrier diffusion in determining light yield and proportionality of scintillators," IEEE Trans. on Nucl. Sci. 56, 2989 (2009).

Understanding Fundamental Mechanisms of Nonlinearity in Scintillators

F. Gao, Y. Xie, D. X. Wu, S. Kerisit,
L. W. Campbell, R. M. Van Ginhoven, M. P. Prange

Acknowledgements
Babak Sadigh, Daniel Aberg and Stephen Payne (LLNL), Richard Williams and Joel Grim (WFU)

Supported by Office of Nuclear Nonproliferation Research and Engineering (NA22), DOE

Pacific Northwest
NATIONAL LABORATORY

Proudly Operated by Battelle *Since 1965*

Outline

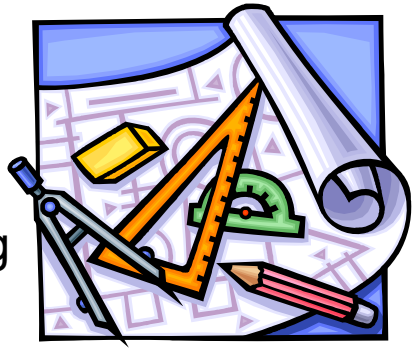

- Physics models
  - Northwest Electron and Gamma Ray Interactions in Matter Code (NWEGRIM) - Electron cascade, electron-hole pair generation, spatial distribution, intrinsic resolution, stopping power et al.
  - Kinetic Monte Carlo - thermalization of e-h pairs, transport of e-h pairs, interaction of excitons with dopants, nonlinearity
- Intrinsic properties
  - Electron cascades, variance, *W* value, maximum light yield – CsI, NaI, $LaBr_3$, BaF_2, CaF_2, SrI_2 , YAP, YAG
  - Spatial distributions of e-h pairs of SrI_2 and $LaBr_3$
  - General rules to guide the design of new scintillator materials
- Kinetics and efficiency of scintillation
  - Electron thermalization
  - Nonlinear quenching

Pacific Northwest
NATIONAL LABORATORY

Physics Models

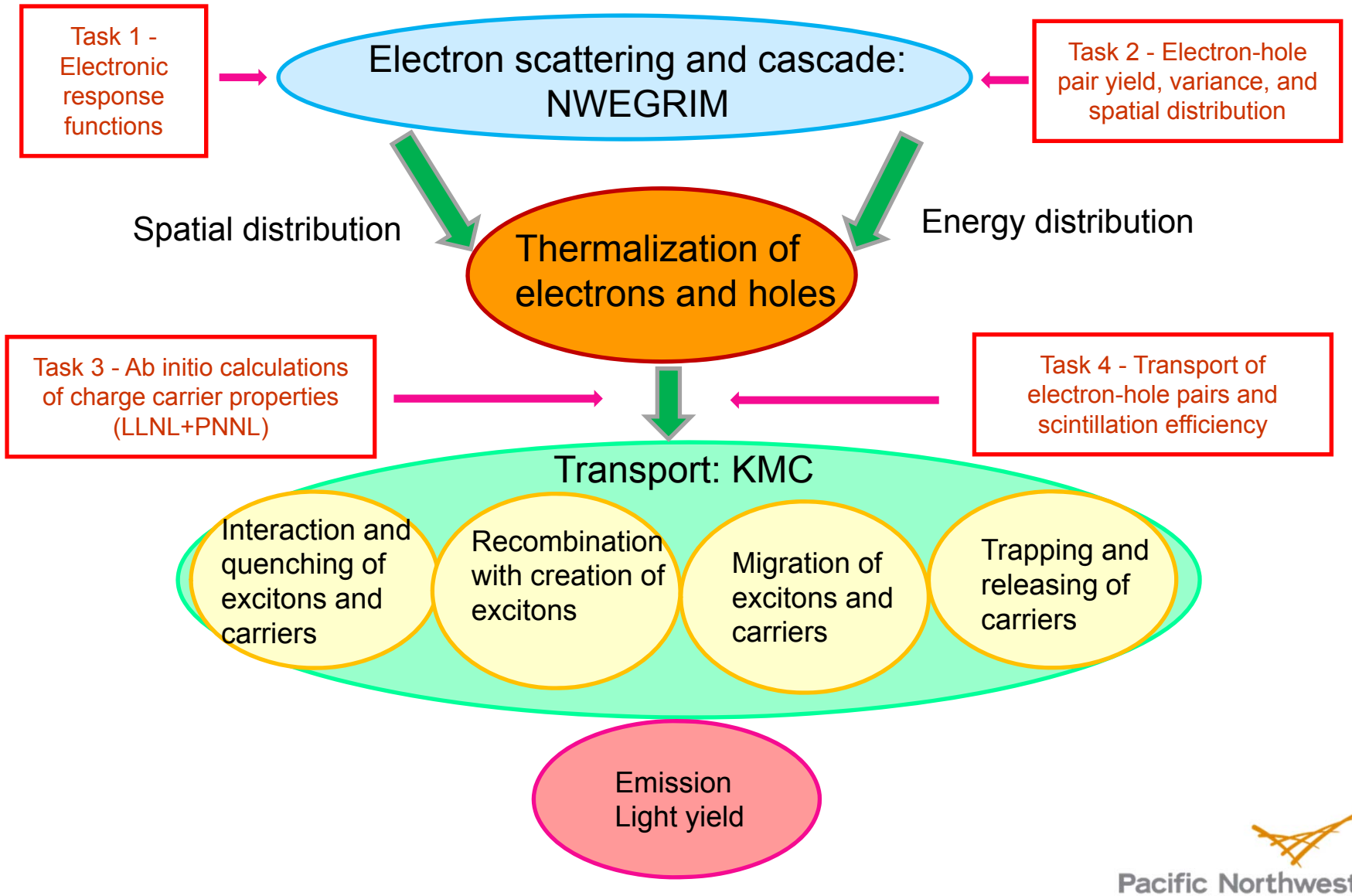

Pacific Northwest
NATIONAL LABORATORY

Physics Models

- ***Ab Initio* Data Model**: Calculate cross sections and secondary spectra of electrons and holes at low energies .
- **Northwest Electron and Gamma Ray Interactions in Matter (NWEGRIM):** Electron-hole (e-h) pair production, intrinsic properties, maximum theoretical light yield, spatial distribution and energy distribution of e-h pairs.
- **Transport of Electron-Hole Pairs and Scintillation Efficiency:** thermalization of e-h pairs, scintillation process, scintillation efficiency and kinetics, light yields, intrinsic energy resolution and nonlinearity .

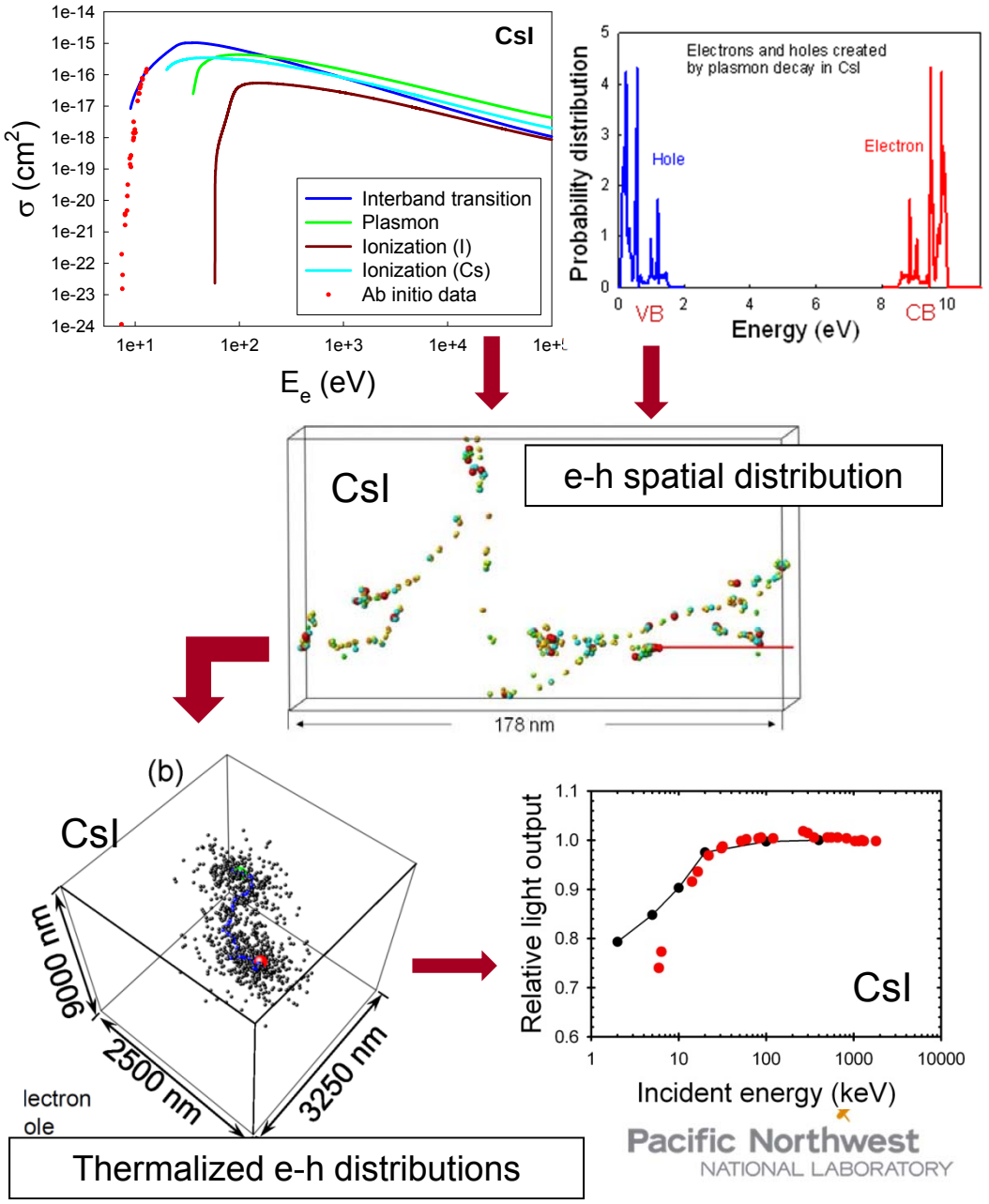

Spatial Distribution of e-h Pairs (example)

- Kinetic process of electron-hole pair creation in NaI (10 keV)

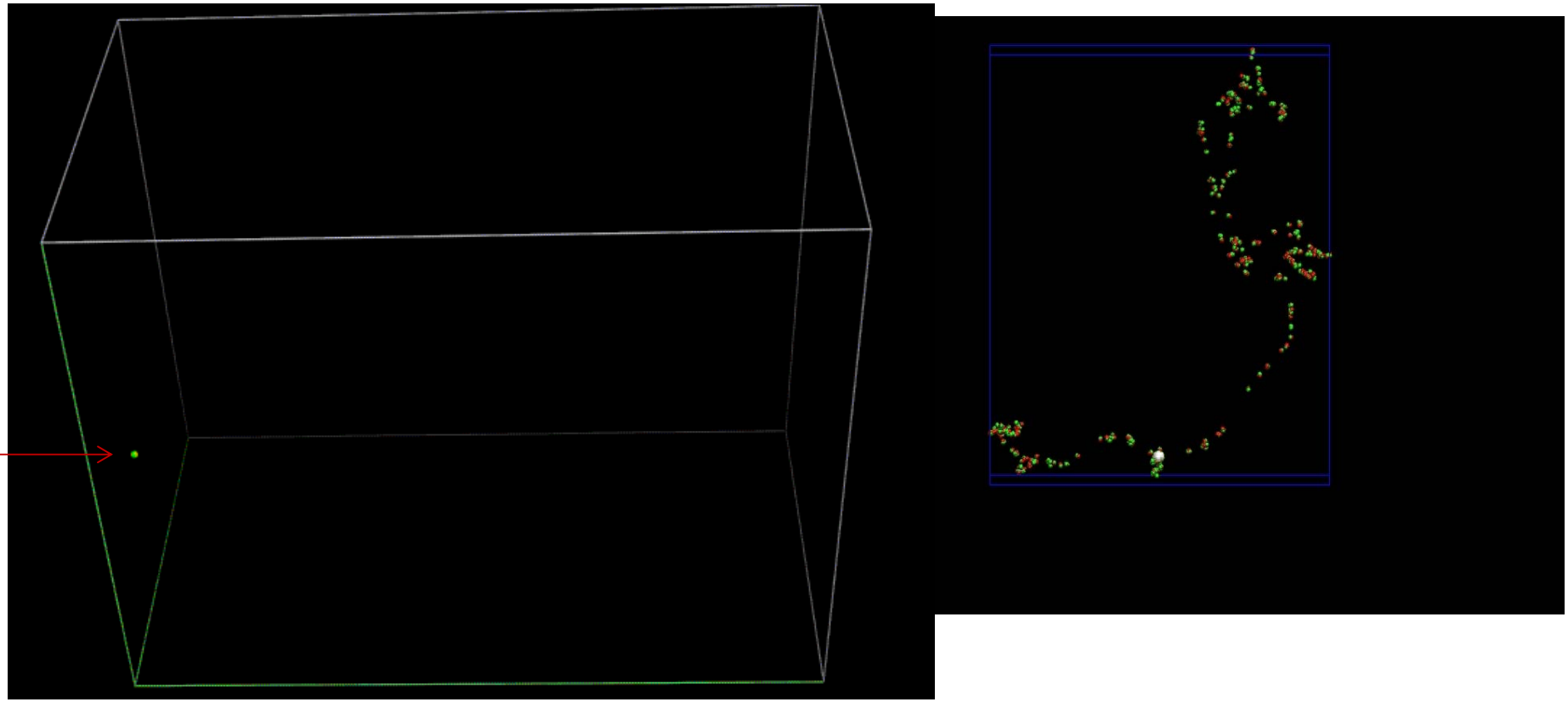

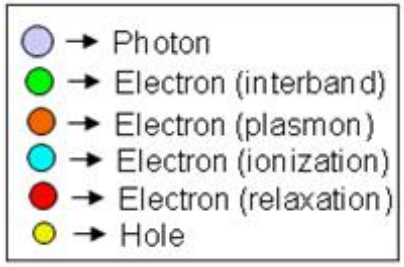

Pacific Northwest
NATIONAL LABORATORY

Spatial Distribution of e-h Pairs (example)

- Track radius, thermalization time and light yield (WFU – Richard Williams)

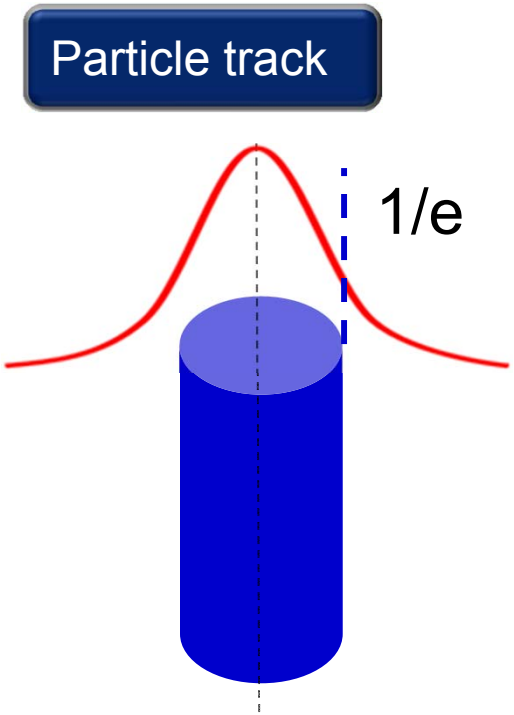

What is the track radius?

$$r_0^2 = \frac{dE/dx}{\pi\left(\frac{I_0\alpha}{h\nu}\right)\beta E_{gap}} = \frac{60\ eV/nm}{\pi\left(0.1\ eh/nm^3\right)(2.5)(5.5)\left(eV/eh\right)}$$

dE/dx = 60 eV/nm at 0.1 keV

r_0 = 3.7 nm in NaI near track end

- NWEGRIM simulations in NaI near track end

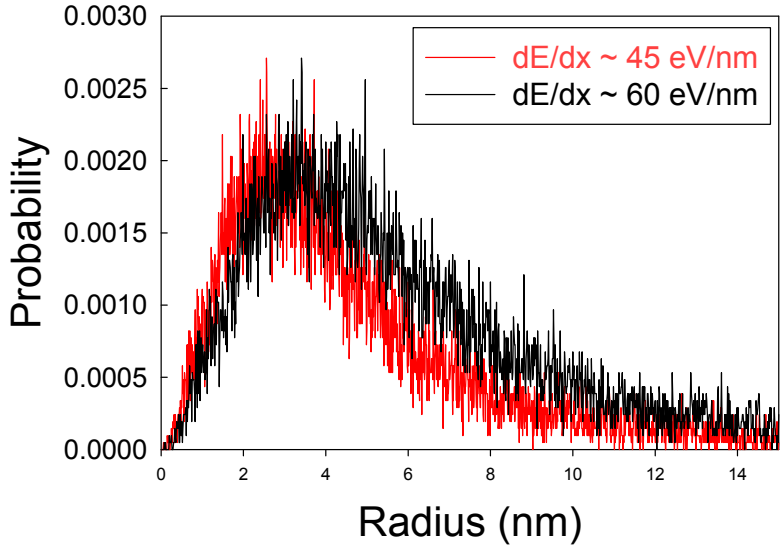

r_0 = 2.8 nm

Rescaled by 60 eV/nm

r_0 = 3.3 nm

Pacific Northwest NATIONAL LABORATORY

Electron Cascades in $LaBr_3$ and SrI_2

- NWEGRIM - SrI_2

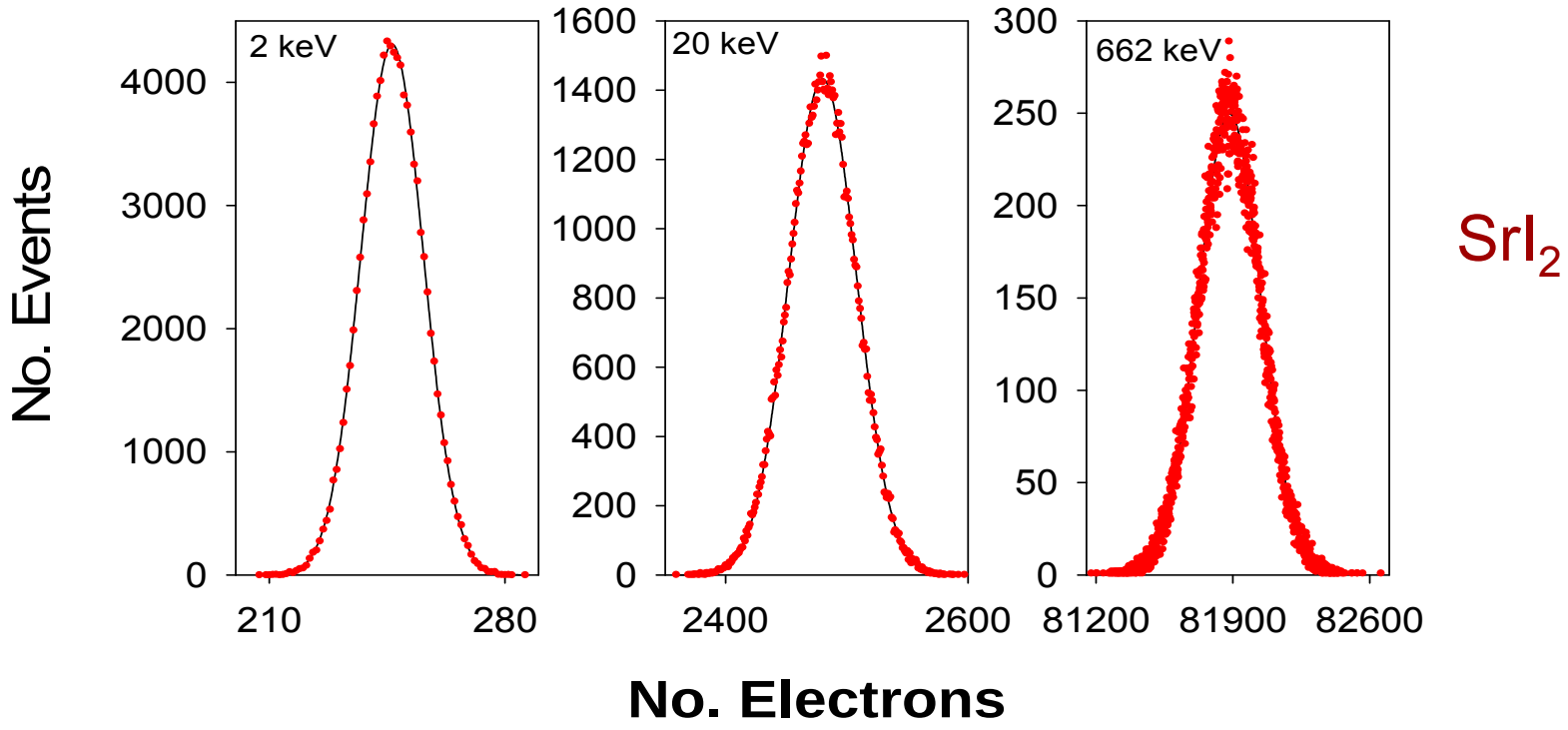

- Symmetric distribution
- Approximate Gaussian distribution
- Distribution is similar, but averaged number of e/h pairs is significantly different for different energies and materials

Pacific Northwest
NATIONAL LABORATORY

Electron Cascades in $LaBr_3$ and SrI_2

- *W* value – mean energy required to create an e/h pair and Fano factor

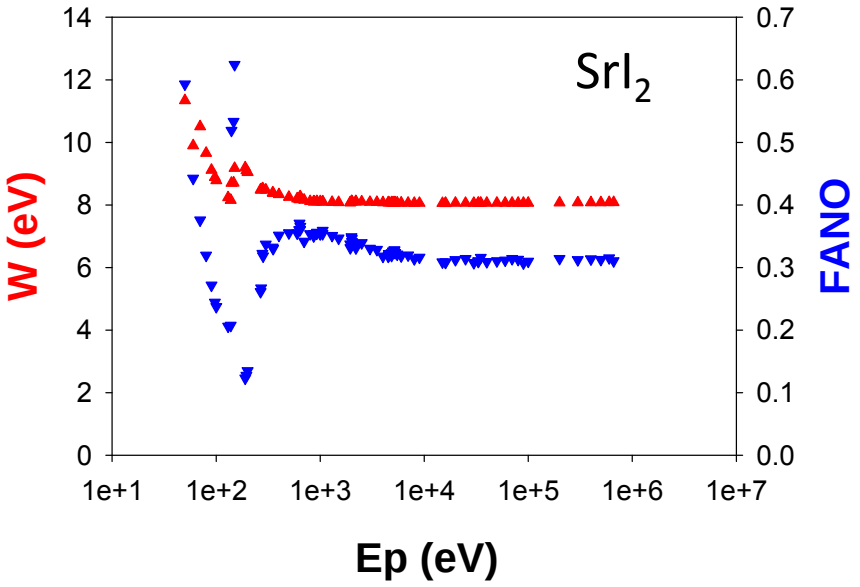

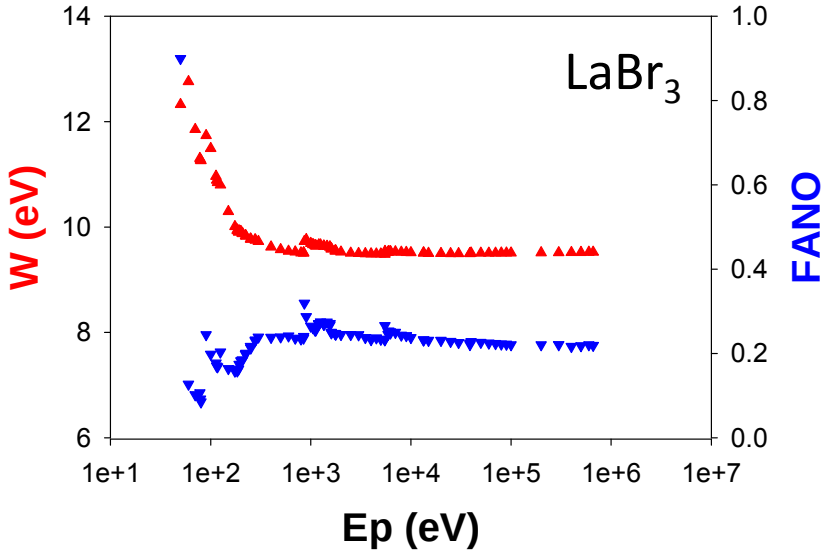

- *W* converges to ~ 8.1 eV (Exp: 15 eV) → ~ 123,457 ph/MeV
- Exp. light yields: 44,700 to 105,263 ph/MeV
- *F* decreases with E_p and approaches ~ 0.3

- *W* converges to ~9.5 eV (Exp: 12 – 25 eV) → ~ 105,263 ph/MeV
- Exp. light yields: 71, 000 to 90, 909 ph/MeV
- Fano factor ~ 0.22

Pacific Northwest
NATIONAL LABORATORY

Electron Cascade: Light Yields

- Estimating light yields

$$L_y = SQ / W$$

S – energy transfer efficiency

Q – luminescence quantum efficiency

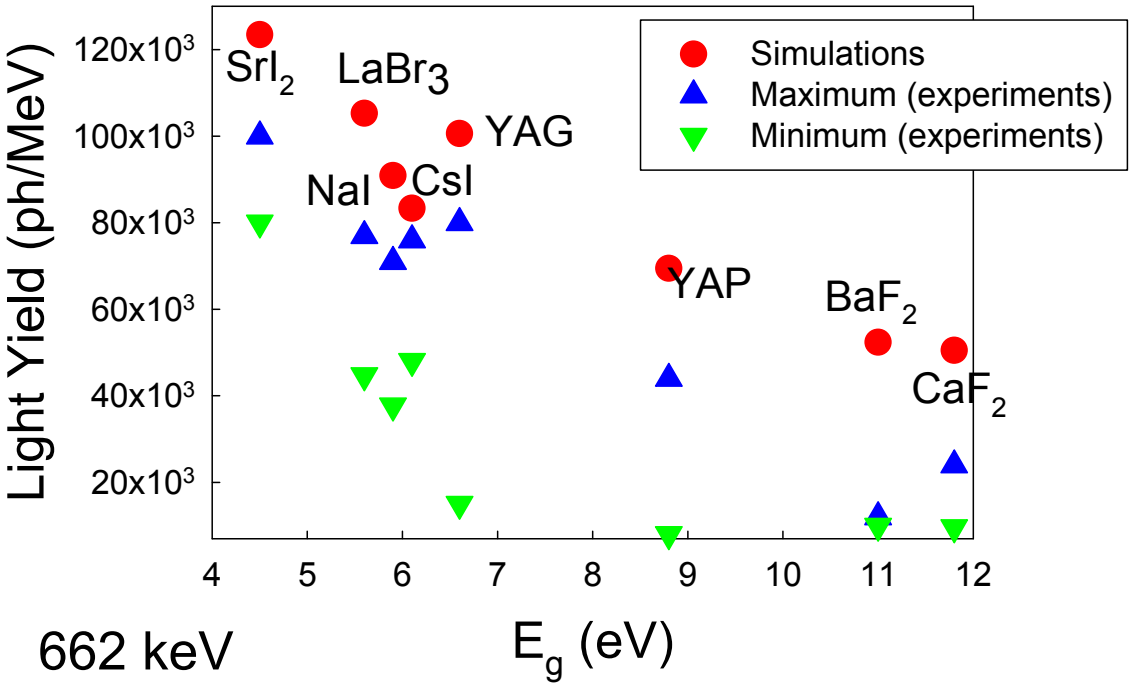

- Light yield decreases with increasing E_g and is comparable with experimental values, and larger than the maximum values obtained by experiments.
- These calculations allow the evaluation of the maximum theoretical light yield as a function of band gap energy.
- The results can be directly compared to experimental measurements, thus providing a possible pathway to validate the simulations.

Pacific Northwest
NATIONAL LABORATORY

Spatial Distribution of e-h Pairs

- Spatial distributions in SrI_2 and $LaBr_3$ (10 keV)

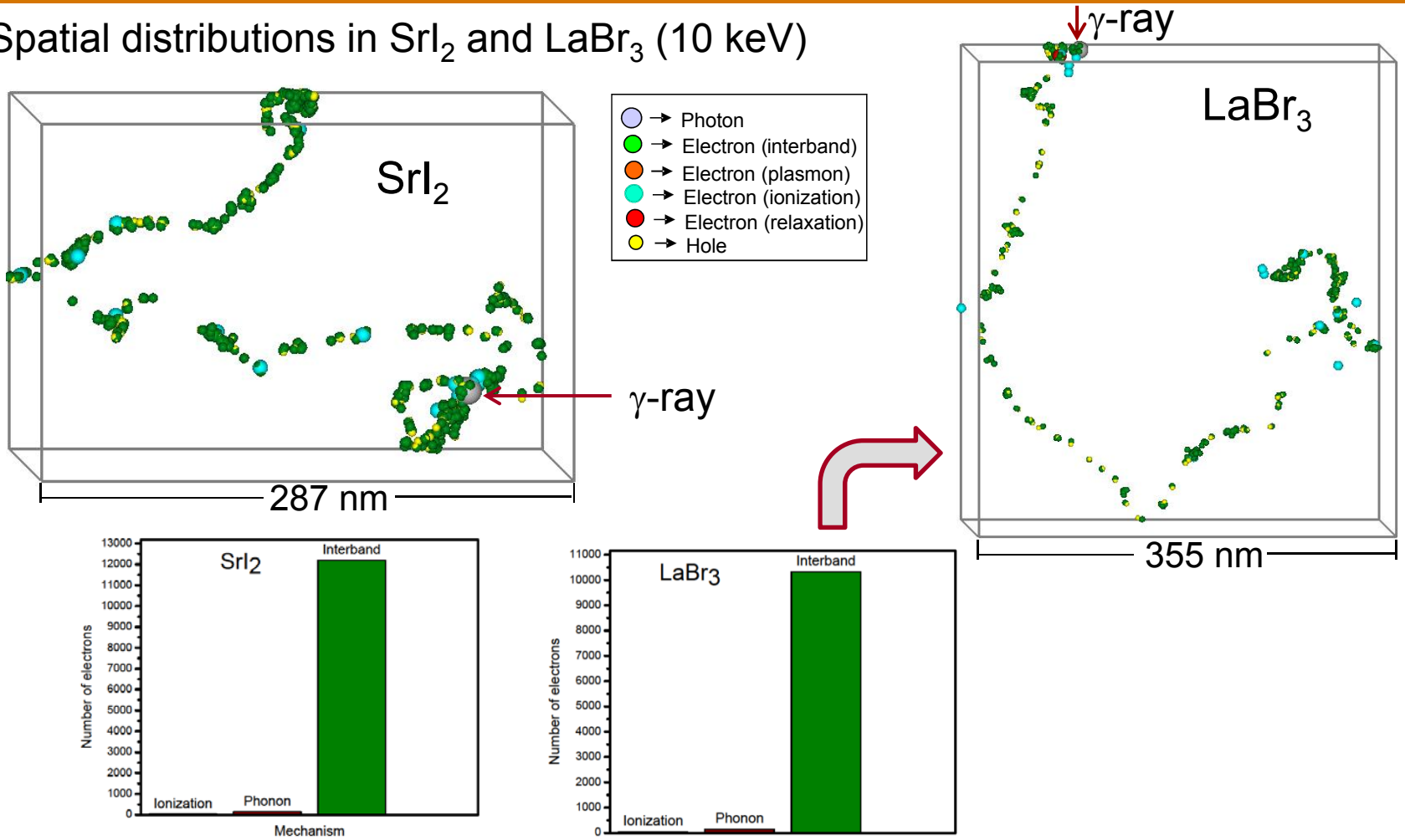

- Similar linear track structure – less quenching of excitons.
- Most e-h pairs are produced by interband transition.

Pacific Northwest
NATIONAL LABORATORY

Spatial Distribution of e-h Pairs

- Spatial distributions in CsI and $LaBr_3$ (10 keV)

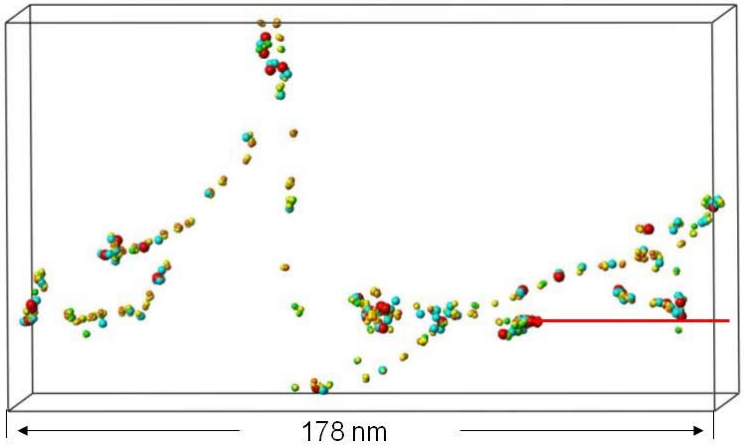

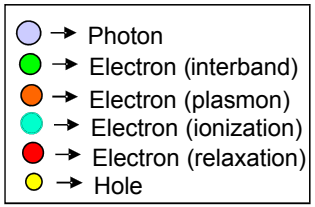

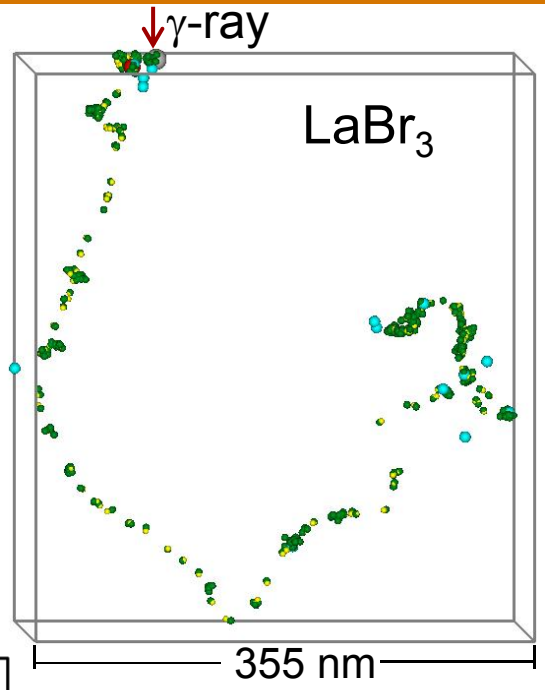

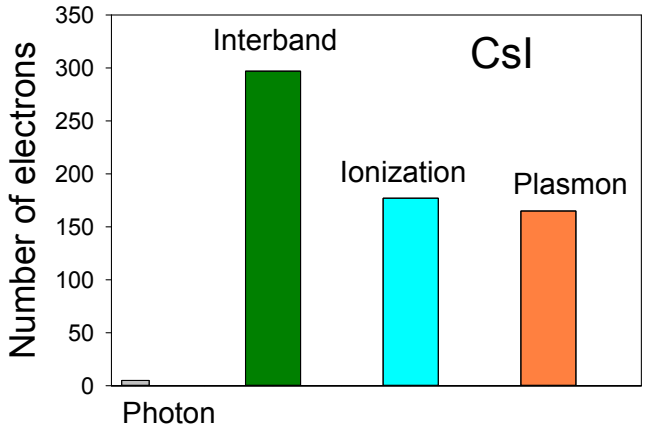

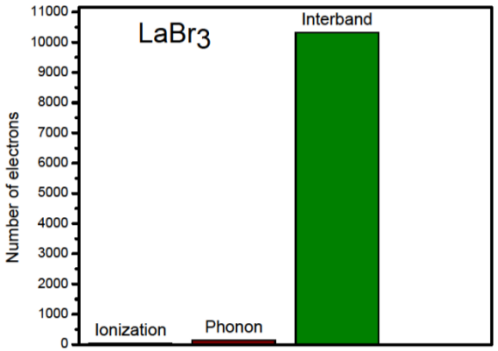

- Slight clustered track structure in CsI.
- Large fraction of e-h pairs is produced by ionization process in CsI, suggesting slightly larger Fano factor.

Pacific Northwest
NATIONAL LABORATORY

Compare to Experimental Results

- Comparison with experimental Fano factor

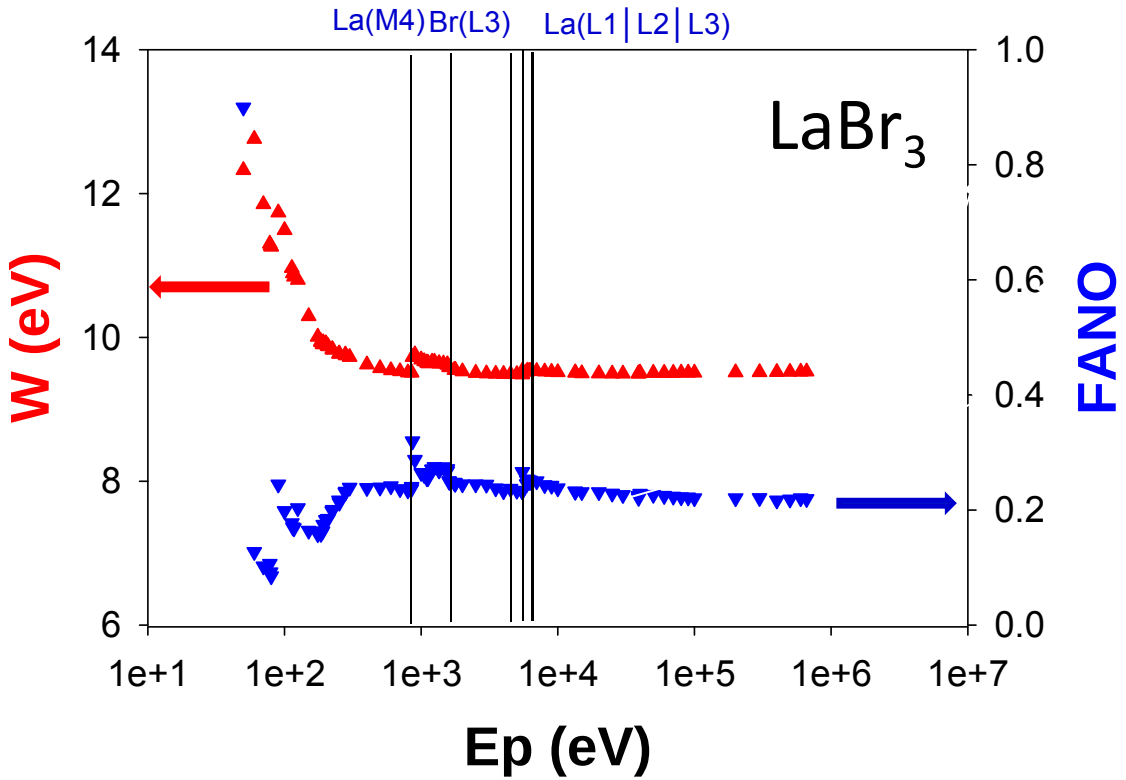

- Fano factor ~ 0.22
- Experimental value of Fano factor ~ 0.1 (A. Bousselham et al., 2009 IEEE Nuclear Science Symposium Conference Record, 2370)
- The optical Fano factor of $LaBr_3$ is very small, comparable to that of good semiconductor detectors

Pacific Northwest
NATIONAL LABORATORY

General Rules

Properties	CaF_2	BaF_2	CsI	NaI	$LaBr_3$	SrI_2
W value (eV)	21.4	19.1	12.0	10.9	9.5	8.1
Max light yield (ph/MeV)	50,505	52,356	83,333	91,743	105,263	123,457
Main channels to generate e-h pairs	Interband (66.4%) Plasmon (31.6%) Ionization (2.0%)	Interband (68.0%) Plasmon (29.3%) Ionization (2.7%)	Interband (76.9%) Plasmon (18.2%) Ionization (4.9%)	Interband (68.9%) Plasmon (29.1%) Ionization (2.0%)	Interband (98.2%) Plasmon (0.0%) Ionization (1.8%)	Interband (98.5%) Plasmon (0.0%) Ionization (1.5%)
Track structure	Clustered	Clustered	Slight clustered	slight clustered	Linear	Linear
Constant light yield for E_p> (keV)	0.8	0.9	10.0	2.0	2.0	0.2
Fano factor	0.24	0.19	0.27	0.31	0.22	0.21

- Small *W* value that increases maximum theoretical light yield.
- Small number of energy loss channels (ideally, only interband transition).
- Linear track structure that decreases the nonlinear behavior at low incident energies.

Pacific Northwest
NATIONAL LABORATORY

Kinetics and Efficiency of Scintillation

❑ *Thermalization of e-h pairs*

A Monte Carlo model of electron thermalization in inorganic scintillators was developed and implemented:

- Uses as input spatial and kinetic energy distributions of e-h pairs from NWEGRIM
- Includes electron scattering with both longitudinal optical and acoustic phonons
- Scattering rates and angles calculated using phenomenological models
- Includes the effects of internal electric fields
- Includes the effects of activator concentration
- Applied to alkali iodide (CsI, NaI) and alkaline-earth fluoride (CaF_2, BaF_2) scintillators

Pacific Northwest
NATIONAL LABORATORY

Kinetics and Efficiency of Scintillation

- Spatial distribution of thermalized electrons + self-trapped holes

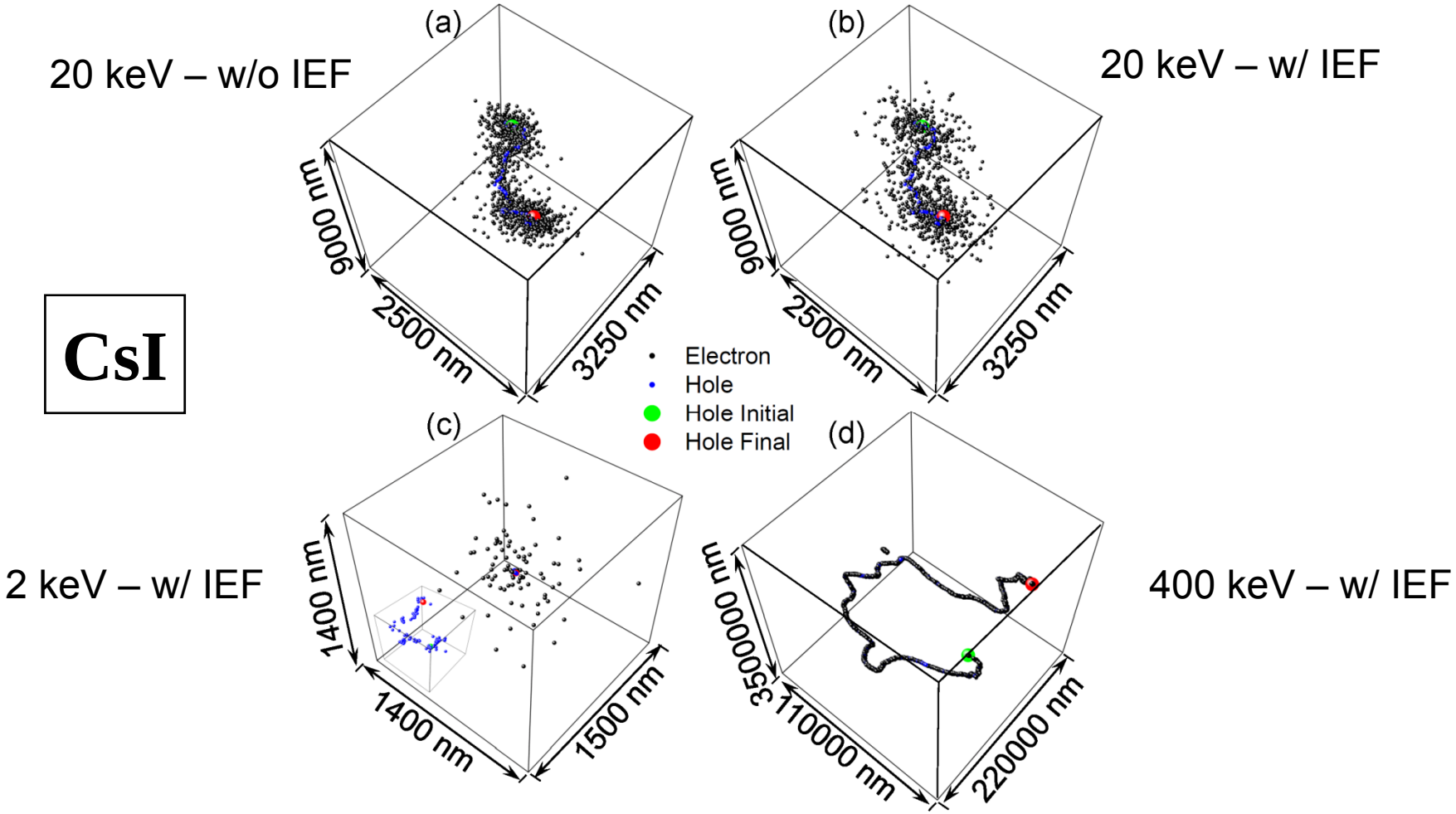

- Electron-hole pair distributions are complex.
- e/h-pair spatial distributions are not homogenous → **effect on nonlinear processes**.

Kinetics and Efficiency of Scintillation

- Spatial distribution of thermalized electrons + self-trapped holes

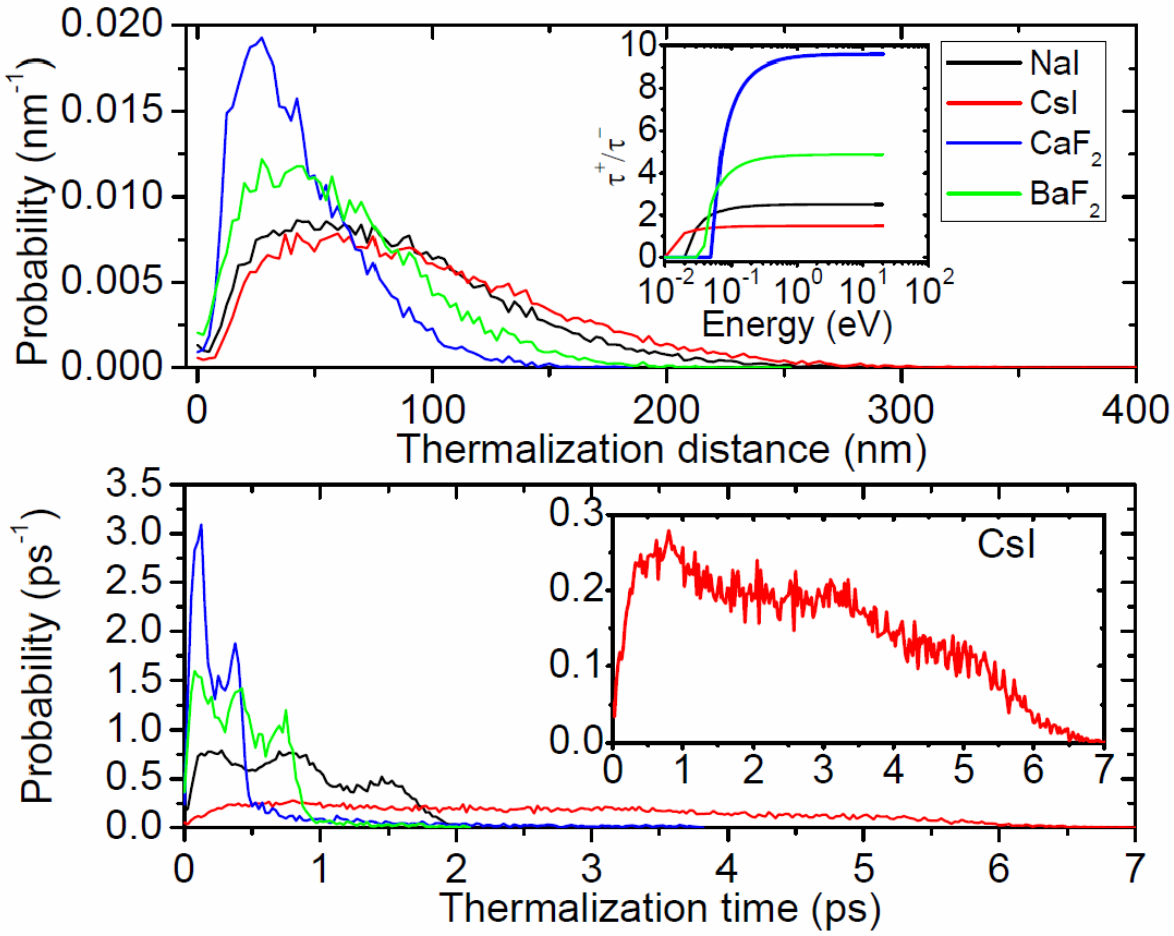

- e-h pair recombination is fast (fraction of ps) on the timescale of thermalization (few ps) → **difficult to probe experimentally**.
- Electrons that escape electric field of self-trapped holes can travel far from the track → **affects extent of trapping**.
- Increased proportion of separated electron-hole pairs at high incident energies → **incident energy dependence.**
- LO phonon energy is a key factor affecting the electron thermalization distances and times.

Pacific Northwest
NATIONAL LABORATORY

Kinetics and Efficiency of Scintillation

- KMC simulations of z-scan experiments (Richard Williams, WFU) test STE interactions

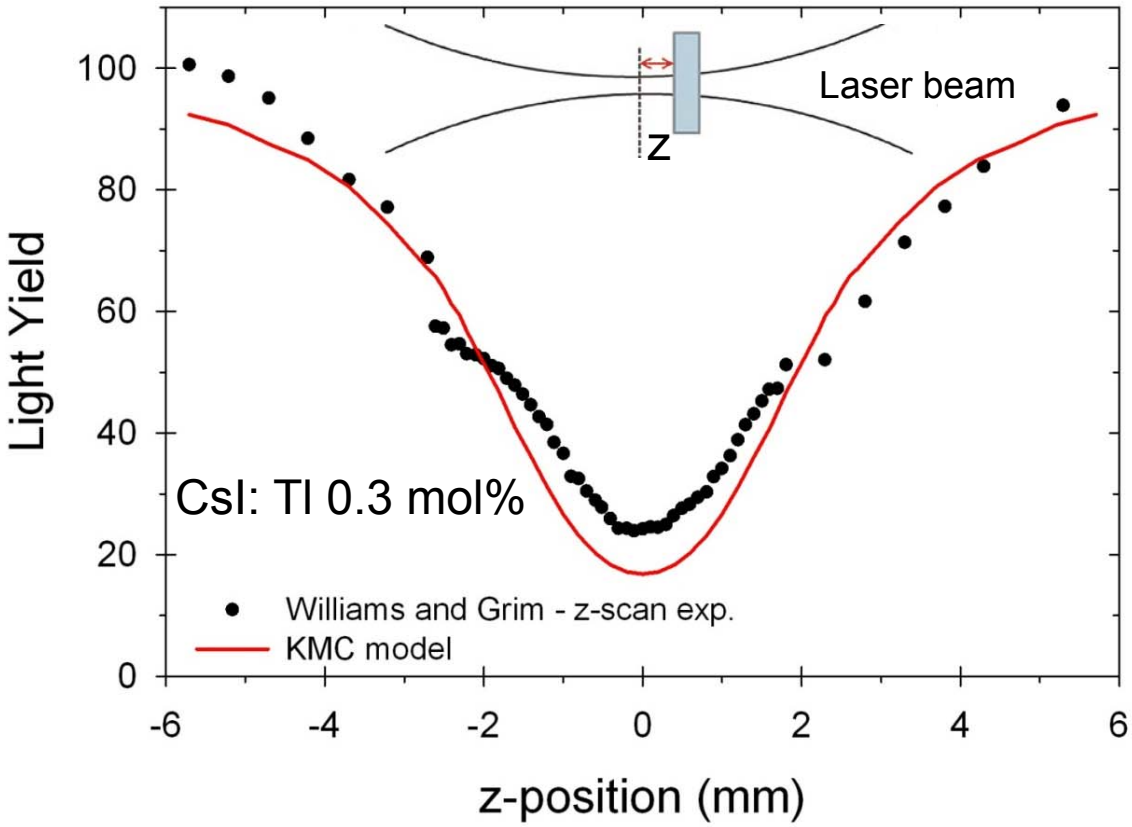

- Can be used to validate STE-STE interactions
- Use new STE-STE interaction parameters with NWEGRIM spatial distributions

Pacific Northwest
NATIONAL LABORATORY

Kinetics and Efficiency of Scintillation

Nonlinear quenching

Density-dependent light yield experiments were simulated in collaboration with Prof. Williams (WFU) to improve parameterization of interactions between self-trapped excitons.

Second-order nonlinear quenching via dipole-dipole Förster interactions:

$$k(r) = A\left(\frac{R_{dd}}{r}\right)^6$$

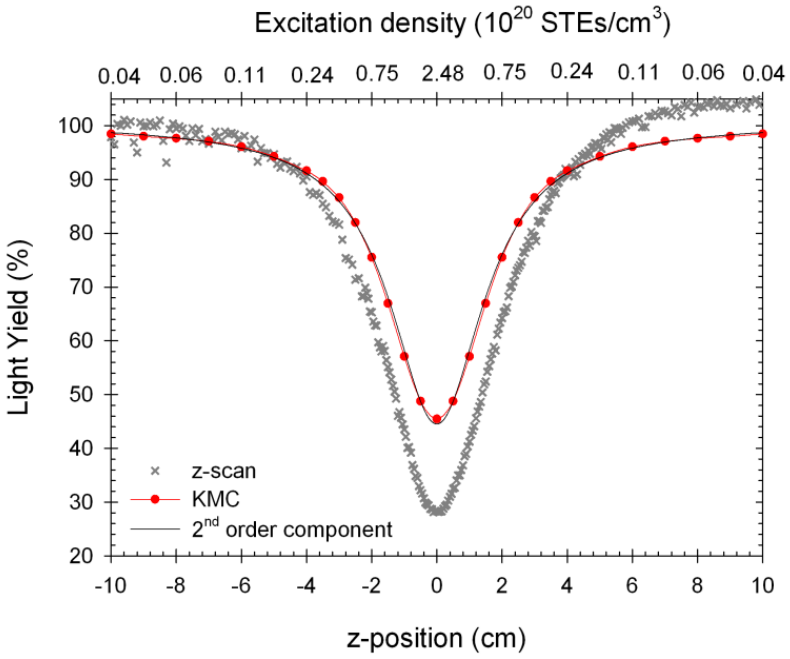

CsI:0.3 mol% Tl – 5.9 eV excitation

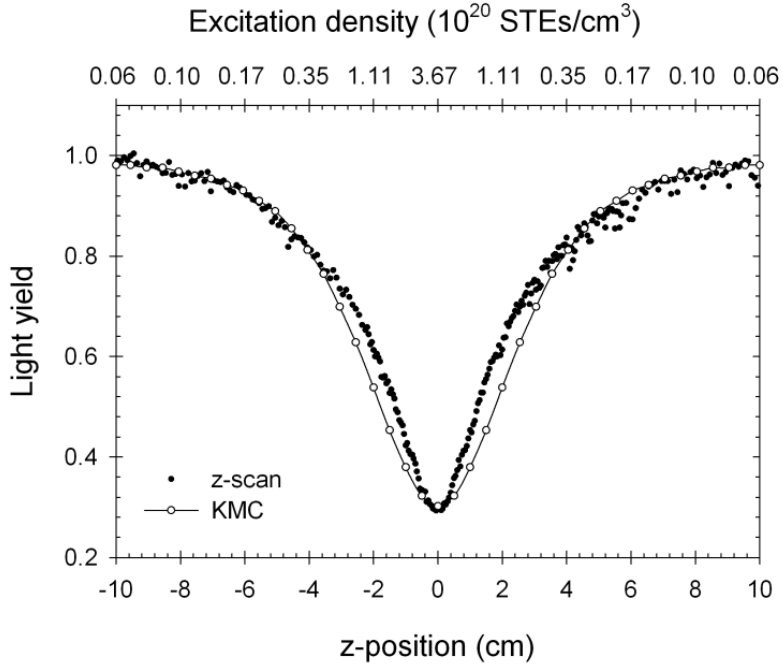

NaI:0.1 mol% Tl – 5.9 eV excitation

Good agreement is obtained with experimental data on second-order nonlinear quenching within the framework of the existing KMC models.

Pacific Northwest
NATIONAL LABORATORY

Kinetics and Efficiency of Scintillation

- Timescale for nonlinear quenching

Simulations allow for determining time evolution of species populations (STE,STH, Tl^0, $(Tl^+)^*$,…).

STE population initially decreases due to STE emission, Förster transfer, and thermal dissociation (which leads to the formation of STHs and Tl^0 sites).

All STEs disappear within 2-3 ns.

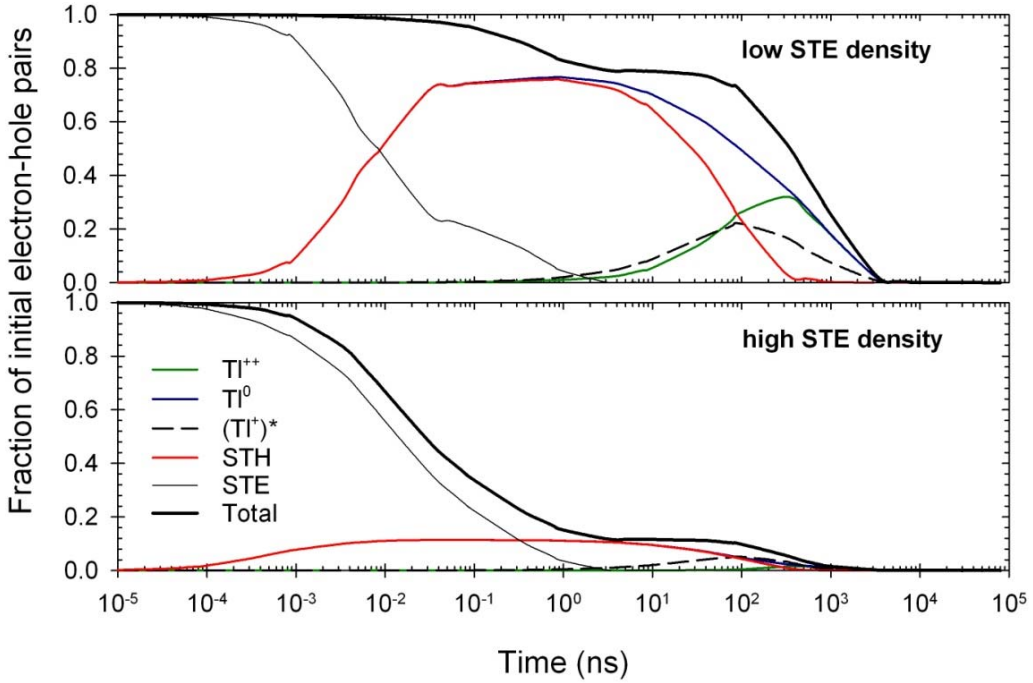

Publications

"Kinetic Monte Carlo model of scintillation mechanisms in CsI and CsI(Tl)"
S. Kerisit, K.M. Rosso, B.D. Cannon *IEEE Trans. Nucl. Sci.* (2008) 55, 1251-1258.

"Kinetic Monte Carlo simulations of excitation density dependent scintillation in CsI and CsI(Tl)"
Z. Wang, R.T. Williams, J.Q. Grim, F. Gao, S. Kerisit *Phys. Status Solidi B* (2013) 250, 1532-1540.

"Kinetic Monte Carlo simulations of scintillation processes in NaI(Tl)"
S. Kerisit, Z. Wang, R.T. Williams, J.Q. Grim, F. Gao *IEEE Trans. Nucl. Sci.* (2013) **in review**.

Pacific Northwest
NATIONAL LABORATORY

Summary

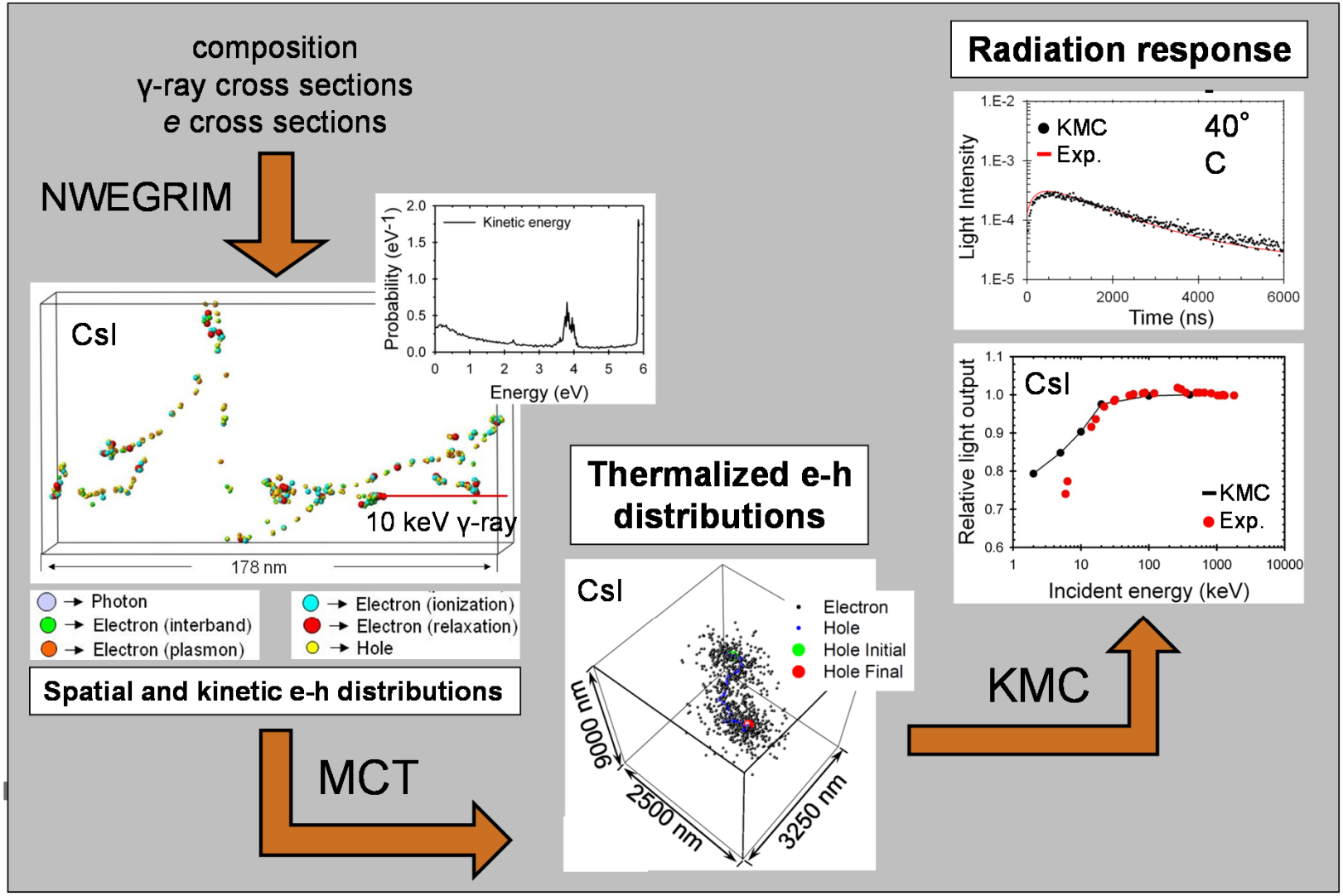

- It is now possible to quickly simulate complete series of scintillator materials, such as the alkali halide and alkaline-earth halide classes, helping candidate search for new scintillator materials.

Pacific Northwest
NATIONAL LABORATORY

Microscopic Mechanisms of Electron-Hole Generation and Their Spatial Distribution Scintillators

F. Gao, Y. Xie, D. X. Wu, S. Kerisit, M. P. Prange,
L. W. Campbell, R. M. Van Ginhoven

Acknowledgements
Babak Sadigh, Daniel Aberg and Stephen Payne (LLNL), Richard Williams and Joel Grim (WFU)

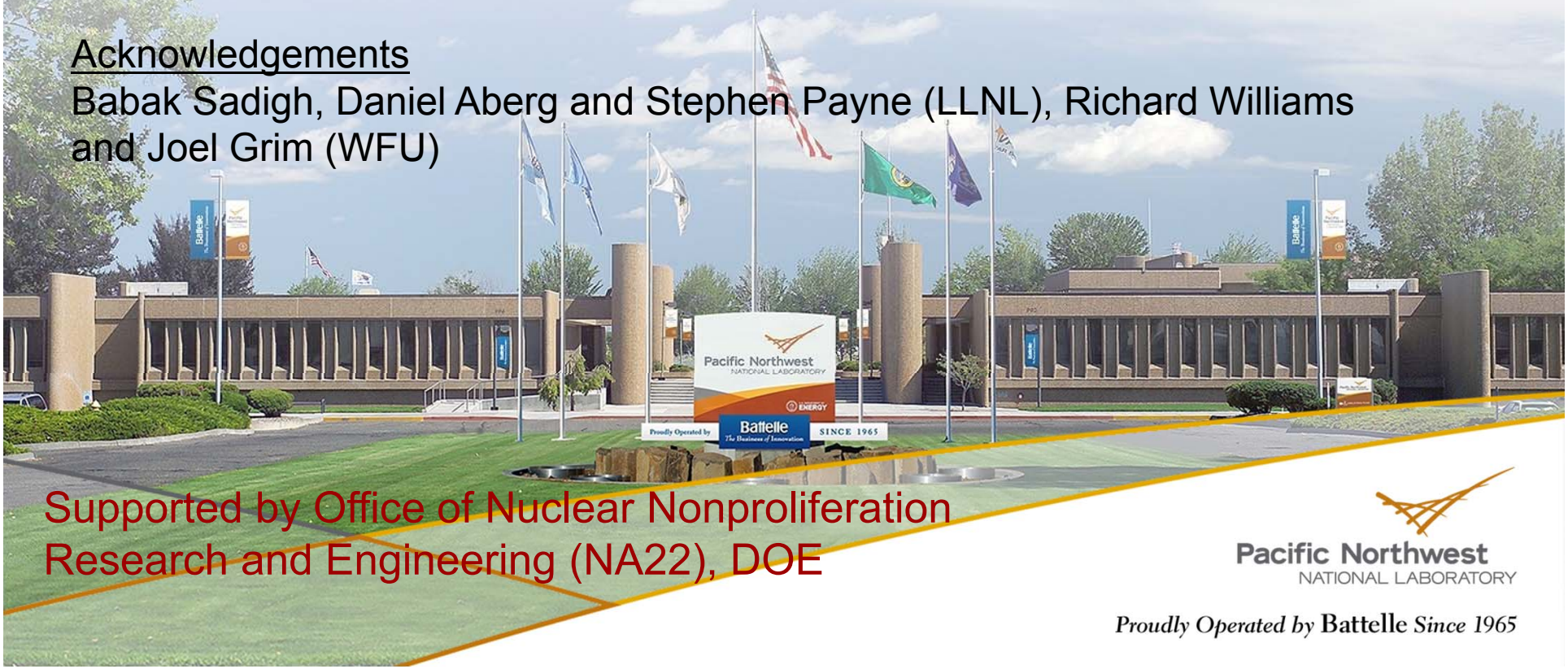

Supported by Office of Nuclear Nonproliferation Research and Engineering (NA22), DOE

Pacific Northwest
NATIONAL LABORATORY

Proudly Operated by Battelle *Since 1965*

Outline

- Physics models
  - Ab initio data model – Cross sections at low energies and plasmon decay spectrum
  - Northwest Electron and Gamma Ray Interactions in Matter Code (NWEGRIM) - Electron cascade, electron-hole pair generation, spatial distribution, intrinsic resolution, stopping power et al.
  - Kinetic Monte Carlo - thermalization of e-h pairs, transport of e-h pairs, interaction of excitons with dopants, nonlinearity
- Intrinsic properties
  - Electron cascades, variance, *W* value, maximum light yield – CsI, NaI, $LaBr_3$, BaF_2, CaF_2, SrI_2 , YAP, YAG
  - Stopping power and its fluctuation, spatial distributions of e-h
- Further consideration
  - Validating the simulations
  - General rules to guide the design of new scintillator materials

Pacific Northwest
NATIONAL LABORATORY

Physics Models

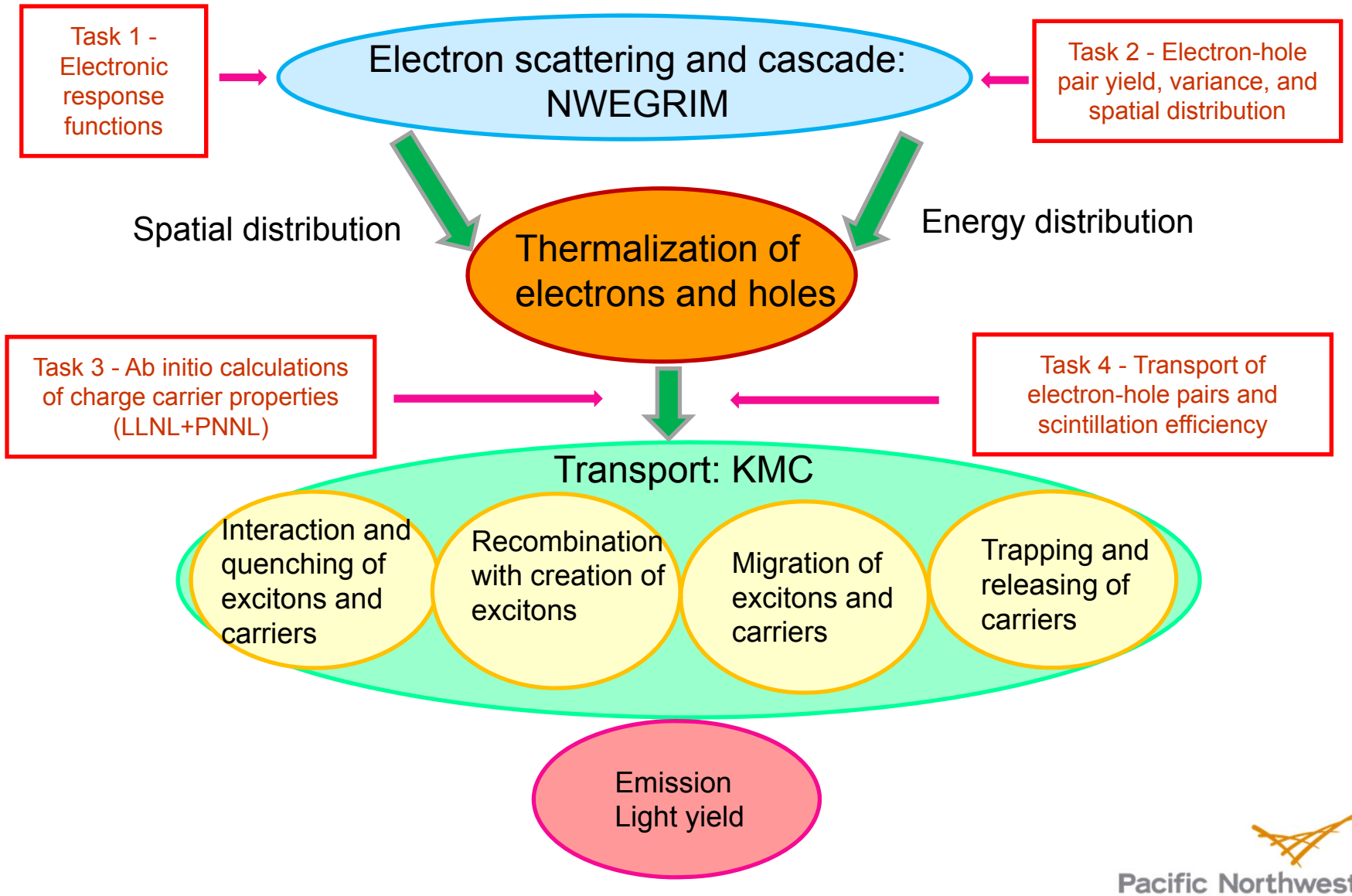

Pacific Northwest
NATIONAL LABORATORY

Ab Initio Data Model

- **Electronic Response Functions**

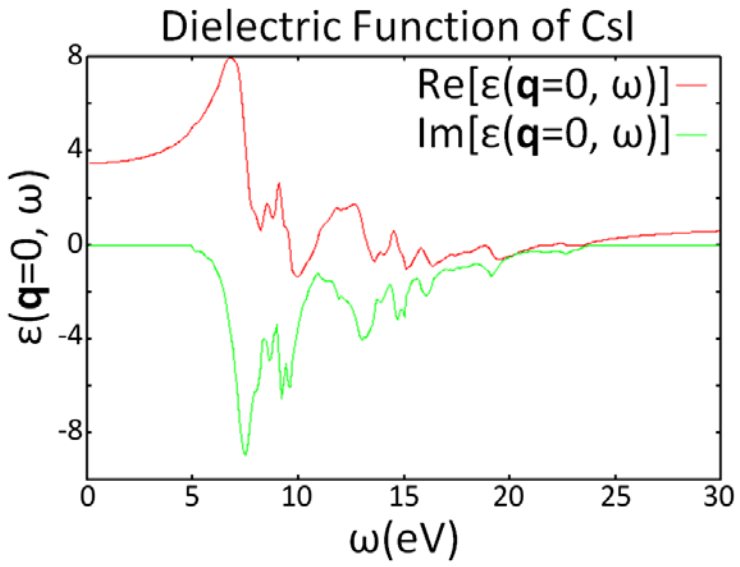

Calculated Properties (CsI, NaI, $LaBr_3$, SrI_2, BaF_2 and CaF_2)

- Screening
- Quasiparticle Energies
- Rate of electronic excitations by radiation electrons
- Plasmon decay spectrum

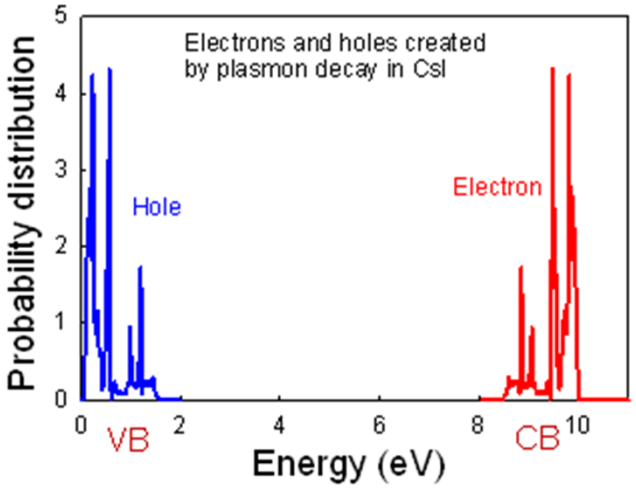

- Plasmon decay spectrum

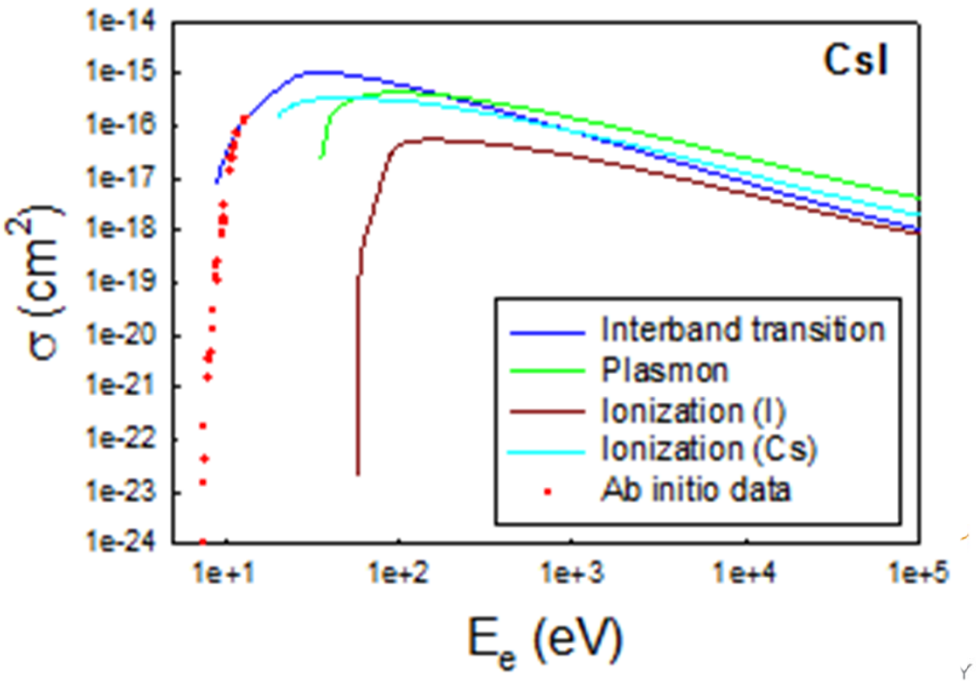

Ab Initio Data Model

- **Examples**

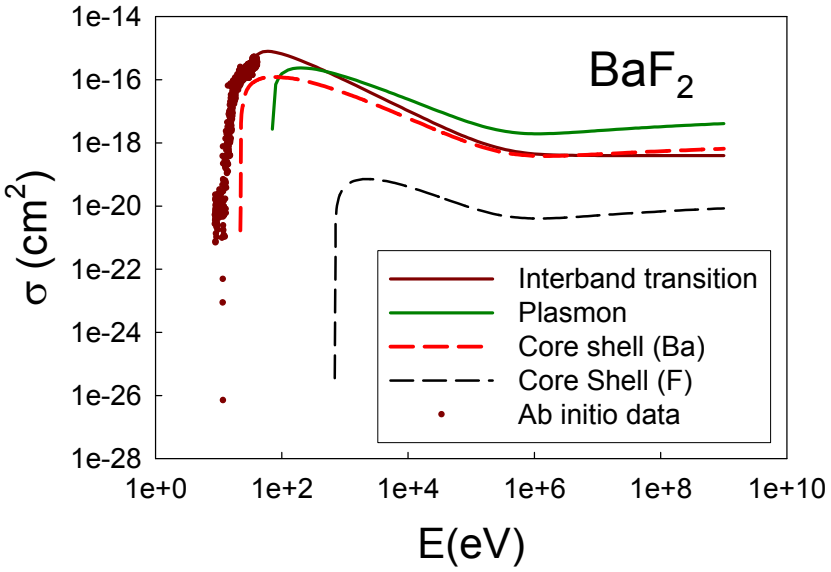

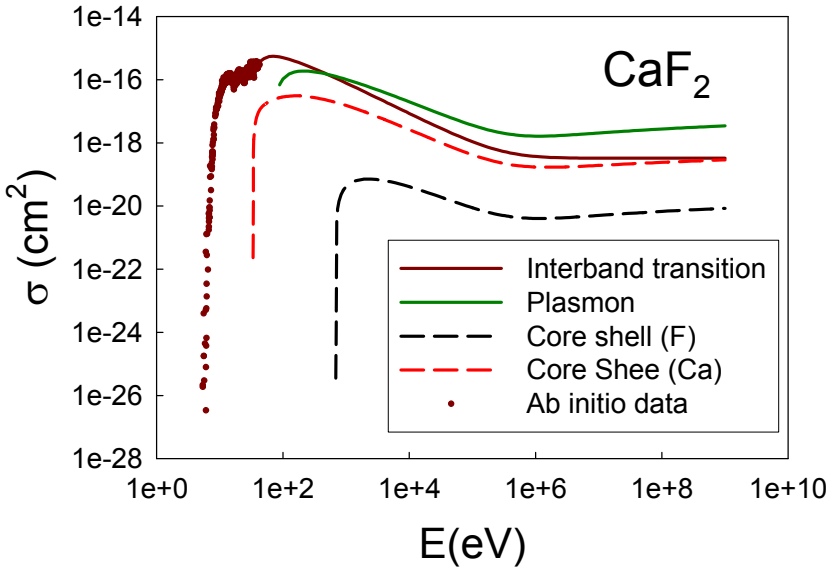

- Electrons created by plasmon decay

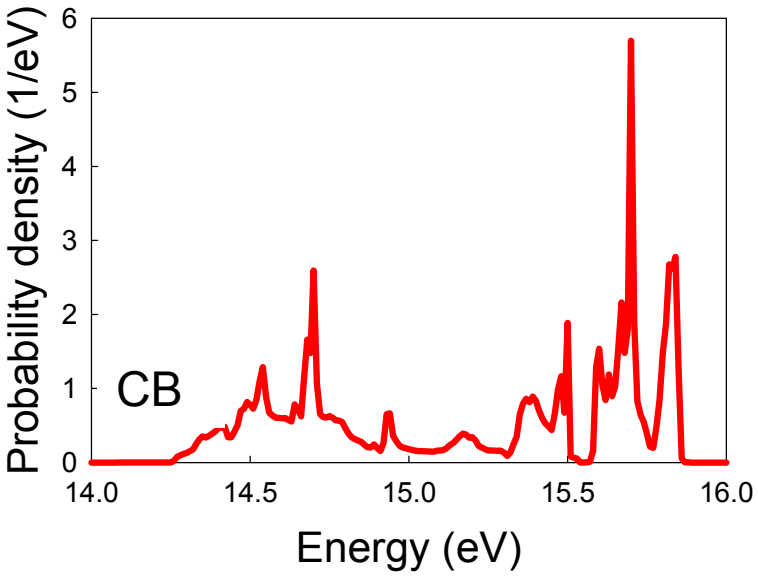

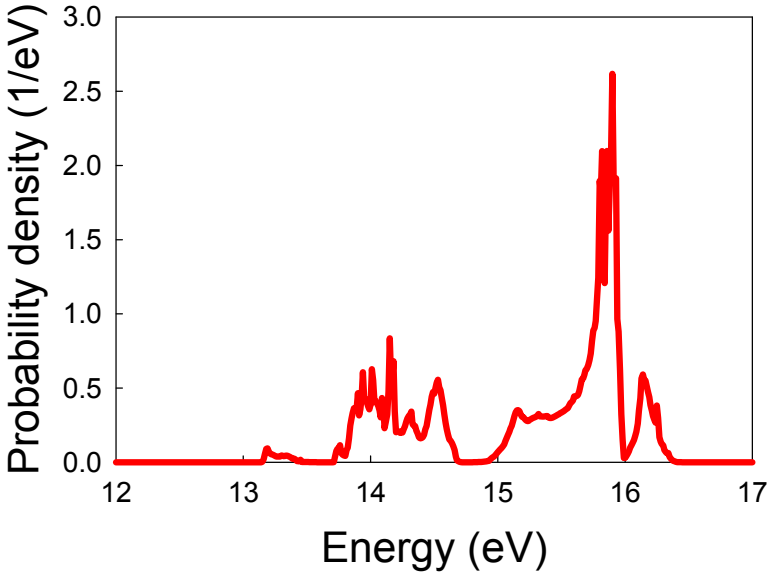

Physics Models

- **Northwest Electron and Gamma Ray Interactions in Matter (NWEGRIM):** Electron-hole (e-h) pair production, intrinsic properties, maximum theoretical light yield, spatial distribution and energy distribution of e-h pairs.
- **Transport of Electron-Hole Pairs and Scintillation Efficiency:** thermalization of e-h pairs, scintillation process, scintillation efficiency and kinetics, light yields, intrinsic energy resolution and nonlinearity .

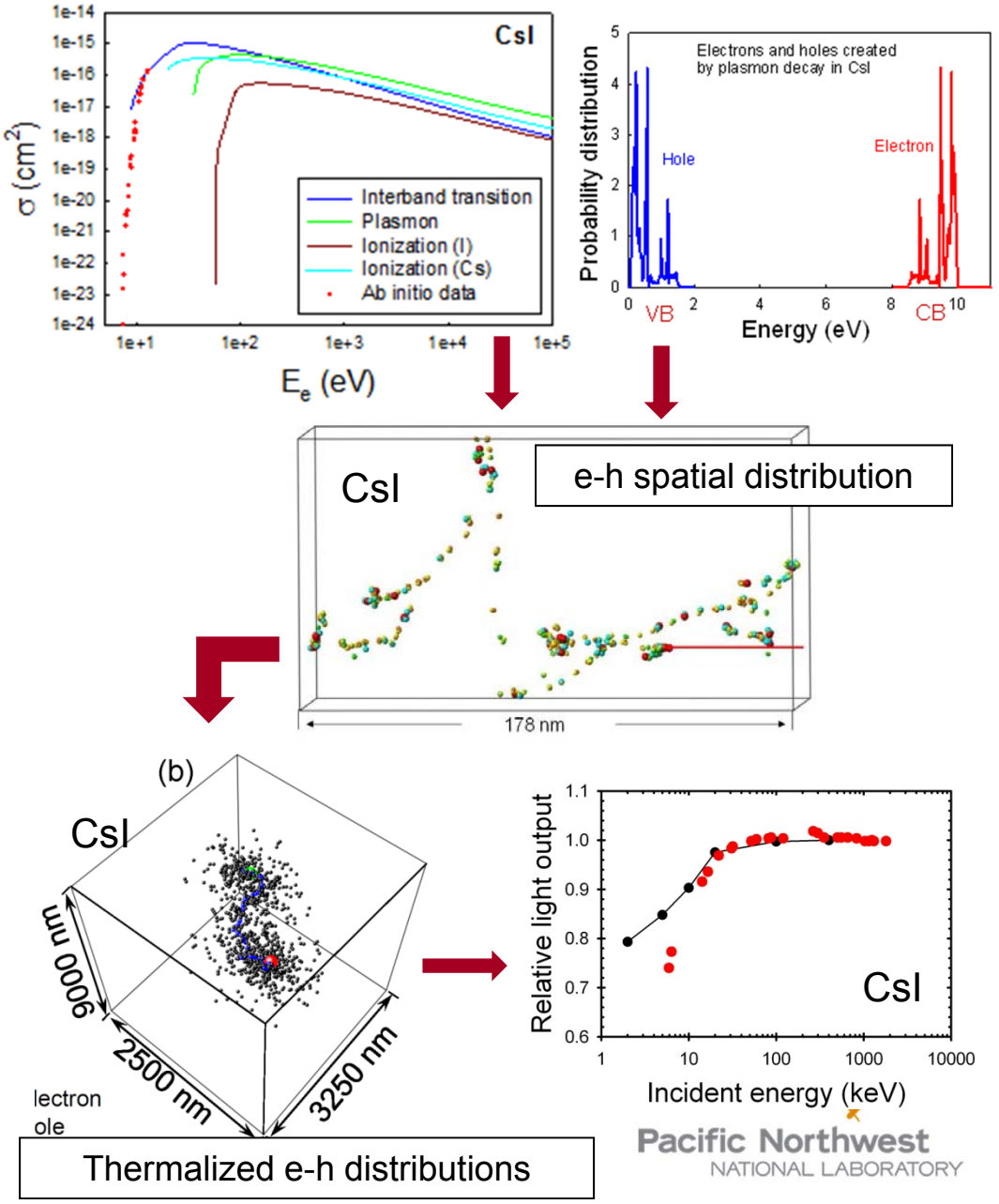

NWEGRIM: Features

- **Low cutoff energy**
  - Other transport codes have a cutoff energy well above the energy of valence electron excitations. Therefore, most ionization events are handled only in an average way, i.e. as a continuous reduction of energy of the ionizing particle
- **Can predict average energy per charge carrier**
  - Other transport codes obtain the final number of charge carriers only through absorbed energy estimates and rely on separate estimate of average energy per charge carrier.
- **Can simulate microscopic spatial distributions and energy distributions of e-h paires**
  - Other transport codes calculate electron-hole (e-h) pair density (or number of e-h pairs)

$$\rho = \frac{1}{W}\frac{dE}{dx}$$

Need to know *W* value from other theories or experiments

- **Can calculate intrinsic properties directly**
  - Fano factor and intrinsic energy resolution - directly related to semiconductors
- **Can calculate stopping power and its fluctuations**
- **Can determine dominant energy loss mechanisms in different detector materials**

Pacific Northwest
NATIONAL LABORATORY

Electron Cascades in $LaBr_3$ and SrI_2

- NWEGRIM - SrI_2

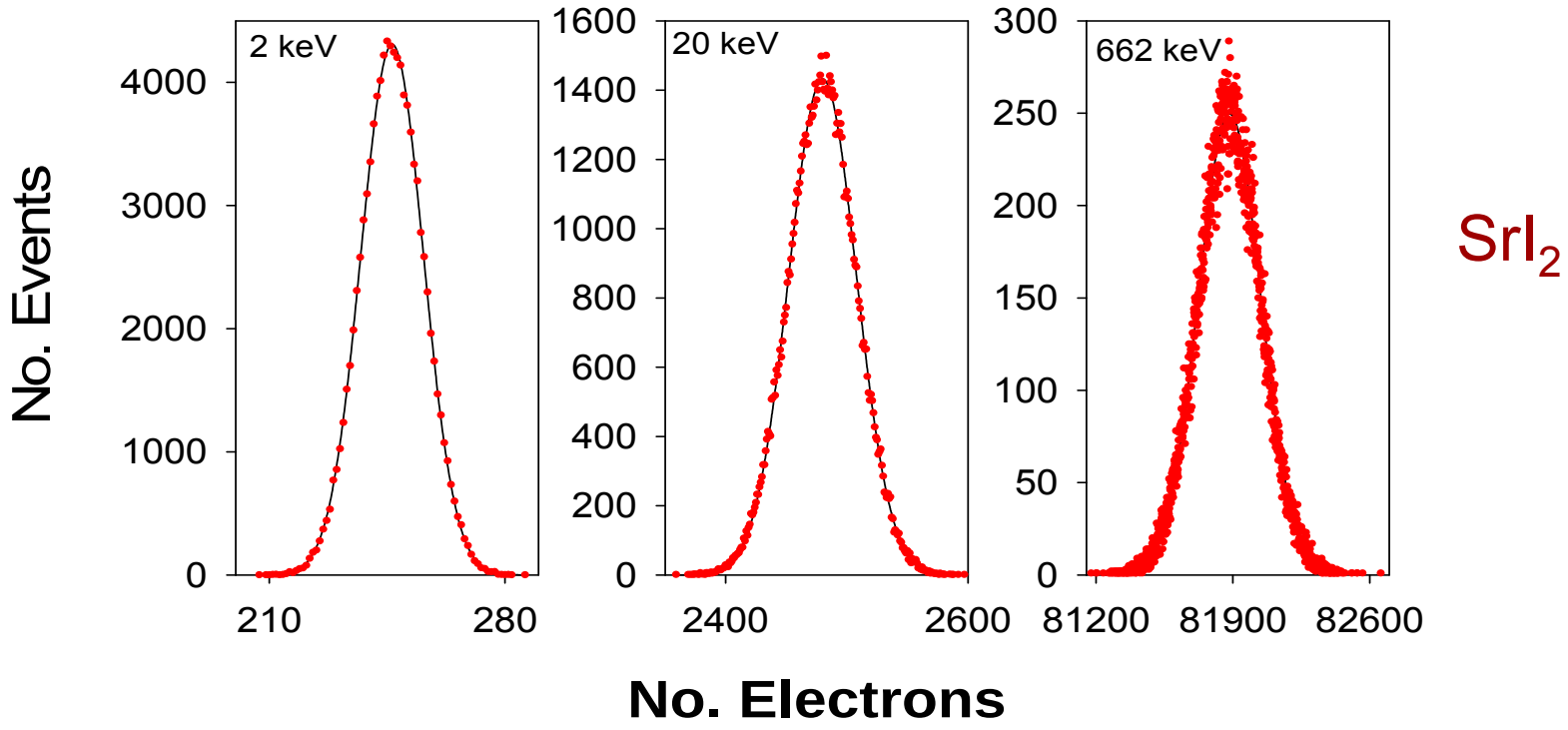

- Symmetric distribution
- Approximate Gaussian distribution
- Distribution is similar, but averaged number of e/h pairs is significantly different for different energies and materials

Pacific Northwest
NATIONAL LABORATORY

Electron Cascades in $LaBr_3$ and SrI_2

- *W* value – mean energy required to create an e/h pair and Fano factor

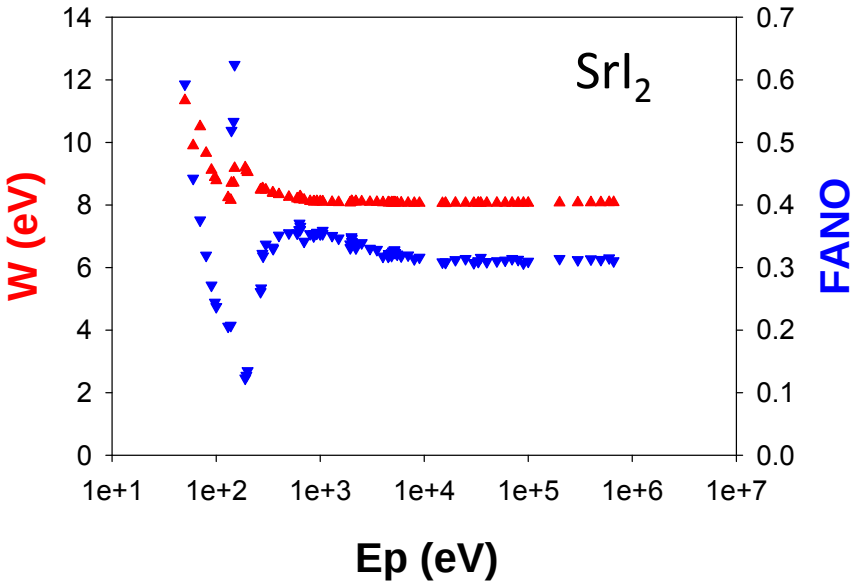

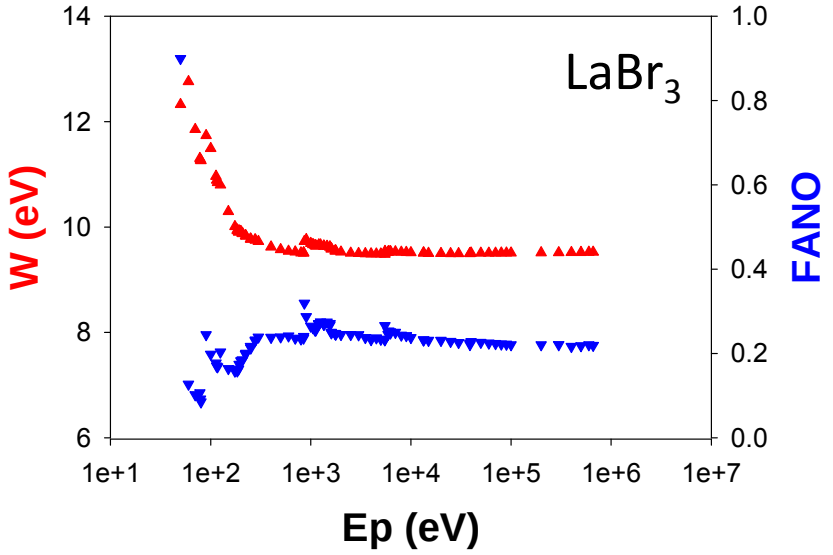

- *W* converges to ~ 8.1 eV (Exp: 15 eV) → ~ 123,457 ph/MeV
- Exp. light yields: 44,700 to 105,263 ph/MeV
- *F* decreases with E_p and approaches ~ 0.3

- *W* converges to ~9.5 eV (Exp: 12 – 25 eV) → ~ 105,263 ph/MeV
- Exp. light yields: 71, 000 to 90, 909 ph/MeV
- Fano factor ~ 0.22

Pacific Northwest
NATIONAL LABORATORY

Stopping Power and Fluctuation

- Most previous simulations of e-h pairs – only consider track structure of secondary electrons created by photons to evaluate dE/dx [NIMA 563 (2006) 116]

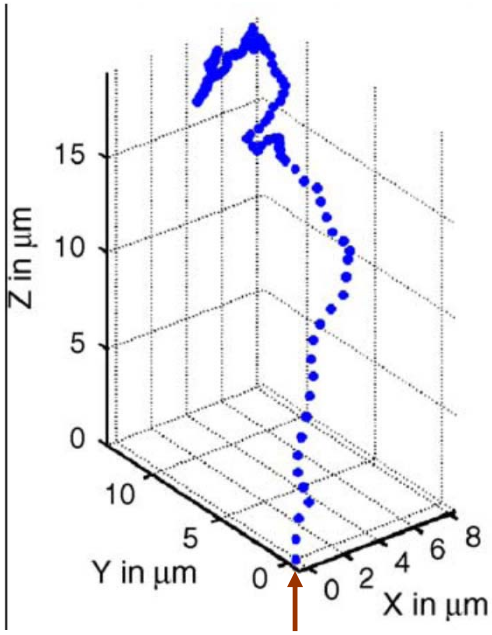

Total deposited energy: 100 keV electron in CdZnTe – linear electron cascade

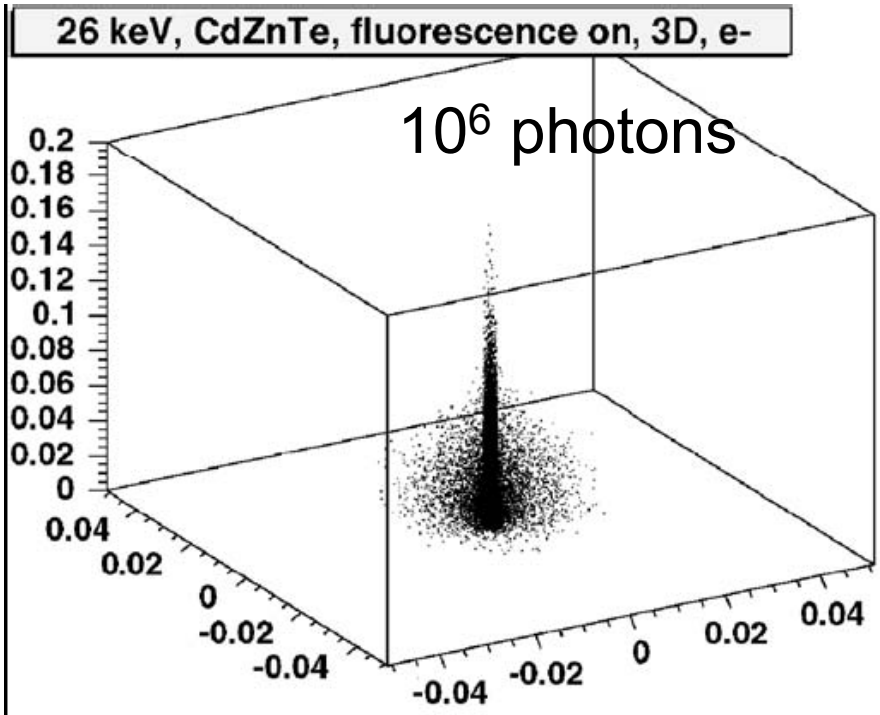

- e-h pair density (or number of e-h pairs) - $\rho = \frac{1}{W}\frac{dE}{dx}$

  W – mean energy required to create an electron-hole pair

Pacific Northwest
NATIONAL LABORATORY

Stopping Power and Fluctuation

- Stopping power (*dE/dx*) and its fluctuation
  - Providing important inputs for the rate-theory-based model of scintillation processes or phenomenological Model

- Thin film – allow electron to collide one and two times

Monte Carlo: $\left(\frac{dE}{dx}\right)_{total} = \left(\frac{dE}{dx}\right)_{Ioniztion} + \left(\frac{dE}{dx}\right)_{E-H} + \left(\frac{dE}{dx}\right)_{Plasmon}$

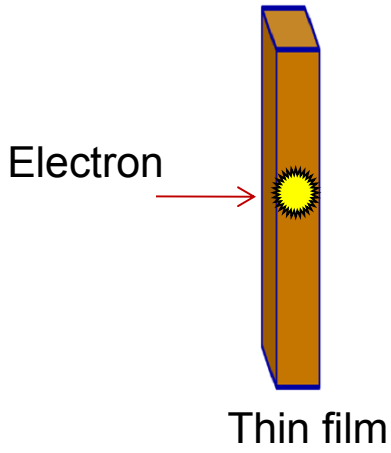

Bethe-Bloch model:

$$\frac{dE}{dx} = \frac{2\pi e^4 \rho_e}{E} \ln\left(\frac{1.16(E+cI)}{I}\right)$$

Landau's fluctuation:

$$L = (2\pi)^{-1/2}\left(\frac{2\pi e^4 \rho_e}{E}\right)^{-1} \exp\left\{-\left(\frac{1}{2}\right)\left[\Delta + \exp(-\Delta)\right]\right\}$$

$$\Delta = \left(\frac{2\pi e^4 \rho_e}{E}\right)^{-1}\left[\left(\frac{dE}{dx}\right) - \left(\frac{dE}{dx}\right)_{Bethe-Bloch}\right]$$

Stopping Power and Fluctuation

- Stopping fluctuation

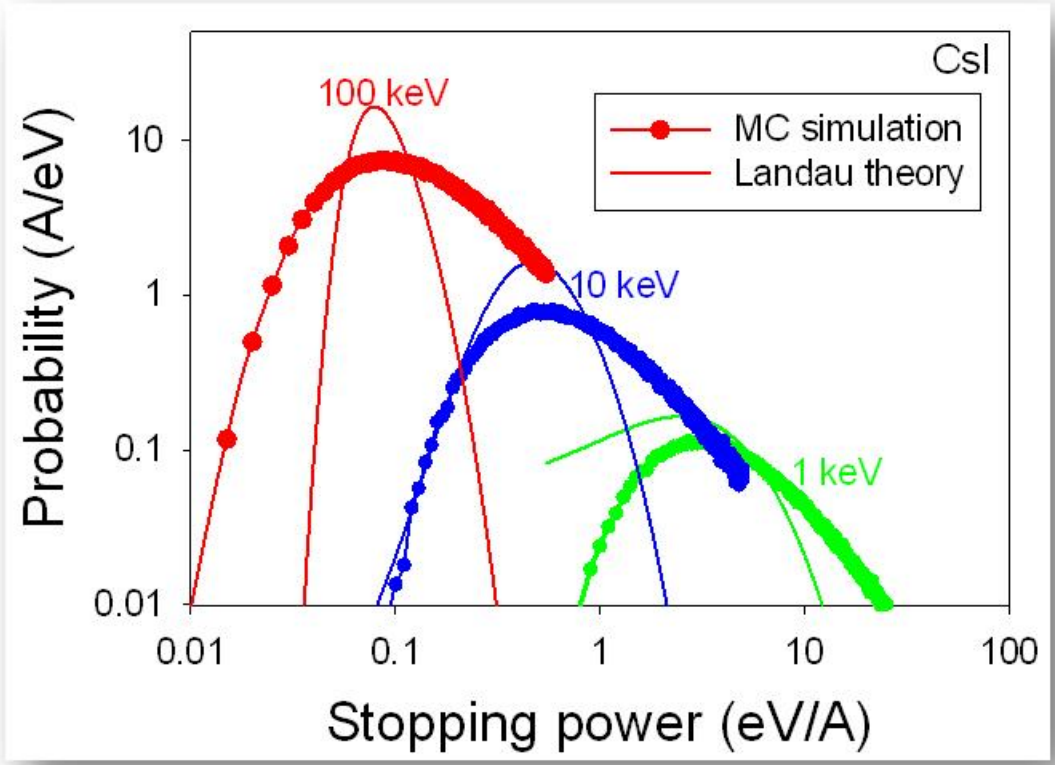

- In general, the peak positions are consistent with those predicted by Landau theory for all the energies considered.
- It seems that the distribution by MC simulations has a long tail.

Pacific Northwest
NATIONAL LABORATORY

Stopping Power and Fluctuation

- Stopping power for different materials

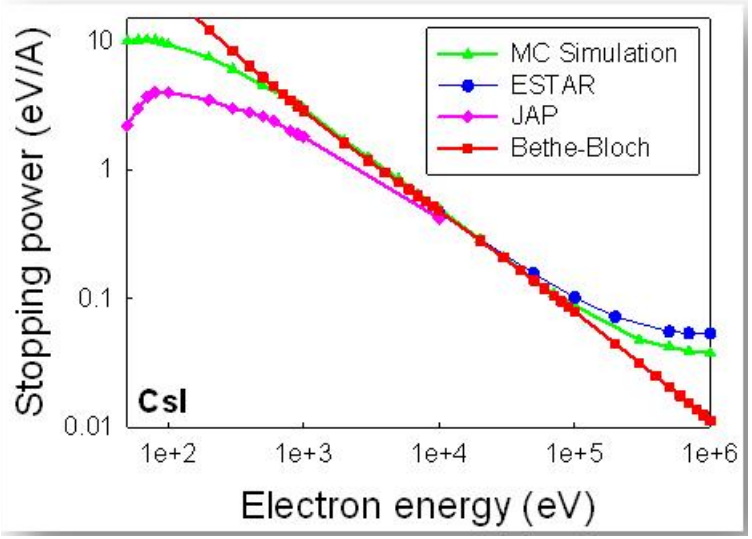

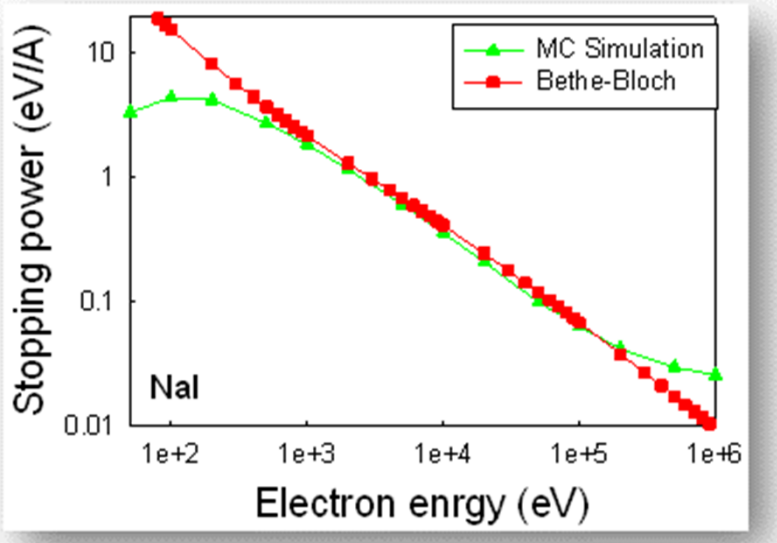

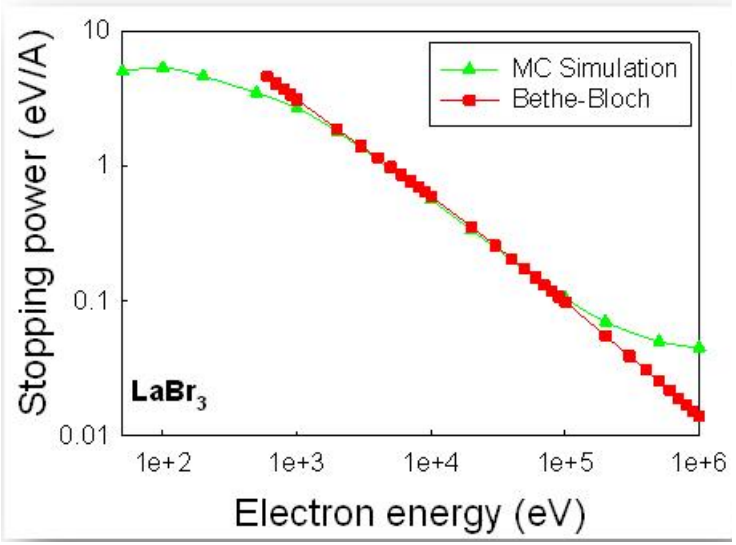

- Stopping powers at intermediate energies are in good agreement with those by Bethe-Bloch calculations.
- Stopping powers at lower and higher energies are different from those by Bethe-Bloch calculations.

Pacific Northwest
NATIONAL LABORATORY

Spatial Distribution of e-h Pairs

- Spatial distributions in SrI_2 and $LaBr_3$ (10 keV)

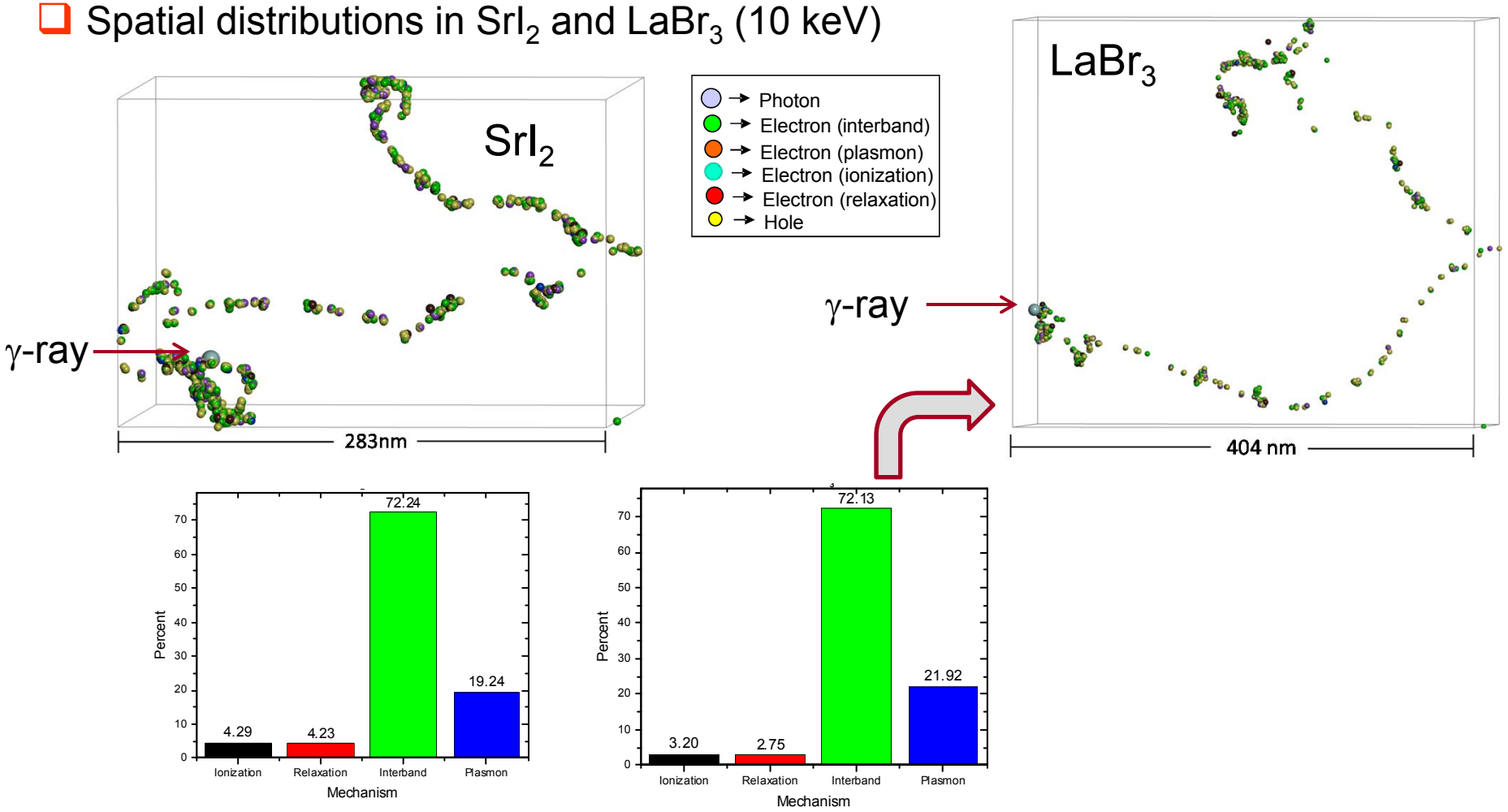

- Similar linear track structure – less quenching of excitons.
- Most e-h pairs are produced by interband transition.

Pacific Northwest
NATIONAL LABORATORY

Spatial Distribution of e-h Pairs

- Spatial distributions in CsI and $LaBr_3$ (10 keV)

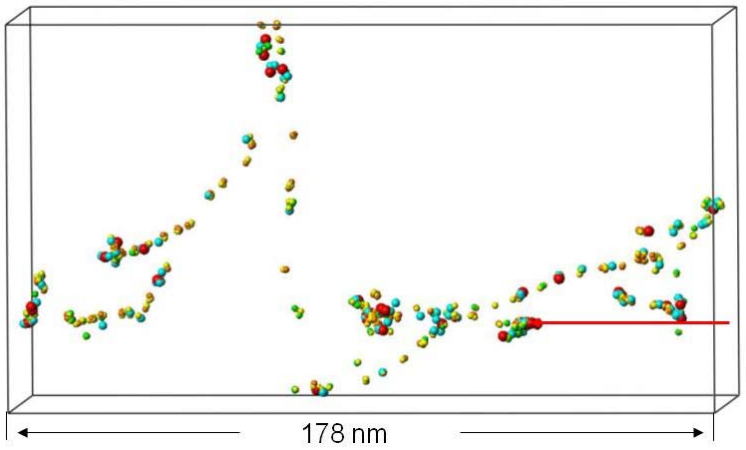

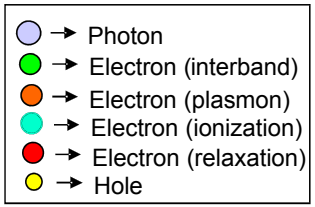

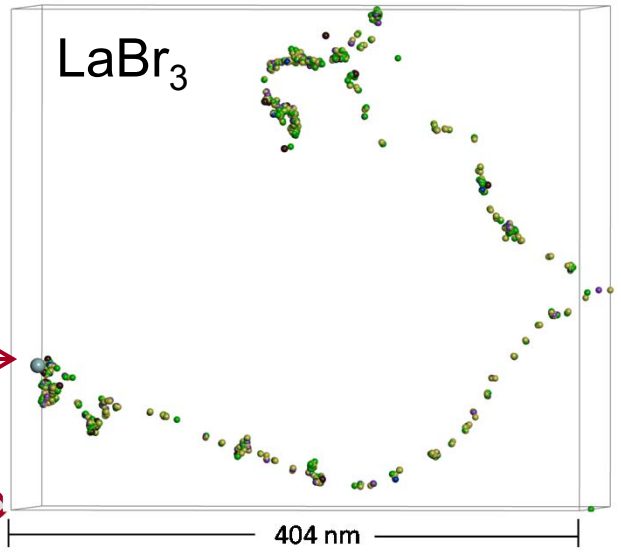

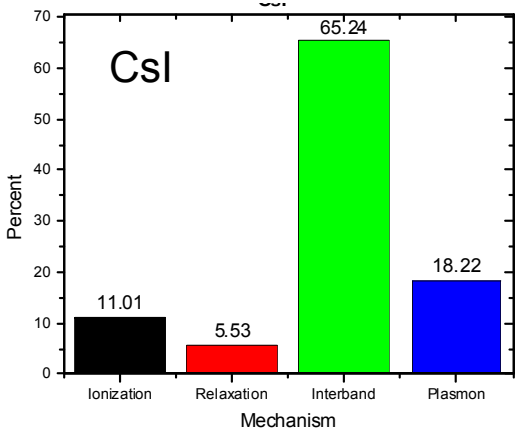

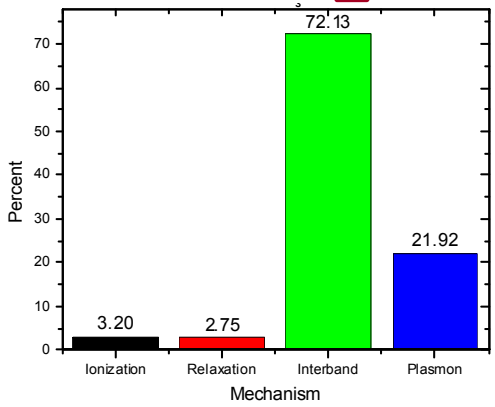

- Slightly clustered track structure in CsI.
- Large fraction of e-h pairs is produced by ionization process in CsI, suggesting slightly larger Fano factor.

Pacific Northwest
NATIONAL LABORATORY

Spatial Distribution of e-h Pairs (example)

- Kinetic process of electron-hole pair creation in NaI (10 keV)

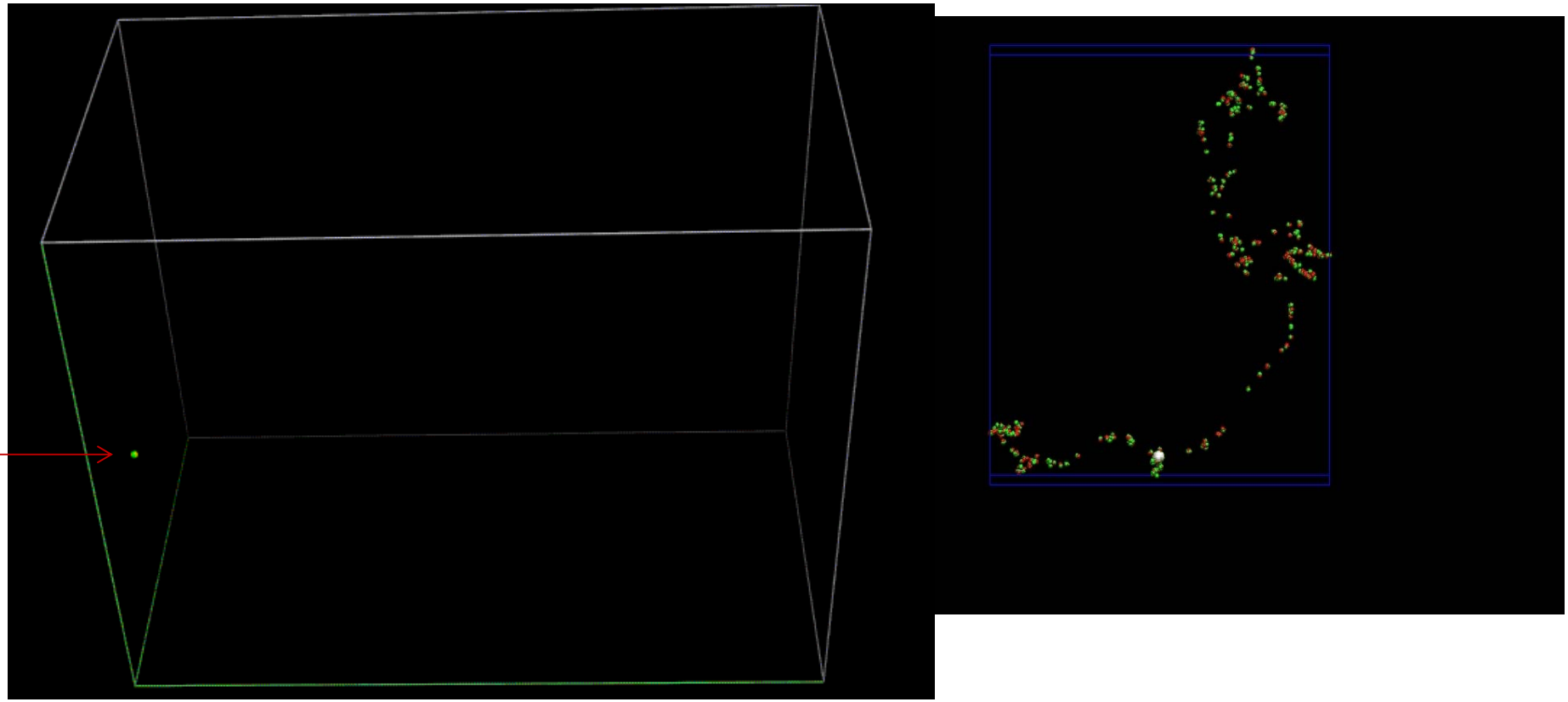

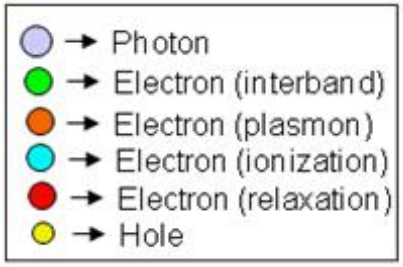

Pacific Northwest
NATIONAL LABORATORY

Compare to Experimental Results

- Theoretical light yields

$$L_y = SQ / W$$

S – energy transfer efficiency

Q – luminescence quantum efficiency

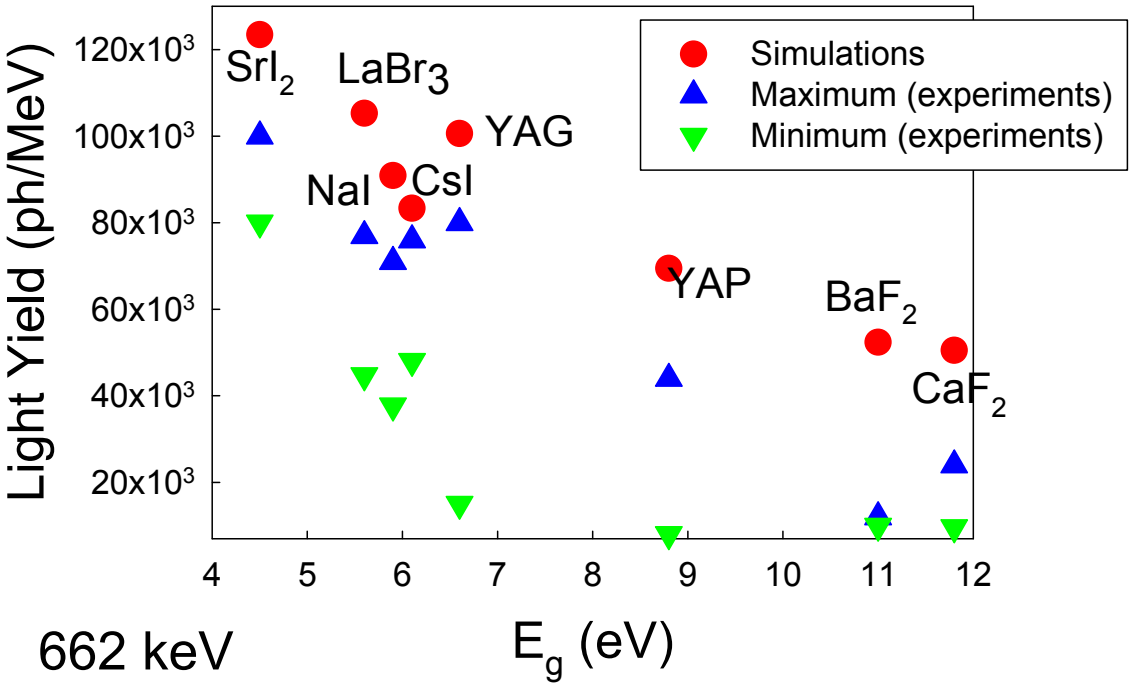

- Light yield decreases with increasing E_g and is comparable with experimental values, and larger than the maximum values obtained by experiments.
- These calculations allow the evaluation of the maximum theoretical light yield as a function of band gap energy.
- The results can be directly compared to experimental measurements, thus providing a possible pathway to validate the simulations.

Pacific Northwest
NATIONAL LABORATORY

Compare to Experimental Results

- Comparison with experimental Fano factor

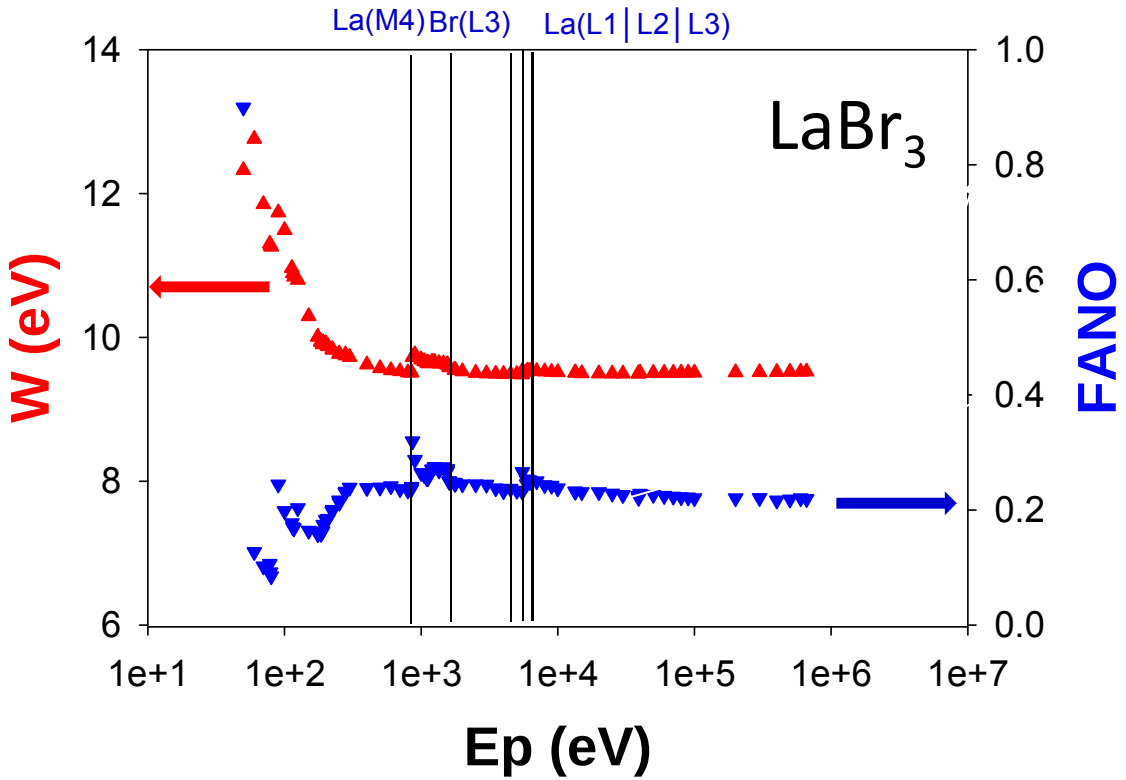

- Fano factor ~ 0.22
- Experimental value of Fano factor ~ 0.1 (A. Bousselham et al., 2009 IEEE Nuclear Science Symposium Conference Record, 2370)
- The optical Fano factor of $LaBr_3$ is very small, comparable to that of good semiconductor detectors

Pacific Northwest
NATIONAL LABORATORY

Compare to Experimental Results

- Track radius, thermalization time and light yield (WFU – Richard Williams)

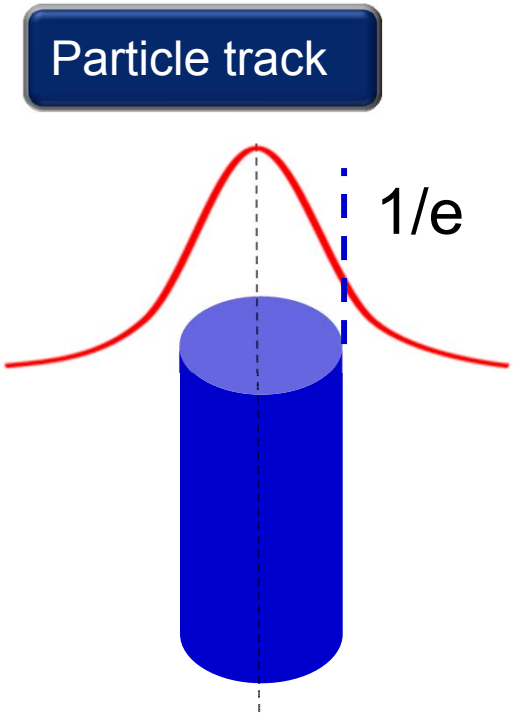

$$r_0^2 = \frac{dE/dx}{\pi\left(\frac{I_0\alpha}{h\nu}\right)\beta E_{gap}} = \frac{60\ eV/nm}{\pi\left(0.1\ eh/nm^3\right)(2.5)(5.5)\left(eV/eh\right)}$$

dE/dx = 60 eV/nm at 0.1 keV

r_0 = 3.7 nm in NaI near track end

What is the track radius?

- NWEGRIM simulations in NaI near track end

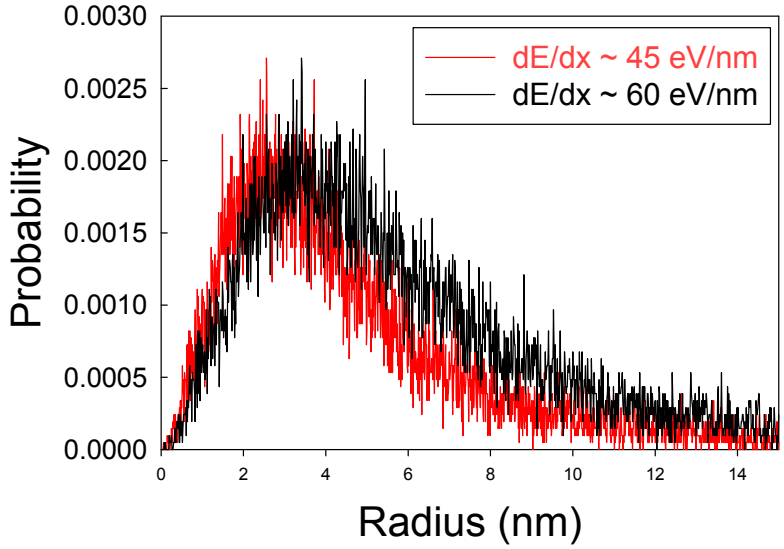

r_0 = 2.8 nm

Rescaled by 60 eV/nm

r_0 = 3.3 nm

Pacific Northwest NATIONAL LABORATORY

General Rules

Properties	CaF_2	BaF_2	CsI	NaI	$LaBr_3$	SrI_2
W value (eV)	21.4	19.1	12.0	10.9	9.5	8.1
Max light yield (ph/MeV)	50,505	52,356	83,333	91,743	105,263	123,457
Main channels to generate e-h pairs	Interband (63.1%) Plasmon (31.6%) Ionization (4.4%)	Interband (63.7%) Plasmon (29.3%) Ionization (4.1%)	Interband (65.2%) Plasmon (18.2%) Ionization (11.1%)	Interband (60.21%) Plasmon (29.1%) Ionization (6.4%)	Interband (72.1%) Plasmon (21.9%) Ionization (3.2%)	Interband (72.2%) Plasmon (19.2%) Ionization (4.3%)
Track structure	Clustered	Clustered	Slightly clustered	slightly clustered	Linear	Linear
Constant light yield for E_p> (keV)	0.8	0.9	10.0	2.0	2.0	0.2
Fano factor	0.23	0.19	0.30	0.28	0.21	0.23

- Small *W* value that increases maximum theoretical light yield.
- Small number of energy loss channels (ideally, only interband transition).
- Linear track structure that decreases the nonlinear behavior at low incident energies.

Summary

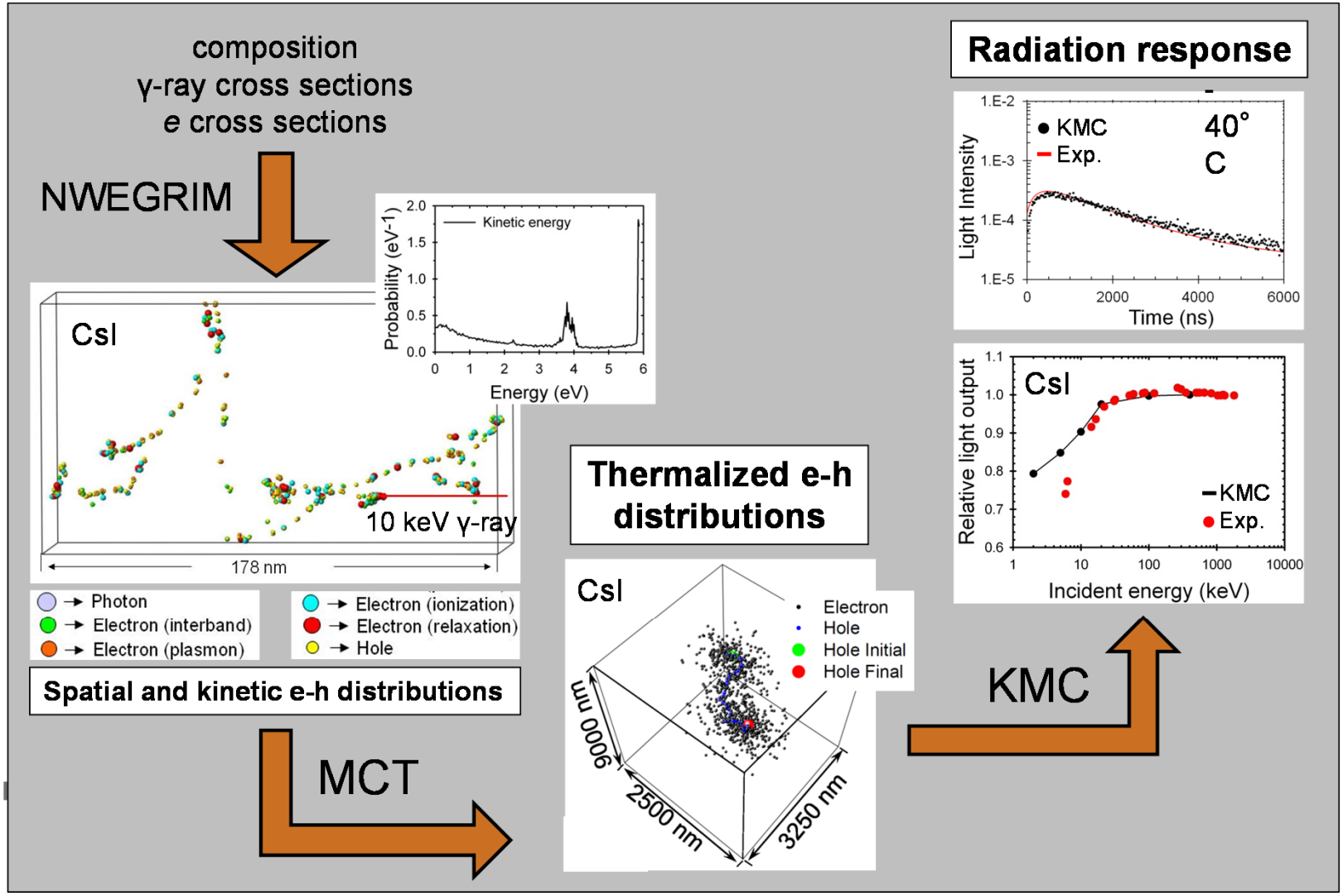

- It is now possible to quickly simulate complete series of scintillator materials, such as the alkali halide and alkaline-earth halide classes, helping candidate search for new scintillator materials.

Pacific Northwest
NATIONAL LABORATORY

Phys. Status Solidi B **250,** No. 8, 1532–1540 (2013) / **DOI** 10.1002/pssb.201248587

physica status solidi b
www.pss-b.com
basic solid state physics

Kinetic Monte Carlo simulations of excitation density dependent scintillation in CsI and CsI(Tl)

Zhiguo Wang[1], Richard T. Williams[2], Joel Q. Grim[2], Fei Gao[1], and Sebastien Kerisit[*,1]

[1] Fundamental and Computational Sciences Directorate, Pacific Northwest National Laboratory, Richland, WA 99352, USA
[2] Department of Physics, Wake Forest University, Winston-Salem, NC 27109, USA

Received 6 December 2012, revised 7 February 2013, accepted 13 February 2013
Published online 14 March 2013

Keywords inorganic scintillators, kinetic Monte Carlo, nonlinear quenching, non-proportionality, scintillation mechanisms

* Corresponding author: e-mail sebastien.kerisit@pnnl.gov, Phone: 509-371-6382, Fax: 509-371-1226

Nonlinear quenching of electron–hole pairs in the denser regions of ionization tracks created by γ-ray and high-energy electrons is a likely cause of the light yield non-proportionality of many inorganic scintillators. Therefore, kinetic Monte Carlo (KMC) simulations were carried out to investigate the scintillation properties of pure and thallium-doped CsI as a function of electron–hole pair density. The availability of recent experimental data on the excitation density dependence of the light yield of CsI following ultraviolet excitation allowed for an improved parameterization of the interactions between self-trapped excitons (STE) in the KMC model via dipole–dipole Förster transfer. The KMC simulations reveal that nonlinear quenching occurs very rapidly (within a few picoseconds) in the early stages of the scintillation process. In addition, the simulations predict that the concentration of thallium activators can affect the extent of nonlinear quenching as it has a direct influence on the STE density through STE dissociation and electron scavenging. This improved model will enable more realistic simulations of the non-proportional γ-ray and electron response of inorganic scintillators.

1 Introduction High-energy photons and electrons that penetrate scintillator materials create tracks of electron–hole pairs, also referred to as ionization tracks, with densities that vary as the energetic particle slows down inside the solid. Relaxation of ionization tracks eventually leads to the emission of many lower-energy scintillation photons, a phenomenon that is exploited, for example, in radiation detection and γ-ray spectroscopy. Key scintillation properties, such as emission spectra, decay times, and light yields, strongly depend on the kinetics and efficiency of the relaxation of ionization tracks. The variation of the ionization track density as a function of the incident particle energy can also lead to non-proportionality, a phenomenon whereby the yield of scintillation photons normalized to the incident energy is not constant with incident energy. Although the non-proportionality of inorganic scintillators has been studied quite intensively (see for example, reviews [1–4] and references therein), its underlying mechanisms remain incompletely identified.

From a solid state physics perspective, non-proportionality challenges our understanding of (i) the dependence of ionization tracks on incident particle energy, (ii) the relaxation of small high-excitation-density regions, and (iii) the competition among the processes that dictate the light yields of scintillators. From an application perspective, non-proportionality is the main source of degradation of the energy resolution in radiation detection and γ-ray spectroscopy with inorganic scintillators [5, 6] and, therefore, there is great interest in understanding the root cause(s) of non-proportionality in order to help guide the search for new and improved scintillator materials.

Significant progress has been made towards developing models of the elementary processes that take place in ionization tracks and give rise to the electron or photon response of inorganic scintillators. These elementary processes include the creation of excited states, the transport of excited carriers through the scintillator lattice, and the quenching of excitations as they propagate. Approaches employed to model these processes include minimalist phenomenological models [7, 8], kinetic models [9–13], diffusion models [14–16], and microscopic models that explicitly deal with individual electron–hole pairs [17–20].

Accurately describing the rate and extent of nonlinear quenching in conditions relevant to ionization tracks has amounted to one of the most challenging tasks faced by scintillation models to date; mostly due to the considerable difficulties in obtaining experimental data for parameterization and validation of the models. For example, we previously used kinetic Monte Carlo simulations (KMC) to evaluate the contribution of an annihilation mechanism between self-trapped excitons (STE) to the non-proportional scintillation response of pure CsI at low temperature [18]. Although the KMC simulations suggested that STE–STE annihilation could account for the non-proportional behavior of CsI, this process could not be independently parameterized and its probability was used as a variable.

Fortunately, experimental data on nonlinear quenching is now beginning to become available [15, 16, 21–27]. For example, Williams and co-workers recently investigated the excitation density dependence of the light yield of pure and thallium-doped CsI and NaI using ultraviolet (UV) excitation [16, 27]. In these experiments (referred to hereafter as z-scan experiments), 0.5-ps pulses of 5.9-eV light were used to generate electron–hole pair densities estimated to be consistent with the denser regions of ionization tracks created by γ-rays and energetic electrons. The excitation density was controlled by varying the distance between the sample and the UV-beam waist thus allowing for scintillation decay curves and light yields to be determined as a function of excitation density.

Therefore, in this work, we make use of a KMC model of scintillation mechanisms in CsI and CsI(Tl), developed in a previous study [17] and based on the kinetic model of Dietrich and Murray [28], to model the excitation density dependence of the kinetics and efficiency of scintillation in the z-scan experiments. Our aim is to identify the relevant elementary processes, determine and parameterize the extent of nonlinear quenching due to STE–STE interactions, and thus develop a more accurate model for simulating the relaxation of ionization tracks. The KMC model makes use of an explicit atomistic representation of the crystal lattice, thallium sites and individual electron–hole pairs and assigns probabilities for each individual elementary process based on rate parameters (i.e., activation energies and pre-exponential factors).

One of the advantages of the KMC model is that it can use as input realistic ionization tracks produced by the Monte Carlo code NWEGRIM (Northwest Electron and Gamma Ray Interaction in Matter) [29–32]. NWEGRIM follows the collisions of each individual particle generated during the energy cascade and can generate a microscopic-level three-dimensional description of ionization tracks. Therefore, in combination with progress made recently in simulating electron thermalization in alkali and alkaline-earth halides [19, 20], these techniques and models provide a path toward modeling the response of inorganic scintillators at the level of individual electron–hole pairs. Such an approach is attractive as it has the potential ultimately to account for any heterogeneity of the ionization tracks, scintillator lattice, or activator distribution, incorporate input from first-principles calculations, and lead to the development of a predictive simulation framework.

The focus of this study is on CsI, pure and thallium doped, as it was studied in both our previous modeling work [17] and the experimental work of Williams and co-workers [16, 27]. It should be noted that CsI is also attractive for its wide-spread use as a radiation detection material, simple crystal structure, large deviation from proportionality and frequent use as a model system for studying non-proportionality.

2 Computational methods

2.1 Kinetic Monte Carlo model The KMC model was developed and implemented in a previous study [17] and was based on the model originally developed by Dietrich and Murray [28] to describe the kinetics of scintillation of thallium-doped alkali halides. In the KMC model, the scintillator lattice and all the relevant species are represented explicitly and the diffusion of self-trapped holes (STH) and STE is treated using a random-walk approach. The model considers a number of scintillation processes, as illustrated in Fig. 1.

All electron–hole pairs begin the simulations as STE, for reasons to be explained in Sections 2.3 and 3.1. STEs can diffuse through the lattice and be trapped at Tl^+ sites. STEs can also decay radiatively or non-radiatively or interact via dipole–dipole Förster transfer, a non-radiative transfer whereby a first STE decays by emitting a virtual phonon, which is absorbed by a second STE. In addition, STEs can undergo dissociation. Indeed, recent picosecond time-resolved measurements of optical absorption by Williams and co-workers [33] showed that, in CsI doped with 0.3 mol% of Tl, the absorption band due to STEs decayed on the time scale of picoseconds and was replaced by a band that was assigned to Tl^0. This experimental result indicates that a STE electron, possibly in an excited bound state, may be scavenged by tunneling transfer to a nearby Tl^+ site to

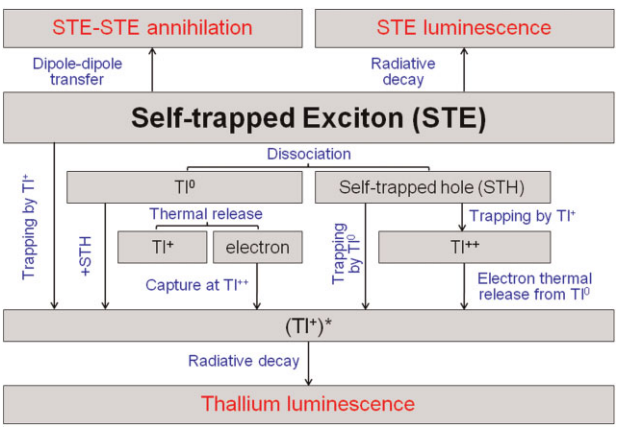

Figure 1 (online color at: www.pss-b.com) Schematic of the elementary species (black), elementary processes (blue), and possible final outcomes (red) considered in the KMC model of scintillation.

form Tl^0. Therefore, the dissociation of a STE results in the formation of a STH and a Tl^0 site. A STH can diffuse through the lattice and trap at Tl^+ or Tl^0 and Tl^0 can release its electron to be trapped at a Tl^{++} site and thus form $(Tl^+)^*$.

Overall, scintillation light can be emitted by radiative decay of either STE or excited thallium ions, which can be formed by three different mechanisms: (i) diffusion of a STE and capture at a Tl^+ site; (ii) diffusion of a STH and capture at a Tl^0 site; and (iii) diffusion of a STH and capture at a Tl^+ site to form Tl^{++}, followed by thermal release of an electron from a Tl^0 site and capture at Tl^{++}.

For each elementary process, the rate, k, is described by an Arrhenius equation,

$$k = A\exp\left(\frac{-W}{k_B T}\right), \tag{1}$$

where A is the pre-exponential factor, W the activation energy, k_B the Boltzmann constant, and T is the temperature. In previous work [18], second-order quenching of STEs was simulated by assigning a probability for annihilation when a STE hopped to a site already occupied by another STE. This is replaced in this work by dipole–dipole Förster transfer between STEs. Förster transfer is an exception to Eq. (1) in that the rate is dependent on the distance between STEs [34]:

$$k(r) = B\left(\frac{R_{dd}}{r}\right)^6, \tag{2}$$

where R_{dd} is the Förster transfer radius and B is set to the STE radiative decay rate following the formulation of Vasil'ev [34] used subsequently by Kirm et al. [21] and Williams et al. [16]. The model parameters are given in Table 1 and discussed in the next section.

The KMC algorithm is executed using the following algorithm: (i) the rate of each process is calculated using Eqs. (1) or (2); (ii) a process is selected with a probability proportional to its rate using a random number; (iii) the selected process is executed; (iv) time is increased by $-\ln x/\Gamma$, where x is another random number and Γ is the sum of all rates. Steps (i)–(iv) are repeated until all electron–hole pairs have undergone radiative or non-radiative decay or have been quenched.

Table 1 Parameters of the KMC model of scintillation.

process	A (s^{-1})	W (eV)
STH diffusion	5.1×10^{12}	0.1500
STE diffusion	5.1×10^{12}	0.1500
STE radiative decay	7.1×10^{8}	0.0000
STE non-radiative decay	1.0×10^{10}	0.1160
STE dissociation[a]	1.7×10^{11}	0.0000
$(Tl^+)^*$ radiative decay	6.0×10^{7}	0.0662
electron thermal release from Tl^0	8.8×10^{6}	0.0880
process	R_{dd} (a_0)	B (s^{-1})
dipole–dipole Förster transfer	8	1.7×10^{8}

[a]This process can take place only if a Tl^+ is available within a $3a_0$ radius.

2.2 Origin of the model parameters Eight processes are considered in the KMC model. Six processes were included in the derivation of the original KMC model [17]: STH and STE diffusion, STE radiative and non-radiative decay, $(Tl^+)^*$ radiative decay, and electron thermal release from Tl^0. Two processes were added for the purposes of this work: STE dissociation and dipole–dipole Förster transfer. All the parameters related to these eight processes are given in Table 1.

STH diffusion occurs via thermally activated hopping to nearest-neighbor sites following 90 or 180° hops of the STH [35]. Initial assignment of the two peaks of thermoluminescence below 100 K (at approximately 60 and 90 K) observed by Sidler et al. [35] led to the conclusion that the 180° hop had a lower activation energy than the 90° one in CsI. However, Barland et al. [36] showed that there was no thermoconductivity peak associated with the 60 K thermoluminescence peak and that its isothermal decay exhibited a $1/t$ dependence, strongly suggesting that this peak was due to recombination through tunneling and not diffusion via 180° hops. Therefore, there is no experimental consensus on the relative activation energies of the two possible hops. Derenzo and Weber [37] computed an activation energy of 0.15 eV for the 180° hop using MP2 level of theory but they did not compute the activation energy for the 90° hop; therefore, this value was used for both types of hops in the KMC simulations. As before [17], the value derived by Keller and Murray [38] from thermal-reorientation experiments of STHs in KI was used for the pre-exponential factor.

At low temperatures, pure CsI shows two main STE emission bands but as the temperature is increased to room temperature only one wide band is observed [39]. Nishimura et al. [39] suggested that the wide band at room temperature originates from the on-center configuration of the STEs (it should be noted that other researchers have shown evidence for the interaction of multiple excitations as a possible alternate origin of this emission [40, 41]). Because the radiative lifetime of the singlet on-center STE is shorter than that of the triplet, the rate of dipole–dipole Förster transfer will be faster for the singlet state. In addition, the experimental data of Williams et al. [16] used in this work for comparison were subject to surface quenching that reduces the observed radiative lifetime. This competing surface quenching depletes the slower triplet light yield more than the faster singlet light yield. Both effects suggest that the experimental data are mainly representing the singlet channel. Therefore, as was done in the original KMC model [17], we make the simplifying assumption that the STE emission in pure CsI originates from a single type of STE at room temperature. However, there is no experimental data available on the activation energy and pre-exponential factor for STE hopping in CsI. Previously [17], the STE diffusion parameters were estimated from a combination of the data on STH and STE hopping in NaI and that on STH hopping in CsI and resulted in STE diffusion being faster than STH diffusion. However, recent electronic structure calculations by two research groups have shown that STEs and STHs are

equally mobile in NaI [42, 43] and this finding is expected to extend to CsI. Therefore, the energy barrier and pre-exponential factors for STEs in CsI were set to be the same as those used for STHs.

In the original KMC model [17], the parameters for STE radiative and non-radiative decay were fitted to the experimental light yield and decay time of pure CsI obtained by Amsler et al. [44] as a function of temperature and under excitation by 511 and 1275 keV γ-rays. The fit initially produced a very small value for the activation energy of the STE radiative decay process (0.011 eV) and a second fit with this activation energy fixed to zero yielded equivalent temperature dependence of the light yield and decay time. Therefore, W in Eq. (1) was set to zero in this work. The STE lifetime derived by Williams et al. [16] from the decay of the STE luminescence of UV-excited pure CsI was shorter than that measured in the bulk by Nishimura et al. [39]. Williams et al. suggested that this shortening of the lifetime for UV excitation was due to quenching on surface defects, which could provide an additional channel for STE decay. Therefore, because this study focuses on modeling the experimental results of Williams et al., the pre-exponential factor of the STE radiative decay process was changed to the inverse of the lifetime derived by Williams et al. to implicitly account for surface quenching.

The parameters for electron thermal release and $(Tl^+)^*$ radiative decay were derived in the original model from the temperature dependence of the scintillation light measured by Valentine et al. [45] following excitation of CsI(Tl) with 511 keV γ-rays. These parameters were kept in the current model with the exception of the pre-exponential factor for $(Tl^+)^*$ radiative decay, which was increased from 1.9×10^7 to 6.0×10^7 to improve the agreement with the kinetics of $(Tl^+)^*$ luminescence reported by Williams et al. [16]. This was a fairly small modification; although Williams et al. [16] did not compare their observed $(Tl^+)^*$ lifetime to previous work, it is possible that, again, differences in excitation energy and densities slightly affected the rate of $(Tl^+)^*$ radiative decay in their experiments.

Turning now to the two processes that were added in the current version of the model, there is no available experimental data to directly parameterize the STE dissociation process; therefore, the rate assigned to this process was based on the observation of Williams et al. [33], from their time-resolved optical absorption data, that the band assigned to STEs essentially disappeared within 6 ps (i.e., the pre-exponential factor for this process was set to $1.67 \times 10^{11}\ s^{-1}$ while the activation energy was set to zero as temperature dependent data would be needed to extract the activation energy). For the dipole–dipole Förster transfer, the parameter B was set to the STE radiative decay rate in analogy with the formulation of Vasil'ev [34]. To exclude the effect of surface quenching and for consistency with the original KMC model [17], B was set to the inverse of the lifetime measured by Amsler et al. [44] in the bulk and at room temperature (6 ns). As one of the goals of this work is to derive parameters for describing nonlinear quenching based on the experimental data of Williams and co-workers [16, 27], the value of R_{dd} was varied by increments of a_0, the CsI lattice parameter, while the other model parameters were kept fixed, until agreement with the z-scan experiments was obtained.

Finally, we note that, in the original KMC model, a prompt capture radius of 1.4 nm was used to model non-thermal capture of holes at Tl^+ sites, as suggested by Hadley et al. [46] and Kaufman et al. [47] in their experimental studies of KI(Tl) and NaI(Tl). This process was not included in the current model as all the electron–hole pairs begin the simulations as STEs. The data compared here are for photon excitation at 5.9 eV, whereas the work of Hadley et al. and Kaufman et al. used X-ray irradiation. In addition, as noted by Williams et al. [16], the excitation energy used in their experiments does not significantly overlap with the D band of Tl^+, which should produce negligible direct excitation of Tl^+.

2.3 Simulation setup The KMC model uses a simple cubic lattice whereby each lattice point represents one unit cell (i.e., 1 Cs^+ ion and 1 I^- ion). In alkali halides, a STH is localized on two neighboring halide ions and forms an X_2^- molecular ion or V_k center. A V_k center can capture an electron to form a STE. Therefore, STHs and STEs are represented in the KMC model as occupying two neighboring unit cells.

The KMC simulations were set to represent as closely as possible the conditions of the z-scan experiments. Based on a band gap energy of 6.05 eV for CsI at 20 K [48] and the observation that the band gap decreases with increasing temperature, the photon energy of the UV pulse in the z-scan experiments (5.9 eV) was close to the band gap energy and higher than the 1s exciton peak (5.6 eV) [49]. The comparison of one-photon [50] and two-photon [48] absorption spectra at low temperature give an experimental exciton binding energy of about 250 meV. Therefore, excitons are stable at room temperature and STEs are stable also, as evidenced by their efficient radiative emission. Therefore, the electron–hole pairs were all assumed to begin the simulations as STE. The STEs were placed on the lattice following an exponentially decaying distribution: $N(z) = N_0 \exp(-\alpha z)$, where z is the depth from the surface in lattice layers, $N(z)$ is the number of excitons at depth z, and α is the absorption coefficient. The absorption coefficient used here was set to approximately twice that derived experimentally by Williams et al. [16] (i.e., 5.0×10^5 vs. $2.7 \times 10^5\ cm^{-1}$) to give a characteristic length of 20 nm instead of 37 nm and thus reduce the extent of the z direction needed in the simulations to encompass the STE distributions. A test simulation was run for $\alpha = 2.7 \times 10^5\ cm^{-1}$, but no significant change was observed.

The simulation cell was a three-dimensional lattice of dimensions $32 \times 32 \times 256$ sites. Given a lattice parameter of 0.457 nm for CsI, this corresponds to real dimensions of $14.6 \times 14.6 \times 117\ nm^3$. The UV beam was assumed to be incident along the z direction. Periodic boundary conditions were applied in the directions perpendicular to the beam but

not in the direction of the beam. The $z = 0$ boundary represented the crystal surface. Given the length of the simulation cell in the z direction relative to the absorption coefficient, the STE population was extremely small at the other z boundary. Tl^+ sites were placed randomly on the lattice to achieve the desired concentration. All the simulations were carried out at room temperature.

Knowing the on-axis laser fluence, the absorption coefficient, the excitation energy, and the position of the beam waist relative to the sample surface, the excitation density can be calculated and parameterized by its value N_0 at the sample surface. The same range of values as used experimentally was used here for N_0.

3 Results

3.1 Light yield of CsI:0.3% Tl as a function of excitation density A series of KMC simulations were performed to calculate the light yield of CsI:0.3% Tl as a function of excitation density. The excitation densities were taken from the experimental estimates, as described in Section 2.3. For each excitation density, the light yield was determined using the average of 400 simulations. Although not necessarily true in practice because of the increase in background light for the positive side, the positive and negative sides of the z-scan should be identical and therefore, for the KMC simulations, the positive side was obtained by simply taking the mirror image of the negative side.

Recent z-scan measurements by Grim et al. [27] comparing $Bi_4Ge_3O_{12}$, NaI:Tl, and CsI:Tl at 5.9-eV excitation indicate that CsI:Tl does not follow purely second-order quenching kinetics (Förster transfer) but shows some contribution from a third-order quenching process (e.g., Auger recombination). Because this work focuses on second-order quenching, a fit to the experimental data with a mixed 2nd/3rd order analytical model [27] was carried out and only the second-order component is considered further in our KMC simulations with Förster transfer. Future work will investigate the effects of incorporating a third-order quenching process in the KMC simulations applied to z-scan experiments with UV excitation energies higher than 5.9 eV and to ionization tracks of high-energy electrons.

The value of R_{dd} was changed in increments of a_0 (i.e., 0.457 nm) until the best possible agreement with the second-order component of the experimental data was obtained. Figure 2 shows the excitation density dependent light yield obtained for $R_{dd} = 8a_0$ along with the yield obtained experimentally from the z-scan experiments and the second-order component [27]. A value of $8a_0$ for R_{dd} corresponds to 3.66 nm, which is close to the value of 3.8 nm derived by Grim et al. [27] from their analytical fit. Notably, Kirm et al. [21] and Nagirnyi et al. [22] derived values of 2.1 and 3 nm, respectively, for Förster transfer in $CdWO_4$ using the same analytical model as used subsequently by Williams and co-workers [16, 27].

Figure 2 shows that excellent agreement with the second-order component of the experimental data can be obtained within the framework of the KMC simulations.

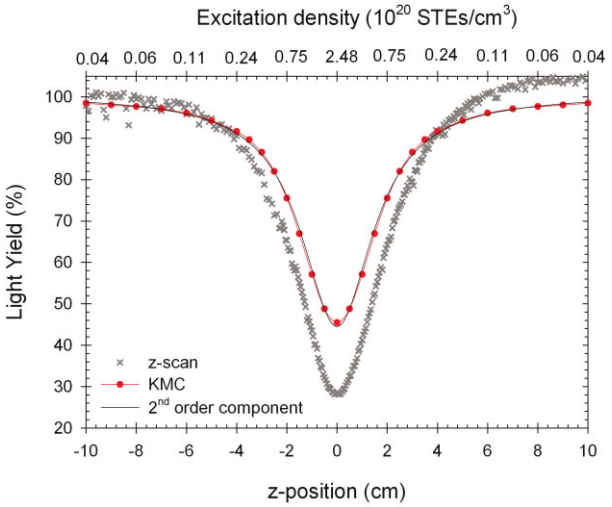

Figure 2 (online color at: www.pss-b.com) Calculated light yield as a function of z-position and excitation density and comparison with the z-scan data and second-order component of Grim et al. [27].

3.2 Scintillation kinetics of CsI:0.3% Tl as a function of excitation density Although the KMC model can reproduce the efficiency of the scintillation process, there remains to determine whether the same model parameters can yield an accurate description of the kinetics of scintillation. Therefore, in Fig. 3, the scintillation decay curves obtained at two excitation densities from 20 000 KMC simulations are compared to those reported by Williams et al. [16]. Experimentally, no noticeable differences were found between the high and low excitation densities and therefore a single curve is shown in Fig. 3 for the experimental data.

As seen experimentally, the KMC model shows a rising time of a few nanoseconds. Experimentally, the scintillation maximum was found at approximately 6.2 ns. The KMC simulations show a slightly delayed maximum; although the

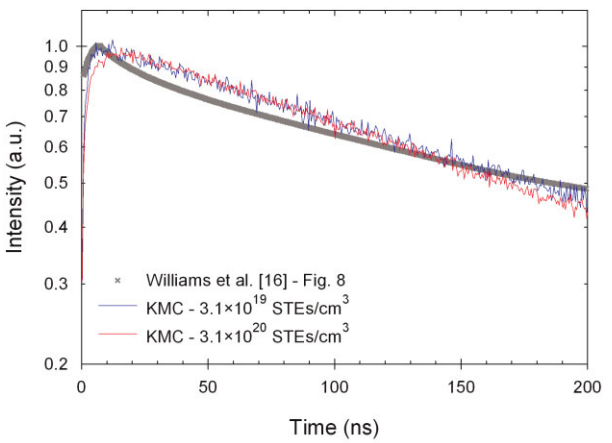

Figure 3 (online color at: www.pss-b.com) Decay curves of the $(Tl^+)^*$ emission of CsI:0.3%Tl calculated at two excitation densities and comparison with the results of Williams et al. [16].

resolution of the streak camera on the 200 ns frame scale is likely to be lower than the difference between the simulations and measurements. In the KMC simulations, the high excitation density curve shows a slight increase after scintillation reaches its intensity maximum, relative to that obtained at low excitation density, and a corresponding slightly faster decrease at later times. Again, it is possible that such differences are too subtle to be observed within the uncertainties of the experimental apparatus employed by Williams et al. [16]. Experimentally, no quenching of the $(Tl^+)^*$ emission was observed with increasing excitation density, which strongly suggests that nonlinear quenching occurs before excitations are trapped at Tl^+ sites and not within the $(Tl^+)^*$ population. Therefore, this process was not included in the KMC model and the results shown in Fig. 3 indicate that, indeed, such a process is not needed to give a good account of the kinetics of the $(Tl^+)^*$ emission.

3.3 Scintillation kinetics of pure CsI as a function of excitation density The same two excitation densities were considered to determine the kinetics of scintillation of pure CsI. As before, the scintillation decay curves were obtained by averaging 20 000 simulations. The agreement is good except in the first 0.3 ns. This can be explained by the fact that there is a finite time required for the formation of STEs from free electrons and holes that is not taken into account in the KMC simulations since all electron–hole pairs are assumed to begin the simulations as STEs. We note that the data of Williams et al. [16] shown in Fig. 4 does not correspond to their raw data but to their fits before introducing the bimolecular growth function that accounts for the rising time of the STE luminescence. The calculated scintillation decay curves also show similar features to the experimental curves reported by Kirm et al. [21] for $CdWO_4$, with fast initial decay followed by exponential decay at later time and greater deviation from exponential decay initially at high excitation densities.

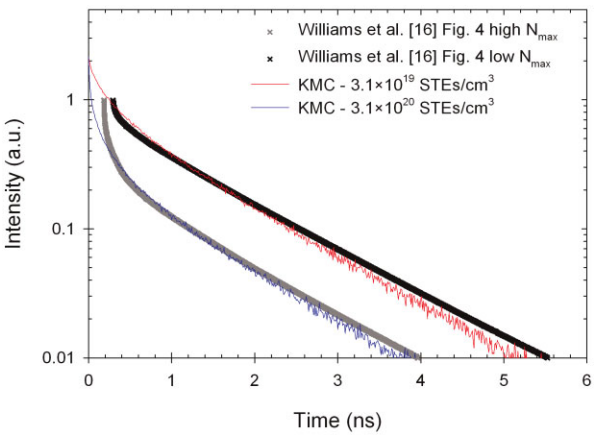

Figure 4 (online color at: www.pss-b.com) Decay curves of the STE emission of pure CsI calculated at two excitation densities and comparison with the curve fits of Williams et al. [16].

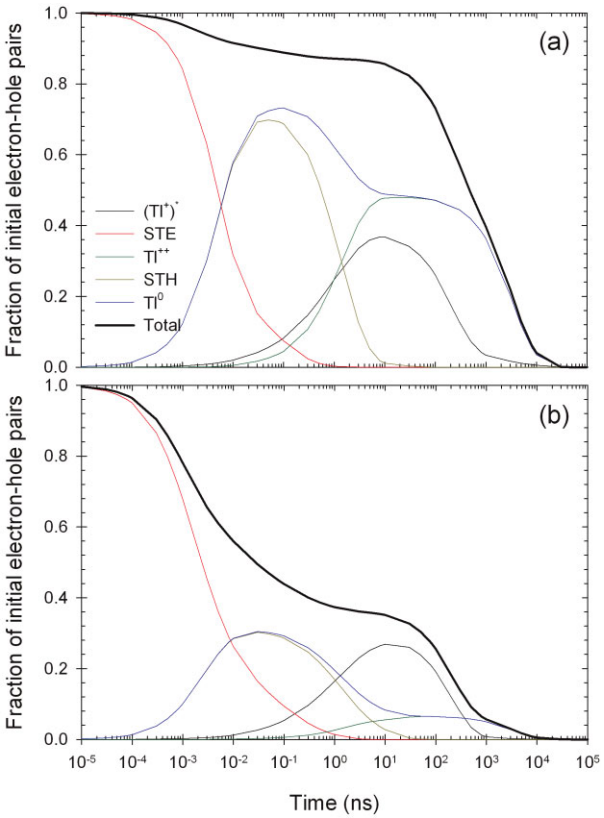

Figure 5 (online color at: www.pss-b.com) Time evolution of the populations of the species considered in the KMC model for CsI:0.3% Tl at (a) low excitation density (3.1×10^{19} STEs/cm^3) and (b) high excitation density (3.1×10^{20} STEs/cm^3).

4 Discussion The time evolution of the populations of each species (STE, STH, Tl^{++}, Tl^0, and $(Tl^+)^*$) are shown in Fig. 5 for excitation densities 3.1×10^{19} and 3.1×10^{20} STEs/cm^3. The general sequence of events is as follows. Early on, on the time scale of picoseconds or even sub-picoseconds, the STE population diminishes due to dipole–dipole Förster transfer and electron scavenging by Tl^+ sites. The latter process appears to culminate at approximately 10 ps, at which point the STH population does not equal the Tl^0 population anymore as the diffusing STHs begin to trap at Tl^+ sites to form Tl^{++} or $(Tl^+)^*$ species. By about 10 ns, all the STHs have been trapped at Tl sites and the Tl^0 and Tl^{++} populations thus become equal in size. Beyond this point, recombination only takes place via thermal release of electrons from Tl^0 to Tl^{++} sites to form $(Tl^+)^*$.

There is no noticeable increase of the $(Tl^+)^*$ population until the STE population has almost completely vanished, suggesting that Tl excitation through STE capture is limited in these conditions and occurs via binary electron–hole recombination instead. This is consistent with the findings of Dietrich et al. [51] for Tl-doped alkali halides excited with high-energy electrons. Interestingly, the KMC simulations indicate that there are two stages in which the population of

electron–hole pairs diminishes (thick black curves in Fig. 5): the nonlinear quenching and photon emission stages; and that these two stages are temporally well separated at both low and high excitation densities. Consequently, results such as those presented in Fig. 5 can help further experimental investigations of scintillation processes by identifying the relevant time scale needed to probe particular mechanisms.

As noted above, the STE population decays mostly via dissociation to form STH and Tl^0 sites on the scale of picoseconds. This is consistent with the time-resolved optical absorption data of Williams et al. [33]. In their study, Williams et al. used a pump-probe laser setup to determine the transient infrared absorption spectra of CsI induced by sub-picosecond two-photon band-gap excitation at room temperature. The absorption band assigned to STEs was seen to disappear in 5–10 ps after excitation of the CsI sample doped with 0.3 mol% Tl, whereas the band assigned to Tl^0 rose within the same time scale. The experimental findings of Williams et al. are consistent with the transient optical absorption measurements of Yakovlev et al. [52], which indicated the presence of only STH and Tl^0 on the time scale of nanoseconds after excitation of a Tl-doped CsI crystal at 80 K. Because the experimental data of Williams et al. [33] guided the parameterization of the STE dissociation process, it is not surprising to observe this agreement; however, the KMC simulations do confirm that STE dissociation is a viable process at this time scale given the other active processes. For example, if STE dissociation happened at a slower rate, the KMC model predicts that a greater extent of Förster transfer and STE radiative and non-radiative decay would be observed, which would be inconsistent with the z-scan and kinetics data.

It is important to note that the STE dissociation process is necessary for the model to account for all experimental observations consistently. Indeed, although the STEs diffuse at the same rate as the STHs in the KMC simulations and thus could potentially explain the rising time observed in the $(Tl^+)^*$ scintillation kinetics, the kinetics of STE emission indicate that the STEs radiatively decay at a rate that is too fast to allow them to survive long enough to diffuse to and be captured at Tl^+ sites. Figure 4 indicates that at least 99% of the STEs have decayed or quenched by 5 ns, i.e., approximately the time it takes to reach the maximum of the $(Tl^+)^*$ luminescence curve (Fig. 3). Therefore, the dissociation mechanism prevents the STEs from decaying radiatively or annihilating via dipole–dipole Förster transfer. This strongly suggests that nonlinear quenching occurs in the very early stages and over a very short amount of time relative to the overall scintillation process.

Finally, given the ability of the KMC model to describe accurately the kinetics and efficiency of scintillation in CsI:0.3% Tl and the kinetics of scintillation in pure CsI, we used this model to predict the effect of Tl concentration on the extent of nonlinear quenching. Figure 6 shows the light yield as a function of excitation density for pure CsI and CsI doped with 0.1 and 0.3 mol% Tl, whereby each curve is normalized to the light yield at −10 cm. It should be noted

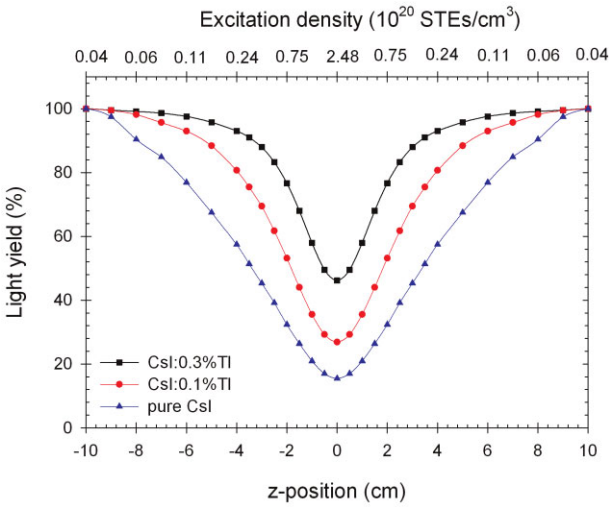

Figure 6 (online color at: www.pss-b.com) Calculated light yield as a function of z-position and excitation density for pure CsI and CsI doped with 0.1 or 0.3 mol% Tl.

that the KMC model may not include all the processes that are affected by the Tl concentration. For example, it does not explicitly account for surface quenching of STEs and this process is likely to play an increasing role as the Tl concentration decreases. However, Fig. 6 suggests that one effect of decreasing the Tl concentration is to increase the relative extent of quenching. This effect is due to a lower extent of STE dissociation at lower Tl concentrations, which allows the STEs to survive longer and thus increases the amount of dipole–dipole Förster transfer, thereby leading to a greater extent of nonlinear quenching. This is supported by the time-resolved optical absorption study of Williams et al. [33] discussed above, which also showed that the rate and extent of conversion between the STE and Tl^0 bands was slower for the CsI sample doped with 0.01 mol% Tl versus that doped with 0.3 mol% Tl. The simulations also predict a slight increase in STE emission when decreasing the Tl concentration from 0.3 to 0.1 mol% Tl, in agreement with experimental luminescence spectra [16].

5 Conclusions A KMC model of scintillation mechanisms in CsI and CsI(Tl), previously developed for simulating the kinetics and efficiency of scintillation of γ-ray irradiated CsI [17], was modified to extend its applicability to high excitation densities. Specifically, a distance-dependent dipole–dipole Förster transfer process was added to the KMC model. Recent experimental data on the excitation density dependence of scintillation light yields offered an unprecedented opportunity to parameterize this process for CsI. Within the framework of the KMC model, good agreement was obtained with the kinetics and efficiency of the scintillation of UV-excited CsI samples. The simulations were then used to identify the general sequence of events following UV excitation and the time evolution of the populations of the principal species involved

in the scintillation process. This approach provides a unique opportunity to calibrate STE–STE interaction parameters for other scintillators. Such microscopic models of scintillation mechanisms can be used in combination with γ-ray-induced ionization tracks calculated by NWEGRIM to investigate the non-proportional response of CsI and other inorganic scintillators.

Acknowledgements The authors acknowledge Drs. Luke W. Campbell, Micah Prange, Renee M. Van Ginhoven, and YuLong Xie for insightful discussions. This research was supported by the National Nuclear Security Administration, Office of Nuclear Nonproliferation Research and Engineering (NA-22), of the U.S. Department of Energy (DOE).

References

[1] P. Dorenbos, J. T. M. de Haas, and C. W. E. van Eijk, IEEE Trans. Nucl. Sci. **42**, 2190 (1995).
[2] J. E. Jaffe, D. V. Jordan, and A. J. Peurrung, Nucl. Instrum. Methods A **570**, 72 (2007).
[3] W. W. Moses, S. A. Payne, W.-S. Choong, G. Hull, and B. W. Reutter, IEEE Trans. Nucl. Sci. **55**, 1049 (2008).
[4] W. W. Moses, G. A. Bizarri, R. T. Williams, S. A. Payne, A. N. Vasil'ev, J. Singh, Q. Li, J. Q. Grim, and W.-S. Choong, IEEE Trans. Nucl. Sci. **59**, 2038 (2012).
[5] M. Moszyński, J. Zalipska, M. Balcerzyk, M. Kapusta, W. Mengesha, and J. D. Valentine, Nucl. Instrum. Methods Phys. Res. A **484**, 259 (2002).
[6] M. Moszyński, Nucl. Instrum. Methods Phys. Res. A **505**, 101 (2003).
[7] S. A. Payne, N. J. Cherepy, G. Hull, J. D. Valentine, W. W. Moses, and W.-S. Choong, IEEE Trans. Nucl. Sci. **56**, 2506 (2009).
[8] S. A. Payne, W. W. Moses, S. Sheets, L. Ahle, N. J. Cherepy, B. Sturm, S. Dazeley, G. Bizarri, and W.-S. Choong, IEEE Trans. Nucl. Sci. **58**, 3392 (2011).
[9] G. Bizarri, W. W. Moses, J. Singh, A. N. Vasil'ev, and R. T. Williams, J. Appl. Phys. **105**, 044507 (2009).
[10] G. Bizarri, W. W. Moses, J. Singh, A. N. Vasil'ev, and R. T. Williams, J. Lumin. **129**, 1790 (2009).
[11] G. Bizarri, W. W. Moses, J. Singh, A. N. Vasil'ev, and R. T. Williams, Phys. Status Solidi C **6**, 97 (2009).
[12] G. Bizarri, N. J. Cherepy, W.-S. Choong, G. Hull, W. W. Moses, S. A. Payne, J. Singh, J. D. Valentine, A. N. Vasilev, and R. T. Williams, IEEE Trans. Nucl. Sci. **56**, 2313 (2009).
[13] J. Singh, J. Appl. Phys. **110**, 024503 (2011).
[14] Q. Li, J. Q. Grim, R. T. Williams, G. A. Bizarri, and W. W. Moses, J. Appl. Phys. **109**, 123716 (2011).
[15] R. T. Williams, Q. Li, J. Q. Grim, K. B. Ucer, G. Bizarri, and W. W. Moses, Proc. SPIE **7805**, 1 (2010).
[16] R. T. Williams, J. Q. Grim, Q. Li, K. B. Ucer, and W. W. Moses, Phys. Status Solidi B **248**, 426 (2011).
[17] S. Kerisit, K. M. Rosso, and B. D. Cannon, IEEE Trans. Nucl. Sci. **55**, 1251 (2008).
[18] S. Kerisit, K. M. Rosso, B. D. Cannon, F. Gao, and Y. Xie, J. Appl. Phys. **105**, 114915 (2009).
[19] Z. Wang, Y.-L. Xie, B. D. Cannon, L. W. Campbell, F. Gao, and S. Kerisit, J. Appl. Phys. **110**, 064903 (2011).
[20] Z. Wang, Y.-L. Xie, L. W. Campbell, F. Gao, and S. Kerisit, J. Appl. Phys. **112**, 014906 (2012).
[21] M. Kirm, V. Nagirnyi, E. Feldbach, M. De Grazia, B. Carré, G. Geoffroy, J. Gaudin, N. Fedorov, P. Martin, A. Vasil'ev, and A. Belsky, Phys. Rev. B **79**, 233103 (2009).
[22] V. Nagirnyi, S. Dolgov, M. Kirm, L. L. Nagornaya, F. Savikhin, V. Sirutkaitis, S. Vielhauer, and A. Vasil'ev, IEEE Trans. Nucl. Sci. **57**, 1182 (2010).
[23] J. Q. Grim, Q. Li, K. B. Ucer, R. T. Williams, A. Burger, P. Bhattacharya, E. Tupitsyn, G. A. Bizarri, and W. W. Moses, MRS Proc. **1341**, 15 (2011).
[24] J. Q. Grim, Q. Li, K. B. Ucer, R. T. Williams, and W. W. Moses, Nucl. Instrum. Methods Phys. Res. A **652**, 284 (2011).
[25] J. Q. Grim, Experimental and Computational Studies of Nonlinear Quenching in Materials used as Radiation Detectors, Ph.D. Thesis, Wake Forest University, Winston-Salem, NC, 2012.
[26] J. Q. Grim, K. B. Ucer, R. T. Williams, A. Burger, P. Bhattacharya, E. Tupitsyn, G. A. Bizarri, and W. W. Moses, IEEE Symposium on Radiation Measurements and Applications, Oakland, CA, USA (2012).
[27] J. Q. Grim, K. B. Ucer, A. Burger, P. Bhattacharya, E. Tupitsyn, E. Rowe, V. M. Buliga, L. Trefilova, A. Gektin, G. A. Bizarri, W. W. Moses, and R. T. Williams, Phys. Rev. B (in press, 2013).
[28] H. B. Dietrich, and R. B. Murray, J. Lumin. **5**, 155 (1972).
[29] F. Gao, L. W. Campbell, R. Devanathan, Y. Xie, L. R. Corrales, A. J. Peurrung, and W. J. Weber, Nucl. Instrum. Methods A **579**, 292 (2007).
[30] F. Gao, L. W. Campbell, R. Devanathan, Y. Xie, Y. Zhang, A. J. Peurrung, and W. J. Weber, Nucl. Instrum. Methods. B **255**, 286 (2007).
[31] F. Gao, L. W. Campbell, Y. Xie, R. Devanathan, A. J. Peurrung, and W. J. Weber, IEEE Trans. Nucl. Sci. **55**, 1079 (2008).
[32] F. Gao, Y. Xie, S. Kerisit, L. W. Campbell, and W. J. Weber, Nucl. Instrum. Methods Phys. Res. A **652**, 564 (2011).
[33] R. T. Williams, K. B. Ucer, J. Q. Grim, K. C. Lipke, L. M. Trefilova, and W. W. Moses, IEEE Trans. Nucl. Sci. **57**, 1187 (2010).
[34] A. N. Vasil'ev, IEEE Trans. Nucl. Sci. **55**, 1054 (2008).
[35] T. Sidler, J. P. Pellaux, A. Nouailhat, and M. A. Aegerter, Solid State Commun. **13**, 479 (1973).
[36] M. Barland, E. Duval, and A. Nouailhat, J. Phys. C, Solid State Phys. **14**, 4237 (1981).
[37] S. E. Derenzo, and M. J. Weber, Nucl. Instrum. Methods A **422**, 111 (1999).
[38] F. J. Keller, and R. B. Murray, Phys. Rev. **150**, 670 (1966).
[39] H. Nishimura, M. Sakata, T. Tsujimoto, and M. Nakayama, Phys. Rev. B **51**, 2167 (1995).
[40] A. N. Belsky, A. N. Vasil'ev, V. V. Mikhailin, A. V. Gektin, P. Martin, C. Pedrini, and D. Bouttet, Phys. Rev. B **49**, 13197 (1994).
[41] A. N. C. Belsky, R. Cortes, A. V. Gektin, P. Martin, V. V. Mikhailin, and C. Pedrini, J. Lumin. **72–74**, 93 (1997).
[42] M. P. Prange, R. M. Van Ginhoven, N. Govind, and F. Gao, (in review, 2013).
[43] B. Sadigh, D. Åberg, and P. Erhart, IEEE Symposium on Radiation Measurements and Applications, Oakland, CA, USA (2012).
[44] C. Amsler, D. Grögler, W. Joffrain, D. Lindelöf, M. Marchesotti, P. Niederberger, H. Pruys, C. Regenfus, P. Riedler, and A. Rotondi, Nucl. Instrum. Methods A **480**, 494 (2002).

[45] J. D. Valentine, W. W. Moses, S. E. Derenzo, D. K. Wehe, and G. F. Knoll, Nucl. Instrum. Methods A **325**, 147 (1993).
[46] W. B. Hadley, S. Polick, R. G. Kaufman, and H. N. Hersh, J. Chem. Phys. **45**, 2040 (1966).
[47] R. G. Kaufman, W. B. Hadley, and H. N. Hersh, IEEE Trans. Nucl. Sci. **17**, 82 (1970).
[48] D. Fröhlich, B. Staginnus, and Y. Onodera, Phys. Status Solidi **40**, 547 (1970).
[49] J. E. Eby, K. J. Teegarden, and D. B. Dutton, Phys. Rev. **116**, 1099 (1959).
[50] K. Teegarden, and G. Baldini, Phys. Rev. **155**, 896 (1967).
[51] H. B. Dietrich, A. E. Purdy, R. B. Murray, and R. T. Williams, Phys. Rev. B **8**, 5894 (1973).
[52] V. Yakovlev, L. Trefilova, and A. Meleshko, J. Lumin. **129**, 790 (2009).

Kinetic Monte Carlo Simulations of Scintillation Processes in NaI(Tl)

Sebastien Kerisit, Zhiguo Wang, Richard T. Williams, *Member*, *IEEE*, Joel Q. Grim, and Fei Gao

***Abstract*—Developing a comprehensive understanding of the processes that govern the scintillation behavior of inorganic scintillators provides a pathway to optimize current scintillators and allows for the science-driven search for new scintillator materials. Recent experimental data on the excitation density dependence of the light yield of inorganic scintillators presents an opportunity to incorporate parameterized interactions between excitations in scintillation models and thus enable more realistic simulations of the nonproportionality of inorganic scintillators. Therefore, a kinetic Monte Carlo (KMC) model of elementary scintillation processes in NaI(Tl) is developed in this work to simulate the kinetics of scintillation for a range of temperatures and Tl concentrations as well as the scintillation efficiency as a function of excitation density. The ability of the KMC model to reproduce available experimental data allows for elucidating the elementary processes that give rise to the kinetics and efficiency of scintillation observed experimentally for a range of conditions.**

***Index Terms*—scintillation mechanisms, nonproportionality, radiation detection, γ-ray spectroscopy, kinetic Monte Carlo.**

I. Introduction

Inorganic scintillators are used extensively for radiation detection and γ-ray spectroscopy. Key properties of inorganic scintillators that determine their application as radiation detectors include their emission spectra, decay kinetics, and light yields. All of these properties are manifestations of the relaxation of ionization tracks that are created when γ-rays (or any ionizing particles) penetrate scintillator materials and produce high-energy secondary electrons that are slowed down through the creation of electron-hole pairs. Therefore, developing a thorough understanding of the elementary processes that dictate the relaxation of ionization tracks is critical to improving the performance of existing scintillator materials and accelerating the discovery of new materials. For example, the phenomenon of nonproportionality, whereby the scintillation yield normalized to the incident energy is not constant with incident energy, is one of the main factors that degrade the energy resolution of inorganic scintillators employed in γ-ray spectroscopy; however, the underlying mechanisms that give rise to nonproportionality have not been fully elucidated and improvements in resolution have not achieved their full potential as a result.

Consequently, significant effort has been directed at identifying and quantifying the elementary processes of scintillation in inorganic materials. In this work, we investigate the kinetics and efficiency of the elementary processes of scintillation in NaI(Tl). NaI has been widely used as a radiation detector since its discovery as a scintillation crystal in 1948 [1] and is often used as a basis for comparison for emerging scintillator materials. Over the years, several theoretical and conceptual models have been developed to explain the scintillation response of NaI [2-6].

Early modeling work by Murray and Meyer (MM) [2] focused on evaluating the scintillation efficiency of NaI as a function of stopping power, dE/dx, in an attempt to put the response to different ionizing particles on the same footing. The MM model assumes that self-trapped excitons (STE) are the sole energy carriers, whereas those electron-hole pairs that fail to recombine as STEs degrade the scintillation efficiency. However, Hill and Collinson [4, 7] later showed that the MM model did not give an accurate representation of the scintillation efficiency at high dE/dx. In addition, work by Dietrich et al. [8] on NaI(Tl) and KI(Tl) and by Delbecq et al. [9] on Tl-doped potassium halides, yielded proof of the presence of Tl^0 and Tl^{++} species resulting from the capture, at Tl^+ sites, of electrons and holes, respectively. These findings provided strong evidence that STEs were not the sole carriers. Therefore, a subsequent model was put forth by Dietrich and Murray (DM) [3], in which the creation of Tl excited states resulted from the binary recombination of electrons and holes (controlled either by hole diffusion or by electron de-trapping) or the prompt capture of an electron and a hole at a Tl site. This three-process model has been used on many occasions to model the scintillation kinetics of NaI [10-11] and other alkali halides, (e.g. CsI [12]). A more recent model developed by Alexandrov et al. [6] extended the DM model to include the dissociation of STEs during their diffusion.

In a previous study [13], we developed a kinetic Monte Carlo (KMC) model of the scintillation mechanisms in CsI(Tl) based on the DM model. The KMC model applied a modified version of the DM model onto a three-dimensional lattice in which all species (activators, holes, excitons, etc) were represented explicitly and treated individually. The KMC

This work was supported by the National Nuclear Security Administration, Office of Nuclear Nonproliferation Research and Engineering (NA-22), of the U.S. Department of Energy (DOE).

S. Kerisit, Z. Wang, and F. Gao are with the Physical Sciences Division, Pacific Northwest National Laboratory, Richland, WA 99352 USA (e-mail: sebastien.kerisit@pnnl.gov; zhiguo.wang@pnnl.gov; fei.gao@pnnl.gov).

R.T. Williams and J.Q. Grim are with the Department of Physics, Wake Forest University, Winston-Salem, NC 27109 USA (e-mail: williams@wfu.edu; grimjq@wfu.edu)

model was found to be capable of reproducing both the kinetics and the efficiency of scintillation in CsI(Tl) and, therefore, was used subsequently to simulate the nonproportionality of CsI at low incident γ-ray energies [14].

Because it does not deal with the scintillation efficiency [3], the original DM model cannot explain the variations in light yield with excitation density and, therefore, it does not allow for modeling the nonproportional behavior of alkali halides. In addition, two recent developments have provided an incentive to revisit the scintillation mechanisms of NaI and generate a KMC model similar to that developed for CsI. Firstly, although STEs were previously thought to diffuse faster than self-trapped holes (STH) in NaI [15-17], recent electronic structure calculations have provided evidence that they are equally mobile in NaI [18-19]. Secondly, previous models of NaI scintillation did not treat potential interactions between excitations and, therefore, could not account for the excitation density dependence of the light yield. Recent experimental work [20-22] has made available data for parameterizing second order quenching interactions, as was done previously for CsI [23]. This approach is expected to lead to improved models of nonproportionality in inorganic scintillators.

Therefore, this work aims to develop a KMC model of scintillation mechanisms in NaI(Tl) in order to identify the processes that give rise to its scintillation properties and study the effects of varying the temperature, Tl concentration, and excitation density. The model parameters are determined using available experimental and quantum mechanical data and the model is evaluated against two types of experimental data: (1) the scintillation kinetics as a function of temperature and Tl concentration following γ-ray excitation (662 keV); and (2) the luminescence yield as a function of excitation density following ultraviolet (UV) excitation (5.9 eV).

II. Computational Approach

The KMC model was developed in a previous study of scintillation mechanisms in CsI(Tl) [13]. In this work, it was extended to consider alkali halides that adopt the rocksalt structure (e.g. NaI). In this implementation, a simple cubic lattice is used, in which each lattice point represents either a cation (Na^+) or an anion (I^-) and periodic boundary conditions (PBC) are applied. STHs form in alkali halides by localizing on two neighboring halide ions and can capture an electron to form STEs. Therefore, STHs and STEs are represented as occupying two neighboring I^- sites. The diffusion of STHs and STEs is treated using a random-walk approach and Tl^+ ions are placed randomly at Na^+ sites to achieve the desired concentration.

The rate, k, of each process is determined by the Arrhenius equation: $k=A\exp(-W/k_BT)$, where A is the pre-exponential factor, W the activation energy, k_B the Boltzmann constant, and T the temperature. The model parameters are given in Table I and discussed in section III.

The KMC program is executed using the following algorithm: (1) the rate of each process is calculated using the Arrhenius equation and is multiplied by the number of species (STE, STH, $(Tl^+)^*$, Tl^0) that can undergo this process; (2) a process is selected with a probability proportional to the product calculated in (1) using a random number, x_1, uniform in (0,1]; (3) the selected process is executed on a randomly chosen species that can undergo this process; (4) time is increased by $-\ln(x_2)/\Gamma$, where x_2 is another random number uniform in (0,1] and Γ is the sum of all rates. Steps (1) to (4) are repeated until all electron-hole pairs have undergone radiative or non-radiative decay.

III. Derivation of the Model Parameters

Six processes are considered in this work when simulating the γ-ray response of NaI(Tl): STH and STE diffusion, STE radiative and non-radiative decay, $(Tl^+)^*$ radiative decay, and electron thermal release from Tl^0. Two additional processes, namely, dipole-dipole Förster transfer and STE dissociation, are also considered when simulating the light yield of UV-excited NaI. A modification is also made to the STE decay rates in these simulations to account for the shortening of the STE lifetime due to quenching at the surface. Modifications made to the KMC model for UV-excited NaI(Tl) will be described in detail in section IV-C.

STH and STE diffusion occurs via thermally activated hopping to near-neighbor sites. In NaI, STHs and STEs can hop in principle to 8 first-nearest neighbors (60° rotation), 4 second-nearest neighbors (90° rotation), 4 third-nearest neighbors (120° rotation), 2 fourth-nearest neighbors (180° rotation). Prange et al. [19] calculated the energy barriers of each of the four near-neighbor hops using density functional theory (DFT) calculations. For both STHs and STEs, they found the 60° and 180° rotations to have lower barriers than the 90° and 120° rotations. Although the calculated values differed slightly, Sadigh et al. [18] also predicted the 60° and 180° rotations to have lower barriers than the 90° and 120° rotations. Therefore, only the 60° and 180° hops are considered in the KMC model. Interestingly, both studies found the barriers for STHs and STEs to be similar, indicating that STEs and STHs are equally mobile in NaI. In the calculations of Prange et al. [19], the average barrier weighted by the number of possible hops for each of the two rotations considered in the KMC model was 0.2246 eV and 0.2108 eV for STHs and STEs, respectively. Therefore, an average energy barrier of 0.22 eV was used for both STHs and STEs. The pre-exponential factor was derived from thermal-reorientation experiments of STHs in KI [24].

There is only very limited experimental data on the activation energy for STE and STH diffusion in NaI. Popp and Murray [15] determined the activation energy for STH rotation (a combination of the 60° and 90° rotations). Their experimental procedure involved measuring the kinetics of decay of the optical density of STHs created by either high-energy electrons or x-rays as they thermally re-orientate following bleaching at very low temperature. The temperature -dependent data yielded 0.18 eV for the activation energy; however, the experimental fits were made for measurements taken between approximately 44 and 52 K suggesting that extrapolating to the temperature range of interest in this study (243 to 333 K) may carry a sizeable uncertainty.

Nagata et al. [16] reported an activation energy for STE diffusion in NaI of 0.07 eV. Taken in conjunction with the activation energy for STH diffusion derived by Popp and Murray [15], this result would suggest that STEs and STHs are not equally mobile in NaI, which goes against the conclusion drawn from the calculations of Prange et al. [19] and Sadigh et al. [18]. However, the value reported by Nagata et al. was not obtained directly from their measurements. Instead, it was determined from a model fit of the change in light yield in the temperature range 5 to 200 K, with the light yield expressed as the ratio of the radiative rate over the sum of the radiative and non-radiative rates. The radiative rate was taken to be the decay time at 5 K (for which the light yield is 1) and the non-radiative rate was expressed as $(A/T^{1/2})\exp(-W/k_BT)$, where A and W were fitted to the light yield data. Nagata et al. assumed that the non-radiative rate stemmed from the surface recombination of STEs and thus equated W with the activation energy for STEs to diffuse to the surface; but additional processes could be involved, such as STE thermal non-radiative decay, quenching at surface sites, or STE dissociation. Therefore, the activation energy reported by Nagata et al. actually represents the effective activation energy of all non-radiative processes rather than the energy barrier for individual STE near-neighbor hops, which is the quantity of interest in our model.

For the STE radiative decay process, the pre-exponential factor was set to the decay time obtained by Nagata et al. [16] for pure NaI at 5 K. The 4.2-eV emission band is the dominant intrinsic emission band in pure NaI under both x-ray [25] and UV excitation [16, 26] and it is thus assumed to be the sole STE emission in the KMC model. As was done by Nagata et al., this process was taken not to be thermally activated and therefore its activation energy was set to zero. Although the parameters for the STE non-radiative decay process could be extrapolated from the data of Nagata et al. [16], these values would likely encompass other processes, as discussed above, since the data of Nagata et al. were obtained for UV excitation (near surface) and the focus of the first part of this work is on the scintillation response to γ-ray excitation. Therefore, the rate parameters for STE non-radiative decay were derived from the experimental data of Moszyński et al. [11], as described in the following paragraph.

Moszyński et al. [11] measured the scintillation kinetics of NaI(Tl) following γ-ray irradiation at 662 keV from 243 K to 333 K. They fitted the scintillation decay curves with two exponential terms (termed "fast" and "slow") from 333 K to 273 K and added a third term below 273 K (termed "superfast"). The parameters for $(Tl^+)^*$ radiative decay and for electron thermal release from Tl^0 were obtained from the temperature dependence of the "fast" and "slow" components, respectively. In the KMC algorithm, electron release from Tl^0 is assumed to lead to electron capture at Tl^{++}. The "superfast" component could be attributed to STE emission but it has a longer decay time (160 ns at 243K [11]) than expected based on the decay time of pure NaI obtained at a similar temperature (20 ns at 220 K [27]). However, the tunneling and/or de-trapping of electrons from Tl^0 to recombine with STHs are likely to cause delayed STE emission [9, 28] in Tl-doped alkali halides. Therefore, the "superfast" component was taken to be due to delayed STE emission and its temperature dependence was used to obtain the parameters for STE effective non-radiative decay (i.e. accounting for the effects of electron release/tunneling from Tl^0).

TABLE I
PARAMETERS USED IN THE KMC MODEL

Process	A (s^{-1})	W (eV)
STH diffusion	5.1×10^{12}	0.220
STE diffusion	5.1×10^{12}	0.220
STE radiative decay (γ-ray)	6.3×10^{6}	0.000
STE effective non-rad. decay (γ-ray)	2.9×10^{6}	0.032
STE effective decay[a] (UV)	1.3×10^{9}	-
$(Tl^+)^*$ radiative decay	3.3×10^{8}	0.110
Electron thermal release from Tl^0	6.2×10^{7}	0.105
STE dissociation[b] (UV)	1.7×10^{11}	-
Process	**R_{dd} (a_0)**	**B (s^{-1})**
Förster transfer (UV)	4.5	7.4×10^{7}

[a]This process accounts for all the STE linear decay rates.
[b]This process takes place only if a Tl^+ is available with a 3 a_0 radius.

An additional factor to consider is the proportion of STEs and STHs in the KMC simulations. Thermal dissociation of STEs is likely in the conditions simulated in this work; therefore, the proportion of STEs should diminish with increasing temperature. Emkey et al. [29] determined experimentally the activation energy for exciton dissociation to be 0.06 eV. Although the first-principles calculations of Prange et al. [19] suggested a lower value (0.02 eV) and the calculations of Sadigh et al. [18] a higher value (0.1 eV), both values are of the same order of magnitude as the experimental value. Wang et al. [30-31] used a phenomenological model of electron thermalization to calculate the probability of electron-hole pair recombination during thermalization and following γ-ray excitation of alkali iodide and alkaline-earth fluoride scintillators. One of the main conclusions of this work was that, although a significant proportion of electron-hole pairs rapidly recombine during thermalization, many electrons were able to travel tens to hundreds of nanometers away from the core of the track before being fully thermalized (these electrons were referred to as "stopped" electrons). The probability for recombination calculated by Wang et al. [31] at room temperature for the highest incident energy considered in that study (0.32 at 400 keV) was used as the reference point from which the probability of STE formation was calculated using the dissociation energy of Emkey et al. [29], as described in the Appendix. Although this approach only provides a rough estimation, which should be refined in the future, it does account for the fact that STEs are likely to thermally dissociate and, as will be shown in section IV-A, it does lead to good agreement with the experimental data of Moszyński et al. [11]. The results were found to not be sensitive to small changes in the probability of STE formation (data not shown).

Using a simple model for describing electron capture at Tl sites during thermalization, Wang et al. [30-31] were also able to evaluate the proportion of "recombined", "stopped" and

"Tl-trapped" electrons as a function of Tl concentration. As described in the Appendix, this data was used to determine the proportion of STHs and STEs as well as the number of initial electron-hole pairs in the KMC simulations as a function of Tl concentration. Indeed, the "stopped" electrons were considered to have travelled too far to be able to recombine with holes within the timescale of interest to this work (a few μs) or to have trapped at defects and impurities and, therefore, they were not considered in the KMC model, which means that different initial numbers of electron-hole pairs were used as a function of Tl concentration.

Finally, the KMC model also considers the thermal trapping of holes, as first suggested by Hadley et al. [32] for KI(Tl) and Kaufman et al. [33] for NaI(Tl), whereby any hole created within a volume of 25 unit cells around a Tl^+ ion is promptly captured at that site. Therefore, a prompt capture radius, r_0, of 19 Å was used in the KMC model.

IV. Results and Discussion

A. Scintillation kinetics as a function of temperature

A series of KMC simulations were performed to calculate the scintillation kinetics of NaI doped with 0.1 mol% of Tl from 243 K to 333 K for comparison with the experimental data of Moszyński et al. [11] obtained for 662-keV γ-rays. Although some of the parameters of the KMC model were determined based on this experimental data set, others were not and, therefore, it is important to evaluate whether the simulated scintillation kinetics are consistent with the data of Moszyński et al. Additionally, this subsection aims to identify the processes that give rise to any changes in the observed scintillation behavior as a function of temperature.

An electron-hole pair density of 10^{18} cm^{-3} was used, which is within the range of densities (10^{16} to 10^{19} cm^{-3}) used by Dietrich and Murray [3] based on the calculations of Katz and Kobetich [34] on the energy deposited by positive ions in NaI. The calculated scintillation decay curves are independent of the electron-hole pair density for densities lower or equal to 10^{19} cm^{-3}. In ionization tracks created by 662-keV γ-rays, the proportion of regions with densities higher than 10^{19} cm^{-3} is expected to be small [14]. For each temperature, the scintillation decay curves were constructed from 1,400 simulations, for a total of approximately 100,000 electron-hole pairs. The simulation cells consisted of 128×128×128 sites. Given a Na^+-I^- interatomic distance of 0.3236 nm [35], this corresponds to a cube with a side length of approximately 45 nm. Activators, STHs, and STEs were placed randomly on the lattice at the start of each simulation. As was done in simulations of CsI(Tl) [13], electrons captured at Tl^+ sites were not positioned explicitly but, instead, a probability x_c was used, when a STH is captured at a Tl^+ site, to determine whether this site has previously captured an electron. This correlation probability was set to the intensity of the "fast" component determined by Moszyński et al. and serves to account for the electrostatic interactions between STHs and Tl^0 sites, which are not included in the KMC model.

In Figure 1, simulation results obtained at four temperatures are compared with the experimental data of Moszyński et al. [11]. There are small differences in a few places; however, we cannot be certain of the significance of those differences because experimental error bars were not provided in [11]. Although, overall, the kinetics of scintillation accelerate with increasing temperature as expected, the experimental data show an interesting behavior in the early times. At low temperatures, NaI exhibits a relatively slow decay, which becomes faster with increasing temperature, but subsequently shows the appearance of an intensity maximum. Moszyński et al. concluded from this observation that NaI followed different mechanisms of scintillation at different temperatures.

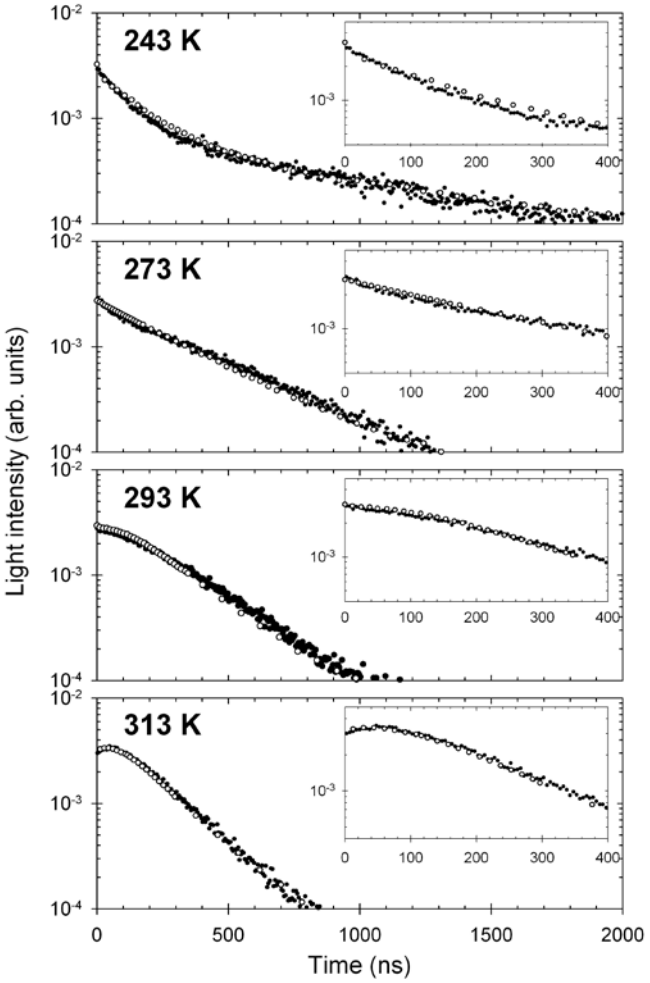

Fig. 1. Comparison of the calculated scintillation decay curves (solid circles) with the experimental data of Moszyński et al. [11] (empty circles) for a range of temperatures. Insets show a close-up of the first 400 ns.

Although only the total light intensity as a function of time can be validated against the data of Moszyński et al., it is of interest to discuss the contribution of the different processes in the KMC simulations in an effort to identify the mechanisms underlying this apparent change in scintillation behavior. Figure 2 shows the contribution of several processes to the total light yield as a function of time for three temperatures. At low temperature, STE/STH diffusion is slow and STEs decay radiatively before STEs and STHs can reach Tl^+ sites. As the temperature increases, the STE population decays at a faster

rate and STEs and STHs diffuse faster; therefore, binary recombination (i.e. sequential capture of an electron and a hole at a thallium site) becomes more dominant in the early times. Eventually, at high temperatures, the contribution of STE emission becomes small and a delayed maximum begins to appear. In summary, the rising time becomes shorter as the temperature increases but is not visible until high temperatures are reached due to the STE emission, which dominates in the early times at low temperatures.

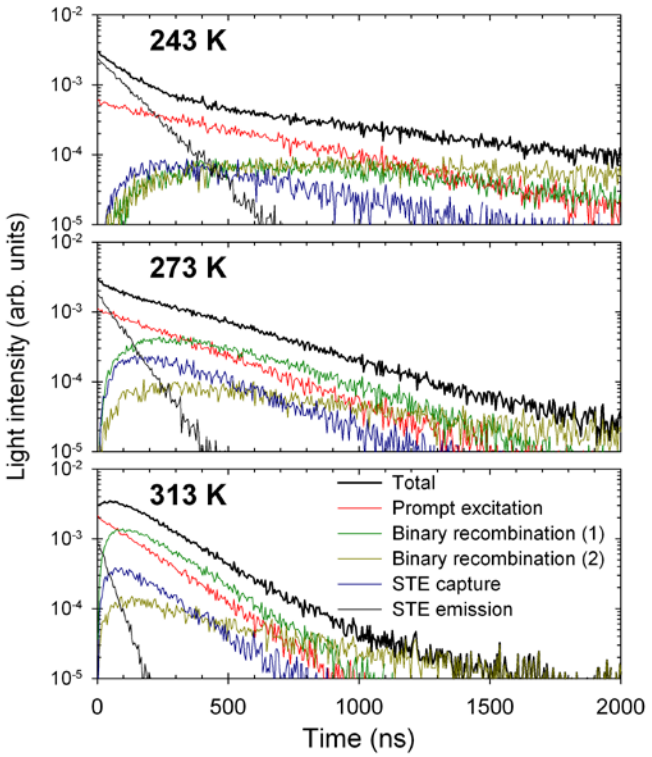

Fig. 2. Contributions from all scintillation processes to the calculated scintillation decay curves obtained at 243 K, 273 K, and 313 K. Binary recombination (1) is that controlled by STH diffusion whereas (2) is controlled by electron thermal release.

A sensitivity analysis was carried out to determine the processes that most affect the agreement between the calculated and experimental scintillation decay curves. To do so, additional series of KMC simulations were carried out. In each series, the rate of one of the six processes (k_x) was varied between 0.1 and 10 times the rate obtained from the parameters in Table I ($k_{norm.}$). Because STH and STE diffusion use the same parameters, their rates were varied simultaneously. For each value of $k_x/k_{norm.}$, the root mean square logarithmic error was calculated from the differences between the calculated and experimental values of the light intensity for each experimental data point. Figure 3 shows the results obtained for two of the temperatures presented in Figures 1 and 2 and indicates that the agreement between the calculated and experimental scintillation kinetics is most sensitive to the rate of $(Tl^+)^*$ radiative decay. This is to be expected as most of the light is emitted by thallium. Figure 3 also suggests that no significant improvement of the agreement with the data of Moszyński et al. could be obtained by changing any of the current process parameters.

B. Scintillation kinetics as a function of Tl concentration

A second series of KMC simulations were performed at 298 K to study the scintillation kinetics of NaI(Tl) for Tl concentrations ranging from 0.001 to 1.0 mol%. The simulation cell size, number of simulations, and reference electron-hole pair density were the same as the simulations described in section IV-A. The experimental data used for comparison in this section were not included in the model parameterization; therefore, this section provides an example of the applicability of the KMC model beyond the conditions used for its parameterization.

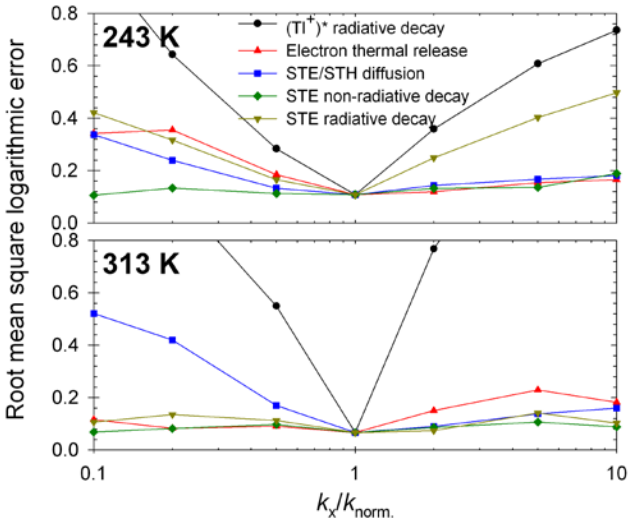

Fig. 3. Sensitivity analysis of the processes used to simulate the scintillation kinetics at 243 K and 313 K.

In Figure 4, the simulation results are compared to the experimental data of Kubota et al. [10] obtained for 662-keV γ-rays. At 0.1 mol%, the calculated light intensity decays slightly more slowly in the later times than the data of Kubota et al. Because this Tl concentration is the same as that used in the comparison with the data of Moszyński et al. [11] and that, in that case, the agreement between the experimental and calculated scintillation kinetics was closer, we conclude that the slight discrepancy in the later times is likely due to differences in sample composition and/or experimental approach used in the two experimental studies.

At 0.22 mol and 0.01 mol%, the experimental data of Kubota et al. [10] show greater fluctuations than at 0.1 mol%, which makes an accurate comparison more difficult. Nonetheless, as seen for 0.1 mol%, the experimental data show a slightly faster decay in the later times. In the early times, the KMC simulations predict that the scintillation decay curves change from a single exponential decay to a flat top. At low Tl concentrations, capture of STEs and STHs at Tl sites is slow and some of the STEs are able to decay radiatively leading to the single exponential decay. As the Tl concentration increases, however, the STEs are captured faster and do not have time to decay radiatively and thus the flat top becomes apparent. It is difficult to compare the very early times at 0.01 and 0.22 mol% Tl due to the large fluctuations in the experimental data in the first few tens of nanoseconds and the lack of data points within approximately 10 ns. Therefore,

it is not possible to definitely confirm or refute this finding. However, it is consistent with the experimental observation of the appearance of an intrinsic emission peak in alkali iodide emission spectra at low Tl concentrations [12, 36].

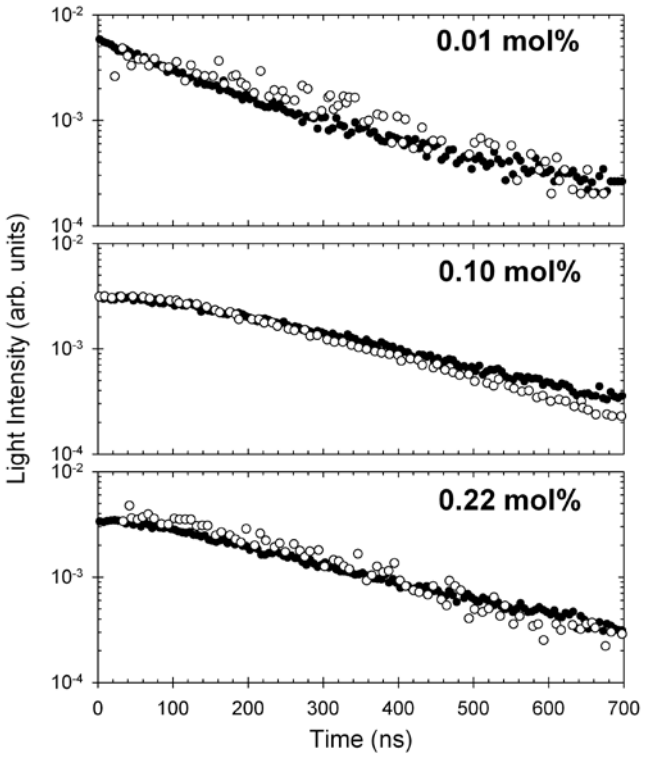

Fig. 4. Comparison of the calculated scintillation decay curves (solid circles) with the experimental data of Kubota et al. [10] (open circles – size of data points commensurate with errors) for a range of Tl concentrations.

From the same set of simulations, the scintillation light yield was also obtained and is compared, in Figure 5, to the experimental data of Kubota et al. [37] and of Harshaw et al. (as given by Murray and Meyer [2]) as a function of Tl concentration. Although there is an increase in STE non-radiative decay as the Tl concentration decreases (from none at 1.0 mol% Tl to 10% of the electron-hole pairs at 0.001 mol% Tl), the dominant factor leading to the decrease in the light yield with decreasing Tl concentration is the increase in the number of "stopped" electrons, which are not explicitly considered in the KMC simulations, as explained in section III. In other words, as the Tl concentration decreases, the probability for electron capture by Tl during thermalization is reduced and more electrons are able to travel away from the core of the ionization track thus leading to a decrease in light output. The general trend with increasing Tl concentration is reproduced by the simulations; albeit with not as steep a rise as seen experimentally. However, parameterization of the electron capture process in the thermalization calculations was only approximate [30] and increasing its probability leads to a steeper rise.

C. Scintillation efficiency as a function of excitation density

A series of KMC simulations were performed at 298 K to investigate the effect of the initial density of electron-hole pairs on the scintillation efficiency and thus model the experiments of Grim et al. [20] on the excitation density dependence of the light yield of NaI(Tl) using sub-picosecond UV excitation (referred to hereafter as z-scan experiments). Several aspects of the computational approach were changed with respect to the approach used in the previous sections to reflect the change in excitation energy and follow the approach used previously for CsI(Tl) [23].

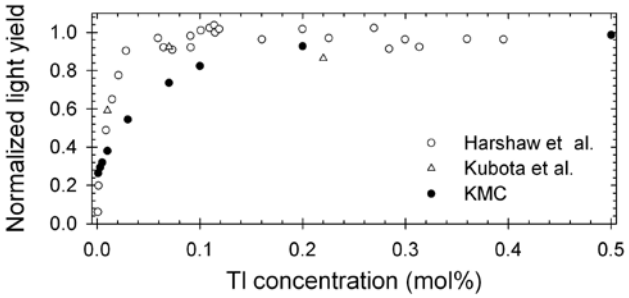

Fig. 5. Comparison of the calculated light yield with the experimental data of Harshaw et al. (as given by Murray and Meyer [2]) and Kubota et al. [37] as a function of thallium concentration.

Eby et al. [38] reported a band gap of 5.8 eV and a 1s exciton peak at 5.56 eV for NaI at 80 K. These values are expected to decrease with increasing temperature; and, indeed, the 1s exciton peak moves to 5.39 eV at room temperature (it was not possible to determine the band gap at room temperature in that study). Therefore, the photon energy of the UV pulse in the z-scan experiments (5.9 eV) is slightly higher than the band gap and the 1s exciton peak and all electron-hole pairs were thus assumed to begin the simulations as STEs.

An exponentially decaying distribution: $N(z)=N_0\exp(-\alpha z)$, where z is the depth from the surface in lattice layers, $N(z)$ is the concentration of STEs at depth z, α is the absorption coefficient and N_0 is the concentration of STEs at the crystal surface, was used to determine the initial position of the STEs on the lattice. N_0 was calculated from the on-axis laser fluence, absorption coefficient, excitation energy, and position of the beam waist used in the z-scan experiments. The absorption coefficient was set to that used by Grim et al. [20] ($\alpha=4\times10^5$ cm^{-1}), who determined it from the optical density spectrum and film thickness reported for NaI by Martienssen [39]. Because of the large transverse size of the laser spot (~17 μm radius at 1/e) relative to the *x*-*y* size of the simulation cell (~10 nm), the transverse distribution profile was assumed to be flat.

The simulation cell was a three-dimensional lattice of dimensions 32×32×512 sites. Given an inter-site distance of 0.3236 nm for NaI, this corresponds to real dimensions of 10.4×10.4×165.7 nm^3. The UV beam was assumed to be incident along the z direction and PBC were only applied in the directions perpendicular to the beam. The lattice was bound by the crystal surface at z=0. Although the lack of PBC at the other end of the lattice introduces an artificial boundary, the number of STEs in that region is very small given the length of the simulation cell in the z direction (165.7 nm) relative to the absorption coefficient (which translates to a characteristic distance of 25 nm). The STE diffusion distance is also small compared to the length of the simulation cell in

the *z* direction (99% of the STEs diffuse over a distance of 22 nm or less for the lowest excitation density considered). Tl^+ ions were placed randomly on the lattice at Na^+ sites to achieve a concentration of 0.1 mol%, as in the experimental sample. The light yield was determined for each excitation density using the average of 400 simulations.

In addition, a few modifications were made to the model parameters relative to those used in the previous simulations. (1) There was no prompt capture radius as all the electron-hole pairs begin the simulations as STEs. (2) Second-order STE quenching is described by dipole-dipole Förster transfer, a non-radiative transfer whereby a first STE decays by emitting a virtual photon, which is absorbed by a second STE, which dissociates as a result. The rate of Förster transfer is dependent on the distance between STEs and is determined by $k(r)=B(R_{dd}/r)^6$, where R_{dd} is the Förster transfer radius and B is equated to the STE radiative decay rate following the formulation of Vasil'ev [40], which was used subsequently by Kirm et al. [41] and Williams et al. [22]. B was set to the inverse of the decay time (13 ns) determined by van Sciver and Bogart [27] from γ-ray excitation of pure NaI at 300 K. (3) STE dissociation was also considered in these simulations, whereby a STE electron, possibly in an excited bound state, may be scavenged by tunneling transfer to a nearby Tl^+ site to form Tl^0. The positions of the electrons at Tl^0 sites were treated explicitly. Experimentally, STE dissociation was suggested from the recent time-resolved optical absorption measurements of Williams et al. [42], which showed, for CsI(Tl), that the STE absorption band decayed on the time scale of picoseconds and was replaced by a band assigned to Tl^0. The same process is likely to take place in NaI and, since there are no direct experimental data to parameterize this process, its rate was set to that used for CsI(Tl) [23]. (4) The STE linear decay processes were modeled by a single effective decay rate, which was set to the inverse of the lifetime derived by Williams et al. [22]. Indeed, the effective lifetimes obtained by Williams et al. by fitting scintillation decay curves obtained for varying excitation densities in pure NaI at room temperature (singlet=0.75 ns, triplet=5 ns) were shorter than the radiative lifetime measured in the bulk (13 ns) by van Sciver and Bogart [27]. As suggested by Williams et al., this effect is likely due to STE quenching at the crystal surface. Therefore, an effective STE decay rate was used to implicitly account for surface quenching, which was not present in the bulk calculations carried out in the previous sections.

R_{dd} was varied in increments of $a_0/2$ to optimize the agreement with the experimental data. This comparison is quantified through the mean-square error between the observed and calculated light yields (LY_o and LY_i, respectively) normalized to the simulation statistical uncertainties, σ_i, for each of the N simulated excitation densities, i ($\chi^2=(1/N)\Sigma_i[(LY_i-LY_o)/\sigma_i]^2$). Figure 6 compares the experimental data from the z-scan measurements of Grim et al. [20] with the calculated light yields obtained with R_{dd}=4.5 a_0, for which χ^2=2.1. The small differences between observed and calculated light yields are likely due to the assumption of flat transverse profile in the KMC simulations. The value of R_{dd} thus obtained corresponds to a distance of 2.91 nm. Grim et al. [20] deduced R_{dd} from fitting the z-scan light yield data with a second-order rate equation model. Using an exciton capture rate of $(6\ ps)^{-1}$ inferred from their time-resolved optical absorption measurements of CsI(0.3% Tl) [42] (no data is yet available for NaI(Tl)) yielded R_{dd}=4.1 nm [20]. However, if the exciton capture rate at 0.1% Tl is instead deduced from linear interpolation of the measurements at 0.3% ($(6\ ps)^{-1}$) and 0.01% ($(100\ ps)^{-1}$) Tl, R_{dd} becomes 2.9 nm, in excellent agreement with the results of this work. For CsI(0.3% Tl), a value of 3.66 nm was obtained from the KMC simulations [23], compared to 3.8 nm derived from the second-order rate equation model of Grim et al. [20].

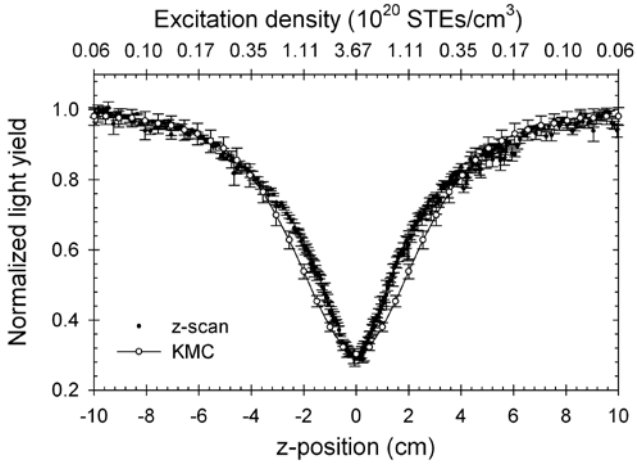

Fig. 6. Comparison of the calculated light yield (open circles) with experimental results of Grim et al. [20] (solid circles – average of 30 runs) for 5.9-eV excitation as a function of the position of the beam waist and excitation density. Error bars correspond to one standard deviation.

In Figure 7, the time evolution of the species populations is shown for two excitation densities. Initially, the STE population decreases due to STE emission, Förster transfer and thermal dissociation, whereby the last process leads to the formation of STHs and Tl^0 sites. At low density, the STH and Tl^0 populations plateau after a few hundred picoseconds, at which point the STH population begins to diminish as STHs are trapped at Tl^+ or Tl^0 sites to form Tl^{++} or $(Tl^+)^*$, respectively. Subsequently, electrons are being released from Tl^0 sites to form $(Tl^+)^*$, which eventually emit light.

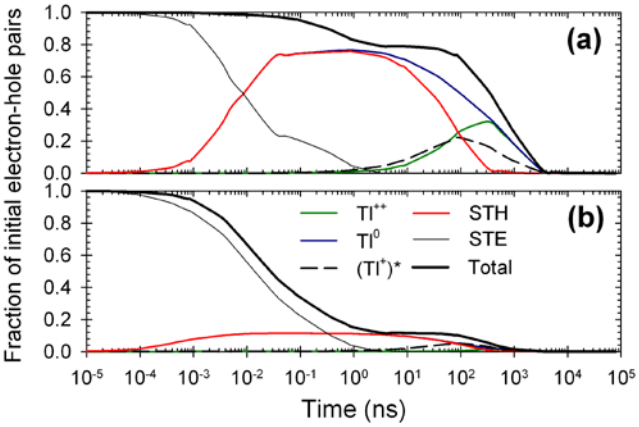

Fig. 7. Time evolution of the species considered in the KMC model at (a) 7.60×10^{18} STEs/cm^3 and (b) 3.67×10^{20} STEs/cm^3.

Figure 7(a) also shows that all STEs disappear within 2-3 ns and the lack of any noticeable increase in the $(Tl^+)^*$ population within this time frame indicates that the formation of $(Tl^+)^*$ via STE capture is negligible. At high density, the sequence of events is similar. One noticeable difference is the fact that the STH and Tl^0 populations plateau more rapidly and while there is still a significant population of STEs. This indicates that Tl^+ sites are saturated by electrons preventing further electron scavenging. Saturation of Tl^+ sites by electrons means that STHs are much more likely to trap at Tl^0 sites than at Tl^+ sites, which leads to a very small Tl^{++} population compared to that observed at low density.

V. Conclusions

A kinetic Monte Carlo model was developed to simulate the scintillation response of NaI(Tl) as a function of temperature, Tl concentration, and excitation density. A set of elementary processes that enables the model to reproduce available experimental data on the kinetics and efficiency of scintillation of NaI(Tl) for a range of conditions was identified and parameterized, including specific parameters for STE second order quenching and energy barriers for STE and STH diffusion from DFT calculations.

Appendix

A. Estimation of the electron populations at 662 keV

In our previous study of electron thermalization [31], the fractions of recombined, Tl-trapped, and stopped electrons were calculated for incident energies up to 400 keV. As they thermalize, electrons can recombine with a hole ("recombined"), become trapped at a Tl site ("Tl-trapped"), or eventually fully thermalize ("stopped"), in which case they are not considered further. The experimental data sets used for comparison in sections IV-A and IV-B [10-11] were both obtained at 662 keV. Although this energy was higher than the maximum energy considered in Wang et al. [31], the fractions of recombined, Tl-trapped, and stopped electrons are linear at the highest incident energies and, therefore, a linear regression was performed using the results obtained between 20 and 400 keV to estimate the value of each fraction at 662 keV. The values thus derived were 0.262, 0.568, and 0.171 for recombined, Tl-trapped, and stopped electrons, respectively.

B. Estimation of the extent of STE recombination as a function of Tl concentration at 662 keV

In Wang et al. [31], the variations in the recombined, Tl-trapped, and stopped populations were also calculated as a function of Tl concentration for 2-keV γ-rays. Therefore, the value of each population as a function of Tl concentration at 662 keV was determined using the variations obtained at 2 keV as the scaling factor:

$$f_x^{662} = \frac{f_x^2}{f_{0.1}^2} f_{0.1}^{662}, \quad \text{(A1)}$$

where f_x^y is the population (recombined, Tl-trapped, or stopped) obtained at energy y and Tl concentration x. For each value of x, the three populations were normalized so that their sum was 1. As mentioned above, the electrons labeled as "stopped" were not considered further. These represent electrons that have trapped at defects or impurities or that have travelled too far to be able to recombine with STHs. Therefore, the number of electron-hole (e-h) pairs initially placed on the NaI lattice in the KMC simulations varied with Tl concentration. Given a number of e-h pairs N that translates to 10^{18} e-h/cm^{-3}, the initial number of e-h pairs in the simulation of Tl concentration x, N_x, was calculated by:

$$N_x = N\left(f_R + f_{Tl}\right) \quad \text{(A2)}$$

where f_R and f_{Tl} are the fractions of recombined and Tl-trapped electrons. The probability for an e-h pair to initially form a STE, P_c, was:

$$P_c = \frac{f_R}{\left(f_R + f_{Tl}\right)} \quad \text{(A3)}$$

The values of f_R, f_{Tl}, f_S, N_x/N, and P_c thus calculated are given in Table AI.

TABLE AI
f_R, f_{Tl}, f_S, N_x/N, AND P_c AS A FUNCTION OF TL CONCENTRATION

Tl mol%	f_R	f_{Tl}	f_S	N_x/N	P_c
0.001	0.290	0.012	0.697	0.303	0.959
0.003	0.290	0.038	0.672	0.328	0.885
0.005	0.288	0.061	0.652	0.348	0.826
0.010	0.289	0.116	0.595	0.405	0.714
0.020	0.284	0.215	0.501	0.499	0.570
0.030	0.280	0.290	0.431	0.569	0.491
0.050	0.275	0.406	0.319	0.681	0.403
0.070	0.269	0.471	0.259	0.741	0.364
0.100	0.262	0.568	0.171	0.829	0.316
0.150	0.252	0.640	0.108	0.892	0.283
0.200	0.245	0.680	0.075	0.925	0.265
0.300	0.233	0.725	0.042	0.958	0.243
0.500	0.219	0.761	0.020	0.980	0.223
1.000	0.204	0.789	0.007	0.993	0.205

C. Estimation of the extent of STE recombination as a function of temperature at 662 keV

To calculate P_c as a function of temperature for a Tl concentration of 0.1 mol%, we write

$$P_c = 1 - P_d, \quad \text{(A4)}$$

where P_d is the probability for exciton dissociation. Assuming that exciton dissociation exhibits Arrhenius behavior, we use the activation energy for exciton thermal dissociation of Emkey et al. [29] (W=0.06 eV) to describe it:

$$P_d = A\exp\left(-W/k_BT\right), \quad \text{(A5)}$$

where the pre-exponential factor, A, is obtained from the value of P_c obtained at T=298 K and given in Table A1:

$$A = \exp\left(\ln\left(1 - P_c^{298}\right) + W/298k_B\right) \quad \text{(A6)}$$

The resulting values of P_c and P_d are given in Table AII.

TABLE SII
P_D AND P_C AS A FUNCTION OF TEMPERATURE

T (K)	P_d	P_c
243	0.403	0.597
253	0.452	0.548
273	0.553	0.447
293	0.658	0.342
298	0.684	0.316
313	0.766	0.234
333	0.875	0.125

ACKNOWLEDGMENT

The authors acknowledge Drs. Daniel Åberg, Luke W. Campbell, Micah Prange, Babak Sadigh, Renee M. Van Ginhoven, and YuLong Xie for insightful discussions.

REFERENCES

[1] R. Hofstadter, "Alkali halide scintillation counters," *Phys. Rev.*, vol. 74, pp. 100-101, May 1948.

[2] R. B. Murray and A. Meyer, "Scintillation response of activated inorganic crystals to various charged particles," *Phys. Rev.*, vol. 122, pp. 815-826, May 1961.

[3] H. B. Dietrich and R. B. Murray, "Kinetics of the diffusion of self-trapped holes in alkali halide scintillators," *J. Lumin.*, vol. 5, pp. 155-170, Jul. 1972.

[4] R. Hill, "The effect on the scintillation efficiency of NaI(Tl) of changes in the thallium concentration and strain. II. Theoretical," *Brit. J. Appl. Phys.*, vol. 17, pp. 1385-1393, Nov. 1966.

[5] J. B. West, "A theoretical model for the migration of energy from the particle track in an inorganic scintillator," *J. Phys. B: Atom. Molec. Phys.*, vol. 3, pp. 1692-1703, Dec. 1970.

[6] B. S. Alexandrov, K. D. Ianakiev, and P. B. Littlewood, "Branching transport model of NaI(Tl) alkali-halide scintillator," *Nucl. Instr. and Meth. A*, vol. 586, pp. 432-438, Mar. 2008.

[7] R. Hill and A. J. L. Collinson, "The effect on the scintillation efficiency of NaI(Tl) of changes in the thallium concentration and strain. I. Experimental," *Brit. J. Appl. Phys.*, vol. 17, pp. 1377-1383, Nov. 1966.

[8] H. B. Dietrich, A. E. Purdy, R. B. Murray, and R. T. Williams, "Kinetics of self-trapped holes in alkali-halide crystals: experiments in NaI(Tl) and KI(Tl)," *Phys. Rev. B*, vol. 8, pp. 5894-5901, Dec. 1973.

[9] C. J. Delbecq, A. K. Ghosh, and P. H. Yuster, "Trapping and annihilation of electrons and positive holes in KCl-TlCl," *Phys. Rev.*, vol. 151, pp. 599-609, Nov. 1966.

[10] S. Kubota, F. Shiraishi, and Y. Takami, "Decay curves of NaI(Tl) scintillators with different Tl^+ concentrations under excitation of electrons, alpha particles and fission fragments," *J. Phys. Soc. Jpn.*, vol. 68, pp. 291-297, Jan. 1998.

[11] M. Moszyński, A. Nassalski, A. Syntfeld-Każuch, T. Szczęśniak, W. Czarnacki, D. Wolski, G. Pausch, and J. Stein, "Temperature dependences of $LaBr_3$(Ce), $LaCl_3$(Ce) and NaI(Tl) scintillators," *Nucl. Instr. and Meth. Phys. Res. A*, vol. 568, pp. 739-751, Dec. 2006.

[12] M. M. Hamada, F. E. Costa, M. C. C. Pereira, and S. Kubota, "Dependence of scintillation characteristics in the CsI(Tl) crystal on Tl^+ concentrations under electron and alpha particles excitations," *IEEE Trans. Nucl. Sci.*, vol. 48, pp. 1148-1153, Aug. 2001.

[13] S. Kerisit, K. M. Rosso, and B. D. Cannon, "Kinetic Monte Carlo model of scintillation mechanisms in CsI and CsI(Tl)," *IEEE Trans. Nucl. Sci.*, vol. 55, pp. 1251-1258, Jun. 2008.

[14] S. Kerisit, K. M. Rosso, B. D. Cannon, F. Gao, and Y. Xie, "Computer simulation of the light yield nonlinearity of inorganic scintillators," *J. Appl. Phys.*, vol. 105, p. 114915, Jun. 2009.

[15] R. D. Popp and R. B. Murray, "Diffusion of the V_k-polaron in alkali halides: Experiments in NaI and RbI," *J. Phys. Chem. Solids*, vol. 33, pp. 601-610, Mar. 1972.

[16] S. Nagata, K. Fujiwara, and H. Nishimura, "Dynamical aspects of excitons in NaI," *J. Lumin.*, vol. 47, pp. 147-157, Nov.-Dec. 1991.

[17] H. Nishimura and S. Nagata, "Hopping motion of self-trapped excitons in NaI," *J. Lumin.*, vol. 40&41, pp. 429-430, Feb. 1988.

[18] B. Sadigh, D. Åberg, and P. Erhart, "First-principles calculations of self-trapping of carriers and excitons in NaI and SrI_2," presented at the 2012 IEEE Symposium on Radiation Measurements and Applications, Oakland, CA, USA, May 16 2012.

[19] M. P. Prange, R. M. Van Ginhoven, N. Govind, and F. Gao, "Formation, stability and mobility of self-trapped excitations in NaI and NaI(Tl)," *Phys. Rev. B*, vol. 87, p. 115101, Mar. 2013.

[20] J. Q. Grim, K. B. Ucer, A. Burger, P. Bhattacharya, E. Tupitsyn, E. Rowe, V. M. Buliga, L. Trefilova, A. Gektin, G. A. Bizarri, W. W. Moses, and R. T. Williams, "Nonlinear quenching of densely excited states in wide-gap solids," *Phys. Rev. B*, vol. 87, p. 125117, Mar. 2013.

[21] J. Q. Grim, Q. Li, K. B. Ucer, R. T. Williams, A. Burger, P. Bhattacharya, E. Tupitsyn, G. A. Bizarri, and W. W. Moses, "Nonlinear quenching rates in SrI_2 and CsI scintillator hosts," *MRS Proceedings*, vol. 1341, pp. 15-20, 2011.

[22] R. T. Williams, J. Q. Grim, Q. Li, K. B. Ucer, and W. W. Moses, "Excitation density, diffusion-drift, and proportionality in scintillators," *Phys. Status Solidi B*, vol. 248, pp. 426-438, Feb. 2011.

[23] Z. Wang, R. T. Williams, J. Q. Grim, F. Gao, and S. Kerisit, "Kinetic Monte Carlo simulations of excitation density dependent scintillation in CsI and CsI(Tl)," *Phys. Status Solidi B*, in press, 2013.

[24] F. J. Keller and R. B. Murray, "Thermal motion of holes in potassium iodide," *Phys. Rev.*, vol. 150, pp. 670-679, Oct. 1966.

[25] R. B. Murray and F. J. Keller, "V_k centers and recombination luminescence in rubidium iodide and sodium iodide," *Phys. Rev.*, vol. 153, pp. 993-1000, Jan. 1967.

[26] W. J. Van Sciver, "Fluorescence and reflection spectra of NaI single crystals," *Phys. Rev.*, vol. 120, pp. 1193-1205, Nov. 1960.

[27] W. J. Van Sciver and L. Bogart, "Fundamental studies of scintillation phenomena in NaI," *IRE Trans. Nucl. Sci.*, vol. 5, pp. 90-92, Dec. 1958.

[28] C. J. Delbecq, Y. Toyozawa, and P. H. Yuster, "Tunneling recombination of trapped electrons and holes in KCl:AgCl and KCl:TlCl," *Phys. Rev. B*, vol. 9, pp. 4497-4505, May 1974.

[29] W. L. Emkey, A. B. Romberger, and W. J. Van Sciver, "Thermal dissociation of photoproduced excitons at the uv band edge in NaI," *Phys. Rev. B*, vol. 20, pp. 5326-5329, Dec. 1979.

[30] Z. Wang, Y.-L. Xie, B. D. Cannon, L. W. Campbell, F. Gao, and S. Kerisit, "Computer simulation of electron thermalization in CsI and CsI(Tl)," *J. Appl. Phys.*, vol. 110, p. 064903, Sep. 2011.

[31] Z. Wang, Y.-L. Xie, L. W. Campbell, F. Gao, and S. Kerisit, "Monte Carlo simulations of electron thermalization in alkali iodide and alkaline-earth fluoride scintillators," *J. Appl. Phys.*, vol. 112, p. 014906, Jul. 2012.

[32] W. B. Hadley, S. Polick, R. G. Kaufman, and H. N. Hersh, "Energy storage and luminescence in KI:Tl at low temperatures," *J. Chem. Phys.*, vol. 45, pp. 2040-2048, Sept. 1966.

[33] R. G. Kaufman, W. B. Hadley, and H. N. Hersh, "The scintillation mechanism in thallium doped alkali halides," *IEEE Trans. Nucl. Sci.*, vol. 17, pp. 82-87, Apr. 1970.

[34] R. Katz and E. J. Kobetich, "Response of NaI(Tl) to energetic heavy ions," *Phys. Rev.*, vol. 170, pp. 397-400, Jun. 1968.

[35] R. W. G. Wyckoff, *Crystal Structures*, Second ed. vol. 1. New York, New York: Interscience Publishers, 1963.

[36] M. Moszyński, M. Balcerzyk, W. Czarnacki, M. Kapusta, W. Klamra, P. Schotanus, A. Syntfeld, and M. Szawlowski, "Study of pure NaI at room and liquid nitrogen temperatures," *IEEE Trans. Nucl. Sci.*, vol. 50, pp. 767-773, Aug. 2003.

[37] S. Kubota, F. Shiraishi, and Y. Takami, "Scintillation process in NaI(Tl): Comparison with scintillation models," *J. Phys. Soc. Jpn.*, vol. 68, pp. 3435-3440, Oct. 2000.

[38] J. E. Eby, K. J. Teegarden, and D. B. Dutton, "Ultraviolet absorption of alkali halides," *Phys. Rev.*, vol. 116, pp. 1099-1105, Dec. 1959.

[39] W. Martienssen, "Uber die Excitonenbanden der Alkalihalogenid-kristalle," *J. Phys. Chem. Solids*, vol. 2, pp. 257-267, Oct.-Dec. 1957.

[40] A. N. Vasil'ev, "From luminescence non-linearity to scintillation non-proportionality," *IEEE Trans. Nucl. Sci.*, vol. 55, pp. 1054-1061, Jun. 2008.

[41] M. Kirm, V. Nagirnyi, E. Feldbach, M. De Grazia, B. Carré, G. Geoffroy, J. Gaudin, N. Fedorov, P. Martin, A. Vasil'ev, and A. Belsky, "Exciton-exciton interactions in $CdWO_4$ irradiated by intense femtosecond vacuum ultraviolet pulses," *Phys. Rev. B*, vol. 79, p. 233103, Jun. 2009.

[42] R. T. Williams, K. B. Ucer, J. Q. Grim, K. C. Lipke, L. M. Trefilova, and W. W. Moses, "Picosecond studies of transient absorption induced by bandgap excitation of CsI and CsI:Tl at room temperature," *IEEE Trans. Nucl. Sci.*, vol. 57, pp. 1187-1192, Jun. 2010.

Advanced Scintillation Materials
September 24th 2013

Mechanisms of Scintillator Radiation Response:
Insights from Monte Carlo Simulations

Sebastien Kerisit, Zhiguo Wang, Dangxin Wu, Micah P. Prange, Renee M. Van Ginhoven, and Fei Gao
Pacific Northwest National Laboratory

Richard T. Williams and Joel Q. Grim
Wake Forest University

Acknowledgements

This project is supported by the National Nuclear Security Administration, Office of Nuclear Nonproliferation Research and Engineering (NA-22), U.S. Department of Energy.

Pacific Northwest
NATIONAL LABORATORY

Proudly Operated by Battelle *Since 1965*

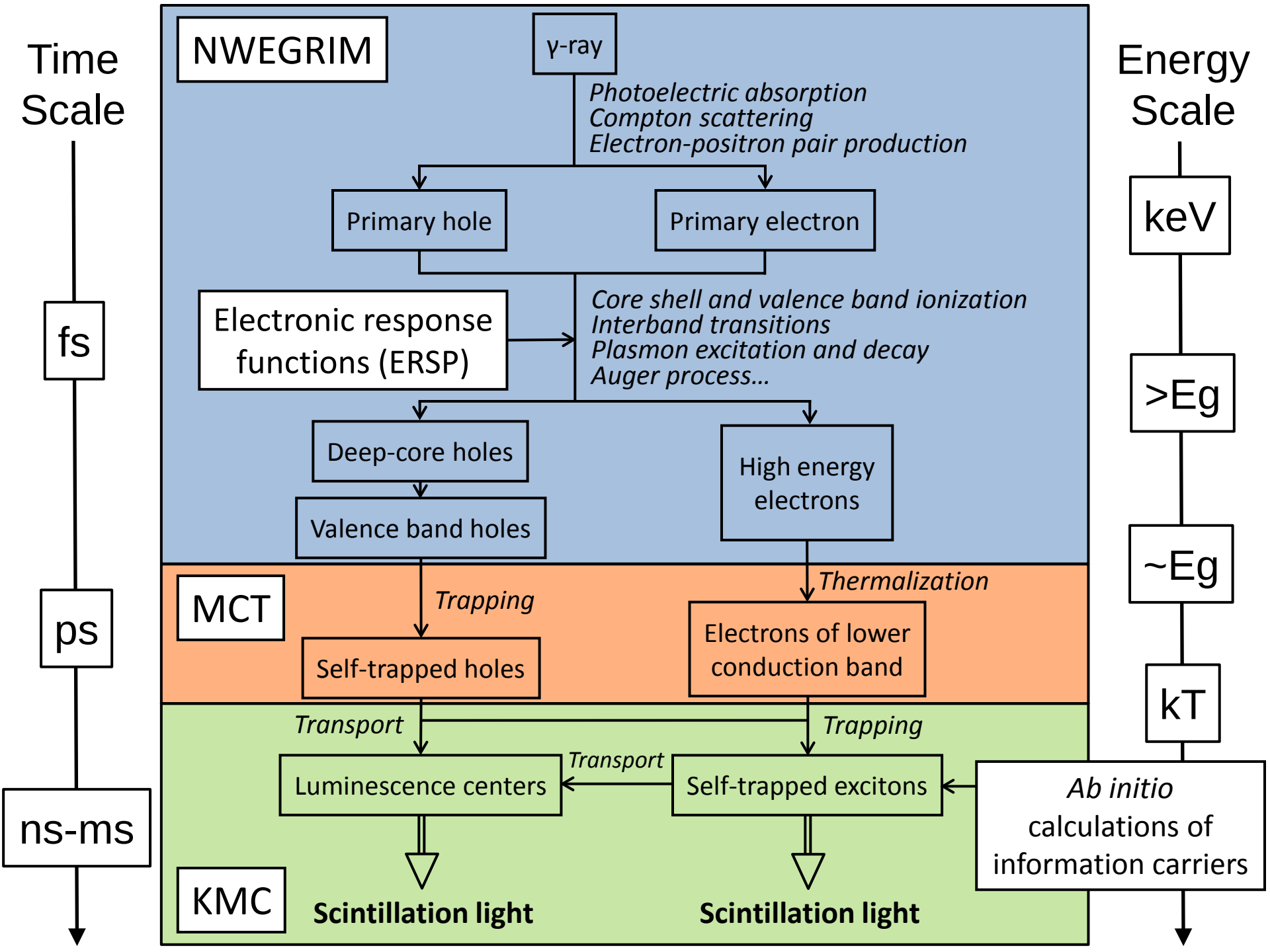
Time Scale
fs
ps
ns-ms
NWEGRIM
γ-ray
Photoelectric absorption
Compton scattering
Electron-positron pair production
Primary hole
Primary electron
Electronic response functions (ERSP)
Core shell and valence band ionization
Interband transitions
Plasmon excitation and decay
Auger process…
Deep-core holes
Valence band holes
High energy electrons
MCT
Trapping
Thermalization
Self-trapped holes
Electrons of lower conduction band
Transport
Trapping
Transport
Luminescence centers
Self-trapped excitons
KMC
Scintillation light
Scintillation light
Ab initio calculations of information carriers
Energy Scale
keV
>Eg
~Eg
kT

Electron thermalization: approach

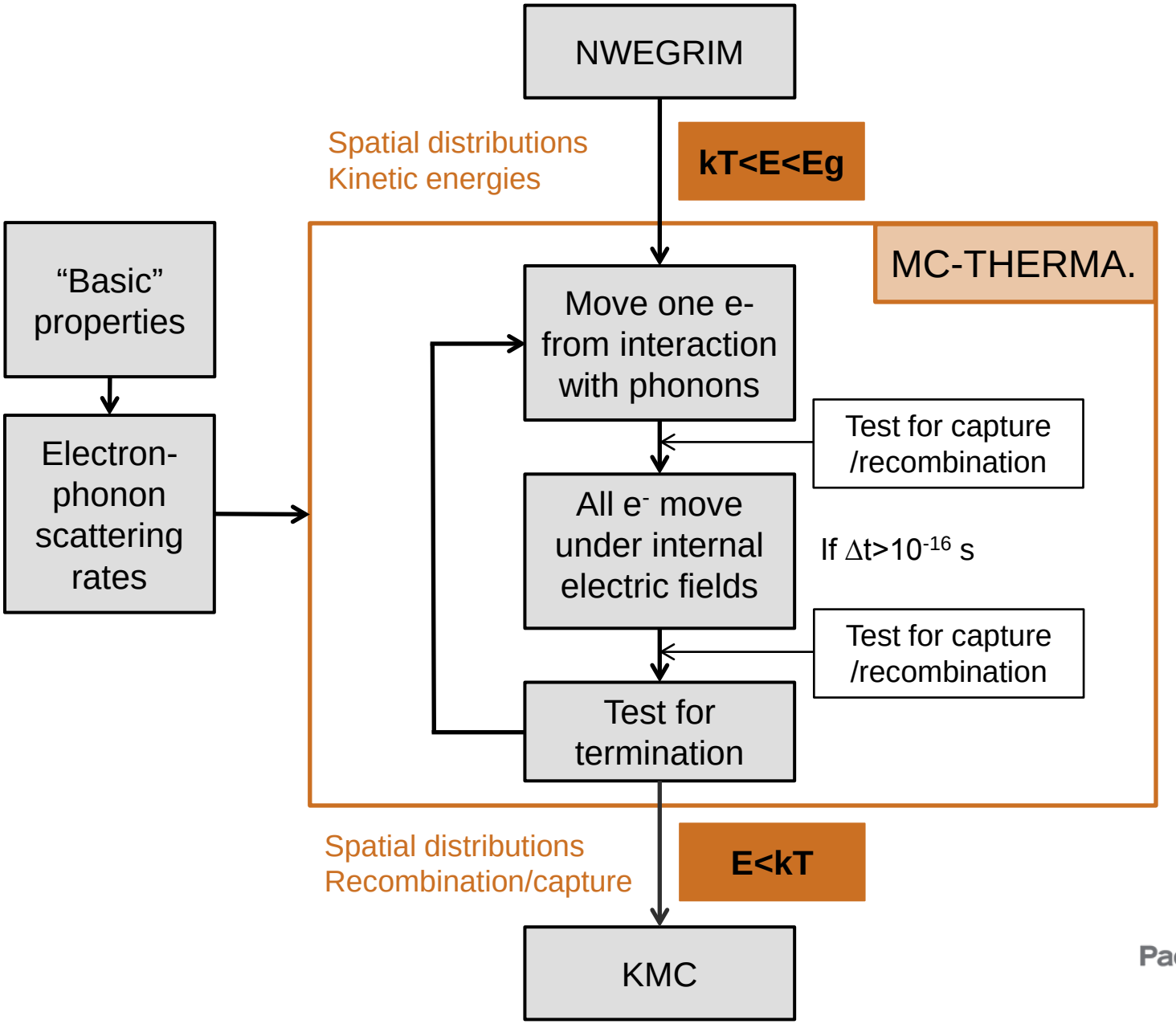

Pacific Northwest
NATIONAL LABORATORY

Electron-phonon interactions

Electron-LO phonon scattering rate

Scattering rates and angles for emission and absorption of LO phonons are calculated using the formulation of Llacer and Garwin[1].

$$\tau_{LO}^{\pm} = \frac{1}{4\pi\varepsilon}\frac{e^2\omega_{opt}\sqrt{m^*}}{\hbar\sqrt{2E}}\left(n_q + \frac{1}{2} \pm \frac{1}{2}\right)\left(\frac{1}{\varepsilon_\infty} - \frac{1}{\varepsilon_0}\right)\ln\left(\frac{1+\sqrt{1\mp\left(\hbar\omega_{opt}/E\right)}}{1-\sqrt{1\mp\left(\hbar\omega_{opt}/E\right)}}\right)$$

where ε is the vacuum permittivity, e is the elementary charge, $\hbar$ is the Planck constant, ω_{opt} is the LO phonon angular frequency, m^* is the electron effective mass, E is the electron kinetic energy, n_q is the phonon occupation number, ε_∞ and ε_0 are the optical and static dielectric constants.

Electron-A phonon scattering rate

Scattering rates and angles for emission and absorption of A phonons are calculated using the formulation of Sparks et al.[2] together with the correction of Bradford and Woolf[3].

Primary parameters

Lattice parameter, dielectric constants, elastic constants
LO characteristic phonon energy, elastic scattering cross section

[1]J. Llacer and E.L. Garwin (1969) *J. Appl. Phys.* **40** 2766
[2]M. Sparks et al. (1981) *Phys. Rev. B* **24** 3519
[3]J.N. Bradford and S. Woolf (1991) *J. Appl. Phys.* **70** 490

Internal electric fields

As electrons thermalize via interaction with lattice phonons, they are also influenced by the electric field due to all the other electrons and holes generated during the energy cascade.

The electron trajectories were calculated using the classical equations of dynamics:

$$\frac{d}{dt}\left[m^{*}v_i\right] = -eE_i \qquad (1)$$

where m^* is the electron effective mass, v_i the velocity of electron *i*, and E_i, the electric field at the position of electron *i*, is defined as:

$$E_i = \sum_{\substack{j=1 \\ j\neq i}}^{N} \frac{1}{4\pi\varepsilon_0}\frac{q_j}{r_{ij}^2}\hat{r}_{ij} \qquad (2)$$

where N is the number of electrons and holes, ε_0 the material's dielectric constant, q_j the charge of particle *j*, r_{ij} the distance between particles *i* and j, and $\hat{r}_{ij}$ the unit vector.

Equation (1) needs to be discretized using a time step Δt.

Pacific Northwest
NATIONAL LABORATORY

Model input

Electron-phonon scattering rates

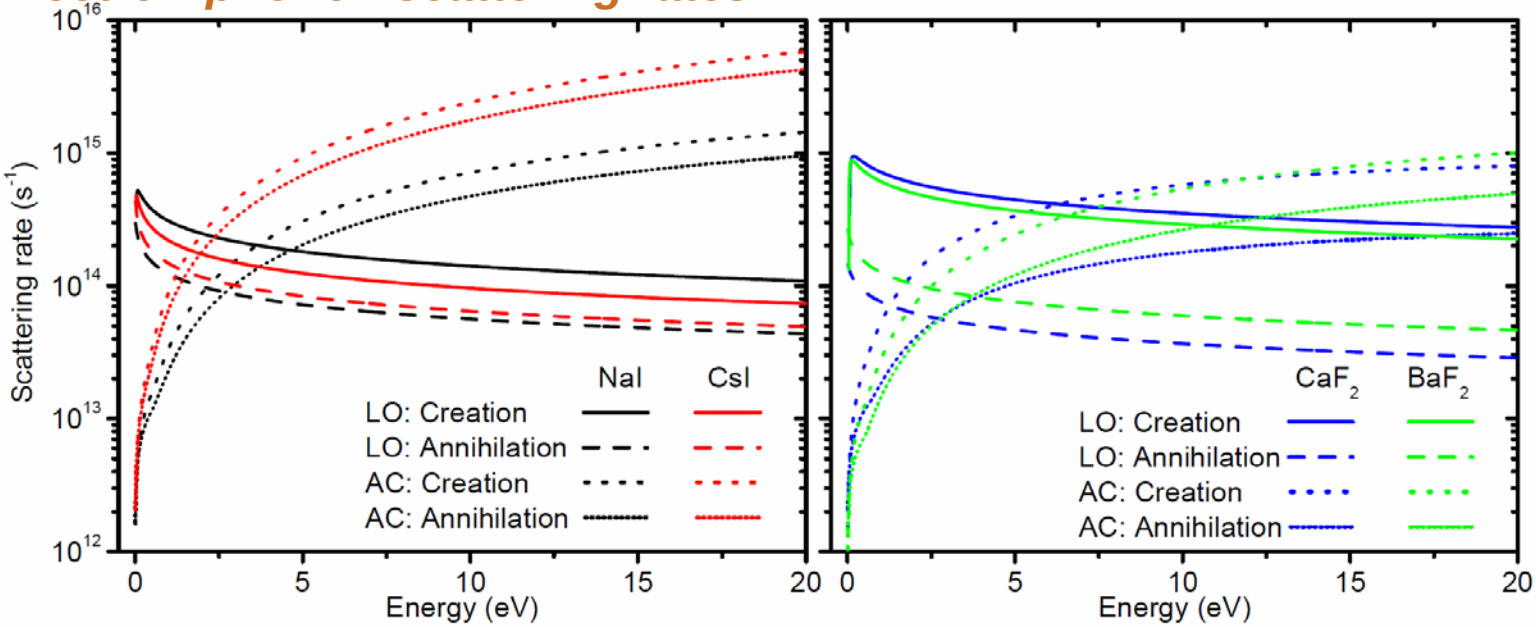

Electron kinetic energy distributions

No incident energy dependence

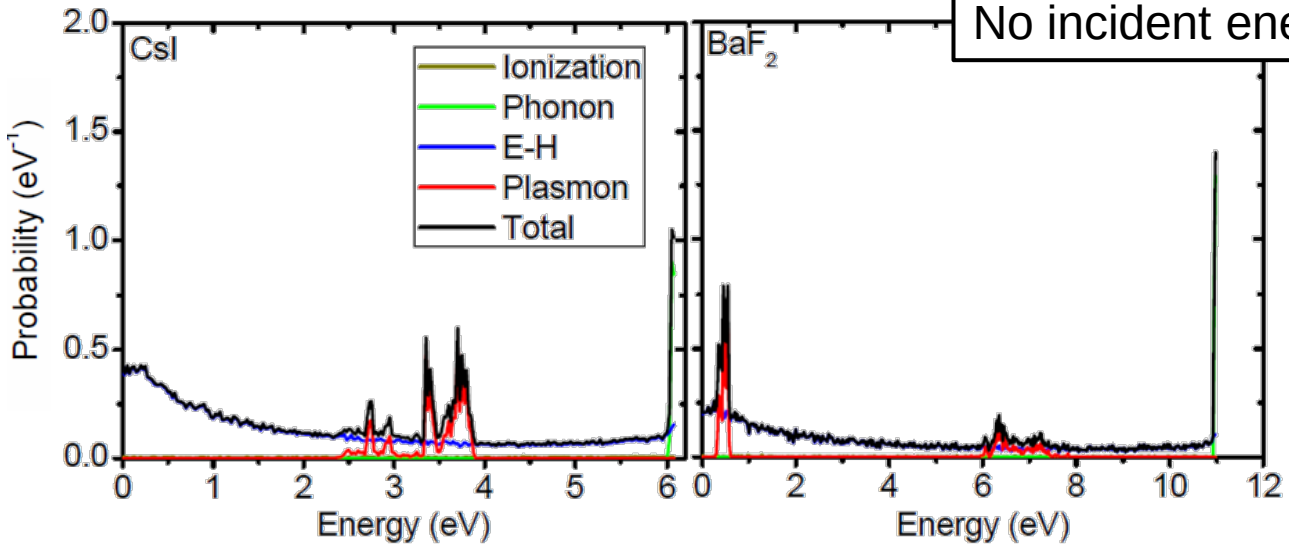

Pacific Northwest
NATIONAL LABORATORY

e/h-pair spatial distributions are complex

CsI

Spatial distribution of thermalized electrons + self-trapped holes

20 keV – w/o IEF

20 keV – w/ IEF

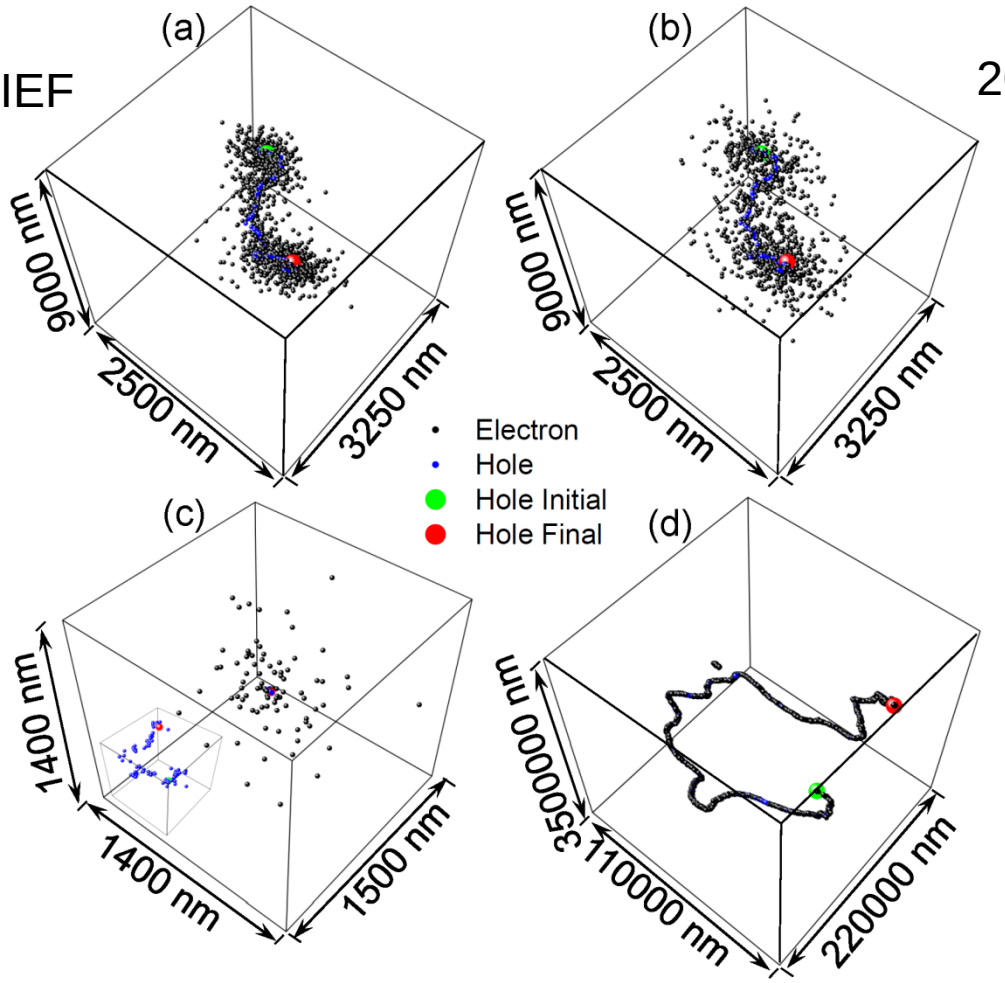

2 keV – w/ IEF

400 keV – w/ IEF

- Current models of e/h-pair transport generally make use of cylinder-shaped tracks with homogeneous excitation densities.
- This work shows that e/h-pair spatial distributions are highly complex → effect on 2nd order processes.

e/h-pair recombination is very fast

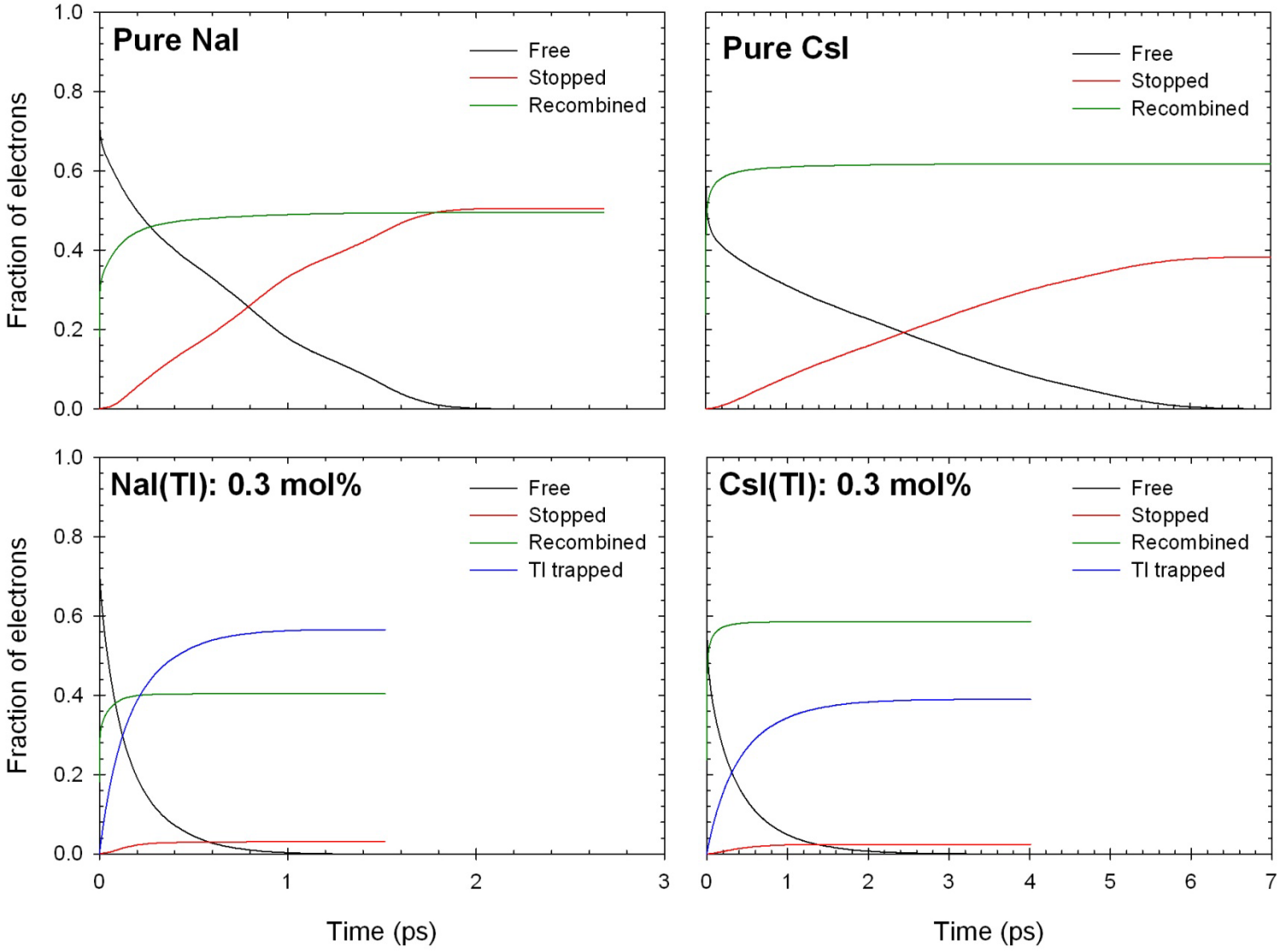

Pacific Northwest
NATIONAL LABORATORY

e/h-pair recombination can be extensive

Pure materials

FWHM decreases with increasing incident energy

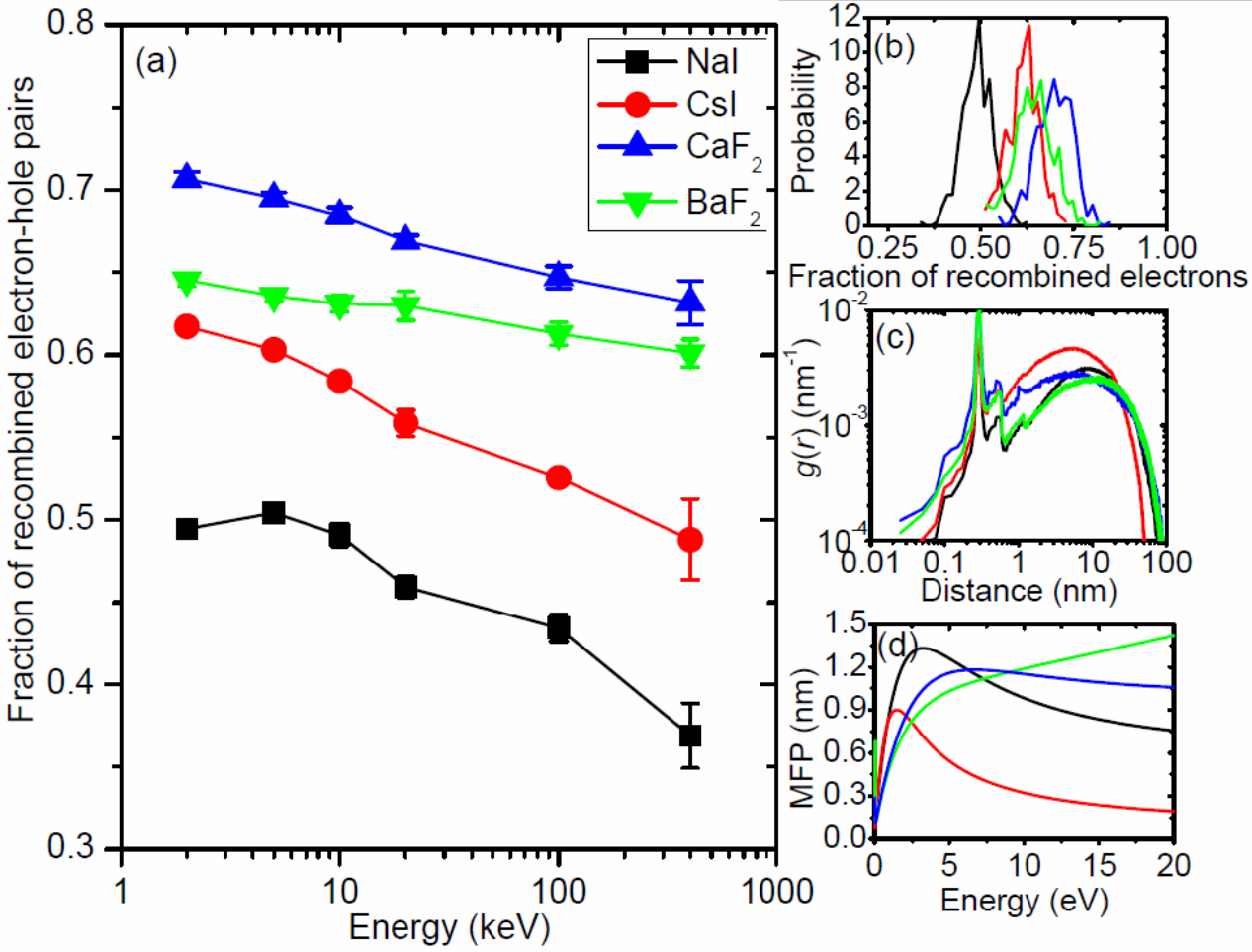

- The increase in stopping power at low incident energies generates high e/h-pair densities, which leads to an increased probability for e/h-pair recombination
- Nonlinearity: increased probability for STE-STE annihilation at low incident energy

Electrons that escape can travel far

Pure materials 400 tracks - 2 keV γ-ray incident energy

Kinetic energy distribution

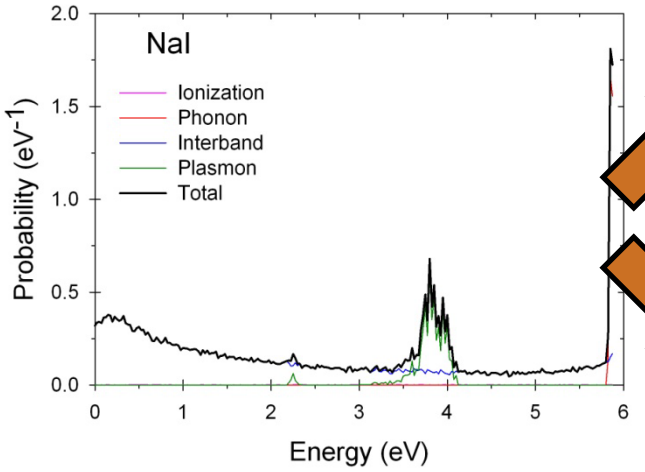

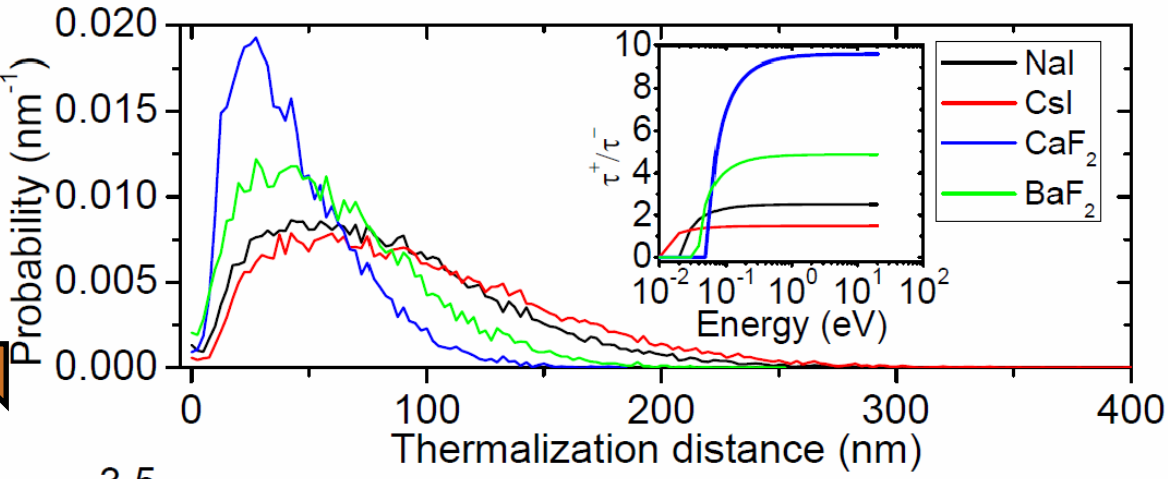

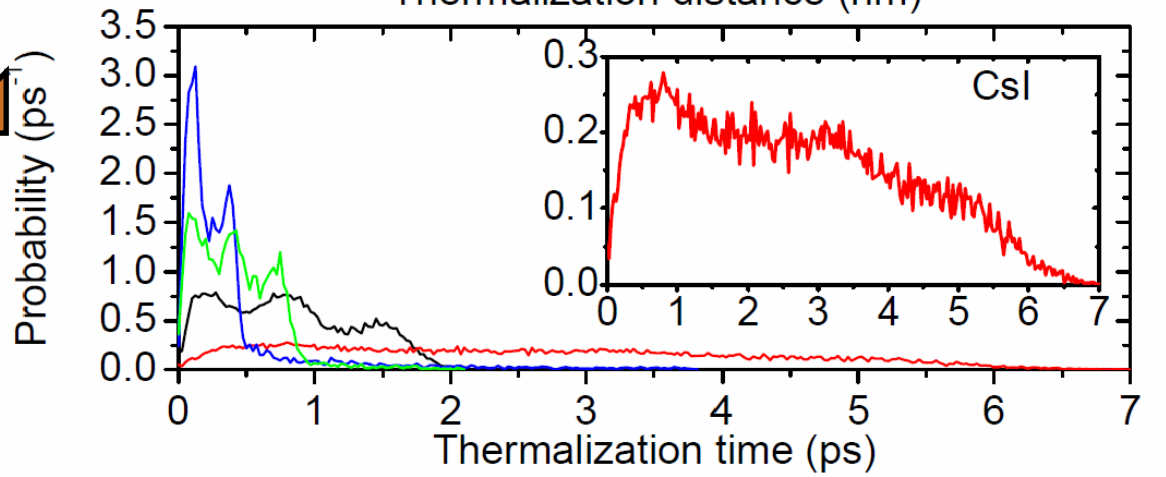

- The greater the LO phonon energy, the greater the difference between the creation and annihilation scattering rates + the more energy is lost to the lattice when creating a phonon.

Electron capture at Tl sites

From an approach described in Ganachaud et al.[1], the probability for electron capture by a Tl ion as a function of its energy is given by:

$$P(E) = S_{capt.} \exp(-\gamma_{capt.} E)$$

where $S_{capt.}$ allows to adjust the spatial frequency of this process and $\gamma_{capt.}$ its energy domain.

$S_{capt.}$ is a function of the electron step length, δ, and the Tl concentration:

$$S_{capt.} = \frac{\delta}{a_{CsI}} f_{Tl^+}$$

where a_{CsI} is the CsI lattice constant and f_{Tl+} is the fraction of unit cells with a Tl ion.

There is no direct method to determine $\gamma_{capt.}$. An arbitrary reference value of 0.56 will be used, which corresponds to a probability of 10^{-3} at the cutoff energy. $\gamma_{capt.}$ will varied to determine its effect on electron thermalization.

Effect of Tl concentration

Tl-doped materials 400 tracks - 2 keV γ-ray incident energy

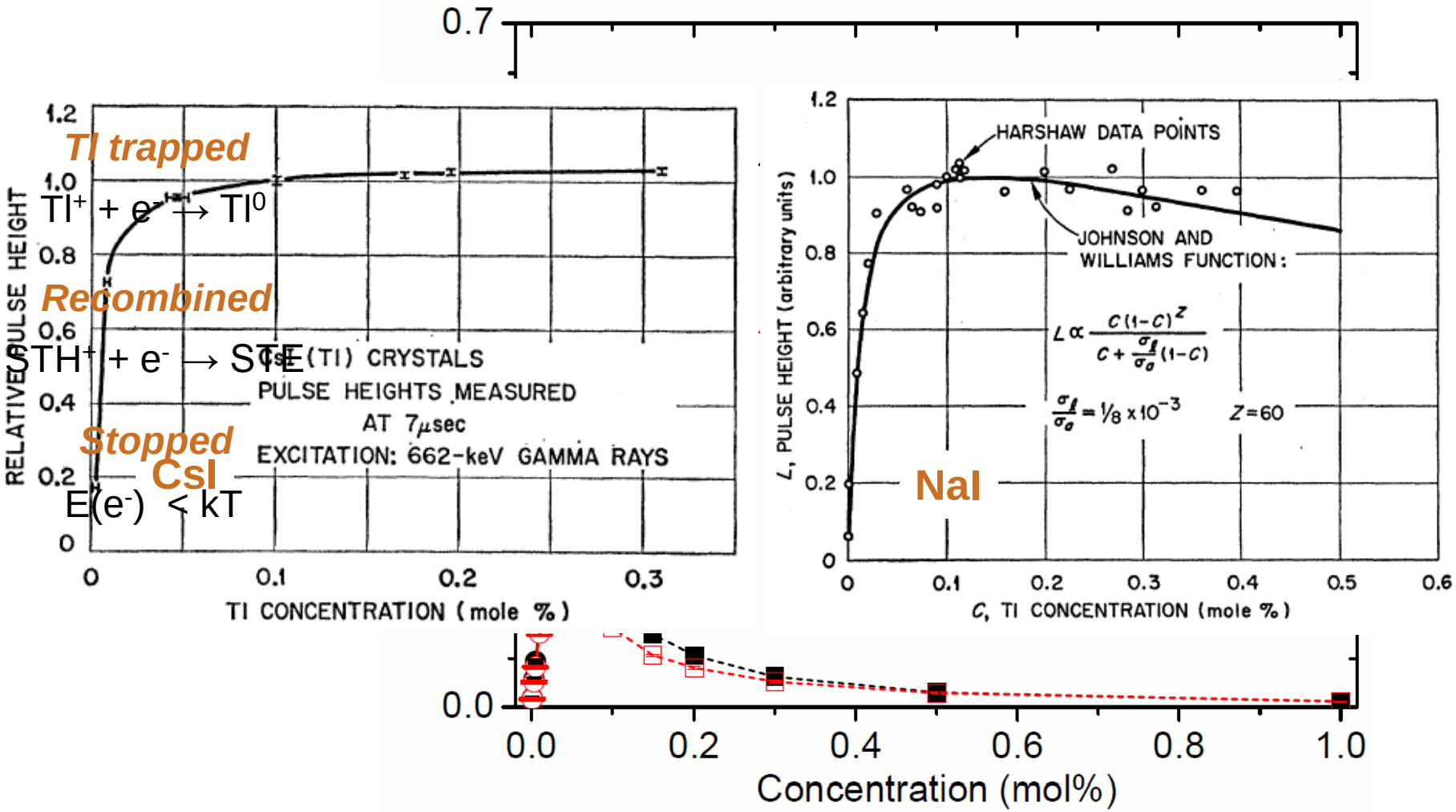

- Consistent with experimental observation that light yield saturates at high concentrations.[1,2]

[1]R. Gwin and R.B. Murray (1963) *Phys. Rev.* **131** 501
[2]R.B.Murray and A. Meyer (1961) *Phys. Rev.* **122** 815

Extent of Tl trapping increases with incident energy

Tl-doped materials

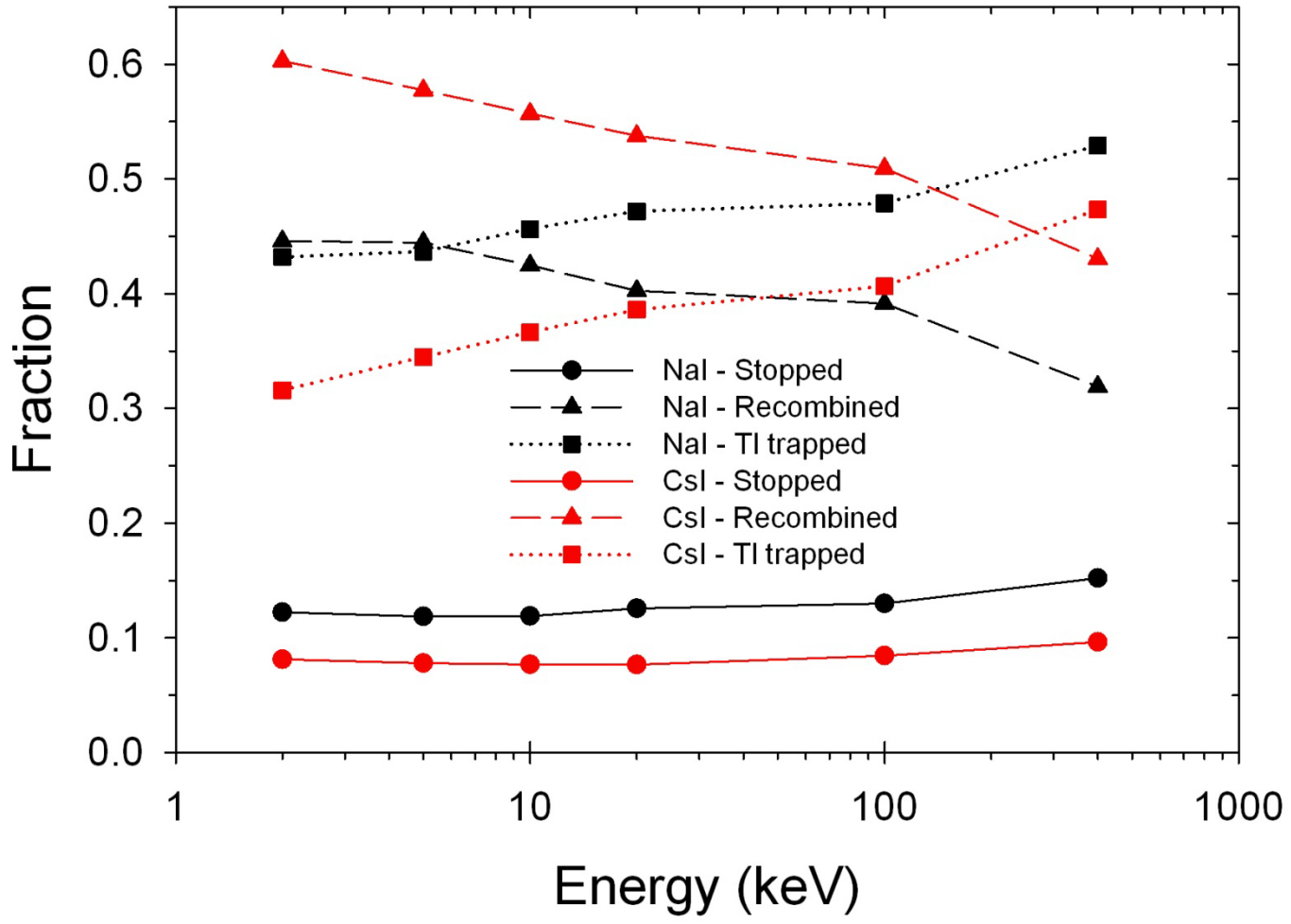

- Nonlinearity: increased proportion of separated e-h pairs at high incident energy

Pacific Northwest
NATIONAL LABORATORY

Electron thermalization: publications

Computer Simulation of Electron Thermalization in CsI and CsI(Tl)
Z. Wang, Y.L. Xie, B.D. Cannon, L.W. Campbell, F. Gao, S. Kerisit
Journal of Applied Physics **110**, 064903 (2011)

Monte Carlo Simulations of Electron Thermalization in Alkali Iodide and Alkaline-Earth Fluoride Scintillators
Z. Wang, Y.L. Xie, L.W. Campbell, F. Gao, S. Kerisit
Journal of Applied Physics **112**, 014906 (2012)

Ab initio electron thermalization model

- Density functional theory describes phonons
- Field of thermalizing particle provides perturbation to quantized phonon system
- Results are rates of energy and momentum transfer as functions of the thermalizing particle velocity

$$\Gamma(\vec{v}) = \sum_{\lambda} \int d^3Q \left| H_{\lambda}\left(\vec{Q}\right) \right|^2 \delta\left(\omega_{\lambda}(\vec{q}) - \vec{Q}\cdot\vec{v} + \frac{Q^2}{2}\right)$$

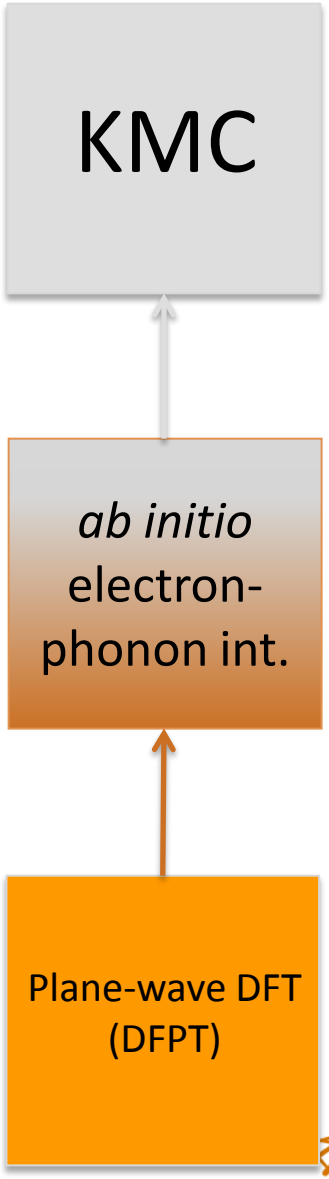

Micah P. Prange

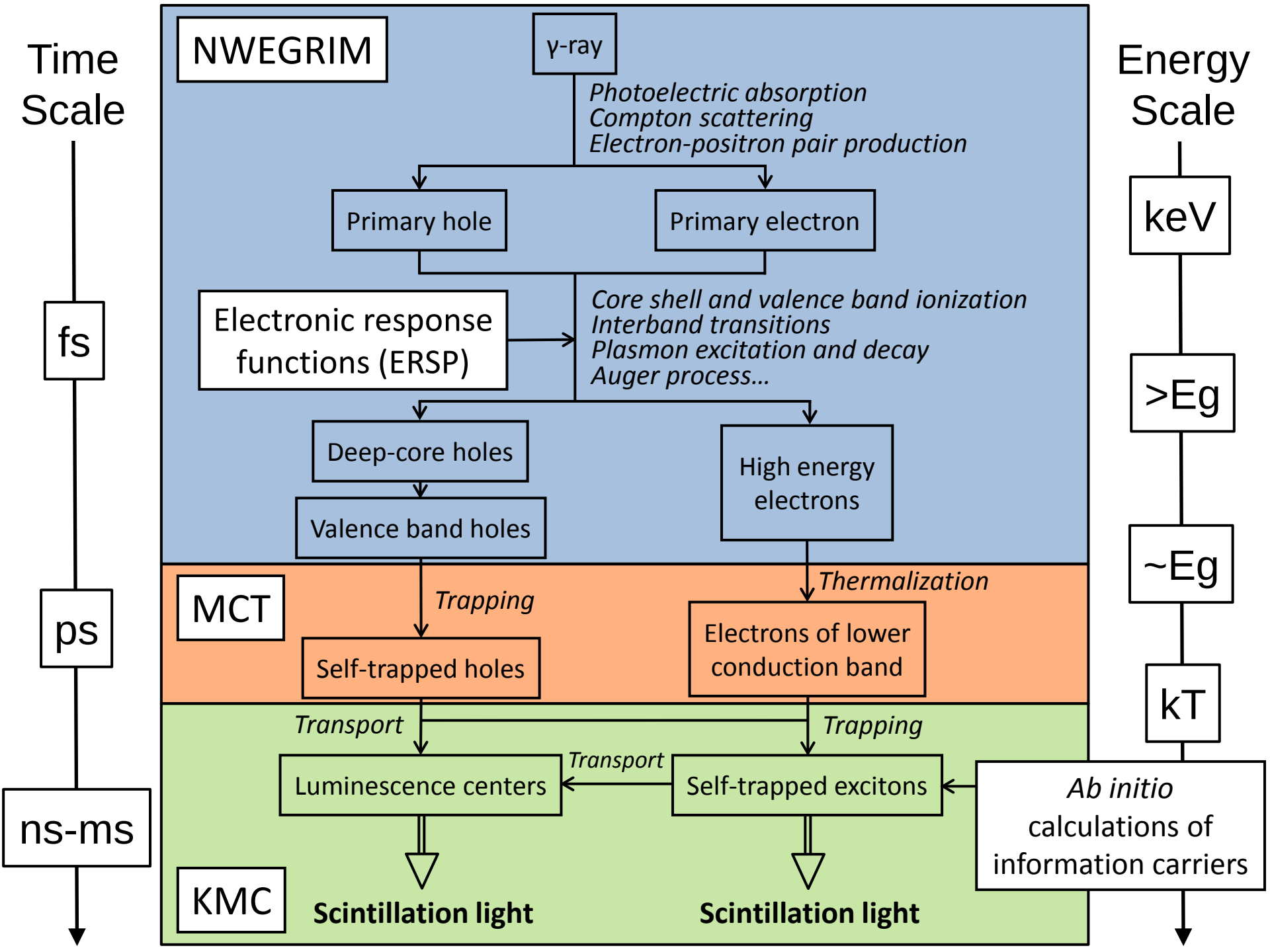
Time Scale
fs
ps
ns-ms
NWEGRIM
γ-ray
Photoelectric absorption
Compton scattering
Electron-positron pair production
Primary hole
Primary electron
Electronic response functions (ERSP)
Core shell and valence band ionization
Interband transitions
Plasmon excitation and decay
Auger process…
Deep-core holes
Valence band holes
High energy electrons
MCT
Trapping
Thermalization
Self-trapped holes
Electrons of lower conduction band
Transport
Trapping
Transport
Luminescence centers
Self-trapped excitons
KMC
Scintillation light
Scintillation light
Ab initio calculations of information carriers
Energy Scale
keV
>Eg
~Eg
kT

Probing nonproportionality

- Scintillation photon yield normalized to incident energy is not a constant.
- Significant source of degradation of energy resolution.
- Despite intensive research, the underlying mechanisms of nonproportionality remain incompletely identified.

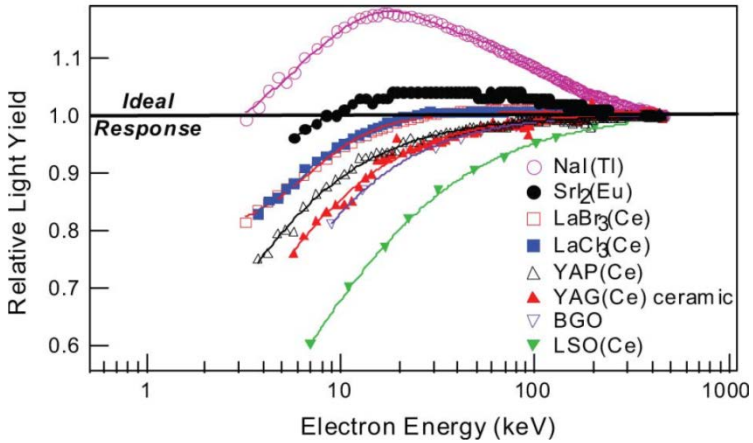

Cherepy et al. (2009) *IEEE TNS* **56** 873

<u>Hypothesis:</u> Nonproportionality is caused by the incident energy dependence of the electron-hole pair density along the ionization track through its effect on the transport and recombination efficiency and kinetics.

- Kinetic Monte Carlo simulations allow for a quantitative test of this hypothesis.
- KMC simulations allow for explicit representation of the inherent heterogeneous nature of ionization tracks.

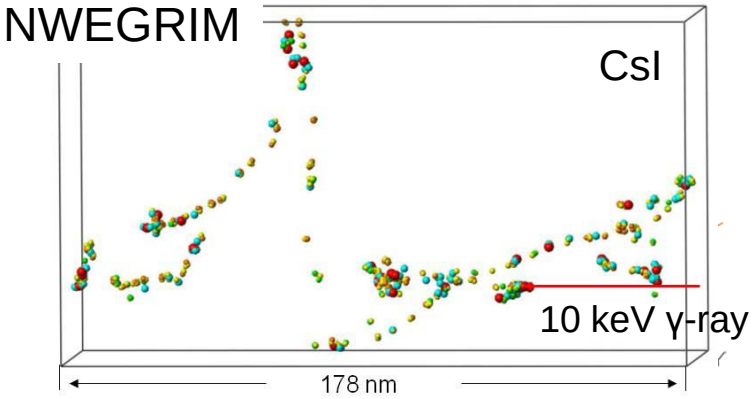

Computational approach

- Atomic-level simulation of the **kinetics and efficiency** of scintillation processes
- A wide range of mechanisms can be simulated
  - Diffusion of holes and excitons; radiative decay of excitons, activators and defects; etc
  - Pre-exponential factor, A, and activation energy, W, needed to parameterize each process.

$$k = A \quad \exp(-W/k_B T)$$

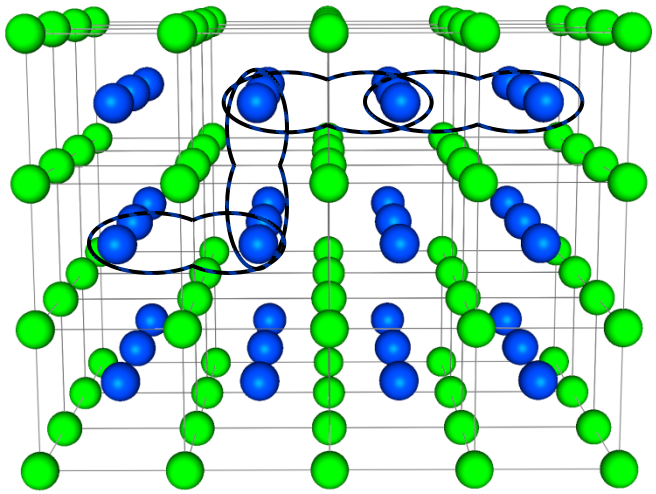

V_k center diffusion in CsI

- A general algorithm has been implemented to consider **any lattice type**
- Efficient use of NWEGRIM-generated electron-hole pair distributions
  - Domain decomposition of distributions for multi-processor simulations
  - Independent of simulation cell size for modeling extended distributions
- Scintillation models derived for CsI, CsI(Tl), NaI(Tl), and $LaBr_3$(Ce)
- Can make use of input parameters derived from *ab initio* calculations performed at PNNL and LLNL
  - STE and STH hopping barriers, iodide vacancy diffusion…

Pacific Northwest
NATIONAL LABORATORY

KMC modeling of z-scan experiments

Simulation setup

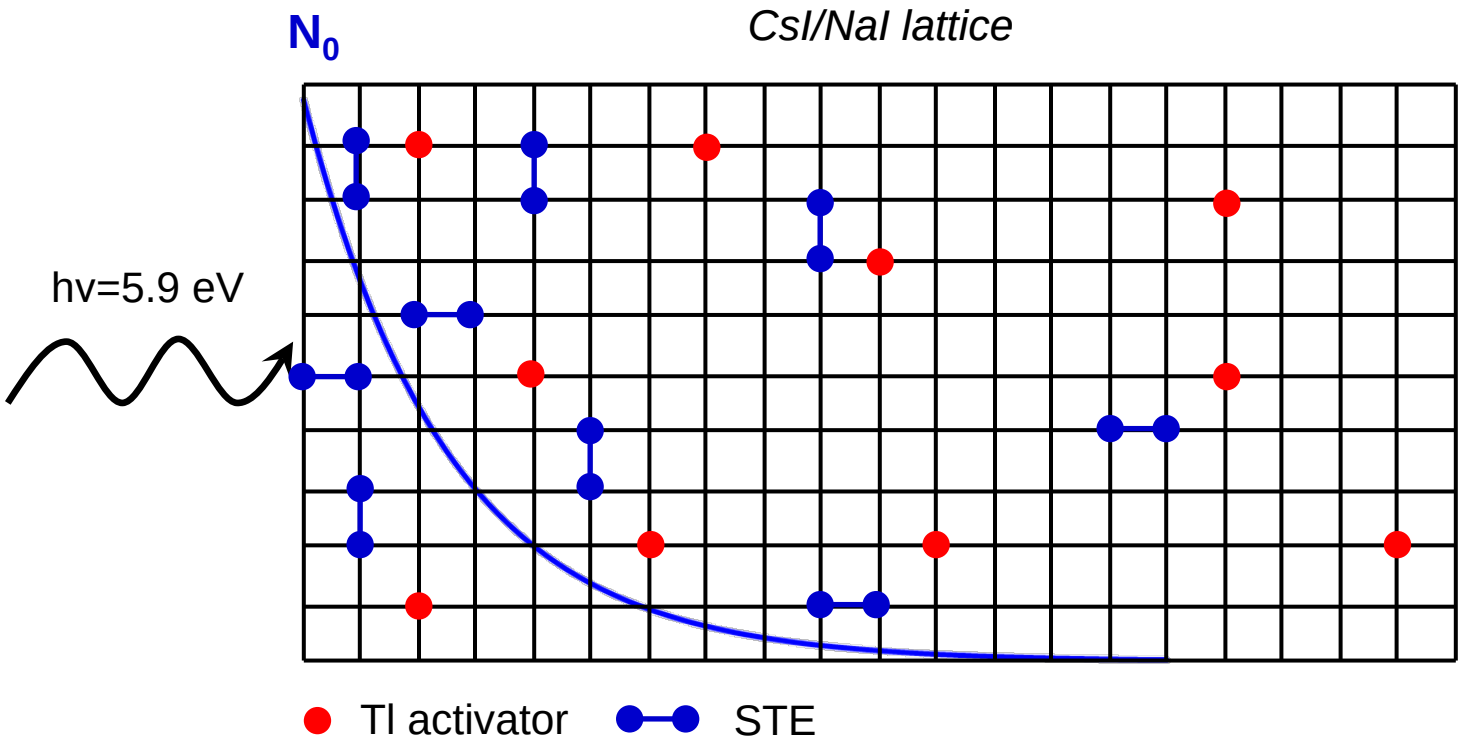

- Typical simulation cell: 32 × 32 × 256/512 = ~10-15 × 10-15 × 120-170 nm^3
- PBC in *x* and *y* directions
- N_0 calculated from on-axis laser fluence, absorption coefficient, excitation energy, and position of beam waist used in the z-scan experiments

Pacific Northwest
NATIONAL LABORATORY

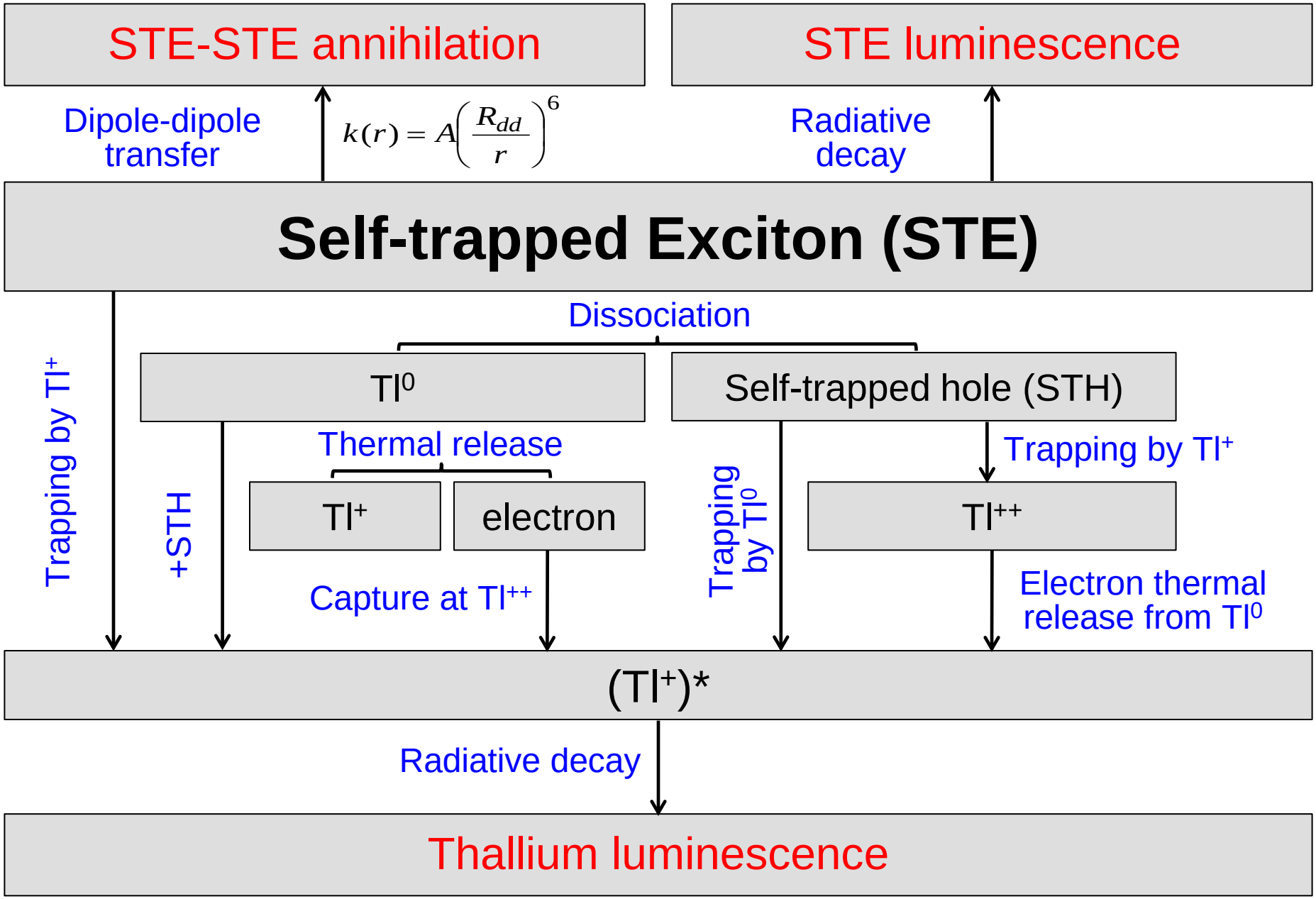
STE-STE annihilation
STE luminescence
Dipole-dipole transfer
$k(r) = A\left(\frac{R_{dd}}{r}\right)^6$
Radiative decay
Self-trapped Exciton (STE)
Dissociation
Trapping by Tl+
Tl0
Self-trapped hole (STH)
Thermal release
+STH
Tl+
electron
Trapping by Tl+
Trapping by Tl0
Tl++
Capture at Tl++
Electron thermal release from Tl0
(Tl+)*
Radiative decay
Thallium luminescence

Model parameters

The majority of model parameters are derived from experimental data…

STE radiative decay STE non-radiative decay	Kinetics and efficiency of scintillation in pure CsI/NaI vs. temperature
$(Tl^{+})^{*}$ radiative decay Electron thermal release	Kinetics of scintillation of Tl-doped CsI/NaI in 100s ns – μs time scale vs. temperature
STE dissociation	Time-resolved optical absorption data Rate of disappearance of STE band[1]
Förster transfer	Free parameter to reproduce data on light yield vs. excitation density[2]

… some important parameters are obtained from first-principles calculations

STH diffusion
STE diffusion

[1]R.T. Williams et al. (2010) *IEEE Trans. Nucl. Sci.* **57** 1187
[2]J.Q.Grim et al. (2013) *Phys. Rev. B* **87** 125117

Pacific Northwest
NATIONAL LABORATORY

First-principles modeling (1)

Combined Solid State and Embedded Cluster Approach

Results

- Structures and formation energies
- Defect ionization potentials
- Migration barriers
- luminescence energies
- energy transfer & luminescence mechanisms

NaI

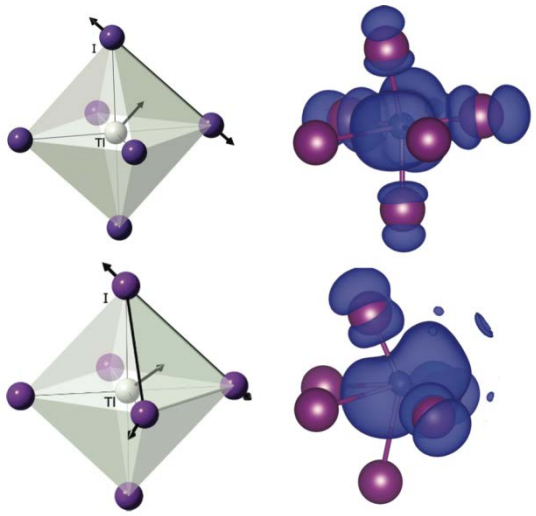

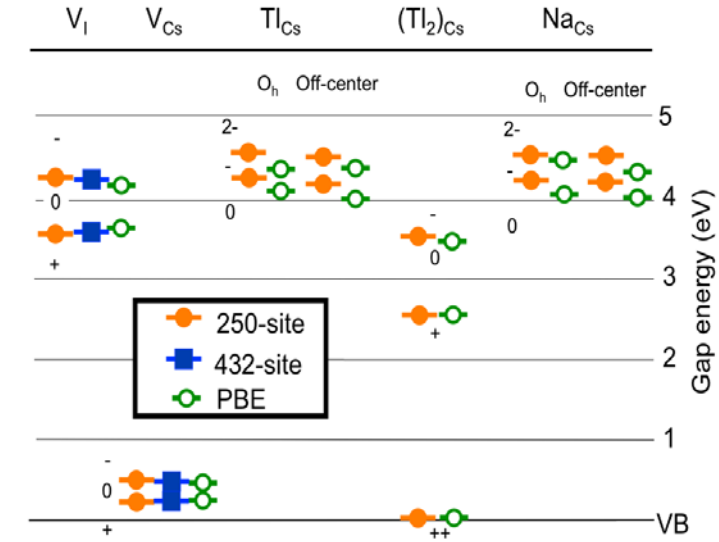

CsI

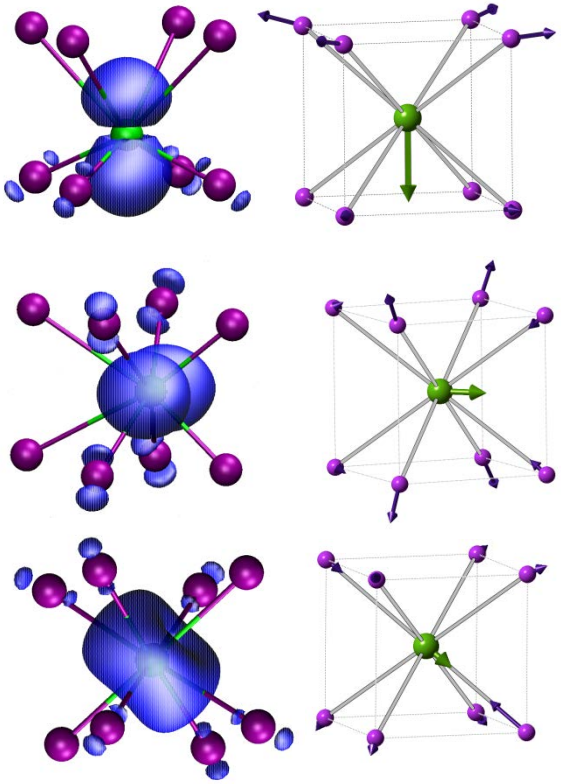

- Complete study of excitons and polarons in CsI using hybrid functionals
- Identify and characterize relevant phonon modes associated with dopant vibration
- Complete reconciliation of bulk and cluster results for both materials

R. M. Van Ginhoven, M. P. Prange, N. Govind

M. P. Prange et al. (2013) *Phys. Rev. B* **87** 115101
R.M. Van Ginhoven and P.A. Schultz *J. Phys: Cond. Matter* (submitted)

Pacific Northwest NATIONAL LABORATORY

First-principles modeling (2)

STHs/STEs in NaI

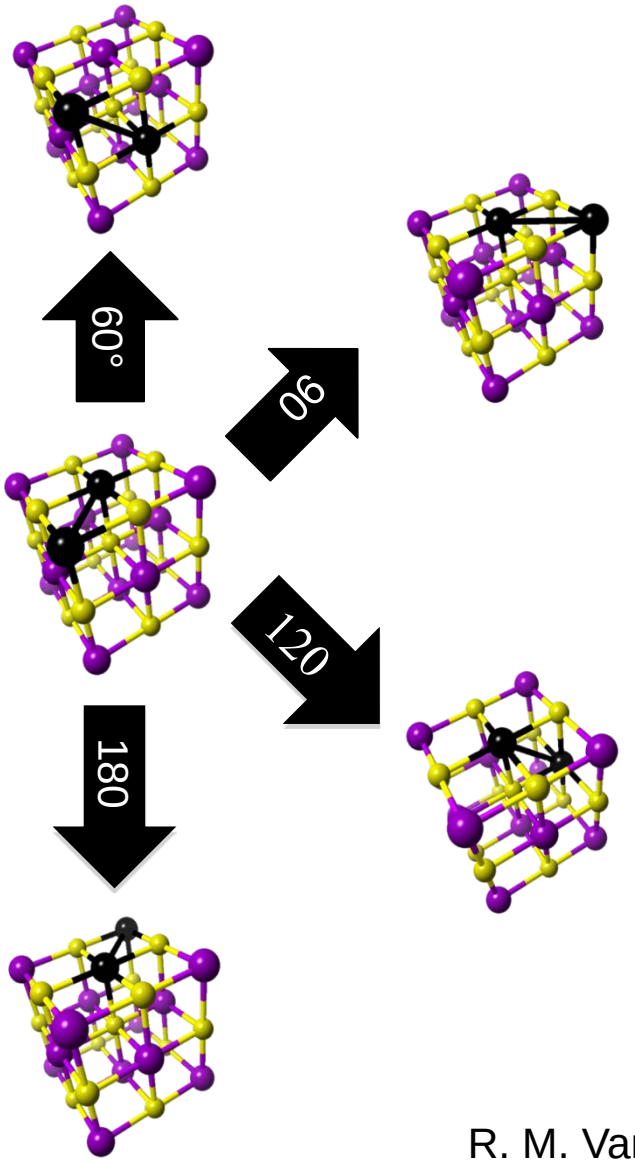

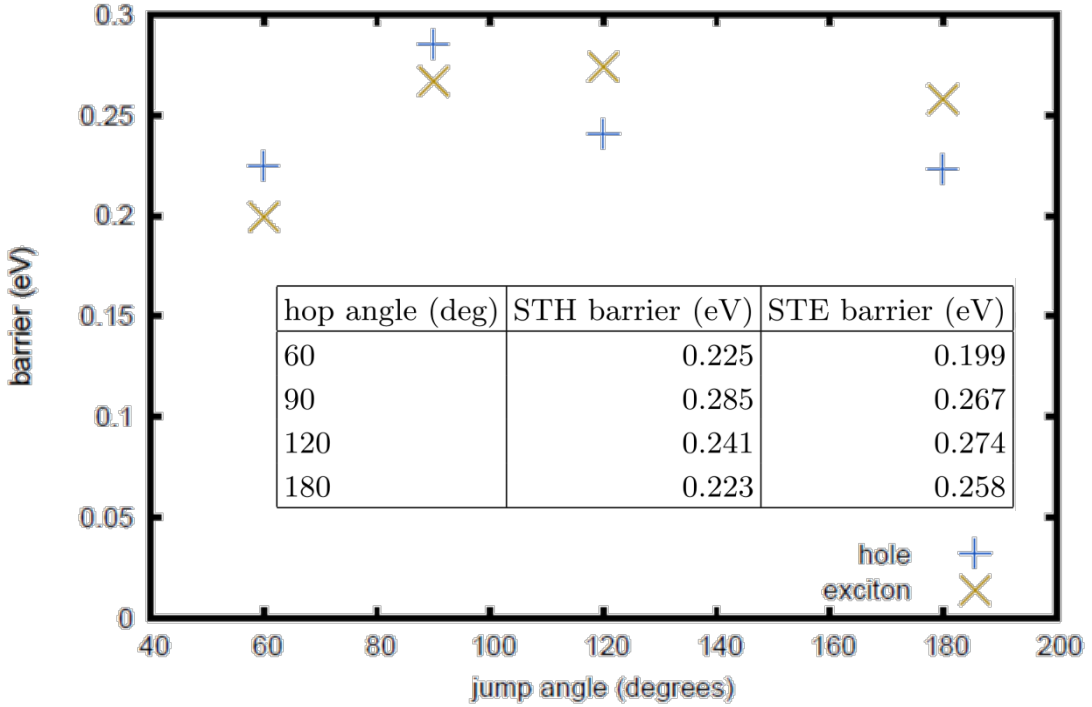

hop angle (deg)	STH barrier (eV)	STE barrier (eV)
60	0.225	0.199
90	0.285	0.267
120	0.241	0.274
180	0.223	0.258

- Calculations predict STEs and STHs are equally mobile in NaI.
- Calculated energy barriers used to describe STE/STH diffusion in NaI.
- MP2 barriers of Derenzo and Weber used for STE/STH diffusion in CsI.

R. M. Van Ginhoven, M. P. Prange, N. Govind

Pacific Northwest NATIONAL LABORATORY

Scintillation efficiency

NaI:0.1 mol% Tl – 5.9 eV excitation

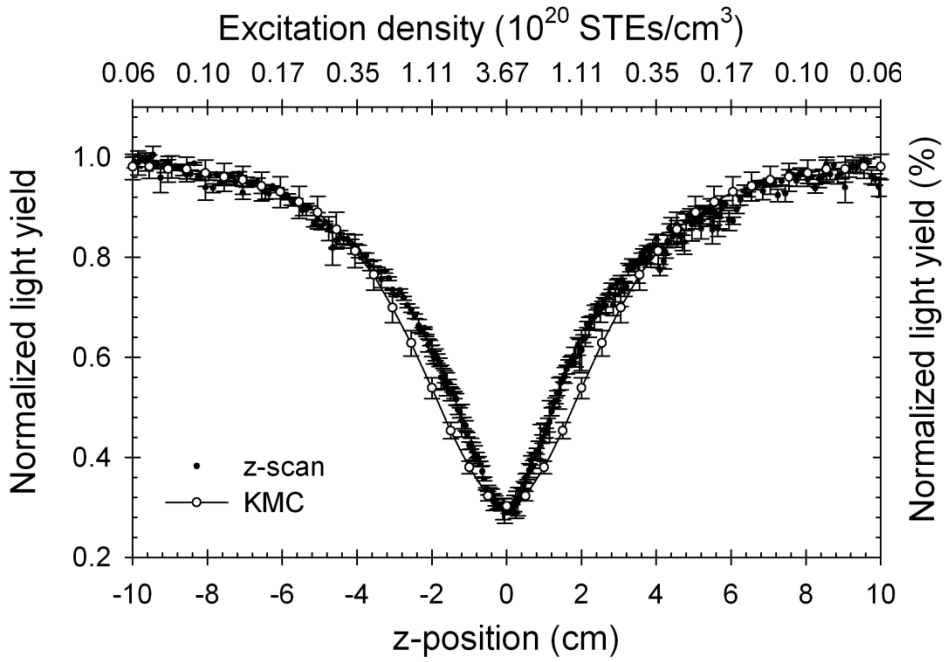

CsI:0.3 mol% Tl – 5.9 eV excitation

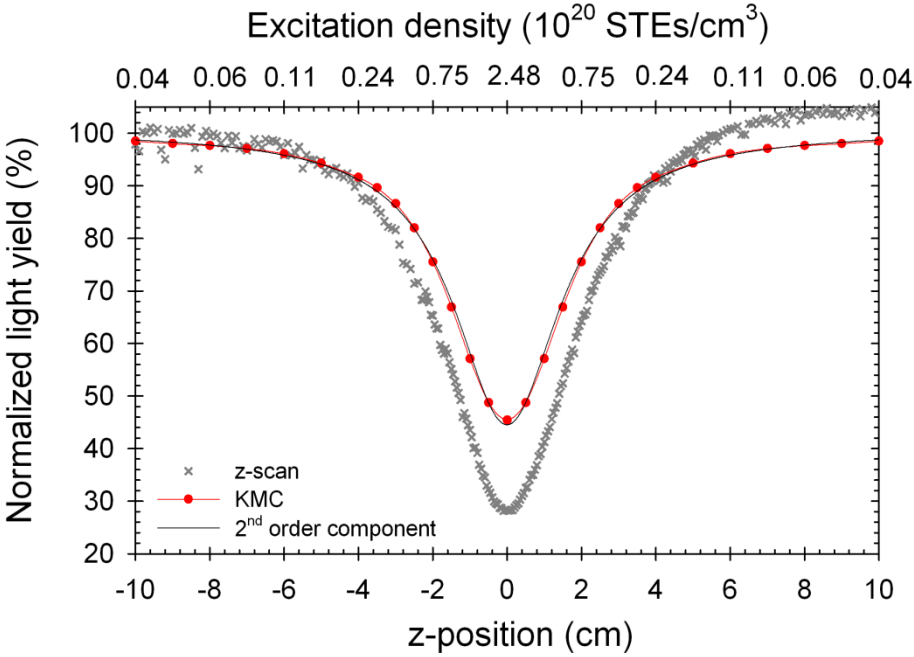

R_{dd} values

NaI(Tl) = 2.91 nm

Grim et al.[1] (analytical) = 2.9 nm

CsI(Tl) = 3.66 nm

Grim et al.[1] (analytical) = 3.8 nm

- For NaI, small differences likely due to the assumption of flat transverse profile
- CsI(Tl) does not follow purely 2nd-order quenching: contribution from 3rd order

[1]J.Q.Grim et al. (2013) *Phys. Rev. B* **87** 125117

Pacific Northwest NATIONAL LABORATORY

Time evolution of e-h pair population

NaI:0.1 mol% Tl – 5.9 eV excitation

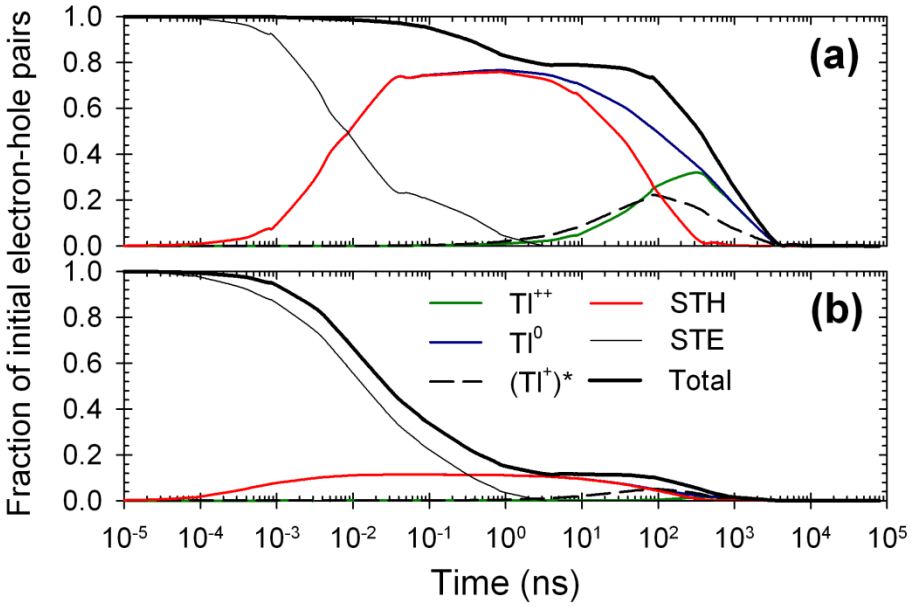

CsI:0.3 mol% Tl – 5.9 eV excitation

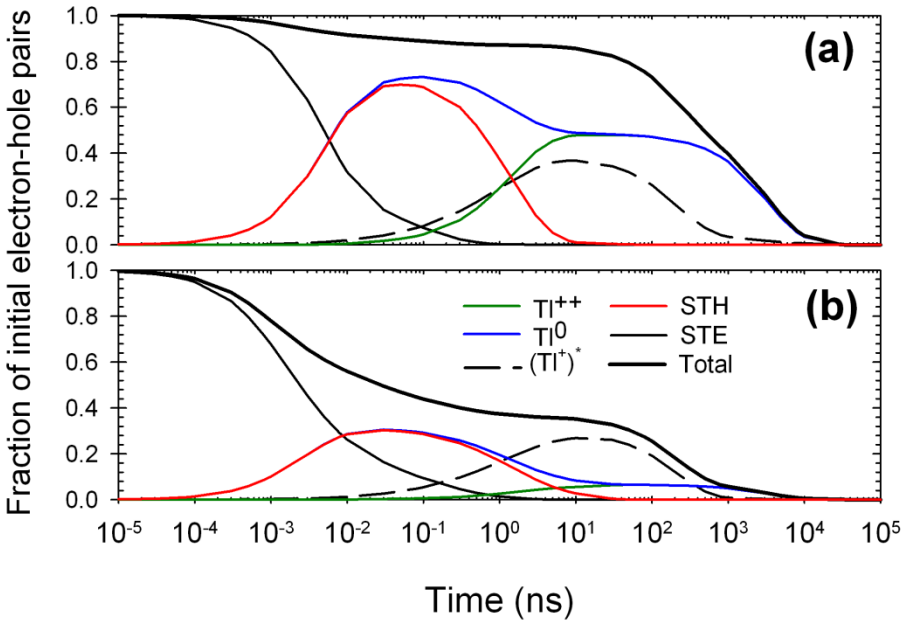

Simulations allow for determining time evolution of relevant species (STE,STH, Tl^0, $(Tl^+)^*$,…).

STE population initially decreases due to STE emission, Förster transfer, and thermal dissociation (which leads to the formation of STHs and Tl^0 sites).

All STEs disappear within 2-3 ns.

Pacific Northwest
NATIONAL LABORATORY

Scintillation kinetics

Same parameter sets also yield agreement with the experimental kinetics of scintillation.

CsI:0.3 mol% Tl – 5.9 eV excitation

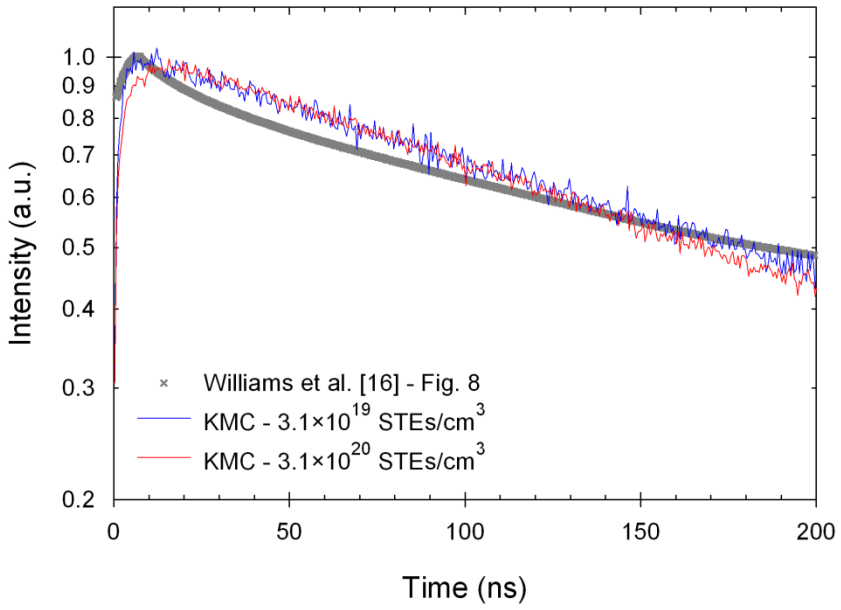

- Rising time of 5-10 ns.
- No quenching of $(Tl^+)^*$ emission.

Pure CsI – 5.9 eV excitation

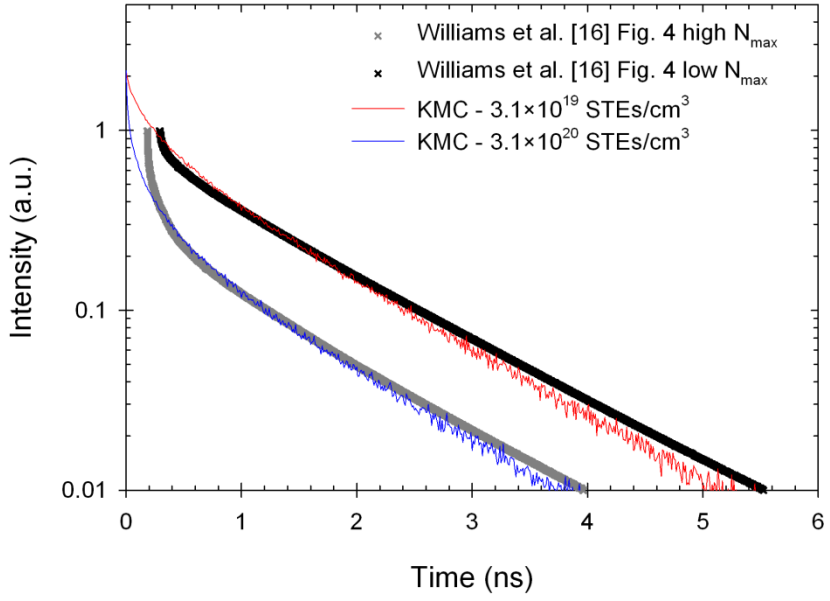

- STE formation time not included.
- Fast initial decay followed by exponential decay.

Exp. data: R.T. Williams et al. (2011) *Phys. Status Solid B* **248** 426

Pacific Northwest NATIONAL LABORATORY

γ-ray excitation: scintillation kinetics

High incident γ-ray energy

Assumes no nonlinear quenching
STE/STH proportion deduce from thermalization calculations

NaI:0.1 mol% Tl – 662 keV γ-rays

Exp. data: Moszynski NIM A 2006

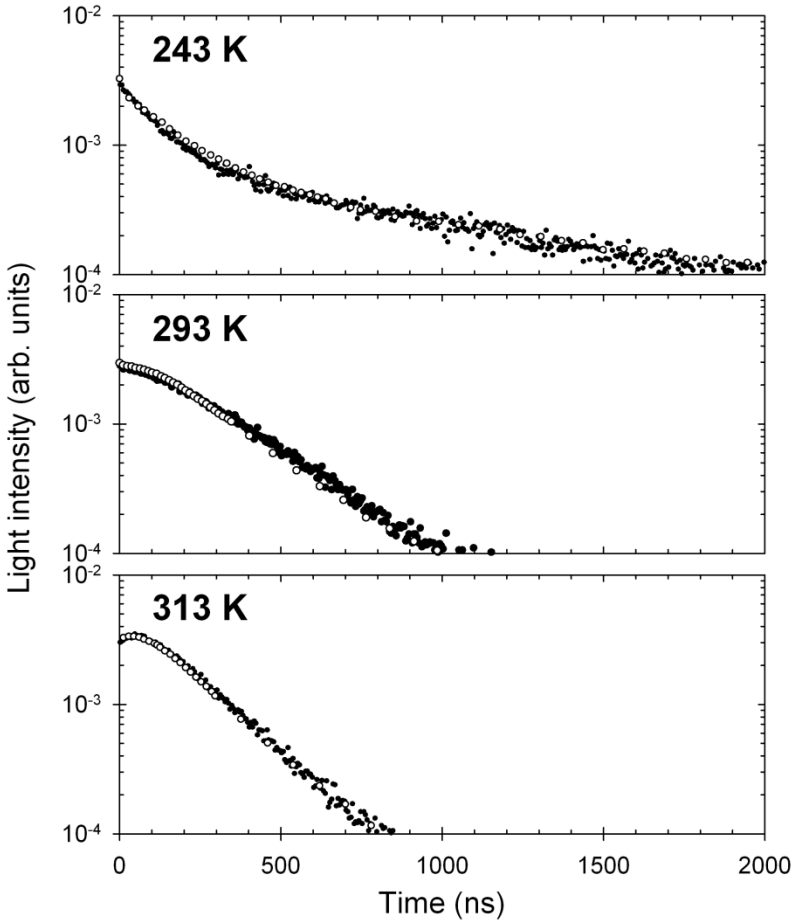

CsI:0.1 mol% Tl – 511 keV γ-rays

Exp. data: Valentine NIM A 1993

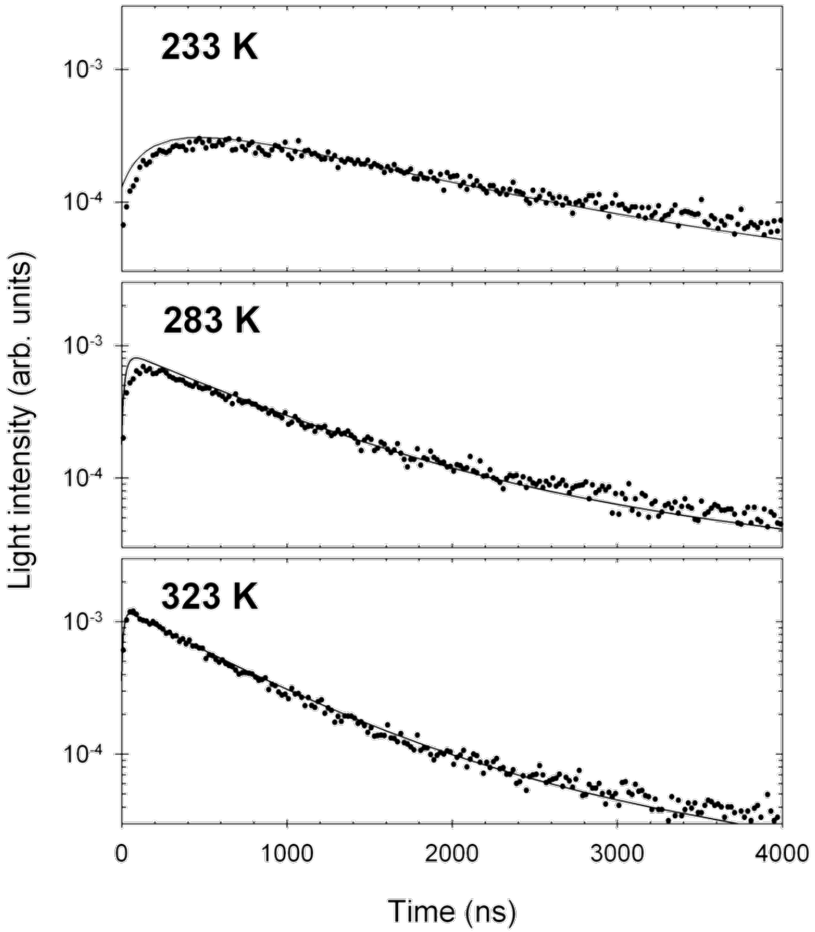

γ-ray excitation: scintillation kinetics

Contributions of different processes in KMC simulations help identify underlying mechanisms

NaI:0.1 mol% Tl – 662 keV γ-rays

Exp. data: Moszynski NIM A 2006

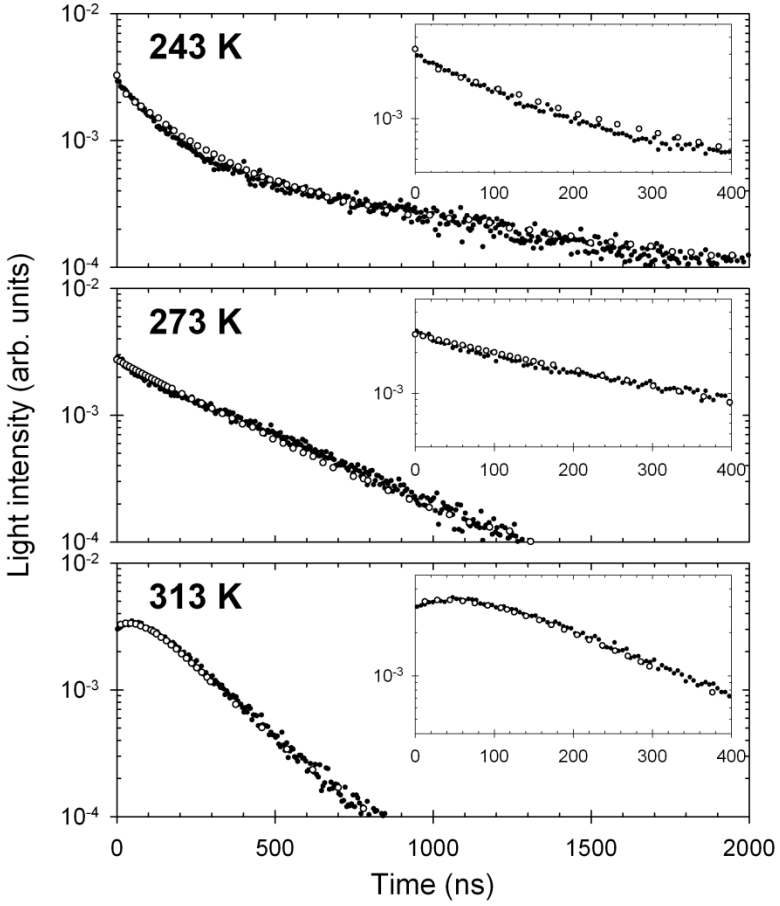

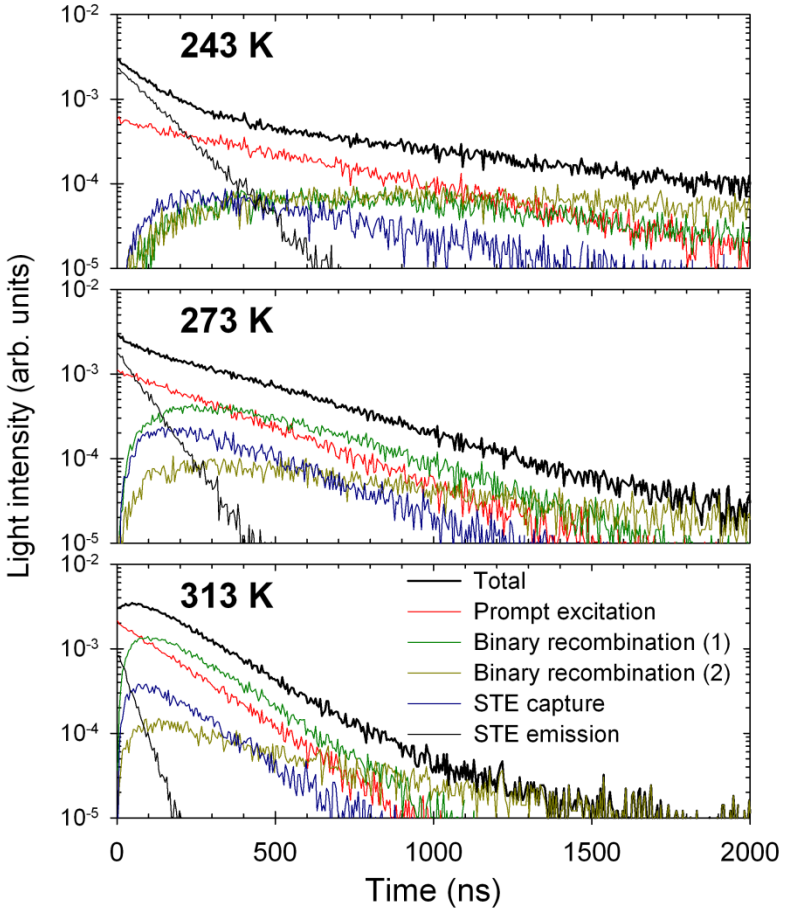

γ-ray excitation: Tl concentration

Tl-doped NaI – 662 keV γ-rays

Exp. data: Kubota JPSJ 1998

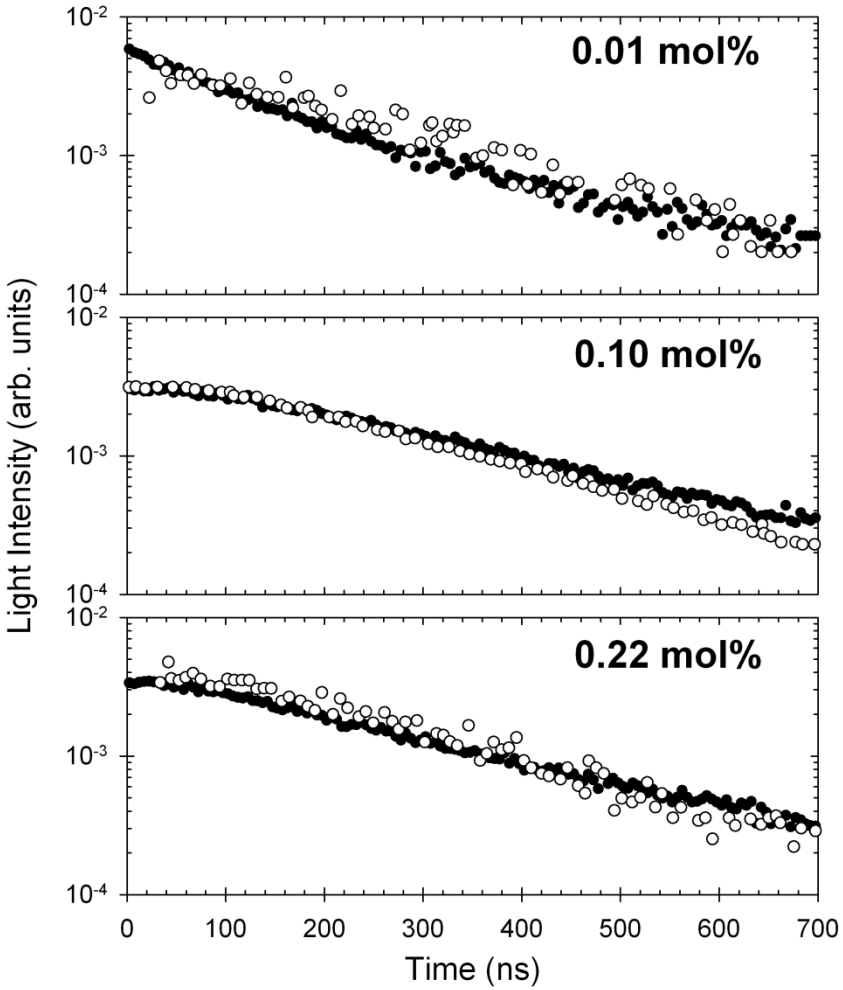

KMC model also allows for simulating kinetics and efficiency of scintillation at high incident γ-ray energy as a function of Tl concentration.

Tl-doped NaI – 662 keV γ-rays

Exp. data: Kubota JPSJ 1998

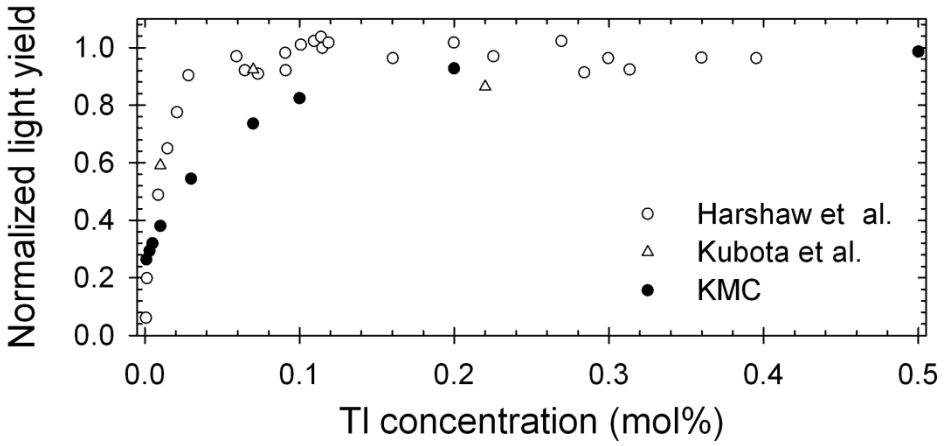

- Increase the proportion of 'stopped' electrons leads to decrease in yield with decreasing Tl concentration.

Pacific Northwest
NATIONAL LABORATORY

Scintillation modeling: publications

Kinetic Monte Carlo Model of Scintillation Mechanisms in CsI and CsI(Tl)
S. Kerisit, K.M. Rosso, B.D. Cannon
IEEE Transactions on Nuclear Science **55**, 1251 (2008)

Kinetic Monte Carlo Simulations of Excitation Density Dependent Scintillation in CsI and CsI(Tl)
Z. Wang, R.T. Williams, J.Q. Grim, F. Gao, S. Kerisit
Physica Status Solidi B **250**, 1532 (2013)

Kinetic Monte Carlo Simulations of Scintillation Processes in NaI(Tl)
S. Kerisit, Z. Wang, R.T. Williams, J.Q. Grim, F. Gao
In review

Conclusion: general model approach

composition
γ-ray cross sections
e cross sections

NWEGRIM

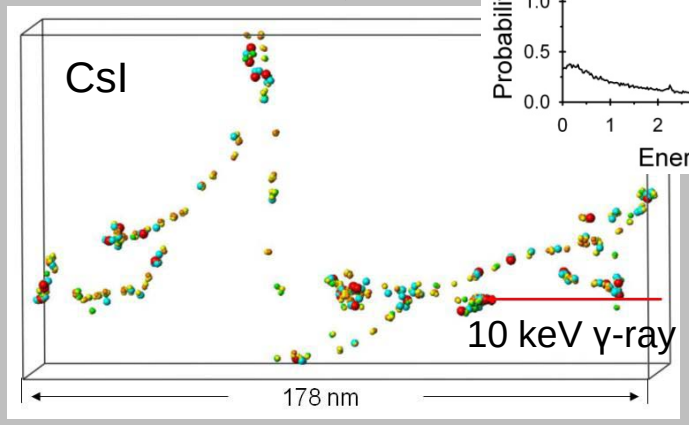

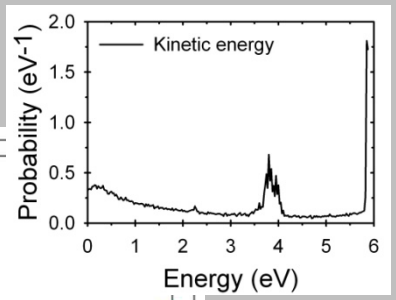

Spatial and kinetic e-h distributions

MCT

Thermalized e-h distributions

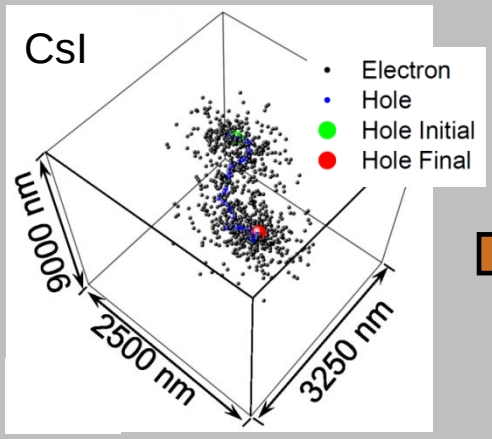

KMC

Radiation response

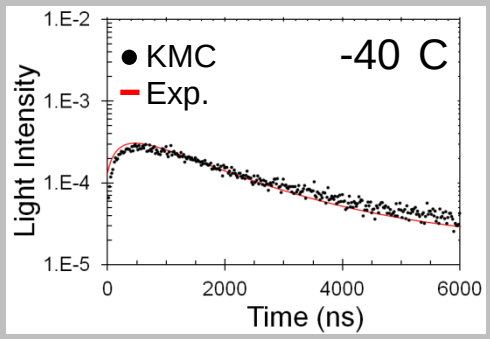

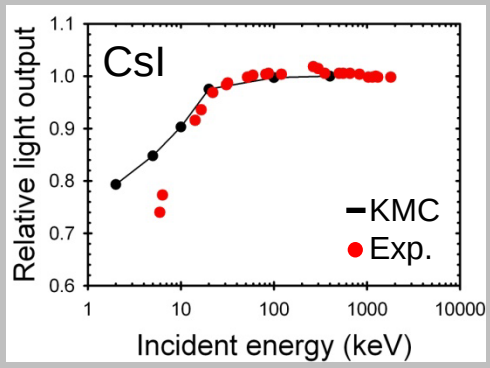

Pacific Northwest
NATIONAL LABORATORY

Proudly Operated by Battelle *Since 1965*

U.S. DEPARTMENT OF
ENERGY

902 Battelle Boulevard
P.O. Box 999
Richland, WA 99352
1-888-375-PNNL (7665)
www.pnnl.gov